Interactions of Proteins with Soft Polymeric Surfaces: Driving Forces and Kinetics

D i s s e r t a t i o n

zur Erlangung des akademischen Grades

d o c t o r r e r u m n a t u r a l i u m

(Dr. rer. nat.)

im Fach Chemie

eingereicht an der

Mathematisch-Naturwissenschaftlichen Fakultät I

der Humboldt-Universität zu Berlin

von

Dipl.-Chem. Nicole Welsch

Präsident der Humboldt-Universität zu Berlin:
Prof. Dr. Jan-Hendrik Olbertz

Dekan der Mathematisch-Naturwissenschaftlichen Fakultät I:
Prof. Stefan Hecht, PhD

Gutachter:
1. Prof. Dr. Matthias Ballauff
2. Prof. Dr. Nikolaus P. Ernsting

eingereicht am: 21.06.2012

Tag der mündlichen Prüfung: 23.10.2012

The important thing in science is not so much to obtain new facts as to discover new ways of thinking about them.

Sir William Bragg

Meiner Familie

Abstract

In the present work the thermodynamics and the kinetic mechanism of protein adsorption to charged and uncharged microgels of colloidal dimension were explored. Due to the potential biotechnological applications of systems at nano-scale the study of the interactions between nanoparticles and biomolecules has become in important research area in nanotechnology. The microgel systems used consist of a polystyrene core onto which a cross-linked network of N-isopropylacrylamide (NiPAm) and varying amounts of acrylic acid is attached. This soft polymeric layer is sensitive towards changes of the temperature, *pH* value and salt concentration of the solution which results in a drastic volume change upon change of one of these triggers. The adsorption process was studied using different proteins, that is, *β*-D-glucosidase from *almonds*, lysozyme from *chicken egg white* and cytochrome c from *bovine heart*. Generally, the secondary structure of these proteins was significantly retained after immobilisation regardless of the charge state of the microgels employed. This may be ascribed to the high flexibility of the microgel networks. Moreover, unlike protein adsorption onto solid surfaces immobilisation into the networks did not compromise the catalytic activity of the proteins. Actually, an enhanced activity was found for some cases. The thermodynamic analysis performed by isothermal titration calorimetry (ITC) and structural investigations by Fourier transform infrared (FT-IR) spectroscopy experiments led to the identification of the main driving forces of protein adsorption. Electrostatic and/or hydrophobic interactions play an important role depending on the charge density of the microgels. Further studies showed that proteins bound to negatively charged gel networks regulate their charge according to the electrostatic potential and to the lowered local *pH* value around the hydrogels. Fluorescence spectroscopy experiments with fluorescent-tagged proteins were suitable to analyse the kinetic uptake of the proteins into the gel networks as well as the reversibility of binding. It was demonstrated that bound proteins are dynamically exchanged by proteins in solution which justifies the application of equilibrium binding models to quantify the adsorption data. Moreover, the adsorption of proteins proceeds in two steps: i) a fast, diffusion-limited binding regime in which the majority of proteins is bound and ii) a second slow binding regime. The latter may be caused by the rearrangement of the proteins within the gel network as direct consequence of the protein-induced microgel shrinkage. The adsorption experiments were extended to binary protein mixtures in order to study competitive protein adsorption. On the basis of the thermodynamics of the adsorption of single proteins a simple theoretical model was developed which is able to predict the adsorption of one protein in presence of other proteins at equilibrium. Thus, it was possible to exactly calculate the composition of proteins which adsorb to the microgel particles after exposure to a solution containing several proteins.

Key words: protein adsorption, nanotechnology, microgels, stimuli-sensitivity, thermodynamics, catalysis, kinetics, reversibility, competitive adsorption

Zusammenfassung

Im Rahmen der vorliegenden Arbeit wurde die Thermodynamik und Kinetik der Proteinadsorption auf neutralen sowie geladenen, kolloidalen Mikrogelen untersucht. Die Analyse der Wechselwirkung zwischen Nanopartikeln und Biomolekülen ist wegen der vielfältigen Anwendungsmöglichkeiten dieser Systeme in der Biotechnologie ein wichtiges Teilforschungsgebiet der Nanotechnologie geworden. Die hier verwendeten Mikrogele bestehen aus einem Polystyrolkern, auf dem ein Netzwerk aus N-isopropylacrylamid (NiPAm) und unterschiedliche Mengen an Acrylsäure aufpolymerisiert ist. Die weiche polymere Schicht reagiert mit großen Volumenänderungen auf Änderungen der Umgebungstemperatur, des *pH*-Wertes oder der Salzkonzentration. Für die Adsorptions-Untersuchungen wurden drei verschiedene Proteine herangezogen: *β*-D-Glucosidase aus *Mandeln*, Lysozym aus *Hühnereiweiß* und Cytochrom c aus *Rinderherz*. Untersuchungen mit Fourier-Transform-Infrarotspektroskopie (FT-IR) zeigten, dass generell die native Sekundärstruktur der Proteine, die auf den Mikrogelen adsorbiert wurden, erhalten blieb. Dies könnte eine Folge der hohen Flexibilität des Mikrogel-Netzwerkes sein. Im Gegensatz zur Proteinadsorption auf festen Oberflächen wurde zudem eine hohe katalytische Aktivität der Enzyme nach der Immobilisierung verzeichnet, die gegenüber derjenigen der freien Enzyme in manchen Fällen sogar erhöht war. Des Weiteren wurden die Triebkräfte des Adsorptionsprozesses mithilfe thermodynamischer Analysen und struktureller Untersuchungen identifiziert. Hierzu kamen die isothermale Titrationskalorimetrie (ITC) und FT-IR Spektroskopie zum Einsatz. Abhängig von der Ladungsdichte der verwendeten Mikrogele sind dabei elektrostatische und/oder hydrophobe Wechselwirkungen entscheidend. Weitere Untersuchungen zeigten, dass im Falle von geladenen Mikrogelen das elektrostatische Potential wie auch der abgesenkte lokale *pH*-Wert innerhalb des Netzwerks eine Änderung des Ladungszustands der adsorbierenden Proteine zur Folge hat. Zusätzlich konnte mithilfe der Fluoreszenzspektroskopie und Fluoreszenz-markierter Proteine die kinetische Aufnahme in die Mikrogele als auch die Reversibilität der Reaktion analysiert werden. Es wurde dabei ein dynamischer Austausch zwischen gebundenen und freien Proteinmolekülen nachgewiesen, welcher die Verwendung von Gleichgewichtsmodellen für die Beschreibung der Proteinadsorption rechtfertigt. Außerdem erfolgt der Vorgang in zwei Schritten: i) ein schneller diffusionslimitierter Schritt, in dem der Hauptteil der gesamten Proteinmenge bindet und ii) ein anschließender wesentlich langsamerer Bindungsvorgang. Letzterer resultiert vermutlich aus der Umstrukturierung der bereits gebundenen Proteine im Gel, der sich der Schrumpfung des Mikrogels als Folge der Proteinadsorption anschließt. Die Adsorptionsexperimente wurden anschließend auf Untersuchungen in binären Proteinmischungen ausgedehnt, um die kompetitive Proteinadsorption zu studieren. Dazu wurde ein einfaches Modell entwickelt, das auf den thermodynamischen Resultaten der Adsorption von Proteinen einer Sorte basiert. Letzteres ermöglicht die Vorhersage der Gleichgewichts-Adsorption in Anwesenheit anderer Proteine. Somit konnte die Zusammensetzung der an dem Mikrogel gebundenen Proteine berechnet werden, nachdem das Mikrogel einer Lösung verschiedener Proteine ausgesetzt war.

Schlagwörter: Proteinadsorption, Nanotechnologie, Mikrogele, Stimuli-Sensitivität, Thermodynamik, Katalyse, Kinetik, Reversibilität, kompetitive Adsorption

Table of Contents

1 The Nano-Bio Interface

Since the development of new synthetic routes for the fabrication of materials at nanoscale with defined physico-chemical properties (*e.g.*, surface charge, geometry, size distribution, etc…) [1], nanoparticles have been object of intense scientific investigation. The reason for their significant scientific and technological impact are their unique size-related properties. Colloidal objects have extremely high surface-to-volume ratios and, thus, exhibit very large interfaces with the surrounding medium. As a consequence these systems show an enhanced chemical reactivity towards components in solution in comparison to the bulk material. This demonstrates the potential superiority of colloidal systems in catalysis and purification processes [2-4] but also in other areas, such as diagnostics, cosmetics, pharmaceutics and food processing. [2-3,5-10] Furthermore, nanoparticulate systems are small enough to interact with the cellular machinery and potentially reach targets which are inaccessible otherwise. Thus, they are ideal drug-delivery systems which direct drugs towards a particular pathway. [11-17] Additionally, immobilisation in the drug-delivery carriers may reduce severe side effects of the payload and may facilitate the use of water-insoluble and labile drugs.

For many applications of colloids, immobilisation of (bio)molecules in colloidal systems, such as proteins, protein-based drugs and DNA/RNA, has become an important field of applied research. Therefore different immobilisation routes have been tested for their use in biotechnological applications each having its own benefits and disadvantages. The main immobilisation techniques are depicted in Figure 1.1. Among these the encapsulation of biomolecules into microcapsules is a well-established technique. [12,18-20] The capsules can be formed from amphiphilic block-copolymers or lipids which self-assemble into vesicles [21] or from the layer-by-layer deposition [18,22] of oppositely charged polyelectrolytes onto templates which are dissolved afterwards. Immobilisation of proteins can be achieved by preloading ([23]; that is, during the formation of the capsule) or post loading of the microcapsules ([24]; *i.e.*, after formation of the capsule). Another possibility of immobilisation is the embedding of biomolecules into membranes [25] or between oppositely charged polyelectrolytes [26-28]. By this strategy, the amount of the immobilised protein can be easily controlled by the number of polyelectrolyte layers deposited.

Covalent attachment [29-32] of biomolecules to the carriers should be preferred for applications with varying experimental conditions in order to prevent leaching of the biomacromolecules upon changing

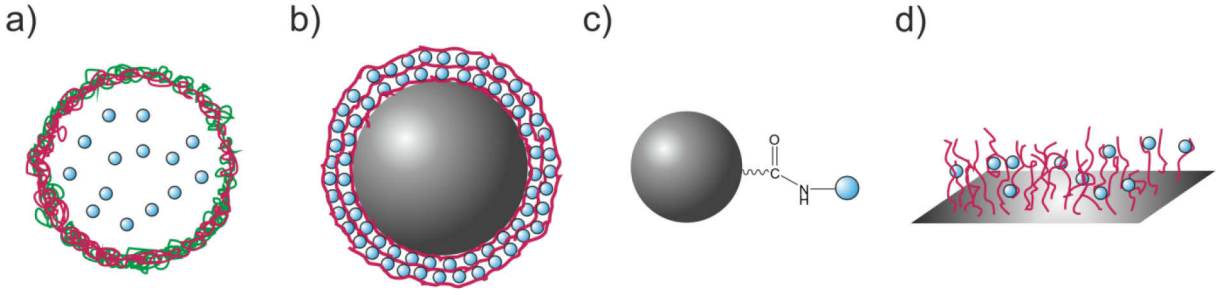

Figure 1.1: Techniques for the immobilisation of biomolecules: a) encapsulation; b) embedding; c) covalent attachment; d) physical adsorption.

of the salt concentration or the *pH* value of the solution. Physical adsorption of biomolecules to surfaces is the simplest method for immobilisation of biomolecules regarding the experimental setup. [33-37] However, there are many interactions between the biomolecule and the surface, such as electrostatic forces and van der Waals interactions, which contribute to the binding reaction and which make the control over this process challenging. As a consequence, colloidal particles incubated in biological media, such as blood, are immediately covered by biomolecules, *e.g.*, proteins, lipids and small molecules, in order to reduce the surface energy. [38-44]

The so-called "protein corona" formed on nano- and microscopic systems largely defines the biological identity of the particles rather than the bare surface. [38,40] Its composition is highly dependent on the surface characteristics of the colloidal particle as well as on the constitution of the biological fluid as shown in Figure 1.2 a. [10] Moreover, it is decisive for the interactions with specific cell types and for the uptake and clearance of the particle as well as for pathobiological responses (Figure 1.2 b). [44-46] For example the adsorption of some proteins may induce blood coagulation (such as prothrombin) or promote removal of the particles by cells of the mononuclear phagocyte system MPS (*e.g.*, opsonins). [45,47-48] Clearance by the MPS finally concentrates particles in the liver and spleen and increases the risk of negative long-term effects. Additionally, binding of proteins to the surface of the nanoparticle may induce misfolding of the bound protein with perturbation of the protein´s biological function as direct consequence. Thus, unfolding of adsorbed proteins may trigger

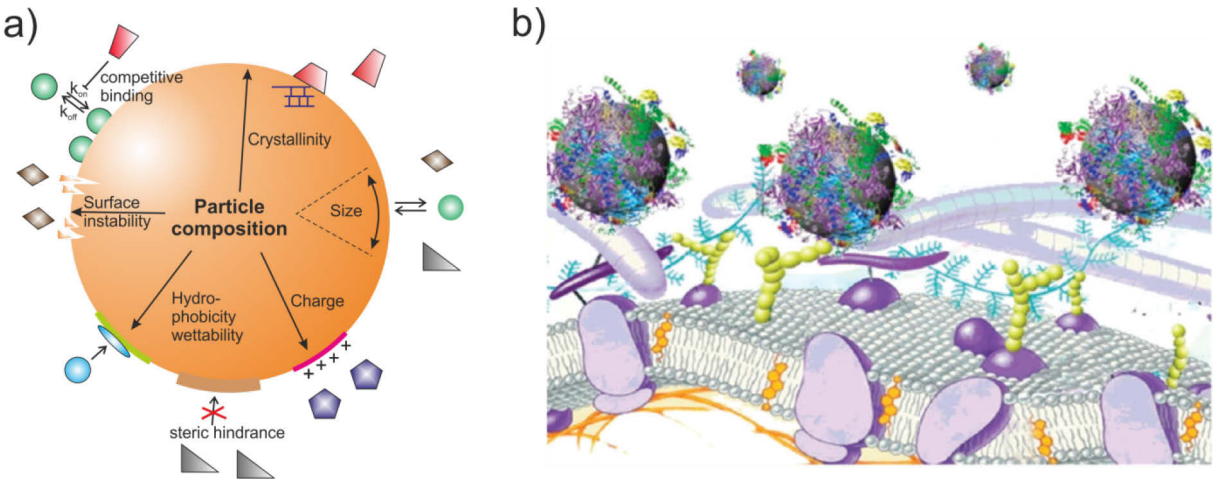

Figure 1.2: a) Schematic representation of the formation of the protein corona around a colloidal particle. The composition of the protein corona depends on the properties of the nanomaterial, *e.g.*, size, hydrophobicity, wettability, charge and crystallinity. The hydrophobicity of the particle surface is important for the protein conformation in the bound state. Protein adsorption may lead to dissolution of compounds initially adsorbed on the particles surface. Protein on and off rates (k_{on}, k_{off}) depend on the material type and protein characteristics. Proteins in the biological medium compete for the same binding site. The concentration of proteins in the fluid and the composition of the biological fluid are crucial for the formation of the protein corona. Adapted by permission from Macmillan Publishers Ltd: Nel, A. E.; Madler, L.; Velegol, D.; Xia, T.; Hoek, E. M. V.; Somasundaran, P.; Klaessig, F.; Castranova, V.; Thompson, M. *Nat. Mater.* **2009**, *8*, 543-557. Copyright © 2009. b) Sketch of the possible interaction/exchange scenarios of colloidal particles covered with a protein corona at the cellular level. Reprinted with permission from Walczyk, D.; Bombelli, F. B.; Monopoli, M. P.; Lynch, I.; Dawson, K. A. *J. Am. Chem. Soc.* **2010**, *132*, 5761-5768. Copyright © 2010, American Chemical Society.

the immune system as well as contribute to the progress of severe misfolding-induced diseases. [9,49-52]

In contrast, the adsorption of specific proteins in their native structure has been shown to promote prolonged circulation times in blood. [45,53] Furthermore, adsorption of lipoproteins, *e.g.*, apolipoprotein, mediates the transport of the particles across the blood brain barrier in living animals [54] stressing the beneficial effects of specific protein adsorption. These experimental findings demonstrate that adsorbed proteins are of central importance when discussing issues related to nanotoxicity. [9,45,47,55-57] For this reason, modelling of the interactions between proteins and the interface of colloidal particles has become a key issue for the safety assessment of these systems. [58-59] Thus, the importance of protein adsorption to nanotechnology has led to a vast amount of literature. Many researchers investigated the interactions between the surface of bare latex- and silica particles with single protein solutions or with a proteome. [33,37,39-40,46,60-65] In analogy, the interactions of proteins with stabilised metal-nanoparticles [5,38,44,49,58,66-67], polymer coated particles [68-69] and vesicles, *e.g.*, liposomes [70], have been studied. In many cases structural changes of proteins bound to these surfaces were observed which were related to the size, charge and surface curvature of the particles.

Binding of proteins is extended to three dimensions when polymer chains are affixed to the colloidal particle surface (referred to as spherical polymer brush, Figure 1.3 a) or when hydrogel particles (Figure 1.3 b and c) are used as carriers. It has been shown that brush layers of poly(ethylene oxide) or zwitterionic polymers are able to suppress or minimise protein adsorption [8,71]. For this reason, they are usually attached to the particles to gain minimum immune response and prolonged circulation times in biological media. [45,72] On the other hand, brushes of polyelectrolytes attached to the particle surface as well as hydrogel particles have shown to exhibit high capacities for proteins. [73-75] For example, Wittemann *et al*. used well-defined spherical polyelectrolyte brushes (SPB) to analyse binding of various proteins as a function of salt concentration in quantitative manner. [73,76-78] Moreover, it was demonstrated that the native conformation of adsorbed proteins was largely retained which points to reversible protein binding. [79-80] The retention of the native protein structure of proteins bound to brushes may be ascribed to the flexible polyelectrolyte chains of the SPB. In comparison to flat surfaces, the charged polymer chains are able to rearrange around the protein to optimise the interactions with the biomolecule while preserving the native protein structure. Thus, soft polymeric layers including brushes and gel networks may generally be suitable to adsorb

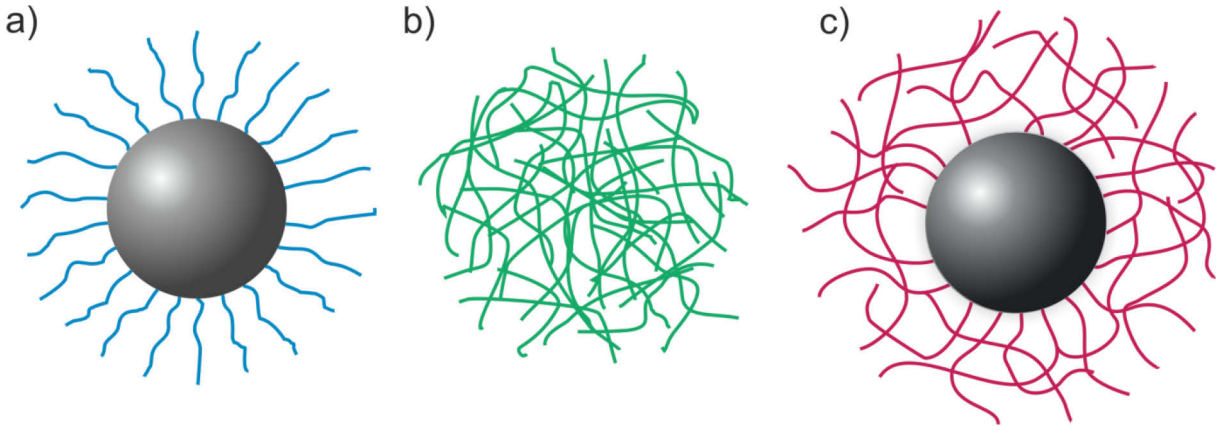

Figure 1.3: Schematic representation of a a) spherical polyelectrolyte brush (SPB, charges not shown); b) hydrogel network, and c) core-shell microgel.

proteins from solution in their native conformation.

The ultimate goal of this research is to control the composition of the protein corona or even its prediction as function of the composition of proteins in solution. However, this is a challenging task as binding of proteins on surfaces is a complex dynamic process. Thus, in order to fully understand these interactions, the thermodynamics of protein binding, the kinetics of adsorption and desorption as well as the exchange of bound proteins by proteins from solution have to be analysed.

For the determination of the thermodynamic binding parameters the question arises whether the adsorption of proteins to a given surface may be regarded as an equilibrium phenomenon. In contrast to irreversible binding reactions, reversible binding can be quantitatively described by equilibrium binding isotherms, *e.g.*, the Langmuir isotherm. [81] In addition, the protein on/off rates are strongly dependent on the carrier system and on the protein characteristics. [10] In particular, the time required for a certain protein to bind to different systems may vary between seconds and hours. [69,82-83] Due to this complexity, only a few studies were devoted to the analysis of the thermodynamics and/or kinetics of protein binding. [66,69,84-85] For example Henzler *et al*. quantified both the thermodynamic driving forces [84] and the kinetic mechanism [82] for protein adsorption on the SPBs previously introduced by Wittemann *et al*. [73] By combining the experimental findings with theoretical considerations it was shown that the protein molecules exhibit a subdiffusive behaviour in a layer of tethered polyelectrolytes. [82] Moreover, thermodynamic studies demonstrated that binding is driven by the gain of entropy. The latter is mainly caused by the release of counterions from the polyelectrolytes of the SPB as well as from the protein surface. [84]

Protein adsorption from protein mixtures, *e.g.*, blood plasma, is even more complex. There are a large number of proteins that may adsorb from the serum to a given colloidal system and the extent of adsorption will also depend markedly on their concentration and the temperature. Moreover, the protein corona may undergo dynamic changes and protein molecules bound to the particle surface in the early stage may be exchanged by others and this process may take seconds to hours. [38,43,86-87] In plasma, the time-dependent exchange of abundant but weakly binding proteins by more strongly binding proteins that are present with lower concentration is termed as Vroman-effect [87-91] and was already discovered in 1969 [92-93]. However, there have been only a few attempts to develop a quantitative description of the Vroman effect and of competitive protein binding in general. [59,86-87,90] This inquiry demonstrates the lack of knowledge of the mechanism of protein binding and the need of further in-depth investigation.

2 Objective of this Thesis

The work of this thesis focuses on the exploration of the mechanism of protein adsorption onto soft polymeric surfaces. The main interest of this study is to gain information on the thermodynamics of protein binding as well as on the kinetic mechanism of this process. Well-defined microgels of core-shell morphology and of colloidal size were synthesised to investigate these complex interactions. Unlike binding on solid surfaces, protein adsorption onto soft polymeric layers attached to colloidal particles may proceed without denaturation of the proteins. Thus, core-shell microgels may serve as excellent model systems for binding of proteins in their native conformation. The secondary structure and the activity of bound enzymes are analysed to verify this statement. In addition, the microgel systems used are designed to respond to different external stimuli. The properties of the microgel are specifically altered by changes of the surrounding solution, such as temperature, *pH* or salt concentration, which in turn modifies the interactions with proteins. The systematic investigation of protein adsorption to stimuli-sensitive core-shell microgels includes the following steps:

- The first part of this work is devoted to the adsorption of proteins to uncharged, thermo-sensitive microgels. This kind of system is switched from a hydrophilic and swollen state to a shrunken and more hydrophobic state upon temperature increase and vice versa. Therefore, the non-electrostatic interactions between proteins and a polymeric layer are analysed using different techniques such as isothermal titration calorimetry (ITC) and Fourier transform infrared (FT-IR) spectroscopy. This study is complemented by the analysis of the protein structure and catalytic activity.
- In another set of experiments protein adsorption on negatively charged core-shell microgels is investigated. These particles are sensitive towards changes of the *pH* value and the ionic strength of the solution and, to minor extent, to changes of the temperature. The role of both, hydrophobic and electrostatic interactions, in protein binding is explored by a systematic thermodynamic study. Due to the introduction of electrostatics also changes of the charge state of the proteins upon binding need to be verified in addition to the analysis of the secondary structure and the activity of adsorbed enzymes to obtain a full quantitative understanding of protein adsorption.
- Based on these results an experimental procedure is developed to investigate the kinetic uptake of proteins into the gel network. The experimental findings are then compared to a kinetic model which is compatible with the results of the thermodynamic analysis of protein adsorption. This line of reasoning is expected to give information on the driving forces of protein adsorption as well as on the kinetic binding mechanism.
- Additionally, experiments are performed which are aimed at assigning protein adsorption to microgels as reversible or irreversible process. This classification is essential to validate the application of equilibrium binding models to interpret the experimental adsorption data.
- Finally, the study of protein adsorption is extended to binding of protein mixtures in order to investigate the competitive adsorption process. This study represents the first analysis of competitive protein adsorption onto three-dimensional networks of colloidal dimension. On the basis of the experimental results gathered a simple theoretical model should be developed to predict the binding of protein mixtures at equilibrium.

3 Fundamentals and Theory

3.1 The Carrier System

3.1.1 Introduction to Stimuli-Sensitive Microgels

Microgels are composed of intramolecular cross-linked polymeric networks which can absorb large amounts of solvent. [94-95] Moreover, microgels which show high swelling capacities in aqueous media are classed among hydrogels. [94,96] Typically, microgels are of colloidal dimension and, thus, have diameters ranging between 10 nm and 1 µm. [94-95,97-98] Gels in the lower limit of this range are also termed as nanogels. However, gel particles with diameters of several microns up to 100 µm are sometimes referred to as microgels [75,99], too, indicating the lack of a universal definition of these systems. [100]

In this thesis, microgels in the size range < 500 nm have been applied as carrier systems for protein adsorption. These systems have several advantages towards macroscopic gels (> 1µm) and are well-suited to study the interactions with proteins. The main advantage of microgels in the submicron range over macroscopic gels is their very fast response to changes in the environment. This is due to the fact that the time constant of the swelling/deswelling process is directly proportional to the square of the geometrical dimensions of the investigated gel, as shown by Tanaka *et al.* [101] The response time of macrogels is in the range of minutes to hours whereas colloidal microgels reach the swelling-equilibrium within seconds. [101-102] In addition to the fast response, microgels are characterised by their extremely high surface area, their low viscosity and by their mechanical flexibility comparable to human tissue. [2,103] Due to these unique properties, microgels constitute a class of colloidal systems that have potentially important applications in *e.g.*, biomedicine and biotechnology. [3,94,98,104]

There is also a growing interest in microgels in terms of their ability to respond to chemical and physical stimuli. These so-called “smart” microgels can be fabricated from a variety of stimuli-sensitive polymers and functional monomers. [2,94,105-107] In presence of an external stimulus, *e.g.,* temperature, *pH* or ionic strength, “smart” microgels may experience large changes in their physicochemical properties, such as the swelling degree and polarity, resulting in a volume phase transition. [2,94,108-109] As a consequence, stimuli-sensitive microgels can adapt to the surrounding environment and may drastically change their interactions with components in solution. This makes them ideal for the regulated transport of (bio)molecules, for switchable catalysis and for sensing applications. [2,15,107,110-111]

In the domain of stimuli-sensitive microgels, the most commonly studied are thermo-responsive systems. [94,105,112] These microgels undergo dramatic changes in the network swelling as function of temperature due to the change of the solvent quality from good to poor, and vice versa. The most widely studied class of thermo-responsive microgels are those composed of the temperature-sensitive polymer poly(N-isopropylacrylamide) (pNiPAm) which exhibits a lower critical solution temperature (LCST) at ~ 32 °C and, thus, shows inverse solubility upon heating. [94-95,108,113] Due to its LCST

close to the body temperature, pNiPAm has been repeatedly used in studies of protein adsorption. [107,114-115]

Microgels synthesised from pNiPAm inherit the excellent temperature-response of the linear polymer and undergo a sharp volume phase transition from a highly swollen gel network to a shrunken (relatively hydrophobic) globule (Figure 3.1). [2,94]. This transition is accompanied by the release of water which has been hydrogen-bonded to the amide-chains of pNiPAm as well as by the release of hydrophobically structured water around the isopropyl groups of pNiPAm [2,94,105] Thus, the volume phase transition of pNiPAm-based microgels is endothermic and driven by the gain of entropy. [94,116] The corresponding temperature is termed as the volume phase transition temperature (VPTT) which is close to the LCST of the linear polymer. [94,102-103]

When microgels incorporate additional functional groups, such as *pH*-ionisable or redox-active groups, multi-responsive microgels are formed which generate fast and targeted swelling responses to multiple external signals. [97,108,117-119] Thus, combinations of temperature-sensitive polymers with such as *pH*-sensitive components offer further control over the phase behaviour. For example Bütün *et al.* synthesised microgels based on 2-(N-morpholino)-ethyl methacrylate (MEMA) which show response to the solution *pH*, temperature and ionic strength. [97] Additionally, nanomagnetic particles were immobilised into the pMEMA microgels resulting in the gain of responsiveness to the magnetic field. In addition to the design of multi-responsive systems of homogenous composition, microgels with advanced structures, such as core-shell morphology, are developed. [109,120] Core-shell microgels may be designed with either one compartment being stimuli-sensitive or with both compartments, core and shell, responding differently to external triggers. [108-109,121] Recently, Hu *et al.* have reported about the preparation of core-shell microgels containing a mechanically and thermodynamically decoupled temperature-sensitive core and a *pH*- and temperature-dependent shell. [121] Nayak *et al.* synthesised core-shell particles with degradable cores leading to hollow thermo-responsive microgels. [120] Thus, the design of multi-responsive microgels and microgels with core-

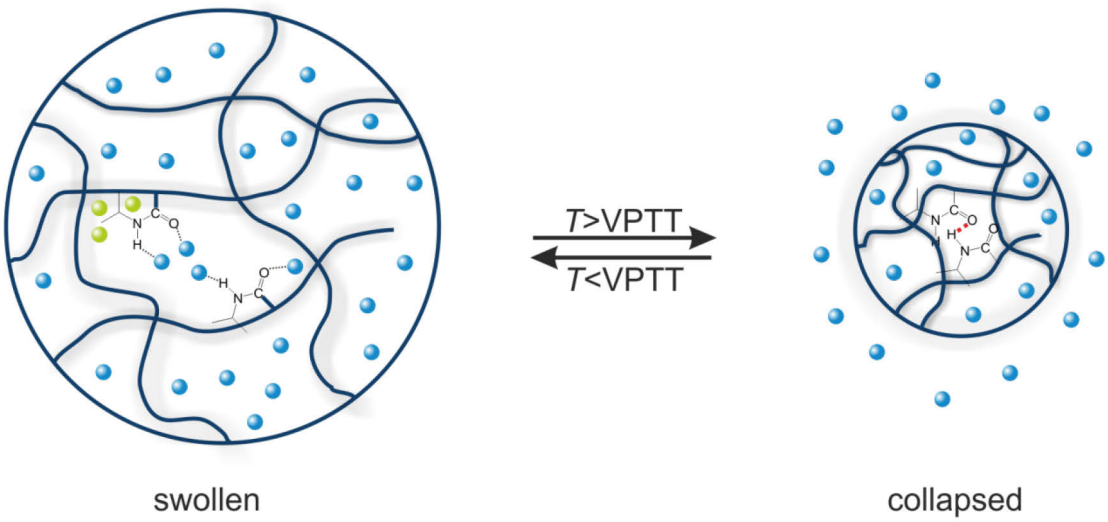

Figure 3.1: Schematic representation of the volume phase transition of pNiPAm-based microgels. Below the VPTT the microgel is swollen by water (blue spheres) where the amide groups of the microgel form hydrogen bonds with water molecules. Additionally, the hydrophobic isopropyl groups cause structuring of the water molecules in proximity of the alkyl groups (green spheres). Above the VPTT water is expelled from the microgels interior releasing the hydrophobically structured water molecules and some water bound to the amide groups.

shell structures gives access to multifunctional colloidal systems and to smart hybrid materials with stimulated interest in encapsulation and release applications. [118]

In the scope of this work, microgels of core-shell morphology are used to study the interactions with proteins (Figure 3.2 a). These microgels consist of a solid polystyrene (PS) core onto which a microgel network of cross-linked pNiPAm is attached. NiPAm was chosen as main monomer for the synthesis of the microgel shell since pNiPAm-based microgels show temperature-response close to the physiological temperature as well as low cytotoxicity. [94,122-124] The shell network of the microgel is typically 50 to100 nm thick and is affixed onto a PS core of ~100 nm in diameter, which defines a solid boundary of the network (Figure 3.2 a). Such core-shell particles represent cross-linked brushes onto defined spherical surfaces. Moreover, the colloidal dimension of the microgel shell ensures that the gel responds very rapidly to environmental stimuli and that a reaction taking place between the gel network and another component, *e.g.*, adsorption of a protein on the gel, reaches its equilibrium in short times. These properties clearly set this kind of gels apart from larger hydrogels which have been employed for protein binding studies earlier. [74-75,125-126]

The synthesis of the core-shell microgels follows a two-step approach established by Dingenouts and co-workers [127]: First, monodisperse PS particles with a thin shell of pNiPAm are synthesised by emulsion polymerisation. Then the microgel network is attached onto the PS core by a second seeded emulsion polymerisation reaction of the monomers NiPAm and N,N´-methylenebisacrylamide (BIS), which is carried out above the VPTT of the microgel. In addition to these uncharged microgels, microgels have been synthesised which carry a negative charge. The negative charges are appended into the microgel network by copolymerisation of the shell with acrylic acid (AAc).

The core-shell microgels have been analysed by several techniques, including dynamic light scattering (DLS), cryogenic transmission electron microscopy (Cryo-TEM), small angle x-ray scattering

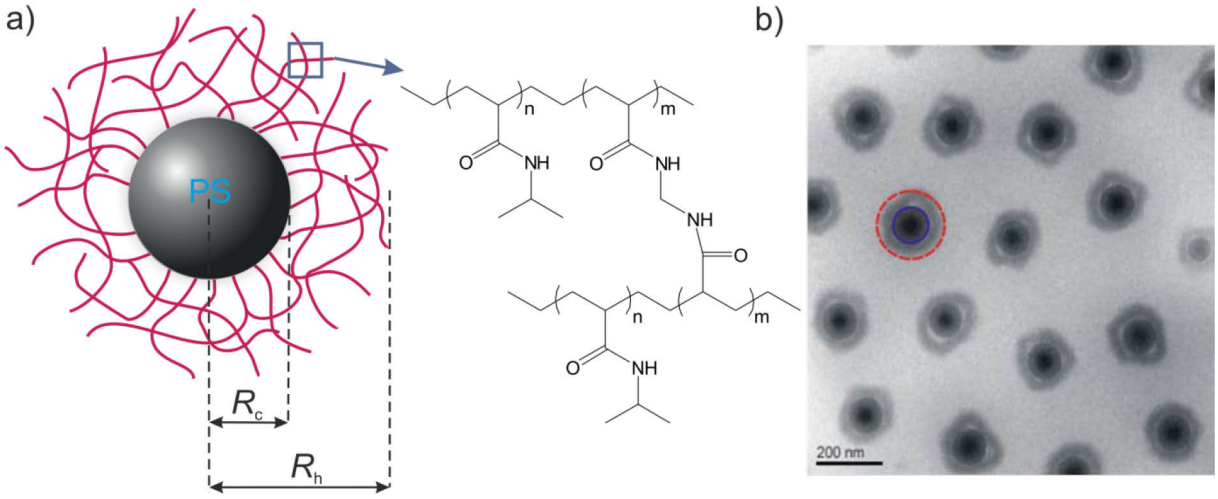

Figure 3.2: a) Schematic depiction of the core-shell microgels including the specific parameters and the chemical structure of the microgel shell. The core-shell microgel has an overall hydrodynamic radius R_h. The core of radius R_c consists of PS and the shell contains NiPAm as main monomer and BIS as cross-linker. b) Cryo-TEM micrograph of a 0.2 wt-% aqueous suspension of core-shell microgels containing 5 mol-% BIS. The sample was kept at room temperature, *i.e.*, below the VPTT, before vitrification. Reprinted from Crassous, J. J.; Wittemann, A.; Siebenburger, M.; Schrinner, M.; Drechsler, M.; Ballauff, M. *Colloid Polym. Sci.* **2008**, *286*, 805-812 with kind permission from Springer Science and Business Media.

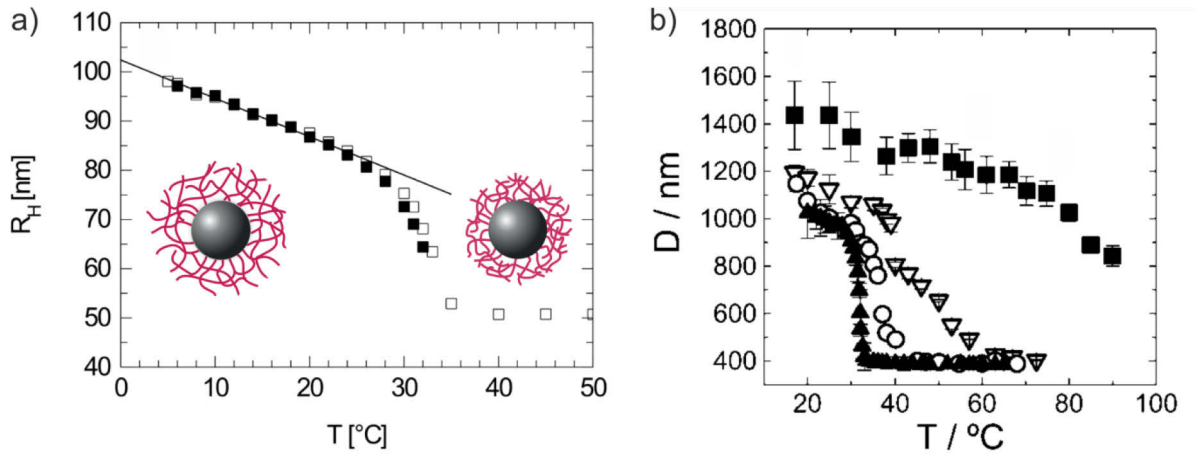

Figure 3.3: a) Hydrodynamic radius R_h of the pNiPAm based core-shell microgel obtained from DLS experiments at various temperatures. The measurements were performed in (■) pure water and (□) 0.05 mM KCl solution. Below the volume transition, R_h decreases linearly in good approximation. The solid line represents the linear regression of the data points ($R_h = -0.7796T + 102.4096$ with T being the temperature). Reprinted with permission from Siebenburger, M.; Fuchs, M.; Winter, H.; Ballauff, M. *J. Rheol.* **2009**, *53*, 707-726. Copyright © 2009, The Society of Rheology. b) Effect of the charge density on the diameter D of the microgel and on the response on temperature. (▲) Uncharged, (○) $pH = 4.1$ (20 % charged), (Δ) $pH = 5.6$ (75 % charged), and (■) $pH = 7.8$ (100 % charged). Reprinted with permission from Capriles-Gonzalez, D.; Sierra-Martin, B.; Fernandez-Nieves, A.; Fernandez-Barbero, A. *J. Phys. Chem. B* **2008**, *112*, 12195-12200. Copyright © 2008, American Chemical Society.

(SAXS), small angle neutron scattering (SANS) as well as rheology. [127-134] Thus, they represent well-defined platforms for the analysis of the protein adsorption. Figure 3.2 b shows the Cryo-TEM image of an uncharged microgel in water. The core-shell morphology of this system is clearly visible. In this case, the Cryo-TEM micrograph was generated below the VPTT of 32 °C, where the microgel network is strongly swollen with solvent. A slight irregular shape of the shell is observed, which is due to the density fluctuations within the network. These inhomogeneities are caused by the thermal fluctuations of the polymer chains which are frozen in by the process of crosslinking as well as by the faster consumption of BIS compared to NiPAm during the synthesis. Thus, the segment density slightly decays at the particle surface. Small angle scattering experiments, *i.e.*, SAXS and SANS measurements, supplement the structural data obtained from Cryo-TEM experiments. [130]

The analysis of the microgel size at varying temperature by DLS results in a pronounced swelling curve of the core-shell microgel. Figure 3.3 a shows the hydrodynamic radius R_h of uncharged core-shell microgels as function of temperature. The shell network undergoes a continuous volume phase transition close to 32 °C from the swollen and hydrophilic state to the shrunken and more hydrophobic state, which is expected for pNiPAm-based microgels. The temperature-induced dehydration of the microgel can be further analysed on molecular level by using Fourier transform infrared (FT-IR) spectroscopy. This technique was used in this thesis to analyse the hydrogen bonding pattern of uncharged microgels in absence and presence of proteins and is described in section 3.1.3. Moreover, Crassous *et al.* [130] showed that the temperature-dependent swelling process of uncharged core-shell microgels can be quantitatively understood by the classical Flory-Rehner theory. [102,135-136]

Charging the network by copolymerisation with ionisable monomers shifts the VPTT to higher temperatures and causes broadening of the transition. [137] In Figure 3.3 b the swelling capabilities of microgels of different charge states are plotted against the temperature. [138] Charged microgels additionally respond to changes of the salt concentration and the *pH* value. For instance the salt- and *pH*-dependent data of the swelling capability of microgels containing 5-mol% acrylic acid is shown in Figure 3.4. Increasing the salt concentration of the solution induces deswelling of the negatively charged microgels until the microgel size approaches a constant value at high salt concentration. Moreover, the shell thickness of microgels containing weak electrolyte groups in the shell is dependent on the *pH* value of the system. Raising the *pH* value increases the dissociation degree of the weak acid groups resulting in swelling of the gel network (Figure 3.4). The decrease of the microgel size at high *pH* values noted in Figure 3.4 is due to the increase of the ionic strength caused by the addition of base.

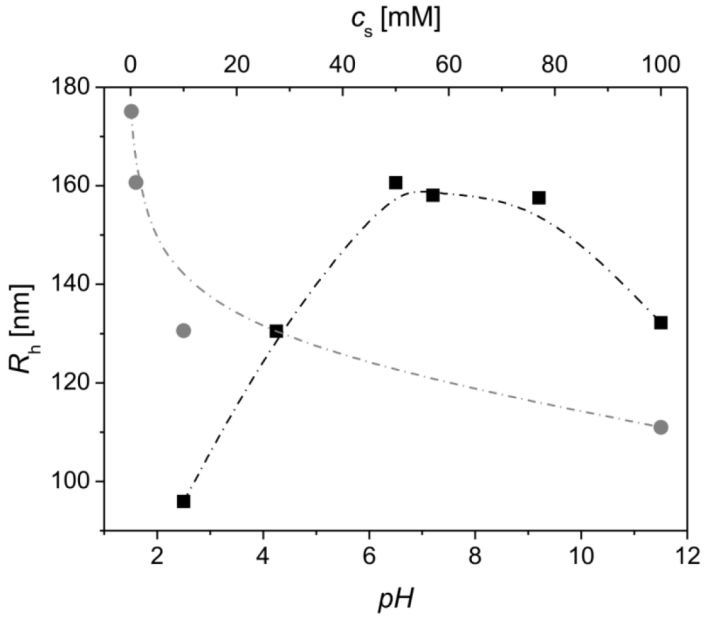

Figure 3.4: Dependence of the hydrodynamic radius R_h of charged core-shell microgels containing 5-mol% AAc on the *pH* value (●) and on the salt concentration c_s (■) of the solution. For the salt-dependent measurements, KCl was used as monovalent salt to adjust c_s. The *pH* value of the solution was ~6.2. For the *pH*-dependent measurements the solutions contained 1 mM KCl. All experiments were performed at 298 K.

3.1.2 Theoretical Description of Microgel Swelling

The equilibrium swelling of polymer gels is determined by the balance between the osmotic pressure P_{osm} acting to swell the gel and the elastic pressure P_{el} of the cross-linked polymer chains counteracting the osmotic swelling. The latter arises from the configurational entropy of the chains and the deformability of the polymer network. Using the theory of rubber elasticity, P_{el} can be identified with the shear modulus G which scales with the volume $V^{-1/3}$. [139-140] Thus, P_{el} is given by

$$\beta P_{el} = -BV^{-1/3} \tag{3.1}$$

where B is a constant characterising the particulate polymer-solvent system and β is the thermal energy

$\beta = (k_B T)^{-1}$ with k_B as the Boltzmann constant and T as the absolute temperature. The P_{osm} of neutral polymer gels is solely determined by the osmotic pressure mixing term P_{mix} which emerges from the free energy of mixing of the network chains and the solvent molecules and, thus, from the polymer-solvent interactions. This contribution can be expressed by the Flory-Rehner theory [139,141] or by the scaling concept which is given by [140,142]

$$\beta P_{\mathrm{mix}} = AV^{-\mathrm{m}} \tag{3.2}$$

where A is the coefficient which characterises the polymer solvent interactions and m is a scaling exponent that depends on the thermodynamic quality of the solvent for the particulate polymer. [140,142-144] At conditions where the solvent is a good solvent for the polymer chains, P_{mix} scales with m = 9/4. [142] In case of pNiPAm-based microgels, water serves as good solvent below the VPTT and, thus, P_{mix} is described by equation (3.2) with m = 9/4. Increasing the temperature above the VPTT changes the solvent quality from good to poor resulting in an increase of m [145] and in contraction of the network.

The enhanced swelling of charged microgels is caused by the electrostatic potential set by the network charge. The latter is caused by the inhomogeneous distribution of mobile charges (ions) around the (fixed) gel charge distribution and is termed as Donnan potential $\Delta\phi$ for monovalent salt. [81,139,146] The $\Delta\phi$ is related to the ion concentrations as follows: [81]

$$\frac{c_{\mathrm{gel,j}}}{c_{\mathrm{sol,j}}} = \exp\left(-z_{\mathrm{j}}\Delta\phi e\beta\right) \tag{3.3}$$

where $c_{gel,j}$ and $c_{sol,j}$ refers to the concentration of the j-ionic species in the gel and in the bulk, respectively, and z_j is the ion valence. In case of 1:1 electrolytes (monovalent salt), $c_{sol,j}$ can be replaced by the salt concentration c_s. The potential difference $\Delta\phi$ deep inside the gel is then derived from equation (3.3) and by assuming electroneutrality deep inside the gel:

$$c_{\mathrm{s}}\exp(-\Delta\phi e\beta) - c_{\mathrm{s}}\exp(\Delta\phi e\beta) + z_{\mathrm{g}}c_{\mathrm{g}} = 0 \tag{3.4}$$

where $z_g c_g$ is the charge density (per volume) of the gel, with z_g = -1 as the monomer charge valence and $c_g = N_g/V$ as the concentration of fixed charges in the gel where N_g is the number of charged monomers and V is the gel volume. The solution of equation (3.4) is the Donnan potential for a monovalent salt: [81]

$$\Delta\phi = e^{-1}\beta^{-1}\ln\left[\frac{z_{\mathrm{g}}c_{\mathrm{g}}}{2c_{\mathrm{s}}} + \sqrt{\left(\frac{z_{\mathrm{g}}c_{\mathrm{g}}}{2c_{\mathrm{s}}}\right)^2 + 1}\right] \tag{3.5}$$

Moreover, as a result of the unequal ion distribution an extra osmotic pressure, the ionic pressure P_{ion}, is established which is deduced from equations (3.3) and (3.5) to give [139]

$$\beta P_{\mathrm{ion}} = \sum_{j=1}^{N}\left(c_{\mathrm{gel,j}} - c_{\mathrm{s,j}}\right) = 2c_{\mathrm{s}}\left[\sqrt{\left(\frac{z_{\mathrm{g}}N_{\mathrm{g}}}{2c_{\mathrm{s}}V}\right)^2 + 1} - 1\right] \tag{3.6}$$

The expression for the total swelling pressure P is then given by

$$\beta P = \beta P_{\mathrm{mix}} + \beta P_{\mathrm{el}} + \beta P_{\mathrm{ion}} = AV^{-9/4} - BV^{-1/3} + 2c_{\mathrm{s}}\left[\sqrt{\left(\frac{z_{\mathrm{g}}N_{\mathrm{g}}}{2c_{\mathrm{s}}V}\right)^2 + 1} - 1\right] \tag{3.7}$$

In mechanical equilibrium the total pressure vanishes, $P = 0$, which determines the equilibrium gel volume $V(c_{\mathrm{s}})$ at given c_{s}. Increasing of c_{s} reduces the inhomogeneity of the ion distribution and, thus, decreases P_{ion}. This directly results in microgel shrinkage, *i.e.*, the decrease of $V(c_{\mathrm{s}})$. At very high salt concentration P_{ion} is negligible, $P_{\mathrm{ion}} \approx 0$, and the 'neutral' reference gel volume V_{r} is reached. The latter can be determined by the first two terms of equation (3.7) only. Under these considerations the following relations are found:

$$V_0 = \left(\frac{A}{B}\right)^{12/23} \tag{3.8}$$

$$B = \left(\frac{A}{V_0}\right)^{23/12} \tag{3.9}$$

With these equations, the equilibrium condition can be expressed in terms of the deviation of V with respect to V_{r} by

$$\beta P = 0 = AV^{-9/4}\left[1 - \left(\frac{V}{V_{\mathrm{r}}}\right)^{23/12}\right] + 2c_{\mathrm{s}}\left[\sqrt{\left(\frac{z_{\mathrm{g}}N_{\mathrm{g}}}{2c_{\mathrm{s}}V}\right)^2 + 1} - 1\right] \tag{3.10}$$

It has to be emphasised that non-ideality as well as ionic correlation in the microgel, such as Manning condensation, is neglected. The latter is justified in this case since the charge density of the network is too low to induce Manning condensation. Thus, all counterions are osmotic active.

This balance approach can be used not only to describe the volume change of the microgel but also to describe its mechanical properties, *e.g.,* the compressibility of the network, and their dependence on the salt concentration. The compressibility is determined by the bulk modulus K (inverse compressibility) which is defined by $K=-V(\partial\beta P/\partial V)$. [147] This leads to the following expression for K

$$K = AV^{-9/4}\left[\frac{9}{4} - \frac{1}{3}\left(\frac{V}{V_{\mathrm{r}}}\right)^{23/12}\right] + {z_{\mathrm{g}}}^2{N_{\mathrm{g}}}^2\left[2c_s V^2\sqrt{\left(\frac{z_{\mathrm{g}}N_{\mathrm{g}}}{2c_{\mathrm{s}}V}\right)^2 + 1}\right]^{-1} \tag{3.11}$$

Noteworthy, this equation is strictly capable to analyse the mechanical properties of microgel suspensions below the VPTT and for suspensions containing monovalent salt only. For samples containing polyions, such as proteins, the bulk modulus is expected to deviate from the value calculated from equation (3.11) especially if proteins bind to the microgel network by, *e.g.*, hydrophobic and electrostatic interactions.

3.1.3 Hydration and Dehydration of Stimuli-Sensitive Microgels

The pattern of the FT-IR-spectra of acrylamide based hydrogels is very sensitive towards the formation of intramolecular hydrogen bonds between the polymer chains as well as of intermolecular hydrogen bonds between the polymer chains of the gel and the solvent molecules. Since the volume phase transition of the temperature-sensitive polymers and hydrogels can be understood in terms of hydrogen bonding patterns, [148] FT-IR-Spectroscopy is widely used to obtain quantitative information about the phase transition of temperature-sensitive acrylamide based polymers [149-155] and hydrogels [148,156-158] at molecular level. The wavenumbers and assignments of the peaks of pNiPAm which are sensitive to hydration and dehydration, respectively, are compiled in Table 3.1. The most important bands of the spectrum to investigate the formation of hydrogen bonds are the amide I and amide II vibrational modes since these comprise the bending and stretching vibrations of the amide groups.

Table 3.1: Main vibrational modes of hydrated and dehydrated pNiPAm. [154]

Wavenumber [cm^{-1}]	Band assignment[a]	Wavenumber [cm^{-1}]	Band assignment
2 982	υ_{as}(hydrated CH_3)	1 650	υ(C=O···H–N)
2 971	υ_{as}(dehydrated CH_3)	1 625	υ(C=O···H_2O)
2 940	υ_{as}(hydrated CH_2)	1 560	υ(N–H···H_2O)
2 926	υ_{as}(dehydrated CH_2)	1 535	υ(N–H···O=C)

[a] The term υ_{as} describes antisymmetric vibrations of the respective chemical bond.

The temperature-dependent FT-IR spectrum of the pNiPAm hydrogel in Figure 3.5 illustrates the sensitivity of the IR-bands towards the hydrated state of the polymer chains: Below the VPTT of the gel, the amide I band (mainly contributions from C=O stretching vibrations) consists of one single component with a maximum at 1 625 cm^{-1}. [148,158] This peak is caused by the stretching vibrations of C=O groups that form strong hydrogen bonds to water. In contrast, in the collapsed state of pNiPAm the intensity at 1 625 cm^{-1} is decreased and a shoulder appears at higher wavenumbers (~1 650 cm^{-1}). This blue shift of the amide I mode, *i.e.*, the emergence of a second component, is induced by the dehydration of the polymer chains. [154,158-159] Thus, the second component is assigned to C=O groups which form weaker intra- or intermolecular hydrogen bonds to the N-H groups of the polymer chains. Moreover, this analysis demonstrates that below the VPTT water molecules totally replace the N-H groups and the carbonyl groups form hydrogen bonds to water molecules exclusively. Heating the system above the VPTT leads to partial breakage of the hydrogen bonds to water and to the entropically favoured formation of C=O···H-N hydrogen bonds. [149]

The amide II band of pNiPAm in H_2O can also be fitted with a single Gaussian component at low temperature with its maximum at ~1 560 cm^{-1}. [151,154] This band is attributable to N-H groups which form hydrogen bonds to water. During the phase transition, the amide II band is shifted towards larger wavelengths and above the VPTT this mode is described by two components with peaks at 1 560 cm^{-1} and 1 535 cm^{-1}. [151,154] The band at lower wavenumbers is caused by the bending vibration of N-H groups which are hydrogen-bonded to C=O groups. Thus, dehydration of the

polymer causes a blue shift of the vibrational modes of the C=O group which acts as hydrogen-bond acceptor and a red shift of the vibrational band of the N-H group which acts as hydrogen-bond donor. Information concerning the hydration changes of the alkyl groups of pNiPAm during the phase transition can be obtained from the C-H stretching vibrations between 2 840 and 3 000 cm^{-1}. [154-155] In particular, the vibrational modes of the CH_3 groups of the side chain and CH_2 groups of the main chain are located at around 2 980 and 2 940 cm^{-1}, respectively, below the VPTT. During the heating process a red shift of the vibrational modes of the alkyl groups is observed indicating dehydration of the hydrophobic groups. [155] Further studies investigated the influence of charges on the phase transition of charged copolymers and hydrogels by IR-spectroscopy. The presence of carboxyl groups results in additional vibrational modes in the IR spectra which give further information about ionisation effects on the volume phase transition. [152,157] Noteworthy, the copolymerisation of NiPAm with charged molecules, *e.g.*, acrylic acid, does not affect the peak positions of the vibrational modes of NiPAm in the linear copolymers and charged hydrogels. [152,157]

In conclusion, the temperature-dependent analysis of the IR-spectra of acrylamide based polymers and hydrogels demonstrates that the vibrational modes are strongly influenced by hydrogen bonds. Thus, FT-IR spectra recorded at different temperatures relate the structural changes of the microgel to changes of the hydrogen bonding pattern. Similarly, FT-IR spectra of unloaded microgels and microgels which are saturated by proteins may reveal changes in the amide I and II bands since proteins may induce breakage of hydrogen bonds between water molecules and the amide groups of the gel and formation of hydrogen bonds to the amide groups of the protein. Consequently, FT-IR analysis of loaded microgels may also give information about the interactions between the microgels and proteins. This is shown in section (4.2.3).

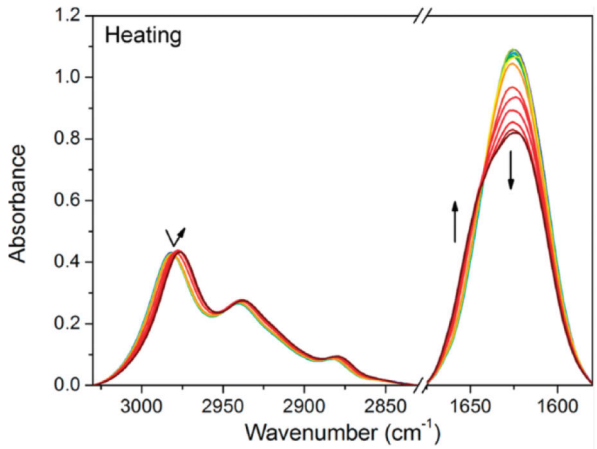

Figure 3.5: Temperature-dependent FT-IR spectra of a pNiPAm hydrogel in D_2O. The temperature was varied between 301 and 313 K. The arrows mark the change in intensity upon heating. Reprinted with permission from Sun, S.; Hu, J.; Tang, H.; Wu, P. *J. Phys. Chem. B* **2010**, *114*, 9761-9770. Copyright © 2010, American Chemical Society.

3.2 Proteins

3.2.1 Model Proteins

In this thesis, three different proteins, namely *β*-D-glucosidase (*almonds*), lysozyme (*chicken egg white*) and cytochrome c (*bovine heart*), have been used to study the interactions with the core-shell microgels. The structure and function of these proteins are briefly described in the following section.

3.2.1.1 β-D-Glucosidase

β-D-Glucosidase (EC 3.2.1.21) is assigned to the class of glycoside hydrolases (EC 3.2.1) and catalyses the hydrolysis of (1→4)-*β*-glycosidic bonds between carbohydrate residues as well as between carbohydrate and non-carbohydrate moieties in *β*-D-glucosides. [160-162] In particular, it is an exocellulase which acts on the non-reducing residue of the glycosides. Given the central role of oligo- and polysaccharides in biological processes, *β*-D-glucosidase is an abundant enzyme in many organisms. For example, *β*-D-glucosidase plays an important role in the enzymatic hydrolysis of

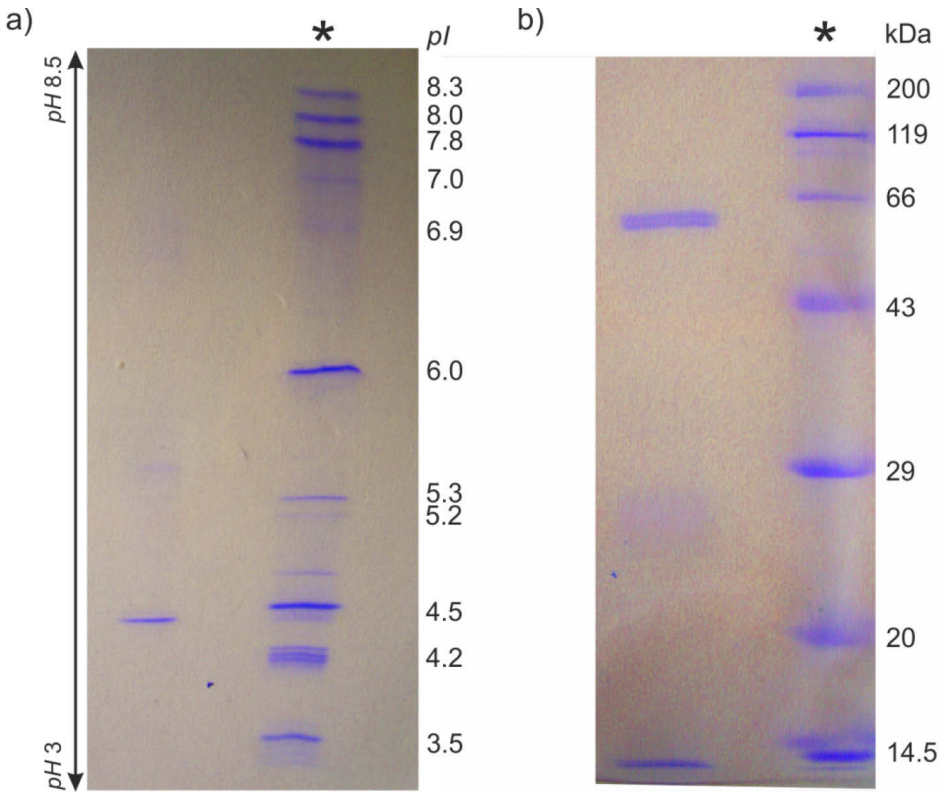

Figure 3.6: a) Coomassie stained IEF gel lanes for *β*-D-glucosidase from *almonds* and the isoelectric point standard. The asterisk (*) marks the isoelectric point standard lane. The isoelectric points of the proteins in the standard ladder are reported on the right for reference. b) Coomassie stained SDS-PAGE gel lanes for *β*-D-glucosidase from *almonds* and the molecular weight standard. The asterisk (*) marks the molecular weight standard lane. The molecular weights of the proteins in the standard ladder are reported on the right for reference. The low molecular weight band visible in the lane of *β*-D-glucosidase corresponds to the front marker.

cellulose in some organisms, such as bacteria and fungi. [163-164] Moreover, the enzyme is used in many industrial applications, *e.g.*, in pharmaceutical, cosmetics and food industry. [164]

The *β*-D-glucosidase from *almonds* is a large two-chain polypeptide with identical subunits each having a molecular weight of ~65 000 g mol^{-1}. [165] The enzyme is known to exist in a number of isoenzymic forms which differ in their isoelectric points (*pI*). The isoelectric point of one of these forms was determined to 7.3. [165] In order to identify the isoform or mixture of isoforms in the protein sample used in this thesis, isoelectric focusing (IEF) experiments have been performed. Figure 3.6 shows the resulting gel, in addition to the sodium dodecyl sulfate polyacrylamide gel electrophoresis (SDS-PAGE) of *β*-D-glucosidase. The SDS-PAGE gel unambiguously shows a main band at ~62 000 g mol^{-1}. This molecular weight corresponds to the mass found for the monomeric form of *β*-D-glucosidase. Moreover, a weak and fuzzy band between 20 000 and 29 000 g mol^{-1} points to a slight contamination by smaller proteins. IEF of the purchased *β*-D-glucosidase leads to a strong band at *pH* ~4.4 which is identified as the isoelectric point of the dominating isoform of the *β*-D-glucosidase sample used for the protein binding experiments. Consequently, the enzyme has an overall negative charge at neutral *pH* and, thus, at the conditions chosen for adsorption.

To date, the primary sequence of this enzyme has not been resolved, and thus structural investigations regarding the tertiary structure are missing. However, He *et al*. resolved a part of the primary sequence of the active centre. [166] Owing to the conserved structure of the catalytic centre, *β*-D-glucosidase from *almonds* has been assigned to the Family I of the glycoside hydrolases. [167] Structural investigations of Family I glucosidases revealed that these enzymes have common features regarding their tertiary and quaternary structure. [167] In particular, they are dimeric proteins with identical monomers of globular shape and of $(\beta/\alpha)_8$-*barrel* structure. As example, the quaternary structure of *β*-D-glucosidase from *maize* is shown in Figure 3.7. [167]

Despite the unknown structure of *β*-D-glucosidase from *almonds*, it has been subjected to many kinetic studies in order to reveal the catalytic mechanism. [162,166] The hydrolysis of the substrates at the active centre of *β*-D-glucosidase is a two-step process. Herein, the carboxyl groups of two acidic amino acid residues, *i.e.*, aspartate and/or glutamic acid, act as base and acid catalysts, which is a general motif of glycoside hydrolases (EC 3.2.1). [161-162] In the first step, termed as glycosylation

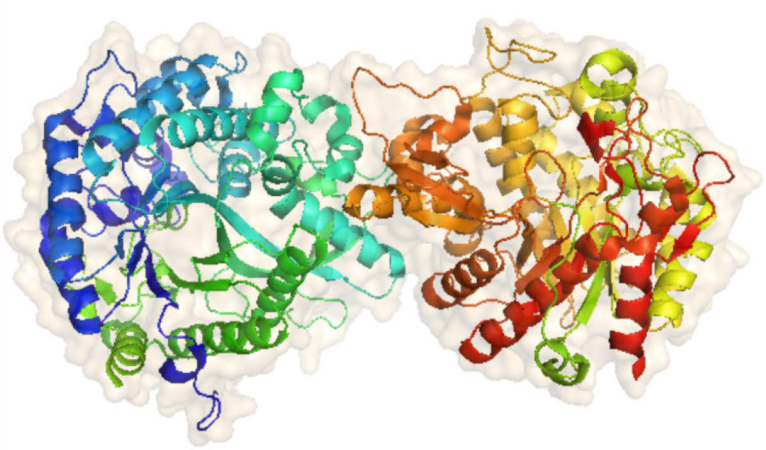

Figure 3.7: Quaternary structure of the isoenzyme ZMGlu1 of *β*-D-glucosidase (*maize*, PDB: 1E1E). The image was generated using PyMOL and the structural data was obtained from the protein data bank PDB. [168]

step, one of the carboxyl groups protonates the glycosidic bond. This is followed by the nucleophilic attack of the second carboxyl group resulting in the cleavage of the C-O bond of the substrate and the formation of the glycosyl-enzyme intermediate. This intermediate reacts with a water molecule in the second step (the deglycosylation step) to release the product and to regenerate the enzyme ready for the next cycle. In case of *β*-D-glucosidase, the catalysed hydrolysis is found to occur with net retention of the anomeric configuration of the substrate and product, respectively. [166] According to the detailed characterisation of the catalytic steps, *β*-D-glucosidase from *almonds* is best suitable to study the impact of protein adsorption on the catalytic activity of enzymes.

3.2.1.2 Lysozyme

Lysozyme (EC 3.2.1.17) is an antimicrobial enzyme that is abundant in secretions of a variety of organisms, including birds, mammals, plants and insects. [169] It belongs to the class of glycoside hydrolases and catalyses the hydrolysis of the (1→4)-*β*-glycosidic linkages between N-acetylmuramic acid and N-acetyl-D-glucosamine in the peptidoglycans of bacterial cell walls. [170] Due to the antibacterial properties, lysozyme has been used in biotechnological applications, *e.g.*, as cell disrupting agent for the extraction of bacterial intracellular products, therapeutic applications and as additive in food. [171-172]

Lysozyme from *chicken egg white* was the first enzyme to have its three-dimensional structure revealed. [173] It is one of the most widely used proteins for experimental and theoretical studies. [174] Lysozyme from *chicken egg white* is a single-chain polypeptide consisting of 129 amino acid residues and has a molecular weight of ~14 300 g mol^{-1}. [173,175] It has an elliptical shape with approximate dimensions of 30x30x45 Å and is regarded as a rigid molecule due to the presence of four disulfide bridges. [173,176] This conformational stability makes lysozyme best suitable for adsorption studies on a variety of surfaces. From the tertiary structure of lysozyme shown in Figure 3.8 a it is visible that the protein consists of six *α*-helices and three *β*-sheets which are connected by flexible loops and are organised into two domains. [174] Moreover, the *α*-helices contribute to about

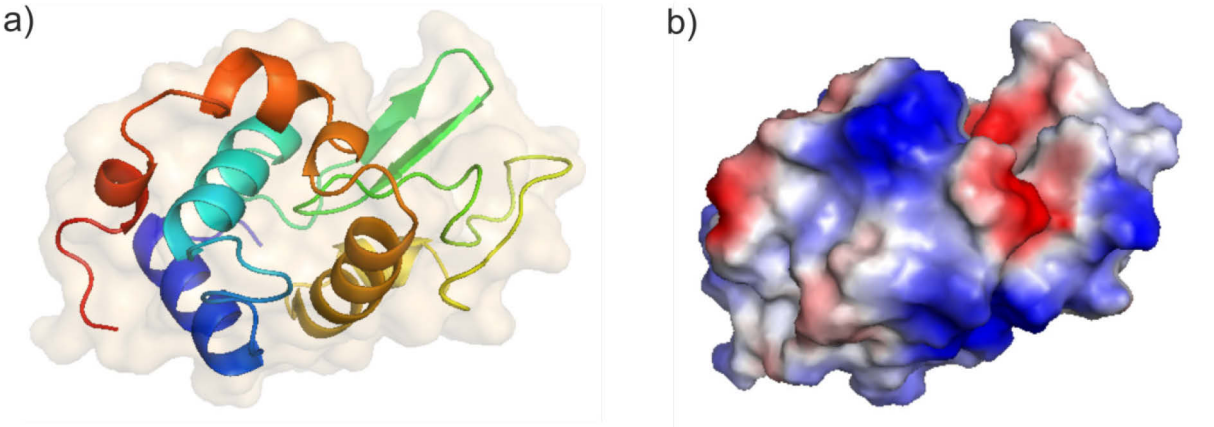

Figure 3.8: a) Tertiary structure of lysozyme (*chicken egg white*, PDB: 193L). The image was generated by PyMOL and the structural data was obtained from PDB. [168] b) Electrostatic surface potential of lysozyme as calculated from the vacuum electrostatics of the protein using PyMOL. The blue colour indicates areas of high positive charge, the red colour shows negatively charged regions of the protein surface and white areas are related to uncharged regions of the surface.

30-40 % to the secondary structure of lysozyme whereas the *β*-sheet content was determined to be less than 10 %. [177-179] Since the protein contains 18 basic and 14 acidic residues, the protein surface is highly charged below and above its isoelectric point ($pI = 11$). The high surface charge is also obvious from the electrostatic surface potential shown in Figure 3.8 b. At physiological *pH* ($pH = 7.2$) lysozyme has an overall net charge of +7. [180-181] However, also a number of strongly hydrophobic side chains are located on the molecular surface. [173] In addition, the active site of lysozyme has been localised within the deep and negatively charged crevice between the two domains. [174] The negative charge arises from glutamic acid 35 and aspartate 52 which have been identified as catalytic residues of the active site. [182] In analogy to *β*–D-glucosidase, the catalytic residues of lysozyme act as proton donor and acceptor which facilitate the hydrolysis of glycosides.

3.2.1.3 Cytochrome c

Cytochrome c is a small heme protein and is an essential component of the cellular respiration in mitochondria where it transports electrons from the cytochrome c reductase to the cytochrome c oxidase. [183] Herein, the electron transport is facilitated by the transition between the ferrous and ferric state of the heme group of cytochrome c. Due to these electron transfer properties cytochrome c is one of the best studied proteins in electrochemistry and is considered as promising biosensor. [184] Additionally, cytochrome c is highly soluble in aqueous solution and, thus, can be used in high concentrations up to 100 g L^{-1}. [185]

Generally, cytochrome c is a globular protein with dimensions of 26x30x32 Å and a molecular weight of ~12 300 g mol^{-1}. [37,184] The structure of cytochrome c from *bovine heart* is depicted in Figure 3.9 a. As obvious from this image, the secondary structure of cytochrome c is composed largely of α-helix (~40%), and almost no *β*-sheet. [179] Moreover, the heme active centre is covalently bound via two cysteine residues and is located in a lateral region of the protein molecule in an area rich of lysine. [184] This positively charged region, also known as front face of cytochrome c, is shown in Figure 3.9 b (left) as electrostatic potential map. Cytochrome c from *bovine heart* is a single-chain

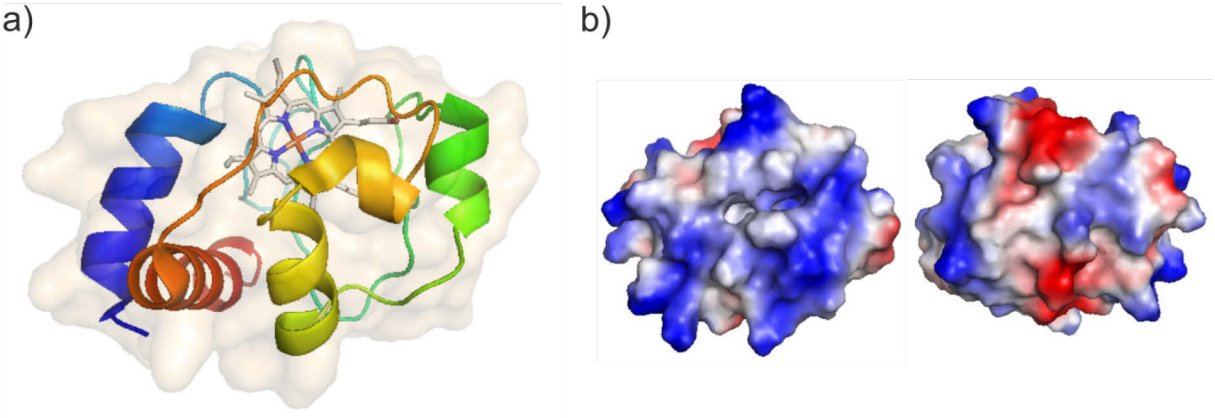

Figure 3.9: a) Tertiary structure of cytochrome c (*bovine heart*, PDB: 2B4Z). The image was generated using PyMOL and the structural data was obtained from PDB. [168] b) Electrostatic surface potential of the front face (left) and back face (right) of cytochrome c as calculated from the vacuum electrostatics of the protein using PyMOL. The blue colour indicates surface areas of high positive charge, the red colour shows negatively charged regions of the protein surface and white areas are related to uncharged regions of the surface.

polypeptide of 104 amino acids and consists of 23 basic and 20 acidic residues. [186] The native form of cytochrome c is characterised by an isoelectric point of 10.8 and has an overall positive net charge of ~+7 at neutral solution. [187] By comparison of the surface potential of the front and back face of the protein (Figure 3.9 b), it is obvious that cytochrome c presents an asymmetric charge distribution on the protein surface which facilitates the electron transfer, and, thus, the redox activity. [184] Moreover, cytochrome c shows peroxidase activity by oxidation of various electron donors, such as 2,2'-azino-bis(3-ethylbenzthiazoline-6-sulfonic acid). [37]

3.2.2 Secondary Structure Analysis

FT-IR spectroscopy was chosen to analyse the secondary structure of the proteins in solution as well as in the adsorbed state. Unlike other techniques, *e.g.*, circular dichroism [188], FT-IR spectroscopy is not limited to optically transparent solutions, but can be also applied to samples that strongly scatter visible light, such as latex particles. [79] Thus, it is suitable to investigate the secondary structure of proteins after adsorption to the microgel particles.

Proteins and peptides show characteristic absorption bands in the IR regime between 1 500 and 1 700 cm^{-1} which can be used to assess the secondary structure as well as conformational changes of proteins in solution. [189-193] The amide I and II bands of the infrared spectra are caused by IR-active vibrations of the peptide backbone and are most sensitive to the protein conformation. [194] Therein, the IR-active stretching vibration of the C=O bond contributes to ~80% to the amide I band. The amide II band is mainly caused by N-H bending and C-N stretching vibrations. The peptide backbone is considered as system of coupled oscillators as the N-H and C=O groups of the peptide backbone are involved in intramolecular hydrogen bond formation. [194] Due to the varying hydrogen bond length, the strength of the intramolecular hydrogen bonds differs for the various structure elements with being strongest for the antiparallel β-sheet. In addition to hydrogen bonding, the vibrational modes are

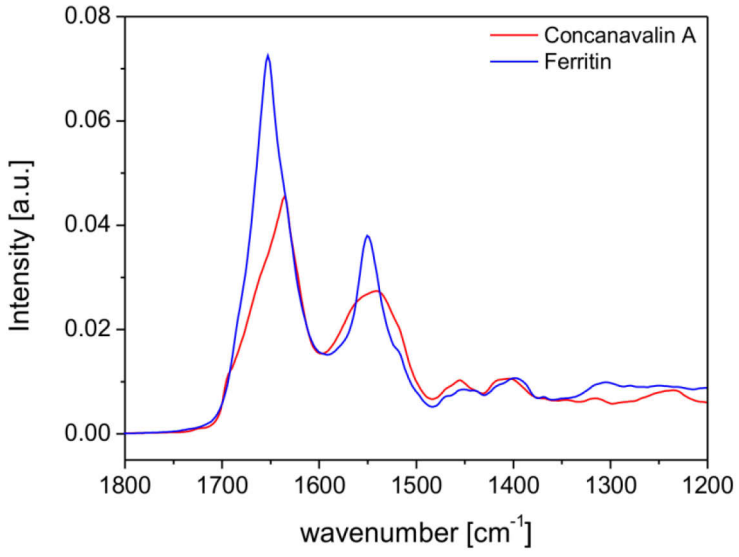

Figure 3.10: FT-IR spectra of concanavalin A (from *Jack beans*, 0.9% α-helix, 46.2% β-sheet) which is rich in β-sheet and ferritin (from *horse spleen*, 72.0% α-helix, 0 % β-sheet) which forms mainly α-helices. The IR data was obtained from the protein infrared database. [195]

sensitive to the coupling of transition dipoles of adjacent peptide bonds. Thus, the position and shape of the amide bands strongly depends on the secondary structure of the protein. For comparison, Figure 3.10 displays the IR spectra of ferritin which is rich in α-helix and concanavalin A which mainly forms β-sheets. Moreover, in Table 3.2 the structural components are assigned to their frequencies at which they appear in the amide I band. [194]

In recent years the measuring technique of FT-IR spectroscopy has improved tremendously. [79,159,177] Due to the development of very thin measuring cells, D_2O could be replaced by H_2O without diminishing the precision of the analysis. The measurement of the protein conformation in H_2O has several advantages over experiments performed in D_2O. For example, incomplete H→D exchange in D_2O makes the analysis of the amide bands very complicated. [196] Additionally, conformational changes induced by dissolving proteins in D_2O were observed. [196-197] Obviously, the use of H_2O as solvent is favoured in order to avoid any misinterpreting of the protein spectra recorded in D_2O. However, FT-IR spectroscopy in H_2O requires very small path lengths, smaller than 6 µm, in order to prevent total absorption of the IR rays by water in the range of the amide Iband. [196] In this case quantitative subtraction of the H_2O/buffer spectrum from the protein transmission spectrum is possible and the secondary structure of proteins dissolved in water can be analysed by taking the amide I and II band into account. [177,196,198-199]

As mentioned above, the amide bands are superimposed by the bands corresponding to the different kinds of structural elements. In order to receive structural information from these broad peaks, several analytical methods have been developed to decompose the amide bands. In many cases, the analysis of the amide I band is sufficient. [159,194,199] Sometimes both the amide I and II band are used to obtain the structural information. [177] In one strategy, the overlapping IR bands of the amide I band are subjected to Fourier deconvolution. [199-200] This method is based on band-narrowing which enables identification of the superimposing components. However, this procedure amplifies the noise of the recorded spectra significantly and the presence of water vapour makes the secondary analysis using Fourier deconvolution very complicated.

The second method is based on shape recognition of the IR bands and a calibration matrix created from IR spectra of proteins of known structure. Usually, these structures were determined by performing X-ray crystallography. Thus, the secondary structure of proteins in solution is considered to be the same as determined from X-ray diffraction for the crystalline form. This calibration set is then analysed by using a partial least square (PLS) method and the secondary structure of the unknown protein is calculated. [177,201] Precise results are obtained by this method using both the amide I and

Table 3.2: Summary of the secondary structure elements contributing to the amide I band. [194]

Wave number [cm^{-1}]	Secondary structure element
1 620 – 1 640	β-sheet
1 640 – 1 650	random coil
1 650 – 1 658	α-helix
1 660 – 1 690	loops
1 670 – 1 680	β-sheet

amide II band of the protein FT-IR spectrum. Furthermore, it has to be assumed that the secondary structure comprises solely four elements: ordered α-helix, unordered α-helix, random coil and β-sheet. Thus, no distinction is made between parallel and antiparallel β-sheets. The standard deviation of the secondary structural elements by this method was calculated to 4.8% for the α-helix, 3.7% for the β-sheet and 5.1% for random coil segments. [177] Several studies can be found where this analysis is successfully applied to the proteins immobilised on SPBs. [79-80,202] Consequently, the FT-IR spectra of the proteins recorded in this thesis, were also analysed using a software program which is based on the PLS method.

3.2.3 Enzymatic Activity Measurements

3.2.3.1 Michaelis-Menten Kinetics

The catalytic efficiency of free and adsorbed enzymes can be quantified by applying the Michaelis-Menten kinetics. [203] This model proposes a two-step reaction which contains a pre-equilibrium between free enzymes and enzymes occupied with substrate as first step: [203]

$$E + S \underset{k_{-1}}{\overset{k_{+1}}{\rightleftarrows}} ES \xrightarrow{k_{\mathrm{cat}}} E + P \tag{3.12}$$

where E signifies the enzyme and S the substrate, respectively. The complex between enzyme and substrate is described by ES and P is the product released from the enzyme active site after conversion. The rate constant k_{+1} and k_{-1} is the rate constant of the formation and cleavage of the ES complex, respectively. The chemical processes following the ES complex formation are described by the overall rate constant k_{cat}. By using this reaction mechanism and by assuming that a steady-state concentration of the ES complex is established, the Michaelis-Menten equation is derived. The latter reads [203]

$$\upsilon = \frac{\upsilon_{\max}[S]}{K_{\mathrm{m}} + [S]} \tag{3.13}$$

where K_{m} is the Michaelis constant, υ is the initial rate of the catalysed reaction, and $\upsilon_{\max}$ is the maximum initial rate at infinite substrate concentration [S].

Figure 3.11 a shows the initial rate υ of the hydrolysis of *o*-nitrophenyl-β-D-glucopyranoside (*o*-NPG) as function of *o*-NPG concentration which is catalysed by free β-D-glucosidase. This reaction is of pseudo-first order and is known to follow the Michaelis-Menten kinetics. The reaction rate increases with increasing [S] and asymptotically approaches its maximum rate $\upsilon_{\max}$. This is caused by saturation of the enzyme active sites with the substrate and, thus, increasing of [S] does not increase the reaction rate above this threshold. The maximum rate is related to k_{cat} via $\upsilon_{\max} = k_{\mathrm{cat}}$ [E] with [E] as enzyme concentration since k_{cat} is referred to as the turnover number for the enzyme, *i.e.*, the number of catalytic turn over events per enzyme molecule that occur per unit of time. [203] Consequently, k_{cat} defines the maximum rate of the reaction with infinite availability of the substrate to the enzyme´s active site. Moreover, k_{cat} is very sensitive to changes of the enzyme structure and changes of the solution conditions. Thus, this parameter serves as direct measure for any perturbation of the tertiary

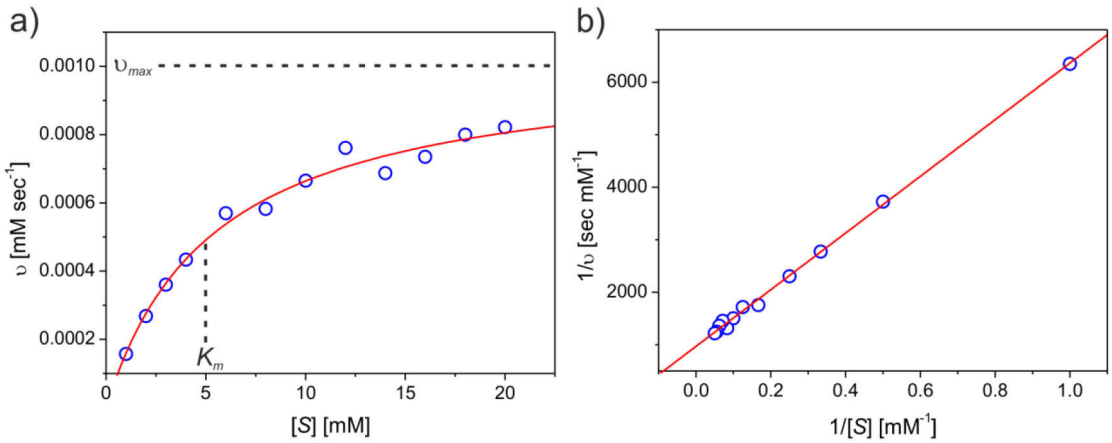

Figure 3.11: a) Plot of the initial rate v of the hydrolysis of *o*-nitrophenyl-*β*-D-glucopyranoside (*o*-NPG) as function of the *o*-NPG concentration. The hydrolysis was catalysed by native *β*-D-glucosidase in 10 mM MOPS buffer *pH* 7.2 at 293 K. b) Lineweaver-Burk plot of the hydrolysis of *o*-NPG catalysed by free *β*-D-glucosidase in 10 mM MOPS buffer *pH* 7.2 at 293 K.

structure and the microenvironment which may be induced by the adsorption of enzymes to the microgel network.

The Michaelis constant equals the substrate concentration that provides a reaction rate that is half of the maximum rate υ_{max}. Additionally, for reactions consisting of a fast established equilibrium between enzyme, substrate and enzyme-substrate complex, *i.e.*, $k_{cat} << k_{-1}$, the K_m is identical to the dissociation constant $K_S = k_{-1}/k_1$. [203] Under these specific conditions, K_m is a measure for the substrate binding affinity to the enzyme active site and the stability of the *ES* complex. For enzyme-substrate systems with values of K_m larger or smaller than K_S the Michaelis constant still serves as relative measure of the stability of the *ES* complex.

In this thesis, the kinetic constants K_m and k_{cat} are determined from non-linear curve fitting of untransformed experimental data to the Michaelis-Menten equation (3.13). However, linearised plots of the kinetic data are helpful when discussing the results and comparing the kinetic parameters of free and adsorbed enzyme. The most commonly used method for linearising the enzyme kinetic data is the method of Lineweaver and Burk. Therefore, the reciprocal of the Michaelis-Menten equation (3.13) is calculated and rearranged to give the basic equation of the double-reciprocal Lineweaver-Burk plot: [203]

$$\frac{1}{v} = \frac{K_m}{\upsilon_{max}}\frac{1}{[S]} + \frac{1}{\upsilon_{max}} \tag{3.14}$$

Thus, the plot of $1/v$ versus $1/[S]$ results in a straight line with K_m/υ_{max} as slope and $1/\upsilon_{max}$ as intercept (Figure 3.11 b). This form of data presentation easily visualises any differences in the kinetic parameters as changes of the slope and intercept are extracted from the plot at first sight.

3.2.3.2 Temperature- and pH-Dependence of the Catalytic Activity

The catalytic efficiency of enzymes shows a non-monotonic temperature profile with a distinct temperature maximum specific for each enzyme. Below the temperature maximum, most enzyme

reactions obey the Arrhenius equation which relates k_{cat} to the activation energy of the transition state of the enzyme-catalysed reaction E_a: [203-204]

$$k_{cat} = A \exp\left(-\frac{E_a}{RT}\right) \tag{3.15}$$

where A is a pre-exponential constant and represents the probability of the reaction to take place and R is the gas constant. At higher temperature, heat-induced denaturation of the protein sets in and compromises the enhancement of the catalytic efficiency predicted by eq. (3.15). Thus, the increase of k_{cat} and the decrease of the fraction of active enzymes with increasing temperature results in a temperature maximum of the catalytic efficiency. The position of this maximum defines the temperature stability of the enzyme. In many cases, it is located between 40 and 50 °C, that is, slightly above the body temperature. [204] However, the temperature maximum is determined by the time-dependent heat inactivation of the protein. Consequently, it is shifted to lower temperatures for longer incubation times of the enzyme at the corresponding temperature. [204]

In order to gain information about the temperature-dependent catalytic activity of enzymes and the influence of immobilisation of enzymes on the latter, the investigation should be restricted to the temperature range over which protein heat denaturation is not significant. Moreover, it is essential to use k_{cat} for this analysis, since the binding affinity, *i.e.*, K_m, is also dependent on temperature. [205] Thus, the analysis of the initial rate v for one substrate concentration will not suffice to analyse the temperature-dependence of the enzyme activity. Instead, k_{cat} has to be determined for each temperature because it is not affected by the temperature-dependence of K_m. The temperature-dependent analysis of enzymes in the free and bound state is described in section 4.2.2.

In addition to the temperature, the enzyme activity exhibits a significant dependence on the *pH* value of the solution. [203-204] The shape of the *pH*-dependent activity curve is determined by two effects: i) the role of ionic groups in the stabilisation of the tertiary structure of the protein and ii) the involvement of acid-base amino acid groups in substrate binding and in the catalytic steps of the reaction. Generally, the protein conformation is stable over a relatively broad *pH* range and denaturation occurs at extremely low and high *pH* values. [204] However, in most enzymes acid-base groups are part of the active site and the protonation state of these groups is essential for the binding and conversion of the substrate. Thus, the enzymatic activity is maximised over a narrow range of *pH* in which the protonation state of the catalytic residues is optimum. For example, *β*-D-glucosidase [206] shows a sharp *pH* optimum at *pH* ~7, whereas lysozyme [207] exhibits a broader *pH* optimum around *pH* ~5. Due to this strong sensitivity of the catalytic activity towards the *pH* value of the environment, enzymes may be exploited as local *pH* meters. Thus, enzymes adsorbed to the microgel network in their native structure may be used to detect local *pH* changes of charged microgels which are probably caused by their electrostatic potential. Results regarding this analysis can be found in section 4.4.4.

3.3 Interactions between Proteins and Microgels

3.3.1 Driving Forces of Protein Adsorption

In this thesis, pNiPAm-based core-shell microgels with varying content of carboxyl groups have been used for the protein binding studies. The amount of acrylic acid, *i.e.*, carboxyl groups, in the microgel shell varied between 0 and 10 mol-%. Thus, the adsorption of proteins has been studied on uncharged microgels and on those with moderate negative charge density.

Uncharged microgels based on pNiPAm exhibit switchable adhesive properties due to their temperature-induced volume phase transition from a hydrophilic and swollen to a shrunken and mainly hydrophobic network. In their pioneering work about protein adsorption on pNiPAm-based microgels, Kawaguchi *et al*. demonstrated that these particles favour protein adsorption in their more hydrophobic state. [208] Several other studies on protein adsorption on microgels and pNiPAm brushes supported these findings, since temperature-dependent binding studies revealed higher amounts of bound protein and higher binding affinities above the LCST of pNiPAm (Figure 3.12). [115,209-212] Moreover, Lindman *et al.* showed that increasing the hydrophobicity of the microgel particles by incorporation of a hydrophobic comonomer increases the binding affinity of *human serum albumin* (HSA). [85] Based on these experimental observations, binding of proteins on thermo-sensitive systems has been ascribed to hydrophobic interactions as dominant driving force. Up until now, a quantitative study regarding the thermodynamics of protein binding as function of temperature is still missing. Moreover, thermodynamic contributions from structural rearrangements, *e.g.*, protein unfolding, have to be considered. Thus, irreversible denaturation of flexible proteins induced by adsorption may have important implications on the affinity and on the safety assessment of these

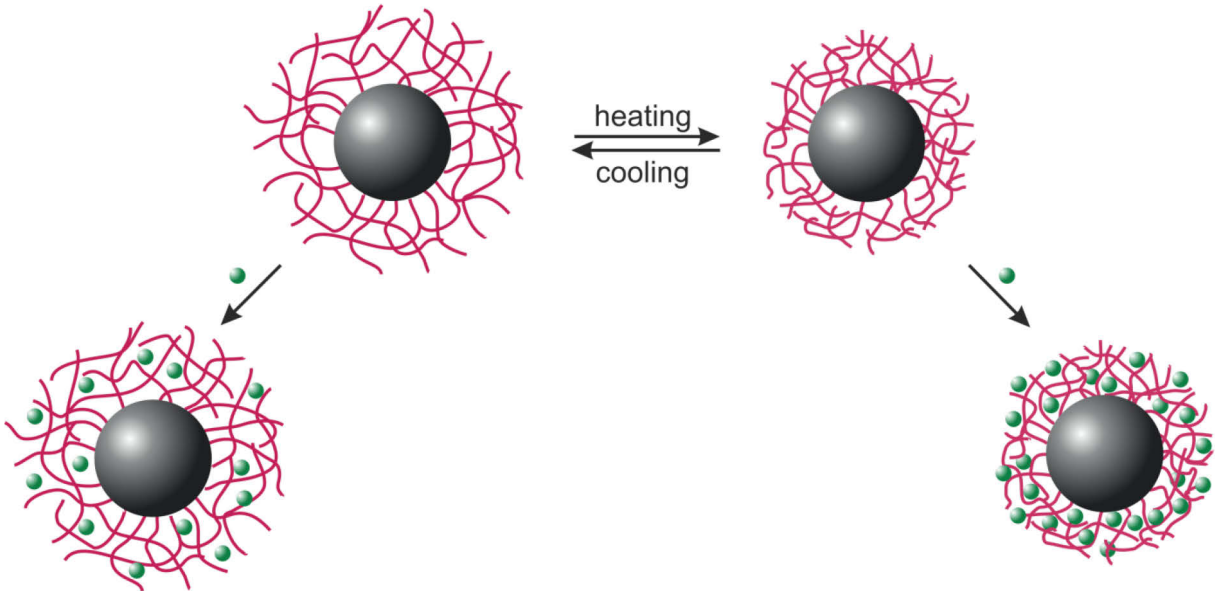

Figure 3.12: Protein adsorption on thermo-sensitive pNiPAm based microgels below (left) and above (right) the VPTT. Below the VPTT the microgel is highly swollen in water and adopts a hydrophilic state whereas in the shrunken state of the microgel network above the VPTT it is more hydrophobic. At higher temperatures the hydrophobic interactions between the carrier and protein are increased which induces stronger binding of proteins above the VPTT.

systems. However, only few studies analysed the conformation, *i.e.*, the secondary and tertiary structure, of the proteins after adsorption to the stimuli-sensitive polymer. [115,213]

Incorporation of negatively charged groups into pNiPAm-based microgels shifts the VPTT to higher temperatures and introduces electrostatic interactions with adsorbing proteins. This leads to a complex interplay of hydrophobic and electrostatic interactions. In general, electrostatic attraction between the microgel and an oppositely charged protein causes high binding affinities [185,214] and a *pH*- and salt-dependence [74,99,185] of the protein adsorption. For example, the electrostatic attraction of a positively charged protein towards a negatively charged microgel is determined by the electrostatic potential difference $\Delta\phi$ between the bulk and the microgel. In Figure 3.13 a, the $\Delta\phi$ of a hydrogel fixed on a planar surface is shown as function of the distance from the surface. The potential is highest close to the surface where it equals the Donnan potential, expressed in equation (3.5), and rapidly decays towards the bulk solution. A protein of net charge z_p will, therefore, experience a favourable electrostatic transfer energy $\Delta W_{el} = z_p e \Delta\phi < 0$. According to equation (3.5), $\Delta\phi$ decreases with an increase in the salt concentration and the electrostatic attraction becomes a function of the latter. Thus, the addition of salt to the solution diminishes the protein loading and the binding strength. [74,185,215] The change of the *pH* value of the solution affects the net charge of the protein surface and the charge density of the microgel network. [74,216] From equation (3.5) it is obvious that strong adsorption is expected at *pH* conditions where the microgel and protein carry an opposite charge. In contrast, in the *pH* regime in which the proteins are net negatively charged, proteins should be excluded from the negatively charged microgel due to electrostatic repulsion, $\Delta W_{el} > 0$. Surprisingly, several binding studies showed that proteins also adsorb on the microgels on the "wrong side" of the isoelectric point where the microgel and protein are equally charged. [216-217]

The complex behaviour of proteins at charged interfaces may be partially explained by a change of the protein charge in proximity of a local electrostatic potential. [218-219] This process, termed charge regulation [181,220], is essential in nature, *e.g.*, for the interactions of proteins with biological entities, such as lipid membranes and DNA. [219] For colloidal particles, charge regulation has been first discussed by Kirkwood and Shumaker. [221] Moreover, it has been shown to be important for protein

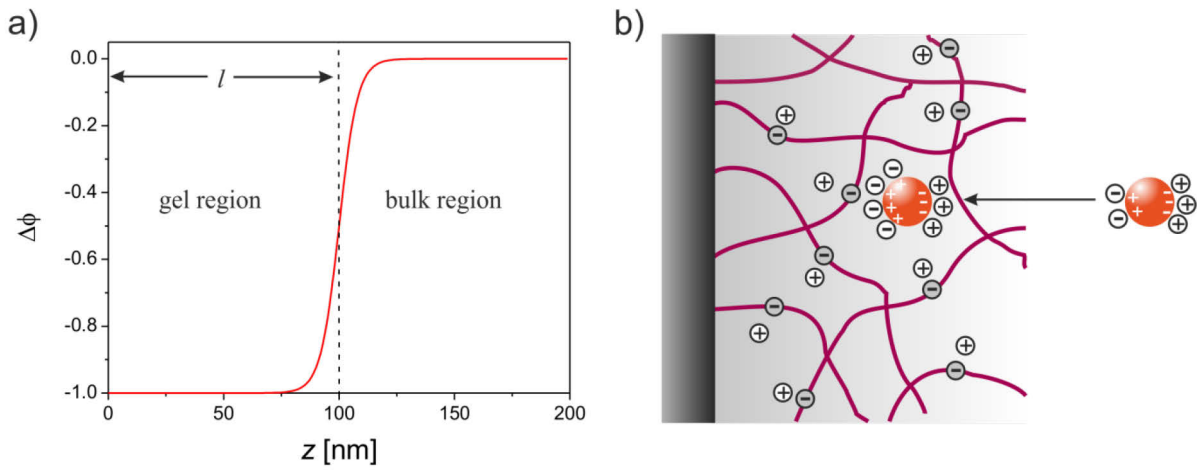

Figure 3.13: a) Local electrostatic potential difference $\Delta\phi(z)$ of a negatively charged gel network with a gel thickness l of 100 nm as function of the distance z from the solid surface. b) Schematic representation of the charge regulation of a protein in proximity to a charged gel network.

adsorption on equally charged planar [222] and spherical polyelectrolyte brushes [223] as well as for proteins in membranes [224].

Figure 3.13 b shows the mechanism of charge regulation for proteins adsorbing on a negatively charged microgel network. Two aspects need to be considered: i) The Donnan potential of the gel network results in an uneven ion distribution between the network and the bulk. This leads to a local *pH* value next to the charged network chains which may be significantly lower than the *pH* value of the bulk solution. [181,223,225] ii) The negative potential of the charged network induces a shift of the pK_a values of the ionisable groups of the protein. [220] Thus, proteins in proximity of the microgel network regulate their charge according to the local *pH* value and to the shifted pK_a values. This process is schematically shown Figure 3.13 b for an overall negatively charged protein approaching the negatively charged hydrogel network. In case of negatively charged proteins, the net charge can be even reversed upon adsorption if the local *pH* value is lower than the isoelectric point. This leads to an overall electrostatic attraction between the protein and the negatively charged particle. Proteins which are positively charged at bulk conditions increase their positive net charge upon binding leading to an even stronger adsorption to the microgel. Noteworthy, charge regulation is salt-dependent and becomes less significant at higher ionic strength of the solution. [225-226] A recent study of Li *et al.* on protein adsorption on large negatively charged microgels revealed that adsorbed proteins adapt a net charge more positive than compared to proteins in the bulk solution. [74]

However, a quantitative thermodynamic examination of this effect is still missing. Moreover, the charge regulation may also affect the catalytic activity of adsorbed enzymes since the catalytic efficiency is very sensitive to the net charge of the protein. This also needs to be considered for further investigation.

The distribution of the charges on the protein surface also affects the electrostatic interactions and the binding affinity. In a study of Bysell *et al.*, it was shown that synthetic peptides with an anisotropic surface charge distribution show higher interaction strengths than peptides having a homogeneous surface charge. [227] Thus, the segregation of the surface charge into highly negatively and positively charged patches increases the electrostatic interactions with charged interfaces. This surface patchiness is essential when comparing the adsorption of proteins of similar size and net charge but different charge anisotropy.

Besides electrostatic forces, the entropic and energetic contributions from hydrophobic interactions must be included into the analysis of protein binding on charged microgels. Studies regarding the adsorption of synthetic peptides of varying hydrophobicity demonstrated that hydrophobic interactions cause moderate protein loading at high ionic strength where electrostatic interactions are no longer active. [227-228] Thus, the presence of hydrophobic interactions can eliminate the complete detachment of the proteins at high ionic strength. Furthermore, they may contribute to the binding affinity at the “wrong side” of the isoelectric point of the protein leading to significant protein loadings at this condition. [216-217]

3.3.2 Modelling of Protein Adsorption

3.3.2.1 Single Protein Solutions

Binding of proteins from single protein solutions on the core-shell microgels is well-described by the Langmuir adsorption isotherm. This model was originally developed by Irving Langmuir in 1916 to describe the adsorption of gas molecules on glass and metal surfaces [229], but can be extended to binding studies in solution. [230] The Langmuir isotherm is an equilibrium binding model and, thus, requires a dynamic equilibrium between adsorbed molecules and those in the surrounding solution. Moreover, it is based on three assumptions: i) The solute binds on the material to form a monolayer. Thus, condensation of additional solutes onto the first layer is precluded. ii) All adsorption sites are equivalent regarding the adsorption energy. iii) There are no interactions between adsorbed solutes which may facilitate or hamper subsequent adsorption (*i.e.*, no cooperative or anti-cooperative binding).

The Langmuir isotherm is applied to treat protein adsorption on a variety of systems, including solid surfaces [231], silica nanoparticles [36], polymer brushes [72] as well as microgels [214]. However, the latter is strictly valid for the description of binding processes where proteins bind reversibly to distinct binding sites with the same energy of binding. Thus, the adsorption processes which are followed by a transition of the bound protein to a tightly bound state via unfolding of the protein structure are not properly described by the Langmuir isotherm. Consequently, additional experiments including the analysis of the equilibrium of binding as well as the analysis of the protein conformation in the bound state, are required to verify whether the Langmuir isotherm is the appropriate model for the given adsorption process.

According to the experimental results illustrated in section 4.2.3 and 4.4.2, adsorption of proteins on core-shell microgels of varying charge density does not perturb the protein structure. Thus, the protein stays in its native conformation and retains its full functionality (*i.e.*, catalytic activity in case of enzymes) when adsorbed on the gel network. These results point to reversible protein adsorption. Indeed, the dynamic exchange between free and adsorbed proteins, *i.e.*, the reversibility of protein adsorption, has been experimentally demonstrated (see section 4.5.3). Moreover, there was no evidence for lateral interactions between proteins bound to the adsorption sites (see section 4.6.2). It has to be emphasised that the adsorption sites of the microgel are distributed within three-dimensions in the gel network and, thus, are not restricted to a two-dimensional solid surface. However, for the derivation of the Langmuir equation (equation (3.17)) using statistical mechanics [230] the arrangement of the binding sites as well as the dimensionality of the system is not relevant. Concluding this, this model is generally suitable to describe the reversible adsorption of molecules onto three-dimensional systems, such as protein adsorption on hydrogels.

The above considerations show that all the prerequisites of the Langmuir model are fulfilled. Thus, the Langmuir isotherm is appropriate to describe the binding of proteins to the core-shell microgels having a total number of N independent binding sites B. The Langmuir equation then relates the fraction of adsorption sites in the gel containing bound protein Θ to the binding constant K_b given by [229-230]

$$\Theta = \frac{K_b[P]}{1 + K_b[P]} \tag{3.16}$$

where $[P]$ is the concentration of protein in solution. For a microgel containing N adsorption sites, Θ is N_b/N, with N_b as the number of proteins bound per microgel.
Thus, the equilibrium binding constant K_b in the Langmuir frame work reads

$$K_b = \frac{[PB]}{[B][P]} = \frac{\Theta}{(1-\Theta)[P]} \tag{3.17}$$

where $[B]$ is the concentration of free binding sites and $[PB]$ is the concentration of occupied binding sites.

3.3.2.2 Competitive Protein Binding

Particles exposed to a solution of different proteins, such as the blood serum, will be immediately covered by a protein corona containing some of the proteins from the surrounding solution. [38,61] Typically, the protein composition of this corona deviates from the molar ratios of the proteins in the solution and may change with time until equilibrium is reached. [61] Vroman and co-workers first observed that the adsorption of fibrinogen from plasma to solid surfaces shows a maximum at intermediate contact time to the interface and at intermediate plasma dilution. [90,92-93] This maximum occurs from the sequential adsorption of proteins from the plasma, starting with the primary adsorption of highly abundant and mobile proteins, such as albumin. [90,232] The latter are rapidly exchanged by the less abundant fibrinogen of higher affinity which itself is displaced by high molecular weight kininogen and other proteins of higher affinity at later stages. [89-90,233] This phenomenon is termed as Vroman effect and may take seconds to hours depending on the plasma concentration. [87,89-91,232] Moreover, it has been shown that the displacement of bound fibrinogen by plasma proteins depends on numerous factors including the temperature and the specific surface chemistry. [87,234] Rapid and extensive Vroman effects are observed on hydrophilic surfaces while the displacement of fibrinogen is found to be slower and less extensive on hydrophobic materials. [89-90] This observation was explained by structural changes of the protein which is bound to hydrophobic surfaces. The latter become more relevant with increasing residence time on the surface and cause irreversible binding on the hydrophobic material. This inhibits the displacement by other plasma proteins and, thus, sequential protein adsorption.
It has to be emphasised that the sequential adsorption is not restricted to plasma proteins but is more general describing the behaviour of adsorbing proteins with respect to each other. [233,235] The composition of the adsorbed proteins at equilibrium strongly depends on the individual protein concentration in solution and the adsorption affinities. Generally, larger proteins have larger binding affinities than smaller globular proteins because they interact over a larger surface area. [114,233,235] On the other hand, smaller proteins are adsorbed more rapidly to the surface due to their larger diffusivities in solution. [114,235] Consequently, the initial adsorption is dominated by kinetics and the smallest proteins of a protein mixture will bind to the solid surface or to the particle at first. Immediately after the early stage, proteins with higher affinity will replace the weakly bound small proteins in a complex series of adsorption and displacement steps. [114] In addition to the composition of the protein mixture, the temperature of the system is also very important because the binding constants of the proteins are temperature-dependent and, thus, the protein corona at low temperature,

e.g., room temperature, may be very different from the one at higher temperatures, *e.g.*, body temperature.

Given the enormous complexity of competitive protein adsorption, there have been only a few attempts to quantify or predict the sequential adsorption of proteins. One of the first approaches to model the Vroman effect was performed by Slack *et al*. [87] The model thus developed differentiates between adsorbed fibrinogen molecules that are bound reversibly and irreversibly, respectively, as a function of time and could qualitatively describe the competitive adsorption on different surfaces. In a different study, Vogler *et al*. came up with a model based on mass-balance equations and on the idea that the protein diffuses from a solution of mixed proteins into a rapidly inflating interphase volume in proportion to individual solution concentrations. [86] According to this model, the discrimination of the competing proteins on the surface is caused only by the relative protein size and is not related to differences in the protein affinities. Szleifer *et al.* studied the thermodynamics and kinetics of proteins and protein mixtures in a generalised molecular theory which is based on the chemical potentials of the species and also includes conformational changes of the proteins upon adsorption. [59] In a further study, this model was extended to model charged proteins to study the effect of charge and charge distribution. [236]

The approach chosen in this thesis starts from the thermodynamic analysis of the adsorption process of the individual proteins comprising the protein mixtures. Based on the binding mechanism and the binding constants of single protein adsorption, a competitive binding model is then developed which predicts the equilibrium binding of protein mixtures. Consequently, this model is not a quantitative description of the time-dependent Vroman effect but predicts the adsorbed amount of each protein in the final stage. In this thesis it is demonstrated that proteins retain their native conformation for at least several days after adsorption to the core-shell microgels of varying charge-density (see section 4.2 and 4.4). In addition, protein adsorption on microgels is found to be reversible (see section 4.5). Thus, proteins bound to the microgel are dynamically exchanged by proteins from solution and a transition to a tightly bound state, that is generally observed for adsorption on solid surfaces, is excluded. As a consequence, theoretical expressions which account for irreversible binding are not included into this model. Moreover, the experimental data and its analysis demonstrate that the proteins adsorb to one set of independent binding sites (see section 4.2, 4.3 and 4.4) and that the adsorption process of single proteins is well-described by the Langmuir isotherm. Under the assumption that different proteins compete for the same type of binding sites B and the number of binding sites N is constant for all the proteins, the competitive Langmuir isotherm is suitable to predict the equilibrium state of the competitive adsorption process. The equations of the competitive Langmuir isotherm for a two-component systems are derived as follows:

Suppose a protein of type P_x binds with affinity $K_{b,x}$ to a binding site of the microgel. A different protein, of type P_y, can bind to the same binding site with affinity $K_{b,y}$:

$$P_x + B \overset{K_{b,x}}{\rightleftarrows} P_xB \quad \text{with} \quad K_{b,x} = \frac{[P_xB]}{[B][P_x]}$$
$$P_y + B \overset{K_{b,y}}{\rightleftarrows} P_yB \quad \text{with} \quad K_{b,y} = \frac{[P_yB]}{[B][P_y]} \tag{3.18}$$

Thus, competitive binding of the protein species reduces the concentration of free binding sites [B] which reads

$$[B] = \left(1 - \Theta_x - \Theta_y\right) N [M]_t \tag{3.19}$$

where Θ_x and Θ_y are the fractions of binding sites containing protein of type P_x and P_y, respectively, and $[M]_t$ is the total microgel concentration. Using this expression for [B] and $\Theta_x N[M]_t$ and $\Theta_y N[M]_t$ for [P_xB] and [P_xB], respectively, Θ_x and Θ_y are given by

$$\Theta_i = K_{b,i}[P_i]\left(1 - \Theta_i - \Theta_j\right) \tag{3.20}$$

with the indices i = x,y and j = y,x. Equation (3.20) demonstrates that the adsorption of proteins of type P_x is reduced by the adsorption of proteins of type P_y, and vice versa. Combining the equations for Θ_x and Θ_y results in the two-component competitive Langmuir equation for the individual proteins of type P_x and P_y: [237]

$$\Theta_i\left([P_i], [P_j]\right) = \frac{K_{b,i}[P_i]}{1 + K_{b,i}[P_i] + K_{b,j}[P_j]} \tag{3.21}$$

If the binding constants $K_{b,x}$ and $K_{b,y}$ are known from adsorption experiments of single protein solutions, the competitive Langmuir equations can be used to predict the composition of the protein corona. For this purpose, [P_x] and [P_y] must be expressed by the known total protein concentrations $[P_x]_t$ and $[P_x]_t$ via $[P_i]=([P_i]_t - N\Theta_i[M]_t)$, with i=x,y. With this, equation (3.21) can be rearranged to give a quadratic equation for $\Theta_j([P_i], [P_j])$. The solution is

$$\begin{aligned}\Theta_j\left([P_i], [P_j]\right) = \Bigg\{ &- \left[1 + K_{b,i}\left([P_i]_t - N\Theta_i\left([P_i], [P_j]\right)[M]_t\right) + K_{b,j}[P_j]_t + N[M]_t K_{b,j}\right] \\ &+ \Big[\left(1 + K_{b,i}\left([P_i]_t - N\Theta_i\left([P_i], [P_j]\right)[M]_t\right) + K_{b,j}[P_j]_t + N[M]_t K_{b,j}\right)^2 \\ &- 4{K_{b,j}}^2 N[M]_t[P_j]_t\Big]^{\frac{1}{2}}\Bigg\}\left(-2N[M]_t K_{b,j}\right)^{-1}\end{aligned} \tag{3.22}$$

It has to be noted that the competitive Langmuir isotherm is solely based on the binding constants of the individual proteins and does not include cooperative phenomena. Thus, it is assumed that proteins of type P_x do not influence the binding affinity of the proteins of type P_y and vice versa. Hence, application of equations (3.21) and (3.22) to experimental data measured on binary mixtures of proteins can decide whether the adsorbed proteins strongly interact within the particles or whether they just compete for the N binding sites available on the particle. Moreover, non-cooperative binding on the microgels is expected especially for the following cases: i) adsorption on uncharged microgels where the microgel is not affected by the bound protein and ii) adsorption of proteins on charged microgels with similar protein surface potentials. Thus, proteins of both types will affect the

electrostatic potential and the microgel structure in the same way. Consequently, facilitated or hampered binding of one protein is not induced by the presence of the other protein.

3.3.3 Thermodynamic Analysis of Protein Binding by Isothermal Titration Calorimetry (ITC)

Isothermal Titration Calorimetry (ITC) has emerged as an important tool in the thermodynamic analysis of molecular reactions in solution. [238-239] For example ITC is heavily used to analyse the binding affinity of proteins with different species, such as ligands, lipids or DNA. [239-241] A special application of this method is the investigation of the thermodynamics of protein adsorption on colloidal systems and nanoparticles. [60,242-243] In this manner, it is possible to compare the binding capacity of a carrier system for different proteins in a systematic fashion. [66,244]

For example Chen *et al.* investigated the binding process of the two different isoforms of *β*-lactoglobulin (BLG), BLG A and BLG B, on positively charged nanoparticles. [245] The binding thermodynamics were determined in relation to the charge density of the protein surface. Henzler *et al*. studied the adsorption of BLG on equally charged SPBs at different salt concentrations by ITC. [84] These experiments gave clear evidence for counterion release to be the binding motif for adsorption of negatively charged proteins on negatively charged SPBs. Moreover, the entropy of binding ΔS_b determined from ITC could be directly correlated to the number of released counterions. The first investigations of protein adsorption on microgels were performed by Linse *et al.* [51] and Lindman *et al.* [85], respectively. Lindman *et al*. analysed binding of HSA onto different uncharged N-isopropylacrylamide/N-*tert*-butylacrylamide microgels below the volume phase transition. [85] Microgels of varying hydrophobicity and curvature were subjected to ITC analysis to obtain information about the nature of interaction between the microgel and the protein. These experiments mentioned are the first systematic efforts to clarify the thermodynamic driving forces of protein adsorption.

In Figure 3.14 typical ITC results of an adsorption reaction on colloidal particles are displayed. Cytochrome c was injected into a solution of negatively charged microgel particles dispersed in the same buffer solution. The general measuring principle of ITC is as follows:

ITC measures the time-dependent uptake or evolution of heat Q upon injections of an aliquot of protein into a solution of microgel compared to a reference cell filled with water. After completion of the experiment the incremental heat ΔQ as a function of the molar ratio between the protein and microgel is calculated from the raw ITC data by integrating the heats of each injection with respect to the time and dividing the integrated heats by the number of moles of injected protein. In a separate experiment the exothermic dilution of cytochrome c is measured which must be subtracted for data evaluation. After correction for the heat of dilution of the protein the total heat change after each injection can be fitted with an appropriate equilibrium binding model to determine the enthalpy ΔH_{ITC}, the binding constant K_b, and the number of binding sites N (Figure 3.14). [246-247]

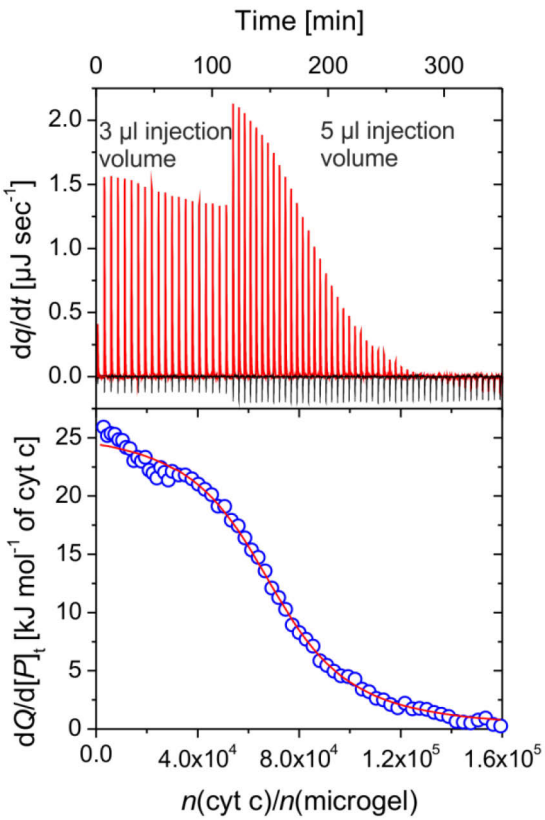

Figure 3.14: ITC data of cytochrome c (cyt c) binding onto CSM-10 particles at 298 K in 10 mM MOPS buffer solution *pH* 7.2. The upper panel shows the raw ITC data with the black spikes as the heat of dilution of cytochrome c. The red spikes are the incremental heat changes corresponding to each injection of cytochrome c into the microgel dispersion. The lower panel shows the integrated heats of each injection (circles) after subtraction of the dilution signal from the overall signal. The solid line represents the fit according to the SSIS model described in section 3.3.3.1.

3.3.3.1 Evaluation of the ITC Data

Since the adsorption of proteins on the microgels is well-described by the Langmuir isotherm, this equilibrium binding model was used as basis to determine the thermodynamic parameters from the ITC data. It considers the binding of proteins on N equivalent adsorption sites on the microgel without any lateral interactions between the bound proteins. Thus, it is referred to the **s**ingle **s**et of **i**ndependent binding **s**ites (SSIS) model in the ITC module of the Origin® 7.0 software supplied by the instrument manufacturer. The underlying equations of the Langmuir formalism in the ITC fitting procedure are explained in the following:

In the Langmuir equation (equation (3.16)), the binding constant K_b is related to the fraction of occupied binding sites Θ and to the concentration of unbound protein $[P]$. Since only the total protein concentration in the total sample volume $[P]_t$ is known, $[P]$ must be expressed by $[P]_t$ via [248]

$$[P] = [P]_t - N\Theta[M]_t \tag{3.23}$$

The value of Θ is determined by combining equation (3.16) and equation (3.23) and by solving the resulting quadratic expression. The solution is:

$$\Theta = \frac{1}{2}\left\{\left(1 + \frac{x}{N} + \frac{1}{NK_b[M]_t}\right) - \sqrt{\left(1 + \frac{x}{N} + \frac{1}{NK_\mathrm{b}[M]_\mathrm{t}}\right)^2 - \frac{4x}{N}}\right\} \tag{3.24}$$

where x is the ratio between the total protein concentration in the volume and the microgel concentration, $[P]_t/[M]_t$. The total heat content Q evolved on addition of a protein is then given by: [248]

$$Q = N\Theta[M]_\mathrm{t}V\Delta H_\mathrm{ITC} \tag{3.25}$$

where ΔH_ITC is the molar enthalpy change measured upon mixing of the protein with the microgel by ITC and V is the active cell volume. Under the assumption that N, K_b and ΔH_ITC are independent of the protein concentration, the equations (3.24) and (3.25) can be combined to give the total heat $Q(x)$:

$$Q(x) = \frac{N[M]_\mathrm{t}V\Delta H_\mathrm{ITC}}{2}\left[1 + \frac{x}{N} + \frac{1}{NK_\mathrm{b}[M]_t} - \sqrt{\left(1 + \frac{x}{N} + \frac{1}{NK_\mathrm{b}[M]_\mathrm{t}}\right)^2 - \frac{4x}{N}}\right] \tag{3.26}$$

However, in a typical ITC experiment not the total heat content $Q(x)$ but the incremental heat upon small and discrete injections of proteins $\Delta Q(x)/\Delta[P]_t$ is measured. Moreover, for the calculation of the change of heat $\Delta Q(x)_i$ resulting from completion of the (i-1)-th injection to completion of the i-th injection, one must also take into account the displaced volume $\mathrm{d}V_\mathrm{i}$:

$$\Delta Q(x)_\mathrm{i} = Q(x)_\mathrm{i} - Q(x)_{\mathrm{i}-1} + \frac{\mathrm{d}V_\mathrm{i}}{V}\left(\frac{Q(x)_\mathrm{i} + Q(x)_{\mathrm{i}-1}}{2}\right) \tag{3.27}$$

Going to the continuum limit, the data are fitted by the derivative $\mathrm{d}Q(x)/\mathrm{d}[P]_t$. With respect to the total volume V the differential heat is given by the following equation: [248-249]

$$\frac{1}{V}\frac{\mathrm{d}Q(x)}{\mathrm{d}[P]_\mathrm{t}} = \frac{\Delta H_\mathrm{ITC}}{2}\left[1 - \frac{-1 + \frac{x}{N} + \frac{1}{NK_\mathrm{b}[M]_\mathrm{t}}}{\sqrt{\left(1 + \frac{x}{N} + \frac{1}{NK_\mathrm{b}[M]_\mathrm{t}}\right)^2 - \frac{4x}{N}}}\right] \tag{3.28}$$

Least square fitting of equation (3.27) and (3.28) to the experimental data then yields the unknown parameters N, K_b and ΔH_ITC. Therefore, the initial values of N, K_b and ΔH_ITC are improved by standard Marquardt methods until no further improvement in the fit occurs with continued iteration. Typically, a sigmoidal curve is measured for $1/V\ \mathrm{d}Q(x)/\mathrm{d}[P]_t$ where $\Delta\mathrm{H}_\mathrm{ITC}$ describes the plateau for the first injections, N the inflection point and K_b the sharpness of the transition at $x = N$.

3.3.3.2 Thermodynamic Analysis

As described above, the fitting of the experimental ITC data yields the thermodynamic parameters *N,* ΔH_{ITC}, and K_b. The remaining parameters, the Gibbs free energy of binding ΔG_b and the binding entropy ΔS_b are calculated according to [81]

$$\Delta G_b = -RT \ln K_b = \Delta H_b - T\Delta S_b \tag{3.29}$$

Hence, adopting the ITC analysis leads in essence to two enthalpies: i) the directly measured enthalpy ΔH_{ITC} and ii) the enthalpy of binding ΔH_b. The latter is obtained from the temperature-dependence of K_b given by

$$\left(\frac{\mathrm{d}\ln K_b}{\mathrm{d}T}\right)_p = -\frac{\mathrm{d}}{\mathrm{d}T}\left(\frac{\Delta H_b - T\Delta S_b}{RT}\right) \tag{3.30}$$

If ΔH_b and ΔS_b are independent of temperature, *i.e.*, the change of the heat capacity ΔC_p of the reaction is zero, then equation (3.30) gives the van´t Hoff relation [81]

$$\left(\frac{\mathrm{d}\ln K_b}{\mathrm{d}T^{-1}}\right)_p = -\frac{\Delta H_b}{R} \tag{3.31}$$

from which ΔH_b can be easily calculated. Finally, ΔS_b is obtained from the intercept of the van´t Hoff analysis or from the temperature-dependence of ΔG_b, as follows: [81]

$$\frac{\mathrm{d}\,\Delta G_b}{\mathrm{d}T} = -\Delta S_b \tag{3.32}$$

Previous investigations by ITC on protein adsorption and other processes show that ΔH_{ITC} and the van´t Hoff enthalpy ΔH_{vH} do not necessarily agree. [250-255] For example, discrepancies between both enthalpies are frequently observed in differential scanning calorimetry (DSC) protein unfolding experiments. [254,256] In fact, the ratio of $\Delta H_{vH}/\Delta H_{ITC}$ has been used as a 'calorimetric criterion' for the applicability of two state models. [254] Significant differences in the van´t Hoff caloric enthalpy were also found in ligand-RNA binding. [257] Moreover, studies on the binding between *α*-amylase and the subtilisin inhibitor revealed that the calorimetric enthalpy was much larger than the van´t Hoff enthalpy determined from surface plasmon resonance (SPR) binding constants. [252]

There has been much discussion about the disparate results obtained by calorimetric and van´t Hoff analysis. Changes of C_p were observed in the calorimetric experiment that were not apparent in the van´t Hoff analysis and could account for a portion of these inconsistencies. [251,253] This is especially true for reactions with small values of ΔC_p in the range of $|\Delta C_p| < 200$ cal mol^{-1} K^{-1}. In this case, ΔC_p biases the slope of the van´t Hoff plot without producing curvature in the plot that is discernible within the noise levels in the data. [251] On the other hand, previous theoretical and experimental studies demonstrated that the presence of linked equilibria do not contribute to the differences between ΔH_{ITC} and ΔH_{vH} even when binding is incorrectly assumed to be a simple equilibrium binding reaction. [258-259] However, irreversible reactions, such as irreversible aggregation, could negate the van´t Hoff analysis resulting in significant discrepancies between ΔH_{ITC} and ΔH_{vH}.

Another likely source of the discrepancy is the contribution of processes to the direct calorimetric measurement that are not included in the description of the binding event. The latter may be temperature-dependent changes in the water-structure [260-261] and other independent processes [253], such as buffer interactions, mixing and non-linked conformational changes. Hence, ΔH_{ITC} may contain contributions that are not related to the binding process. In contrast, ΔH_{vH} is correlated to the binding constant K_b, *i.e.*, to the adsorption process, only. ITC experiments performed at different temperatures allow one to obtain both quantities and a thorough comparison of ΔH_{ITC} and ΔH_b may lead to these additional processes.

3.3.4 Kinetics of Protein Adsorption

The results in section 4.4.1 and section 4.5.3 demonstrate that protein adsorption on microgels is a reversible process between protein and microgel and that the Langmuir isotherm provides an excellent description (see equation (3.16)) for the equilibrium binding process. For this reason, the kinetics of protein adsorption is analysed by using the kinetic Langmuir model:

$$\frac{\mathrm{d}\Theta}{\mathrm{d}t} = k_{on}\frac{[B][P]}{N[M]_t} - k_{off}\frac{[PB]}{N[M]_t} = k_{on}(1-\Theta)([P]_t - N\Theta[M]_t) - k_{off}\Theta \tag{3.33}$$

where k_{on} and k_{off} is the adsorption and desorption rate, respectively, $[M]_t$ is the total microgel concentration, and $[P]_t$ is the total protein concentration in solution. This equation shows that the overall adsorption rate $\mathrm{d}\Theta/\mathrm{d}t$ depends on both k_{on} and k_{off} as it would be expected for reversible reactions. Equation (3.33) can be further simplified by using the relationship $K_b = k_{on}/k_{off}$ and by substituting the parameter k_{off} for k_{on}/K_b. In addition, K_b can be determined from other experiments, *e.g.*, ITC analysis, and, thus, the only unknown left in equation (3.33) is k_{on}. The analytical solution for $\Theta(t)$ was derived by Azizian. [262] Therefore equation (3.33) was rearranged to give a quadratic equation:

$$\frac{d\Theta}{\mathrm{d}t} = a\Theta^2 + b\Theta + c \tag{3.34}$$

where

$$a = k_{on}N[M]_t \tag{3.35}$$

$$b = -\left(N[M]_t + [P]_t + \frac{1}{K_b}\right)k_{on} \tag{3.36}$$

$$c = k_{on}[P]_t \tag{3.37}$$

By integrating the quadratic equation (3.34), the following analytical solution is obtained: [262]

$$\Theta(t) = \frac{\gamma(\exp(\lambda t) - 1)}{2a\left(1 - \frac{\gamma}{\xi}\exp(\lambda t)\right)} \tag{3.38}$$

where

$$\lambda = \sqrt{b^2 - 4ac} \tag{3.39}$$

$$\gamma = b - \lambda \tag{3.40}$$

$$\xi = b + \lambda \tag{3.41}$$

Equation (3.38) is the analytical expression of the time-dependence of Θ for reversible adsorption processes which obey the Langmuir isotherm and, thus, is termed as the Langmuir rate equation. At the boundary condition t→∞, the binding process reaches equilibrium and the fraction of occupied binding sites at equilibrium Θ_e is given by:

$$\Theta_e = -\frac{\xi}{2a} = \frac{K_b[P]}{1 + K_b[P]} \tag{3.42}$$

which is the Langmuir equation (compare equation (3.16)). To conclude, fitting of the kinetic adsorption data by this model leads to the absolute values of the rate constants k_{on} and k_{off} which are indicative for the rate-determining step of the adsorption process. Moreover, combining these parameters with advanced kinetic theories may clarify the mechanism of adsorption of proteins on core-shell microgels. This is shown in section 4.5.2 in case of oppositely charged systems.

4 Results and Discussion

4.1 Synthesis and Characterisation of the Microgels

4.1.1 Synthesis

The core-shell microgels used in this thesis were synthesised according to the procedure given by Dingenouts *et al.* [127] and Kim *et al.* [263]. Typically, the synthesis of these particles is performed in two steps. The polymerisation reaction is schematically shown in Figure 4.1. In the first step, the PS-seed latex is made by radical emulsion polymerisation at 80 °C using potassium peroxodisulfate (KPS) as anionic and water soluble radical initiator and sodium dodecyl sulfate (SDS) as emulsifier. A small amount of NiPAm (5 mol-%) is copolymerised in this step which creates a thin shell of pNiPAm chains onto the PS core. The formation of this thin pNiPAm layer has been ascertained by SAXS and SANS investigations and is important for the attachment of the microgel network in the second step of the synthesis. [127] The core particles prepared in this way are stable towards coagulation even after removal of SDS due to electrostatic and steric stabilisation. Therein, the electrostatic stabilisation results from the low amount of permanent negative charges introduced by the initiator. The hydrophilic pNiPAm layer leads to the steric stabilisation below the LCST of pNiPAm where the polymer chains are stretched in water.
After thorough purification of the PS-seed latex by ultrafiltration (UF) against Milli-Q water, the pNiPAm network is affixed to the PS core by a second seeded polymerisation using KPS as initiator.

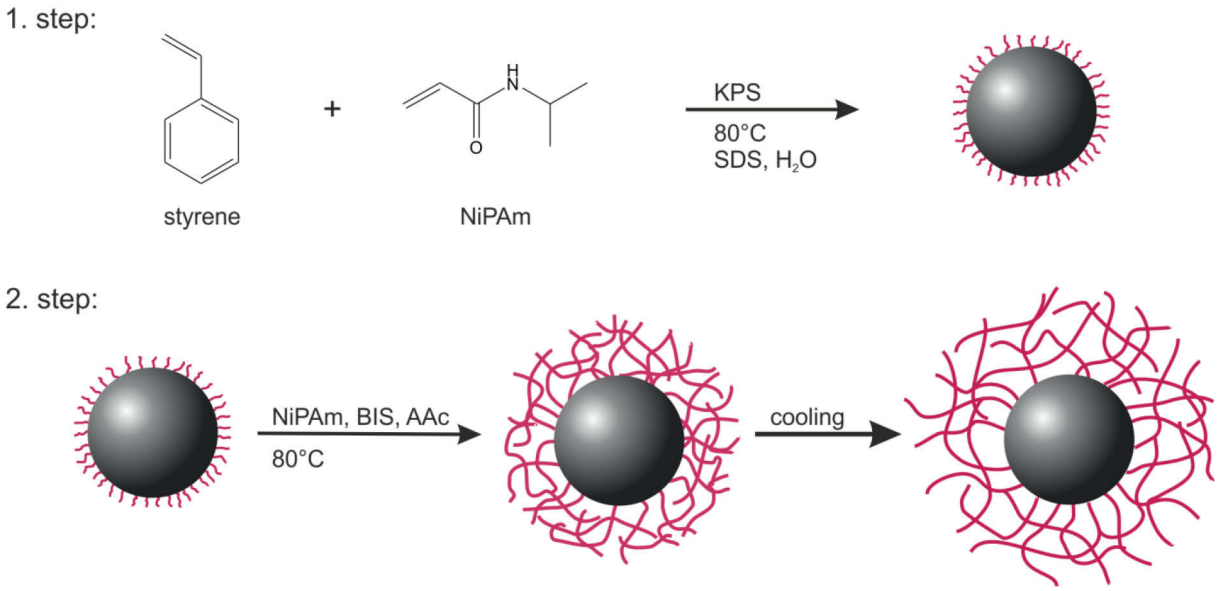

Figure 4.1: Schematic representation of the two-step synthesis of core-shell microgels. In a first step, the PS-seed latex of narrow size distribution is synthesised by emulsion polymerisation. In the second step, a network of NiPAm, BIS, and AAc is attached via seeded polymerisation above the LCST of pNiPAm.

Crosslinking of the pNiPAm shell was done by using BIS, while the charge density of the shell was adjusted by copolymerisation with AAc. This step of the synthesis is carried out in absence of emulsifier to prevent the formation of new particles. Moreover, the temperature of the reaction is set to 80 °C, *i.e.*, above the LCST of pNiPAm.

Most probably, the pNiPAm network is connected to the core particles by a chain transfer reaction. [2] In the initial state of the polymerisation of the hydrophilic monomers, water soluble oligomers are generated in solution. With increasing chain length, the polymer chains start to accumulate on the surface of the PS core particles due to their increasing hydrophobicity above the LCST, enabling chain transfer to small pNiPAm chains of the core particle. Thus, the core-shell microgels are obtained in their shrunken state. The suspension of the core-shell particles, however, remains stable at temperatures even above the volume phase transition of the microgel, where the particles are no longer stabilised by steric repulsion. Coagulation of the core-shell microgel particles is prevented by the electrostatic repulsion of the carboxylate and sulfate groups coming from the polymerisation of AAc and KPS. After synthesis of the particles, the microgels were extensively cleaned by ultrafiltration against Milli-Q water for at least four weeks.

Three different core-shell microgel systems have been prepared for the protein adsorption studies which differ in the composition of the shell network regarding the crosslinking density as well as the acrylic acid content. Table 4.1 summarises the composition as well as the size and molecular weight M_w of these microgels. The AAc content of the shell varies between 0 and 10 mol-% in order to prepare uncharged and moderately charged microgels for the protein immobilisation experiments. Moreover, a core-double-shell microgel (CSM-0-2) has been synthesised which consists of two shells of distinct charge densities. The synthesis of the second shell was performed subsequently after the attachment of the first shell according to analogous experimental instructions. This system has been prepared, because microgels consisting of two stimuli-sensitive shells have a more complex phase diagram and, thus, may be interesting for the analysis of protein binding at various experimental conditions.

Table 4.1: Composition of the shell network of the microgels used for the protein adsorption studies. The given amounts of NiPAm, BIS, and AAc are the molar feeding ratios chosen for the synthesis.

Microgel	NiPAm [mol-%]	BIS [mol-%]	AAc [mol-%]	M_w [g mol^{-1}]	R_h [nm][a]
CSM-0	95	5	0	1.42 x 10^9	134.3 ± 0.5
CSM-10	85	5	10	1.18 x 10^9	172.1 ± 0.2
CSM-0-2	98.5	1. shell: 1.5	1. shell: 0	5.22 x 10^8	159.2 ± 1.0
	96	2. shell: 1.5	2. shell: 2.5		

[a] The hydrodynamic radius R_h of the microgels was measured in 10 mM MOPS buffer *pH* 7.2 at 298 K.

4.1.2 Characterisation

After thorough purification, the particle systems were characterised by using different analytical methods. The morphology and the size distribution of the core latex and the core-shell microgels were analysed by electron microscopy. Figure 4.2 a displays a field-emission scanning electron microscopy (FE-SEM) image of the PS-seed latex. According to this image, PS core particles of narrow size

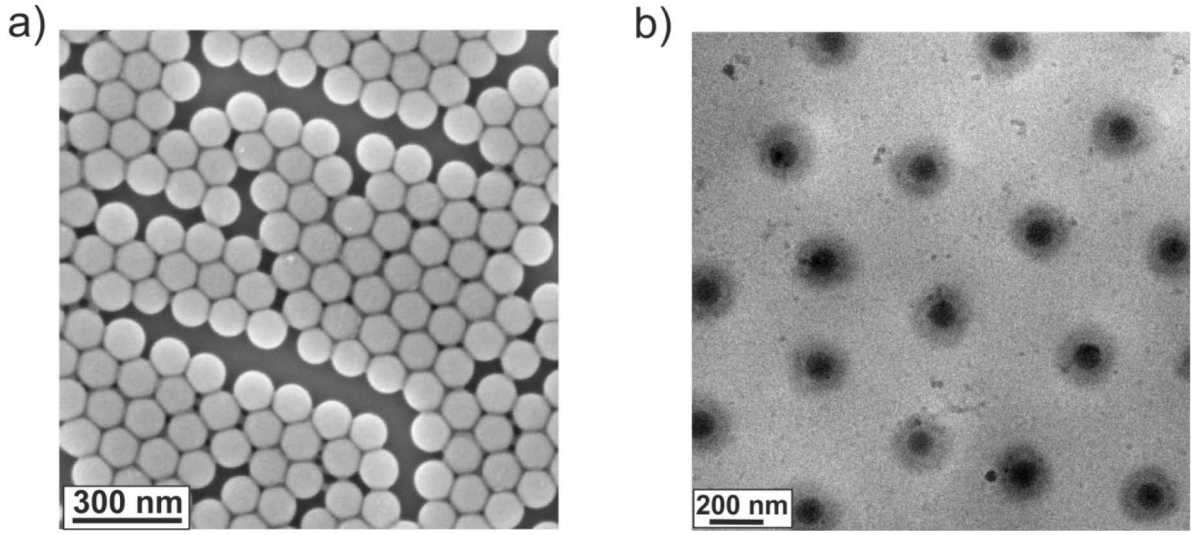

Figure 4.2: a) FE-SEM micrograph of PS core particles in water. b) Cryo-TEM micrograph of a 0.1 wt-% aqueous suspension of uncharged core-shell microgels CSM-0. The sample was kept at room temperature before vitrification.

distribution have been prepared. Moreover, the mean particle radius was determined to (53.8 ± 3.0) nm. This is, however, smaller than the hydrodynamic radius of (62.2 ± 0.7) nm obtained from DLS measurements. The smaller size of the particles in the FE-SEM micrograph results from the drying process during the sample preparation which leads to compression of the PS core and to the collapse of the thin pNiPAm shell. In contrast, the hydrodynamic radius determined from DLS experiments represents the radius of the particles in their water swollen state. Thus, DLS and FE-SEM analyse the particle size in different experimental conditions. Under these considerations, the values obtained by these methods are in good agreement. It has to be noted that for the synthesis of the core-double-shell microgel CSM-0-2, smaller PS core particles were used as seed to obtain particles of a R_h comparable to the hydrodynamic radii of the other ones. The PS core of CSM-0-2, in this case, has a mean radius of (34.9 ± 2.5) nm in the FE-SEM and a R_h = (42.5 ± 0.6) nm as measured by DLS.

The monodisperse PS particles represent ideal seed particles for the synthesis of core-shell microgels of narrow size distribution and defined geometry. However, the core-shell morphology of the microgels cannot be investigated by FE-SEM since the microgel shell collapses during drying. Thus, Cryo-TEM was used to analyse the microgels in situ instead. For this technique, the sample solutions are vitrified by using liquid ethane. During the fast vitrification of the gel, the physical state of the microgel at solution conditions is maintained and, thus, collapsing of the microgel network is prevented. Consequently, the microgel shell can be analysed in its fully swollen state. Moreover, Cryo-TEM allows to analyse the influence of the temperature [264] and salt concentration on the swelling degree of the microgel. Figure 4.2 b shows a Cryo-TEM micrograph of the uncharged microgel CSM-0 in water at room temperature, *i.e.*, below the VPTT of the pNiPAm gel. The thermo-sensitive shell can be clearly seen in this image which shows a corona around the spherical PS core. Obviously, all core particles are covered by a pNiPAm shell of similar thickness leading to core-shell microgels of narrow size distribution. Moreover, the size of the microgel obtained from this image is comparable to the hydrodynamic radius calculated from DLS measurements. It has to be noted, that in case of charged particles the network around the PS core particles is more difficult to identify, since the extra

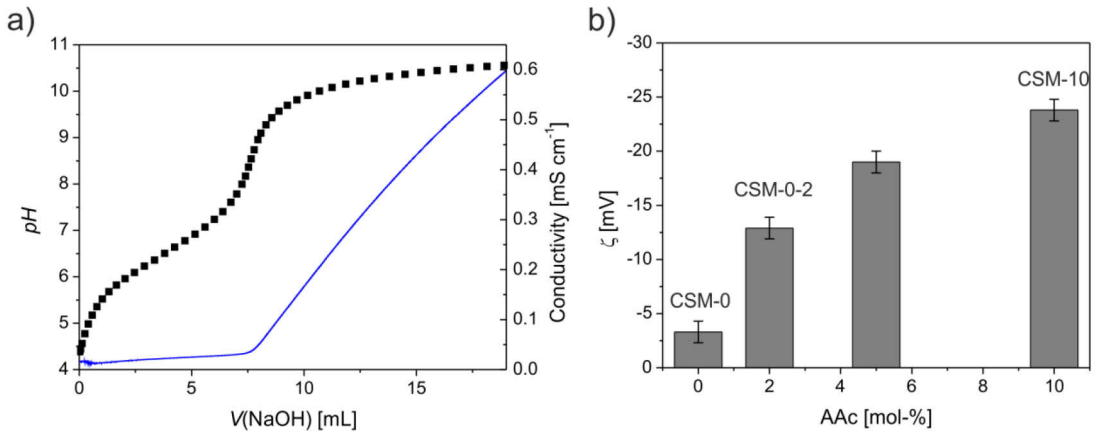

Figure 4.3: a) Potentiometric (■) and conductometric (—) titration data of the charged microgel CSM-10 dispersed in water. b) Zeta potential ζ of the microgels CSM-0, CSM-0-2 and CSM-10. Additionally the zeta potential of a microgel containing 5 mol-% AAc is shown. The measurements were performed in 10 mM MOPS *pH* 7.2 at 298 K.

swelling of the network induced by the Donnan potential (see section 3.1.2) leads to a reduced electron density and, thus to a decreased contrast between the network and water.

Understanding of the phase behaviour of the microgel particles is very important for the protein binding studies. In case of charged microgels, the swelling behaviour is mainly determined by the electrostatic contribution to the pressure inside the network. Thus, for the theoretical analysis of the charged microgels, the exact charge density, *i.e.*, the content of ionised AAc, has to be known. To determine the quantity of AAc incorporated into the shell of the microgels CSM-10 and CSM-0-2, potentiometric and conductometric titration were performed. Figure 4.3 a displays the titration curve of CSM-10. From the experimental titration data, the incorporation yield of AAc into CSM-10 was calculated to ~92 %, which corresponds to an AAc amount of 9.2 mol-%. In analogy, the incorporation yield of AAc into CSM-0-2 was determined to ~81 % resulting in a relative amount of 2.0 mol-% AAc within the second microgel shell. Since only the fraction of deprotonated AAc groups within the microgel network will contribute to the electrostatic pressure of the gel, the fraction of ionised carboxylic acid functional groups at a given *pH* value is determined from the titration curves, according to the theory described in the experimental section (section 6.3.3). From this, also the *pH*-dependent pK_a value of the carboxyl groups in the gel is calculated (equation (6.6)). In case of CSM-10, the analysis leads to a dissociation degree α_{diss} of ~0.87 and a pK_a value of 6.3 at *pH* 7.2. Thus, the pK_a value of the carboxyl groups within the microgel is increased by two units compared to the one of AAc in solution (pK_a(AAc) = 4.25 [265]). This phenomenon is termed as polyelectrolyte effect and is based on the mutual interactions of adjacent charged residues within the charged polymer. [266] Moreover, the values found for CSM-10 are in concordance with the results obtained for similar microgel systems in other studies. [267]

The different charge densities of the microgels CSM-0, CSM-0-2 and CSM-10 give rise to different electrophoretic mobilities resulting in distinct zeta potentials ζ of the microgels. The zeta potentials of the microgels were calculated using the Henry-equation (equation (6.3) and (6.4)) and are shown in Figure 4.3 b. The highest value for ζ was found for CSM-10 which is in line with the charge densities of the microgels. Although, the microgel system CSM-0 carries no carboxyl groups, a low zeta

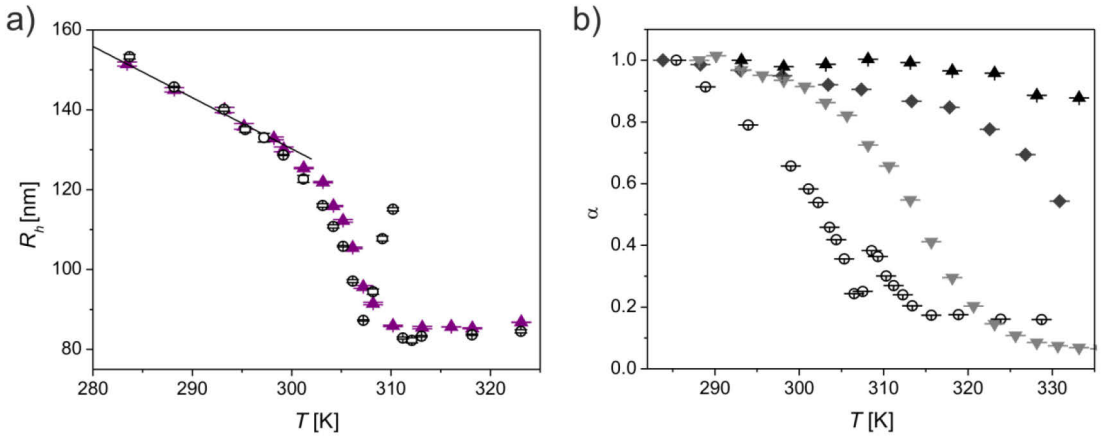

Figure 4.4: a) Temperature-dependent swelling curve of CSM-0 obtained from DLS experiments at various temperatures in a solution of (▲) 0.1 mM KCl, *pH* 6.2, and (○) 10 mM MOPS buffer, *pH* 7.2. Below the VPTT, R_h decreases linearly with increasing temperature. The solid line represents the linear regression of the data points. b) Temperature-dependent swelling ratio α of core-shell microgels with varying AAc content in 10 mM MOPS, *pH* 7.2: (○) CSM-0; (▼) CSM-0-2; (♦) 5.0 % AAc and (▲) CSM-10.

potential of ζ ~-4 mV has been measured. This is ascribed to the low amount of sulfate groups present in the gel network and on the PS surface introduced by the initiator KPS.

Owing to the different charge densities, the microgels CSM-0, CSM-0-2, and CSM-10 differ in their temperature-dependent swelling behaviour. The hydrodynamic radius of CSM-0 suspended in a 0.1 mM KCl solution, *pH* 6.2, and in 10 mM 3-(N-morpholino)propane sulfonic acid (MOPS) buffer solution, *pH* 7.2 is shown in Figure 4.4 a as a function of temperature. In 0.1 mM KCl solution, the uncharged microgel exhibits a continuous phase transition from the highly swollen network to the shrunken state with a VPTT of ~32 °C which is close to the LCST of linear pNiPAm. Below the VPTT a linear reduction of R_h is observed which is caused by the slow increase of the network hydrophobicity. Moreover, no coagulation was noticed during the DLS measurement above the VPTT. Thus, the microgel stays in the dispersed state due to the presence of weak electrostatic repulsion. Obviously, the absolute size as well as the VPTT of CSM-0 is not modified by changing the solvent from KCl solution to 10 mM MOPS buffer solution. This indicates that electrostatic interactions play a minor role regarding the swelling degree of the microgel. However, microgels dispersed in 10 mM MOPS buffer show an unexpected phenomenon above the VPTT which was not observed for the 0.1 mM KCl solution: Increasing the temperature slightly above the VPTT induces a re-swelling of the microgel. When the temperature is further increased by 1 to 2 °C the microgel shrinks again and reaches the value observed for the 0.1 mM KCl solution. The swelling of the microgel in this small temperature range is most probably explained by specific interactions with the MOPS molecules of the buffer solution which is strongest slightly above the VPTT. It is known that the MOPS molecules are highly hydrated by water molecules due to their high dipole moment and that the interactions between water and the pNiPAm chains are affected by the buffer molecules, especially at high buffer concentrations. [268] Thus, the reversible interactions with the strongly hydrated MOPS molecules slightly above the VPTT may induce the re-swelling of the gel network. Further temperature increase favours the formation of intramolecular hydrogen bonds between the pNiPAm chains of the gel which

causes the replacement of MOPS molecules and shrinking of the microgel similar to the situation in the 0.1 mM KCL solution.

Figure 4.4 b shows the swelling degree α of the different charged microgels used in this thesis as a function of temperature. The swelling degree α is defined as $\alpha = (R_{h,T}^3/R_{h,0}^3)$ where $R_{h,T}$ is the particle hydrodynamic radius at a given temperature T and $R_{h,0}$ is the hydrodynamic radius of the microgel in the completely swollen state. As can be seen from the temperature-dependent swelling capabilities of CSM-0, CSM-0-2, and CSM-10 in Figure 4.4 b, the phase behaviour of the microgel is drastically changed with increasing charge density. In particular, the presence of charges inside the microgel shell increases the VPTT and broadens the volume phase transition. Thus, for charged microgels, the balance between the electrostatic pressure and the mixing as well as the elastic contribution to the pressure inside the gel will determine the equilibrium radius of the microgel (see section 3.1.2). In a solution of low salt concentration, the Donnan potential $\Delta\phi$ is high which induces a high βP_{ion} and thus, additional stretching of the gel network. Increasing the ionic strength of the system diminishes the difference of the ion concentration between the bulk and microgel phase and, thus, leads to a decrease of βP_{ion}. The result is a salt-induced deswelling of the microgel network. This is shown in Figure 4.5 for the charged microgel CSM-10 up to a salt concentration of 1 M. It is observed that the gel shrinks monotonically and saturates at a radius close to 139 nm. The best fit by equation (3.10), which is also shown in Figure 4.5, yields very good agreement in nearly the whole range of salt concentrations. Only in the very low salt regime the fit deviates slightly from the experimental data. From the fitting of the experimental swelling data by equation (3.10) the radius of neutral reference microgel was determined to $R_r \approx 138.5$ nm. The mechanical balance approach is suitable to characterise the stiffness of the microgel. Using equation (3.11) the bulk modulus of the CSM-10 particles at 7 mM ionic strength and 298 K is calculated to $K \approx 98$ kPa. The order of magnitude of the latter is consistent with measurements of the elastic modulus of similar hydrogels. [141,269]

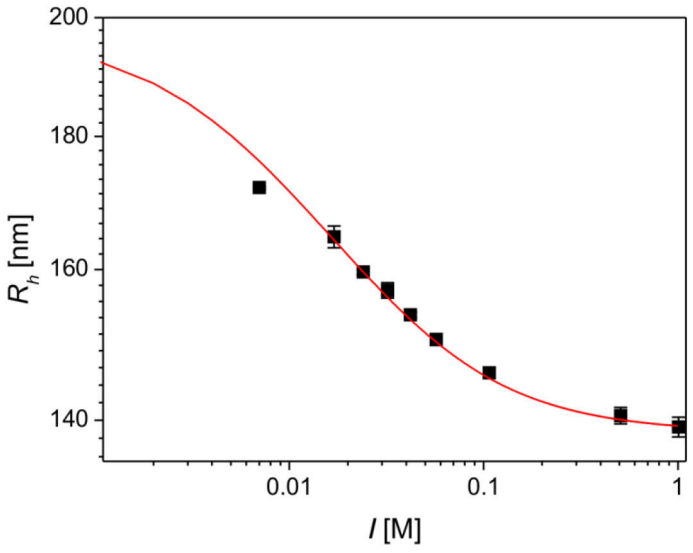

Figure 4.5: Hydrodynamic radius R_h of CSM-10 as a function of the ionic strength I of the bulk solution at 298 K and a *pH* value of *pH* 7.2. The microgel was dispersed in a 10 mM MOPS buffer solution containing 0 to 1.0 M NaCl. The solid line represents the fit according to equation (3.10).

From the characterisation of the microgel particles prepared in this thesis it is concluded that these systems are very well suited to explore the interactions of proteins with a biocompatible polymeric surface: The size distribution of the core-shell microgels CSM-0, CSM-0-2, and CSM-10 is quite narrow and the thickness of the surface layer can be derived precisely from their hydrodynamic diameter. The latter is in the range between 70 and 120 nm and, thus, is small enough to react to changes in the surrounding solution in short times. The morphology and the composition of the shell of the particles are controlled by the synthetic strategy chosen, leading to well-defined polymer networks carrying a given number of weak charges. In case of CSM-10, the *pH* value and the concentration of the co- and counterions are fully determined by the Donnan-equilibrium between the ions inside and outside of the network. Moreover, the swelling pressure can be quantitatively described by the swelling theory described in section 3.1.2. Hence, the *pH* value and the salt concentration within the shell are well-controlled and can be adjusted by added salt.

4.2 Thermo-sensitive Microgels as Protein Carriers

The first part of the protein binding experiments focuses on the analysis of protein adsorption on the thermo-sensitive microgel system CSM-0 which carries no additional carboxyl groups and exhibits mainly non-electrostatic interactions towards the proteins. Due to the missing charge, the structure and swelling capability of CSM-0 is solely determined by the environmental temperature, while it is independent of the ionic strength and *pH* value of the solution (compare section 4.1.2).

The enzyme *β*-D-glucosidase has been chosen as model protein, since it has been subject to many kinetic studies and, thus, is well characterised regarding the catalytic mechanism. Binding of *β*-D-glucosidase was investigated in the swollen state of the microgel, *i.e.*, below the VPTT of ~32 °C, as shown in Figure 4.6. The investigation was supplemented by the secondary structure analysis of the bound and free enzyme as well as by the analysis of the enzymatic activity of *β*-D-glucosidase in its native and in its adsorbed state in terms of Michaelis-Menten kinetics. The characteristic constants K_m and k_{cat} of *β*-D-glucosidase before and after immobilisation are then compared to obtain information about the interaction of the protein with the polymer network.

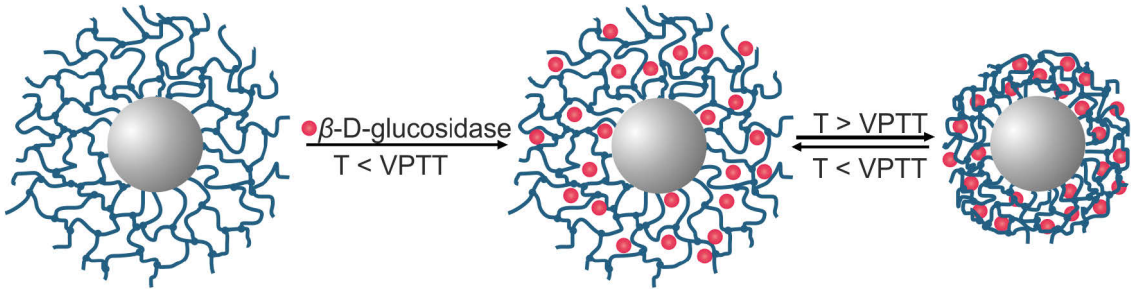

Figure 4.6: Schematic representation of the adsorption of *β*-D-glucosidase on thermo-sensitive microgel particles (CSM-0). The adsorption was conducted at 4 °C in 10 mM MOPS buffer solution *pH* = 7.2 and with a microgel concentration of 1 wt-%. The immobilised enzymes do not impede the volume transition of the microgel. The enzymatic activity test of *β*-D-glucosidase in the adsorbed state was performed at different temperatures below and above the volume phase transition of CSM-0.

4.2.1 Binding Isotherms

First experiments on protein binding on thermo-sensitive microgels reveal high loading capacities and, thus, high efficiency for the immobilisation of proteins. The adsorption isotherm was obtained by the experimental procedure established by Wittemann *et al.* which is shown in Figure 4.7. [77] Given amounts of *β*-D-glucosidase were dissolved in 10 mM MOPS buffer *pH* 7.2 to which a constant quantity of buffer-matched microgel dispersion was added. The total volume was 10 mL and the final concentration of CSM-0 was accounted for 1 wt-%. The samples were stirred for 24 hours at 4 °C for equilibration. After this incubation time, the loaded microgel particles were isolated and washed at room temperature by using the UF cells. Non-bound proteins and proteins of low binding energies are removed by filtering through the membrane of the UF cells and fresh protein-free buffer solution is added over several hours. The mass of free and desorbing proteins was determined spectroscopically from the eluate of the UF experiment. Furthermore, the amount of protein remaining in the bound state was then calculated from the difference of the concentration of depleted protein and the total amount of protein used. In this way, the mass of bound protein per gram microgel τ_{ads} for different enzyme concentrations is calculated by dividing the total amount of protein in the adsorbed state by the total dry mass of microgel in the volume. In contrast to centrifugation, the microgel particles stay in the dispersed state for the whole purification process. For this reason, the adsorption process is not affected by the collapse of the microgel shell or by the aggregation of the particles. However, like in centrifugation experiments the isotherms are gathered by a non-equilibrium procedure. Nonetheless,

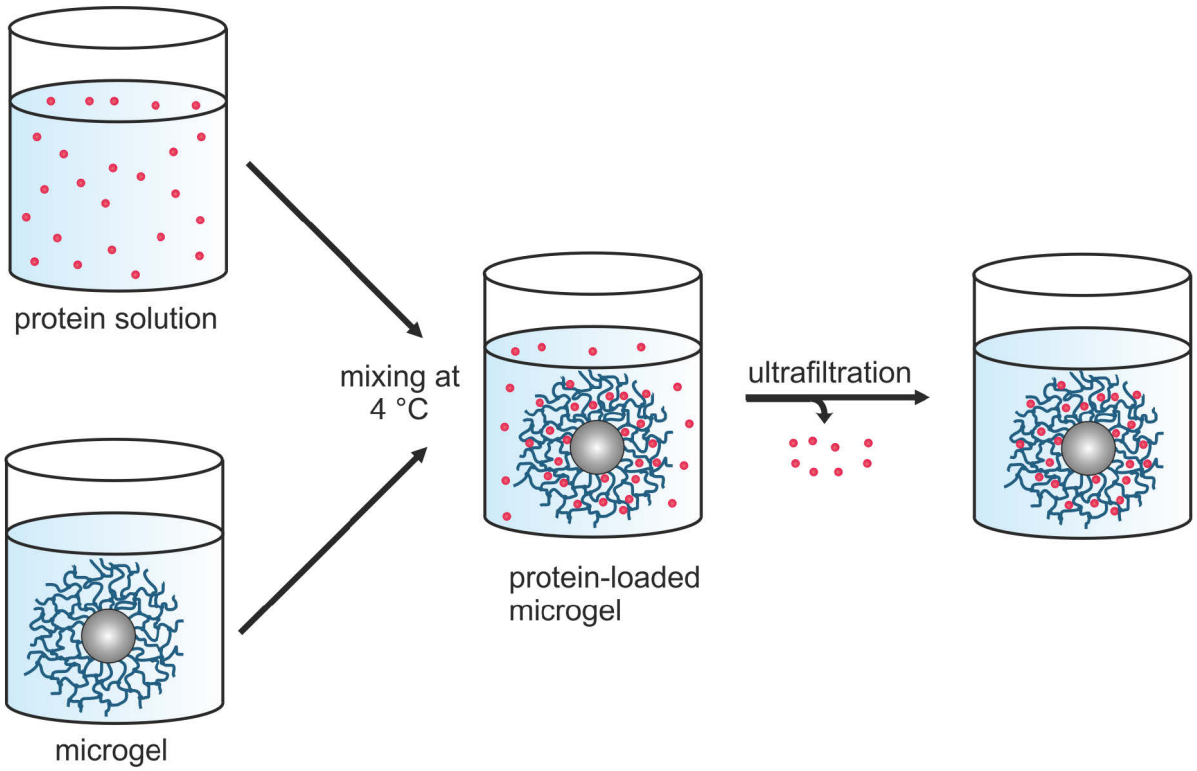

Figure 4.7: Schematic illustration of the adsorption experiment established by Wittemann *et al.* [77] First, given amounts of protein are mixed with the microgel dispersion and incubated for 24 hours at 4 °C, *i.e.*, below the VPTT. After equilibration, free and desorbing proteins are removed by extensive UF to determine the loading of the microgel particles.

these isotherms can be described by the Langmuir isotherm. This is further discussed in section 4.5. According to the experimental procedure, *β*-D-glucosidase is adsorbed onto the microgel below the VPTT and in the highly swollen (hydrophilic) state of the microgel. Figure 4.8 displays the adsorption isotherm obtained by this procedure. Here, the loading τ_{ads} of CSM-0 is plotted versus the specific protein concentration c_{sol} left free in solution. At the chosen conditions, up to 620 mg *β*-D-glucosidase per gram microgel could be adsorbed. This corresponds to a total number of ~6 500 protein molecules of a high molecular weight (~135 000 g mol^{-1} as dimer) in each shell of the microgel network. Consequently, this result indicates that strong interactions between both species exist in the swollen state of the pNiPAm network. The adsorption behaviour of *β*-D-glucosidase can be described by the Langmuir isotherm which is based on equation (3.16). The fraction of occupied binding sites Θ can be related to τ_{ads} via the relation $\Theta = \tau_{ads}/\tau_{ads,M}$, where $\tau_{ads,M}$ is the maximum binding capacity. Using this definition, the Langmuir isotherm is rearranged to give

$$\tau_{ads} = \frac{\tau_{ads,M} K_b c_{sol}}{1 + K_b c_{sol}} \tag{4.1}$$

where c_{sol} is the specific concentration of free *β*-D-glucosidase, *i.e.*, $c_{sol} = [P] M_{w,p}$.
The solid line in Figure 4.8 corresponds to the fit of the experimental data according to equation (4.1). In this way, K_b was determined to ($1.1 \times 10^4 \pm 0.4 \times 10^4$) M^{-1} and $\tau_{ads,M}$ to (1400 ± 300) mg *β*-D-glucosidase per gram microgel. Following from the high capacity of the microgel the enzyme molecules deeply penetrate into the gel network. Additionally, further experiments showed that at given adsorption conditions no leakage or desorption of *β*-D-glucosidase occurs for a longer period of time.

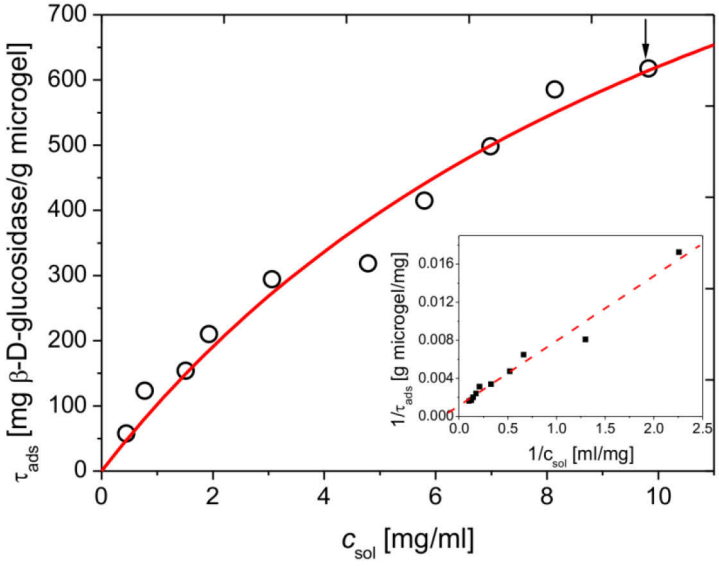

Figure 4.8: Adsorption isotherm of *β*-D-glucosidase obtained from the UF data. The adsorbed amount of *β*-D-glucosidase per gram CSM-0 τ_{ads} is plotted versus the specific concentration of free enzyme c_{sol} in solution. The solid line represents the fit of the experimental data by the Langmuir isotherm according to equation (4.1). The arrow marks the amount of entrapped enzyme used for kinetic and structural investigation (620 mg *β*-D-glucosidase per gram microgel). The inset displays the data as a linearised Langmuir-plot.

The fit by the Langmuir model describes the experimental data very well and suggests that only one type of binding site for the enzyme is present in the microgel. Similar experimental findings have been reported recently for the adsorption of *β*-D-glucosidase from *almonds* on equally charged SPBs [270-271] and other proteins and enzymes on microgels based on pNiPAm. [209,272] Concluding this, the present microgel represents a model system which provides a homogeneous and chemically well-defined surrounding for the immobilised protein.

The high loading capacity and binding affinity observed for CSM-0 and *β*-D-glucosidase may be caused by many possible interactions which need to be verified. These may also include unintended conformational changes of the protein upon adsorption which leads to a pronounced entropy gain and, thus, to a beneficial contribution to the Gibbs free energy of binding. On the other hand, attractive electrostatic interactions can be excluded, since the *pI* of the isoenzyme of *β*-D-glucosidase used is determined to 4.4. Consequently, the enzyme has an overall negative charge at the conditions chosen for adsorption. Charge regulation of *β*-D-glucosidase induced by the microgel is unlikely as the electrostatic potential of the microgel is too weak to induce a shift of the local *pH* value or of the pK_a values of the enzyme. Thus, there is a weak electrostatic repulsion between the protein and the microgel particle instead of weak electrostatic attraction. The main driving forces for immobilisation, therefore, must be sought in other interactions, *e.g.*, the formation of hydrogen bonds between the backbone of the enzyme and the amide side chains of the microgel as well as hydrophobic bonding. [85] Additionally protein unfolding may contribute to the binding strength of the enzyme. In the following, the analysis of the catalytic activity of *β*-D-glucosidase in its free and adsorbed state as a function of temperature is discussed first. These experiments will also give direct information about the conformation of the enzyme since the catalytic activity is very sensitive towards conformational changes. It is noted, that *β*-D-glucosidase was bound to CSM-0 below the VPTT while the kinetic analysis was performed below and above the VPTT. However, desorption of immobilised enzyme induced by the increase of temperature is unlikely since a higher adsorption affinity above the LCST is observed in general. [115]

4.2.2 Enzymatic Activity: Dependence of k_{cat} on Temperature

In this section, the results of the analysis of the hydrolytic activity of adsorbed and native *β*-D-glucosidase at varying temperatures are presented. The activity of *β*-D-glucosidase was analysed by monitoring the hydrolysis of the model substrate *o*-NPG. According to the reaction mechanism described in section 3.2.1, the enzyme attacks the (1→4)-*β*-glycosidic bond of *o*-NPG and cleaves the substrate in a two-step process into *o*-nitrophenol and D-glucose (Figure 4.9).

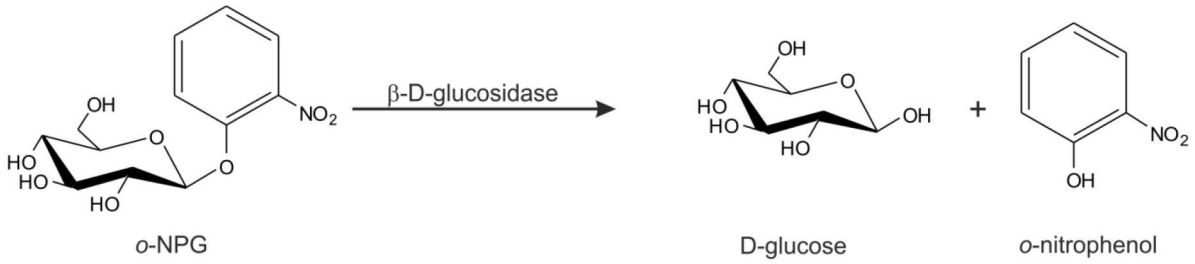

Figure 4.9: Schematic representation of the hydrolysis of *o*-NPG into *o*-nitrophenol and D-glucose catalysed by *β*-D-glucosidase.

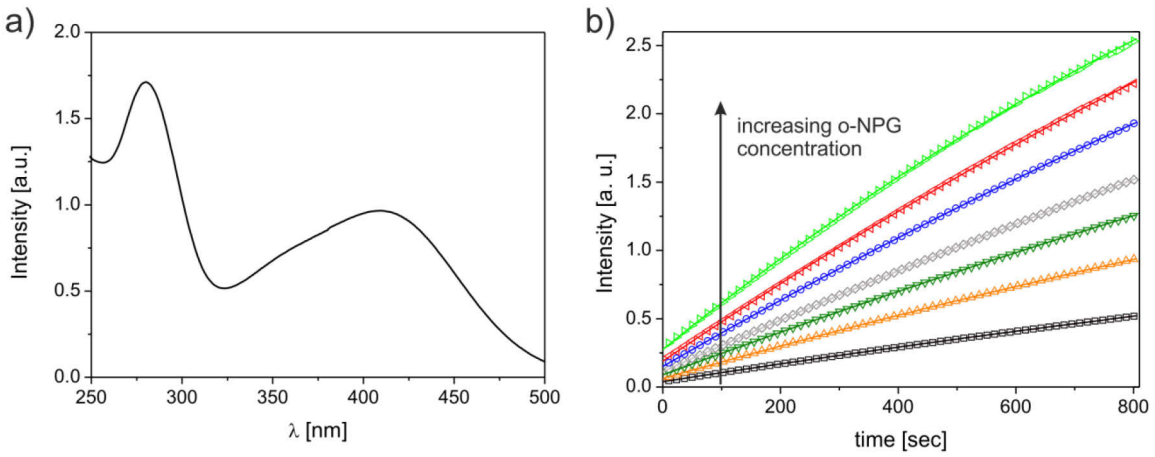

Figure 4.10: a) UV-vis spectrum of 0.05 g L^{-1} *o*-nitrophenol in 10 mM MOPS buffer *pH* 7.2 at 293 K. b) Time-dependent absorption intensity of an enzyme assay containing 0.01 g L^{-1} free *β*-D-glucosidase and *o*-NPG with concentrations ranging from $1x10^{-3}$ to $12x10^{-3}$ M at 405 nm in 10 mM MOPS buffer *pH* 7.2 at 293 K.

The anionic form of the cleaved *o*-nitrophenol is of yellow colour and, thus, shows high values of extinction between 325 and 500 nm in neutral and alkaline solutions, with an extinction maximum around 400 nm (Figure 4.10 a). In contrast, the absorption of light by the substrate in this region is negligible (data not shown). Moreover, the enzyme concentration, *i.e.*, the microgel concentration, of the enzyme assay was very low. Thus, the scattering of light by the particles was drastically minimised and did not compromise the activity tests. Consequently, the initial rate v of the reaction could be determined from the change of the extinction at 405 nm of the enzyme assay with time (Figure 4.10 b). For the kinetic investigation of the catalytic activity of adsorbed *β*-D-glucosidase, the ultrafiltrated sample marked in Figure 4.8 has been used. Thus, all kinetic experiments related to immobilised *β*-D-glucosidase were done using solutions with particles containing 620 mg enzyme per gram CSM-0. Ultrafiltration of the protein/microgel mixture removes protein molecules free in solution from the loaded microgel suspension. As desorption of bound protein upon protein depletion is observed to be very slow (see also section 4.5), this procedure guarantees that the substrate is converted exclusively by immobilised enzyme molecules. Thus, changes of the catalytic activity can be directly related to the adsorption process.

The initial rate v of enzymatic activity for different concentrations of *o*-NPG and different temperatures was evaluated in terms of Michaelis-Menten kinetics (see section 3.2.3.1). The analysis gives access to the characteristic constants K_m and k_{cat} at different temperatures, and thus, allows a quantitative comparison between the activity of free and adsorbed enzyme as a function of temperature. Figure 4.11 a displays the resulting rates v and the kinetic constant k_{cat} for native and adsorbed *β*-D-glucosidase at 293 and 313 K. The evaluation of the data was done by a nonlinear fit according to equation (3.13). Table 4.2 summarises the kinetic parameters which were obtained for the activity measurements of native and adsorbed *β*-D-glucosidase at both temperatures. The values of the Michaelis constant and of the turnover number of the free enzyme at 293 K are comparable to those obtained in preceding studies. [271,273] However, the central point of this investigation is that the

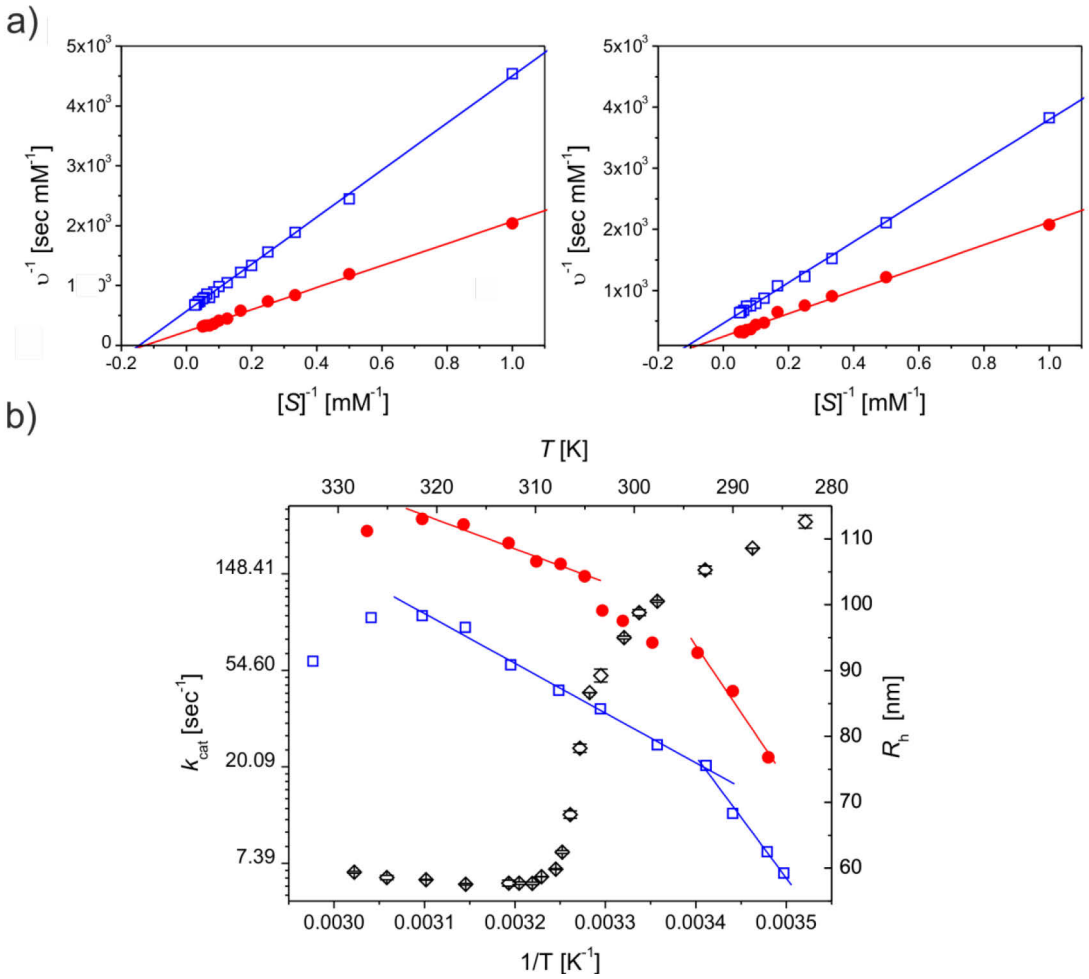

Figure 4.11: a) Lineweaver-Burk plots for the hydrolysis of *o*-NPG catalysed by immobilised (●, 620 mg enzyme per gram microgel) and native *β*-D-glucosidase (□) at 293 K (left) and 313 K (right) in 10 mM MOPS buffer *pH* = 7.2. b) Arrhenius plots of native (□) and immobilised (●) *β*-D-glucosidase (620 mg enzyme per g microgel) in 10 mM MOPS buffer *pH* = 7.2. The turnover number k_{cat} for each temperature was determined from the kinetic analysis according to equation (3.13). The enzyme concentration was located between 0.005 and 0.01 g L^{-1} (native enzyme) and 0.0035 and 0.01 g L^{-1} (immobilised enzyme), respectively, and the substrate concentration varied between 1.0 and 20.0 mM. The solid lines are linear fits of the experimental data according to equation (3.15) to determine the activation energies of the rate-limiting steps of the reaction. In addition, R_h of the carrier is plotted as a function of temperature *T* (◊). The inflection point of this curve is calculated to 304.7 K.

immobilisation of *β*-D-glucosidase onto thermo-sensitive pNiPAm-based microgels results in a remarkable enhancement of the hydrolytic activity by a factor of 3.2 - 3.5. The secondary effect caused by the adsorption of *β*-D-glucosidase is the increase of K_m, which signals a reduced binding affinity. However, the modulation of the latter is much less pronounced than the impact of the immobilisation process on k_{cat}.

In order to further analyse this effect, the catalytic activity of native and adsorbed *β*-D-glucosidase was investigated at temperatures ranging from 285 to 333 K. The kinetic parameters of the free and bound enzyme obtained at all temperatures are gathered in Table 7.1 and Table 7.2 of the supplement, respectively. The values of k_{cat} were evaluated in terms of Michaelis-Menten kinetics and are plotted

according to the Arrhenius equation (equation (3.15)). The Arrhenius plots of *β*-D-glucosidase in the free and bound state are shown in Figure 4.11 b. From these experiments it is concluded that after adsorption to the CSM-0 particles *β*-D-glucosidase is characterised by a larger turnover number compared to the enzyme free in solution for the whole temperature range. Noteworthy, the Arrhenius plot of native *β*-D-glucosidase shows a pronounced inflection point at 293 K, with activation energies of 42.9 kJ mol^{-1} above and 104.8 kJ mol^{-1} below the breakpoint. Weber *et al.* reported that this inflection point is an isokinetic temperature at which the rate-limiting step in hydrolysis catalysed by *β*-D-glucosidase from *almonds* is changed. [274] After immobilisation of *β*-D-glucosidase a change in the slope of the plot is found as well. However, within the temperature range between 293 and 307 K a slight deviation of the Arrhenius plot from linearity is observed. In this temperature window, the increase of k_{cat} with temperature is slowed down while K_m was increased at 305 K (*cf.* Table 7.2 of the supplement). The activation energies were determined from the slopes in the linear regions of the plot and are found to be 115.4 kJ mol^{-1} below 293 K and 28.9 kJ mol^{-1} from 307 to 323 K, respectively. Above the VPTT of CSM-0, E_a of the reaction catalysed by the bound *β*-D-glucosidase is decreased about 30 % when compared to the E_a of the hydrolysis in presence of free *β*-D-glucosidase.

Table 4.2. Kinetic parameters for the conversion of *o*-NPG in 10 mM MOPS buffer *pH* 7.2 catalysed by free and immobilised *β*-D-glucosidase at 293 and 313 K.

Enzyme	Temperature [K]	K_m [mM]	k_{cat} [sec^{-1}][a]
free	293	6.8 ± 1	20.4
free	313	6.8 ± 1	57.8
immobilised	293	9.4 ± 1	65.5
immobilised	313	11.3 ± 1	204.2

[a] Related to *β*-D-glucosidase in its dimeric form with a molecular weight of 135 000 g mol^{-1}.

From this analysis it is concluded that the adsorption of the enzyme to the thermo-sensitive microgel network leads to a slowing down of the catalytic rate within the temperature range where the volume transition of CSM-0 occurs. Furthermore, a smaller value of E_a is found for the bound enzyme above the VPTT compared to the one of the free enzyme. Both phenomena may be caused by the pronounced volume phase transition of the microgel network at 305 K (32 °C), where the size of the microgel shell shrinks ~40 nm. Therefore the mesh size of the microgel network is reduced tremendously upon heating. The latter must lead to a retardation of the diffusion of *o*-NPG within the cross-linked polymer chains. This increase of the diffusional barrier with increasing temperature is followed by a slight decrease of the turnover number. At still higher temperatures the density within the network reaches a constant value and the linear relation between ln k_{cat} with T^{-1} is recovered again. The lower value of E_a above the VPTT implies that diffusional limitations affect the catalytic rate in the shrunken state of the microgel. Analogous observations were made for metal nanoparticles embedded within thermo-sensitive microgel particles. [275]

4.2.3 Analysis of Protein Binding by FT-IR Spectroscopy

In order to explore the interactions of *β*-D-glucosidase with the network, FT-IR spectroscopy in transmission mode has been used. Wittemann *et al.* [79] used this technique to investigate the secondary structure of proteins after adsorption to SPB particles, while Keerl *et al.* [156] studied the structure of bare pNiPAm microgels by this method. Both studies demonstrate that FT-IR

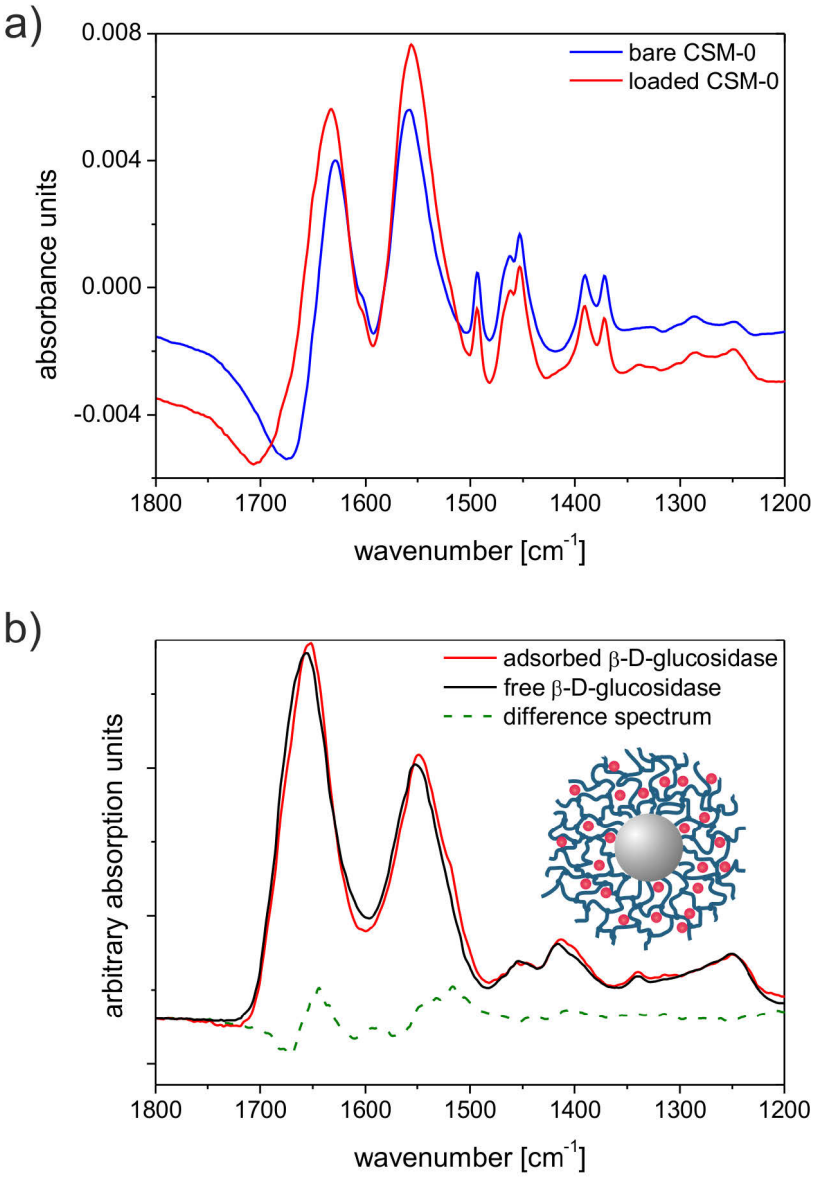

Figure 4.12. a) FT-IR spectra of bare CSM-0 and CSM-0 with immobilised *β*-D-glucosidase (620 mg enzyme per gram microgel) in 10 mM MOPS *pH* = 7.2 at 298 K. Both spectra are normalised to a particle concentration of 1 wt-%. b) FT-IR spectra of native and immobilised *β*-D-glucosidase (618 mg enzyme per gram microgel). The spectrum of immobilised *β*-D-glucosidase was obtained from the spectrum of enzyme-loaded microgel by subtraction of the bare microgel spectrum. The FT-IR spectra of both free and immobilised enzyme are shown after normalisation to the same enzyme concentration. The difference spectrum was obtained by subtraction of the spectrum of the free enzyme from that of the immobilised enzyme.

spectroscopy is well-suited to give information on the conformation of *β*-D-glucosidase in the bound state as well on the binding process of the proteins to microgels. For this purpose, the amide I and II bands of the FT-IR spectrum of free and immobilised *β*-D-glucosidase were analysed. Due to the presence of amide groups in the pNiPAm network the measured spectrum of immobilised *β*-D-glucosidase must be corrected for the absorption of the carrier. Therefore, the IR spectrum of the bare CSM-0 particles dispersed in 10 mM MOPS buffer was recorded at 298 K in a separate experiment and compared to the IR signal obtained for the protein-loaded microgel. Figure 4.12 a shows the spectra of the loaded (620 mg protein per gram microgel) and unloaded microgel particles after normalisation to the same microgel concentration of 1 wt-%. Both the spectrum of the enzyme loaded microgel and of the bare carrier particles show a "negative" band between 1650 and 1700 cm^{-1}. The signal is caused by the subtraction of the reference spectrum from the sample spectrum. As reference of the FT-IR measurements a solution of 10 mM MOPS buffer solution was used. In comparison to the reference solution, water is missing at the location of the microgel particles in the volume of the sample solution. As result, a "negative" water band appears in the sample spectra between 1650 and 1700 cm^{-1}. Beside this band and the dominant amide I and II bands caused by the amide groups of the carrier, two signals at 1452 and 1493 cm^{-1} are observed in the bare microgel spectrum without any overlay by other signals. [79] The latter are ascribed to the C=C stretching vibrations of the aromatic group of the PS core.

After subtraction of the spectra of the bare microgel, the spectra of adsorbed *β*-D-glucosidase could be obtained in good accuracy. In Figure 4.12 b the FT-IR spectrum free *β*-D-glucosidase is compared to the one after immobilisation to the CSM-0 particles. The secondary structure information of the native enzyme is obtained from the amide I and amide II band of the IR spectrum using a PLS algorithm as described in section 3.2.2. The *α*-helix and *β*-sheet content of the native protein structure was calculated to (13 ± 4) % and (3 ± 3) %, respectively. This demonstrates that *β*-D-glucosidase contains unstructured regions to large extent. Moreover, the comparison between both spectra shows that the immobilisation of *β*-D-glucosidase induced both a slight shift of the amide I and amide II band (Figure 4.12 a) and a change in the shape of these peaks (Figure 4.12 a and b).

Protein binding is often accompanied by partial protein unfolding or protein aggregation [231] which affects the FT-IR spectra of the proteins. In particular, unfolded or aggregated proteins strongly absorb between 1610 and 1628 cm^{-1} of the amide I band. [159] However, no increase in this range can be observed and, thus, unfolding of adsorbed *β*-D-glucosidase can definitely be excluded. This is confirmed by the high catalytic activity after immobilisation. Moreover, the differences between the spectra of free and immobilised *β*-D-glucosidase occur between 1615 cm^{-1} and 1660 cm^{-1} and, thus, cannot be caused by a change of the secondary structure: The reduction of the intensity at lower wavenumbers and the increase at higher wavenumbers conflict with a change of the content of *β*-sheet or *α*-helix. [159] However, the modulations of the FT-IR spectrum of adsorbed *β*-D-glucosidase are comparable to temperature-induced shifts in the spectrum of bare pNiPAm microgels (compare section 3.1.3) as shown in the following. Figure 4.13 a displays the FT-IR spectra of CSM-0 at different temperatures between 293 and 313 K: Heating of the polymer above the LCST leads to the emergence of a shoulder at 1657 cm^{-1} at the expense of the intensity at 1626 cm^{-1}. Additionally, the phase transition of the microgel causes a slight shift of the amide II band towards lower wavenumbers. Analogous findings were reported previously. [156] The volume phase transition induces the breakage of intermolecular hydrogen bonds between water molecules and the polymer network and the

formation of intramolecular hydrogen bonds between the C=O and N-H groups of the polymeric chains. This change of the hydrogen bonding pattern during the volume phase transition causes the changes observed in the temperature-dependent FT-IR spectra of CSM-0.

To compare these changes with the modulation of the protein spectra after immobilisation, the difference spectrum of the CSM-0 spectra recorded at 313 and 293 K was calculated and plotted in Figure 4.13 b together with the difference spectrum obtained for *β*-D-glucosidase in the adsorbed and

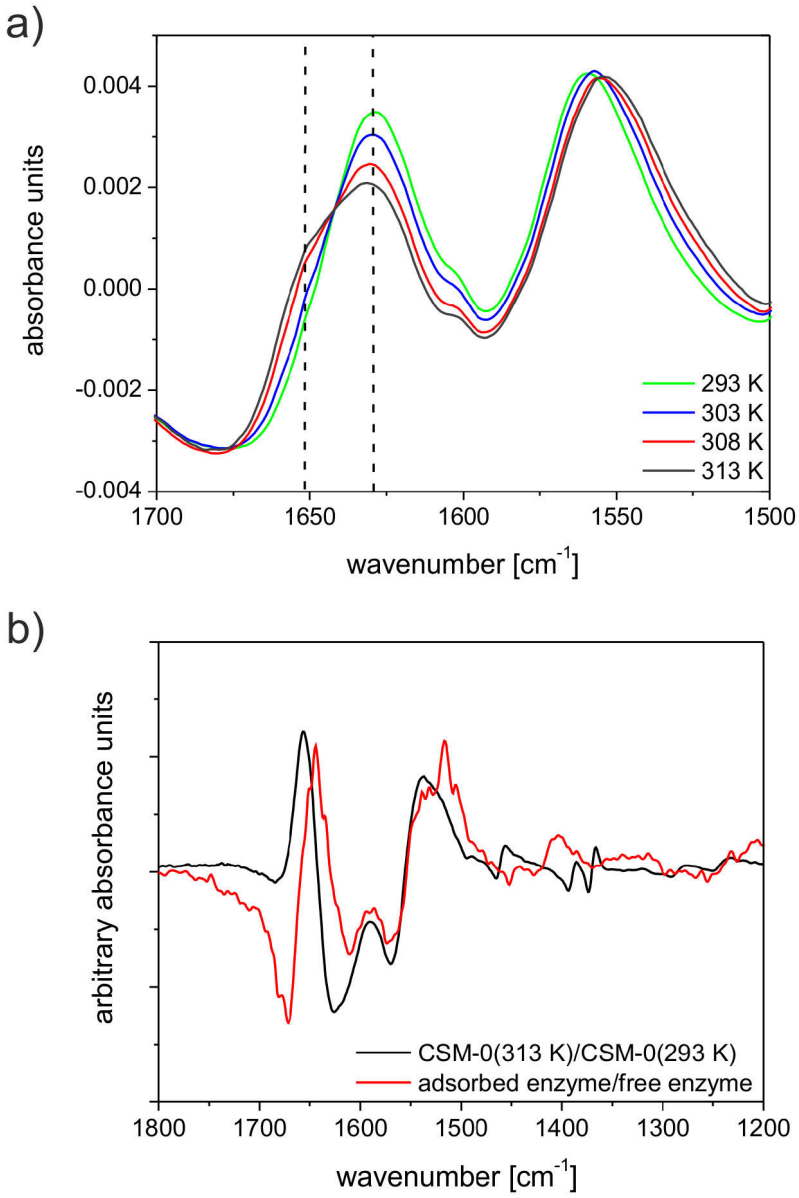

Figure 4.13: a) FT-IR spectra of the bare microgel CSM-0 at different temperatures. The change of the hydrogen binding pattern upon heating above the LCST of the polymer has a great impact on the shape and intensities of the amide I and amide II band: The rise in temperature leads to an increased absorption at 1657 cm^{-1} and a reduced absorption at 1626 cm^{-1}. The higher intensity at 1657 cm^{-1} is attributable to the formation of more intramolecular hydrogen bonds, whereas the drop of intensity at 1626 cm^{-1} is caused by the disruption of hydrogen bonding with water. b) Normalised difference spectra obtained for bare CSM-0 at 313 and 293 K as well as for *β*-D-glucosidase in the adsorbed and native state.

free state. Evidently, both difference spectra show the same minima and maxima. This suggests that analogous interactions are responsible for the changed absorption in the FT-IR spectra. This leads to the conclusion that upon adsorption of *β*-D-glucosidase hydrogen bridges between the enzyme and the microgel are formed and hydrogen bridges to water are broken. Consequently, the changes in the absorption of adsorbed *β*-D-glucosidase are attributed to the rearrangement of intermolecular hydrogen bridges between enzyme and carrier rather than to an altered secondary structure of *β*-D-glucosidase.

Summarising this, the high adsorption capacity of the thermo sensitive microgel shows clear proof of the presence of attractive interactions between *β*-D-glucosidase and CSM-0. FT-IR experiments hint at the formation of hydrogen bonds between the protein molecules and the polymer chains of the network. Moreover, the catalytic constants of the hydrolysis of *o*-NPG are modulated: The increase of K_m is occasionally observed for reactions catalysed by immobilised enzymes. [276] While K_m is influenced by the adsorption of *β*-D-glucosidase only slightly, a dramatic effect is observed in the case of k_{cat}. This significant enhancement of k_{cat} gives direct evidence for a higher enzymatic activity of the adsorbed *β*-D-glucosidase than in the unbound state.

The enhanced activity may be explained as follows: Hydrogen-bonding, especially interactions at the sugar hydroxyl position 2, are decisive for substrate binding and the stabilisation of the transition states. The catalytic glutamate residues inside the active site of the native enzyme are separated by a distance of exactly 5.5 Å, allowing the substrate and a water molecule to bind between them. [162] Hence, small changes of the hydrogen binding pattern in proximity to the active site will affect the electronic dynamics of the active site and, thus, have a significant influence on the hydrolytic catalysis. FT-IR experiments point to the rearrangement of hydrogen bonds upon adsorption and substantiate this argumentation. Moreover, the highly flexible enzyme may change its tertiary and quaternary structure in response to the changed environment. Consequently, a shift of the equilibrium between the monomeric and dimeric form of *β*-D-glucosidase [165] would affect the activity dramatically.

4.2.4 Conclusion

In conclusion, the experiments demonstrate that the adsorption of *β*-D-glucosidase from *almonds* to the microgel particles CSM-0 induces changes within the catalytic centre leading to an increase of the catalytic activity compared to its activity in solution by a factor of ~3. This is in marked contrast to binding to other carrier systems that usually involves a strong decrease of the enzymatic activity. Both the high loading capacity of CSM-0 observed and the increase of the catalytic activity of immobilised *β*-D-glucosidase are probably traced back to the formation of hydrogen bonds between the enzyme and the microgel. In addition, the catalytic properties of immobilised enzymes can be manipulated by the temperature-dependent swelling behaviour of the microgel. Thus, improved carrier particles for enzymes can be obtained by judicious tailoring of the interaction between the protein and the particle.

4.3 Dependence of Protein Adsorption on Temperature – Effect of the Volume Phase Transition

In section 4.2, the adsorption of *β*-D-glucosidase to the thermo-sensitive microgel CSM-0 has been studied below the VPTT, that is, in the hydrophilic state of the microgel. It is now interesting to perform binding studies as a function of temperature in order to analyse the dependence of the thermodynamics of protein binding on the hydrophobicity and mesh size of the gel network. Adsorption studies above the VPTT, however, are hampered by the inset of coagulation of the microgel particles when dispersed in 10 mM MOPS buffer at the higher concentrations which are required for this analysis. To study the influence of the volume phase transition on the thermodynamics of the adsorption process, the thermo-sensitive microgel CSM-0-2 was used instead of CSM-0. The second, slightly negatively charged shell of CSM-0-2 introduces weak electrostatic interactions and provides for high stability even at temperatures above the VPTT and at the high microgel and protein concentrations which are necessary for the thermodynamic analysis. Figure 4.14 depicts the CSM-0-2 particles as well as the interactions with proteins in schematic fashion.
The analysis of the swelling degree α at varying temperatures (see Figure 4.4 b) shows that CSM-0-2 shrinks about 60 % in volume when the temperature is increased from 298 to 312 K and exhibits a volume phase transition close to 310 K. Thus, the microgel is well-suited to study the impact of the volume phase transition on protein adsorption. The thermodynamic parameters for protein adsorption on the thermo-sensitive microgel CSM-0-2 are then determined by performing ITC analysis in 10 mM MOPS buffer *pH* 7.2 at temperatures varying from 288 to 312 K. *β*-D-Glucosidase and lysozyme were used to investigate the interactions with CSM-0-2. Lysozyme is a small globular protein with a molecular weight M_w of 14 300 g mol^{-1} and is positively charged at *pH* 7.2, while *β*-D-glucosidase has a negative net charge and a M_w of 135 000 g mol^{-1} as homodimer, and, therefore, serves as an example of a much larger protein than lysozyme.

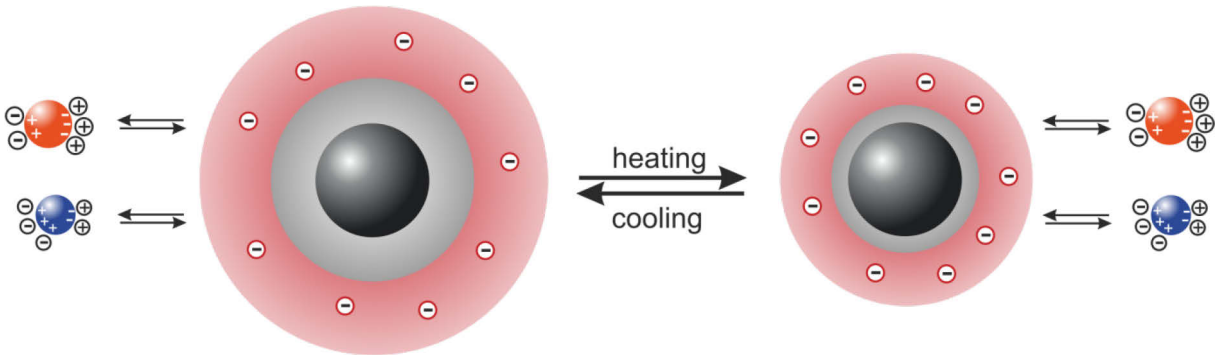

Figure 4.14: Schematic depiction of the core-double shell microgel CSM-0-2 below and above the VPTT of ~310 K as well as the temperature-dependent interaction of this particle with proteins of different size and net charge.

4.3.1 Thermodynamic Analysis of Adsorption of *β*-D-Glucosidase by ITC

First, the ITC data acquired for binding of *β*-D-glucosidase onto CSM-0-2 particles are discussed. For this study, a solution of *β*-D-glucosidase was titrated into a suspension of CSM-0-2 and the change in

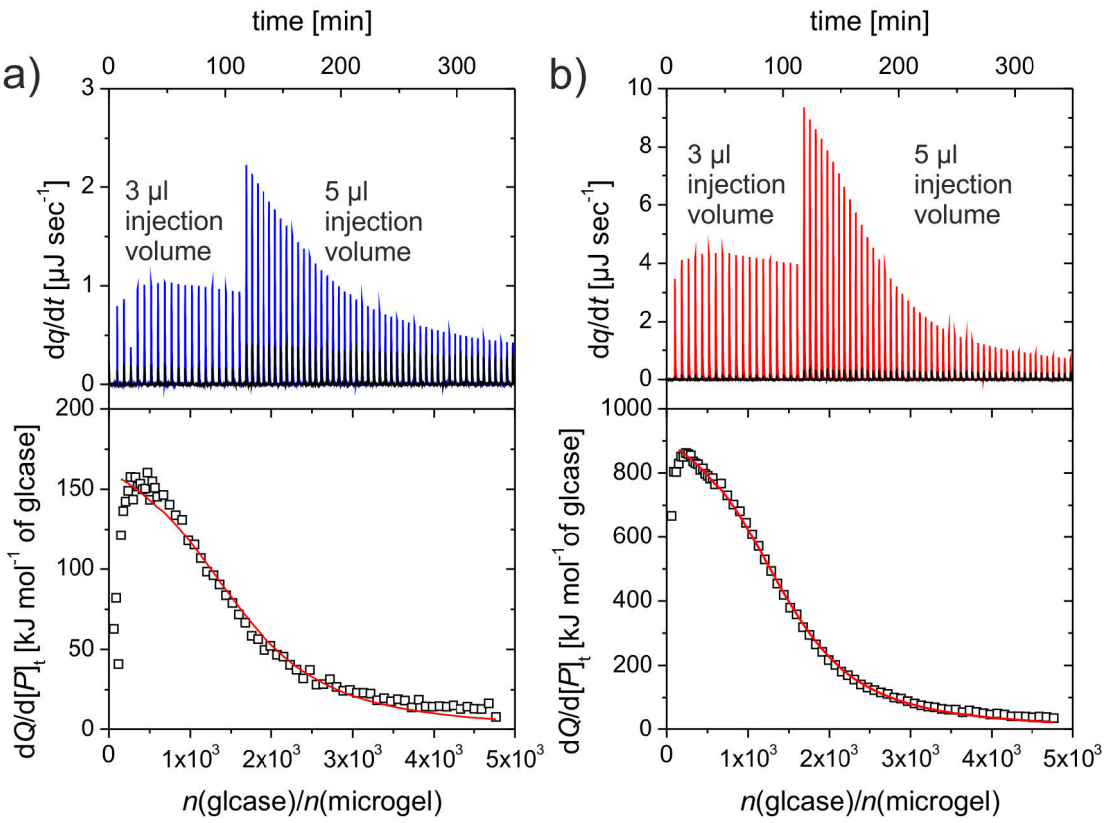

Figure 4.15: ITC data for *β*-D-glucosidase (glcase) adsorption onto CSM-0-2 in 10 mM MOPS buffer *pH* 7.2 at a) 298 K and b) 308 K. The upper panels show the acquired raw ITC data at each temperature. The black spikes (a and b, top) are assigned to the heat of dilution of the protein, while the coloured spikes are the change of heat corresponding to each injection of protein into the microgel dispersion. The lower panels of a and b show the integrated heats of each injection (squares) after subtraction of the dilution from the overall signal. The solid lines represent the fits according to the SSIS model using equations (3.27) and (3.28).

heat was measured over the course of the experiment. Figure 4.15 a (top) depicts the corresponding ITC signal obtained when the enzyme solution is titrated into the microgel dispersion at 298 K. The heat of dilution of *β*-D-glucosidase, *i.e.*, the heat generated by injecting *β*-D-glucosidase into the MOPS buffer solution, is endothermic at 298 K and at all temperatures investigated and needed to be taken into account for the analysis. In contrast to this, the heat of dilution of the CSM-0-2 dispersion during the titration with *β*-D-glucosidase is negligible and, thus, was not considered for data evaluation (data not shown). Figure 4.15 a (bottom) shows the corrected incremental heat as a function of the molar ratio between *β*-D-glucosidase and the microgel. The integrated data shows that mixing of the enzyme with CSM-0-2 results in a pronounced endothermic heat which gradually decays for further titration steps. This demonstrates that *β*-D-glucosidase is adsorbed to CSM-0-2 until saturation of the microgel sets in. It has to be noted that in the very first injection steps, smaller positive heats are observed which point to different binding enthalpies for proteins bound to the microgel in the first stage of the process. However, the lower heat signals arise at very low molar ratios which are close to the resolution of the calorimeter and, thus, the analysis of these data would result in large errors. Consequently, the first data points were not included for further analysis.

Table 4.3: Thermodynamic parameters for the adsorption of *β*-D-glucosidase to the CSM-0-2 particles in 10 mM MOPS buffer *pH* 7.2 at varying temperatures.

T [K]	ΔH_{ITC} [kJ mol^{-1}]	K_b [M^{-1}]	ΔG_b [kJ mol^{-1}]	N_b	$\tau_{ads,M}$ [mg protein/g microgel]
298	168 ± 8	(1.07 ± 0.14) x10^6	-34.4 ± 43	1 620 ± 0.3	419 ± 11
303	326 ± 7	(1.19 ± 0.01) x10^6	-35.2 ± 43	1 570 ± 0.2	406 ± 6
305.5	546 ± 8	(1.30 ± 0.08) x10^6	-35.8 ± 43	1 570 ± 0.1	406 ± 4
308	1 022 ± 9	(1.42 ± 0.05) x10^6	-36.3 ± 43	1 450 ± 0.1	375 ± 2
312	2 269 ± 13	(1.72 ± 0.04) x10^6	-37.2 ± 43	1 310 ± 0.1	339 ± 1

To obtain the thermodynamic information, *i.e.*, ΔH_{ITC}, K_b, and N, from the binding curve in Figure 4.15 a (bottom), the integrated heats are fitted by using the equations (3.27) and (3.28) of the simple SSIS model. This model is based on the Langmuir isotherm and is suitable to describe the ITC data. Thus, *β*-D-glucosidase adsorbs to one kind of binding sites of the microgel, except for the very small portion of *β*-D-glucosidase at the beginning of the adsorption process. Moreover, the adsorption of proteins seems not to be influenced by lateral interactions between bound proteins indicating a non-cooperative mechanism.

The thermodynamic parameters for the adsorption of *β*-D-glucosidase at all temperatures measured are compiled in Table 4.3. The strong endothermic signal arising from mixing of *β*-D-glucosidase with CSM-0-2 shows that the interaction is unfavoured from an enthalpic point of view. This is even more pronounced at higher temperatures as shown in Figure 4.15 b. Increasing the temperature from 298 K to 308 K, *i.e.*, close to the VPTT of the microgel, is associated with a drastic increase of the measured enthalpy ΔH_{ITC}. Moreover, the binding curves calculated for the whole set of temperatures are assembled in Figure 4.16 a. The latter reveal a steep and non-linear increase of ΔH_{ITC} with increasing temperature. Concomitantly, the binding constant K_b is enhanced by a factor of 2 when raising the temperature from 298 to 312 K.

It has to be noted that ΔH_{ITC} may contain additional contributions from processes not linked to the binding equilibrium, as explained in section 3.3.3.2 and as shown in section 4.4 for charged microgels. Thus, ΔH_{ITC} may not be directly related to K_b and the van´t Hoff analysis needs to be performed to determine the thermodynamic binding parameters ΔH_b and ΔS_b. In case of thermo-sensitive microgels, however, the binding process cannot be examined using the linear van´t Hoff analysis since the temperature-induced shrinking of the microgel changes the particle properties resulting in a temperature-dependent binding enthalpy and entropy, *i.e.*, $\Delta S_b(T) \neq$ const. and $\Delta H_b(T) \neq$ const. Also the number of binding sites N becomes a function of temperature in general due to the temperature-dependent volume of the microgel. However, from the sharp increase of ΔH_{ITC} and from the increase of K_b with temperature it can be concluded that the binding process is endothermic and, thus, driven by entropy for the whole temperature range, *i.e.*, $\Delta S_b(T) > 0$.

The positive enthalpy change and the increase in entropy are characteristic for the hydrophobic effect at temperatures below the boiling point of water. [85,230] This phenomenon is frequently explained by solvation/desolvation effects and is also the reason for the entropy-driven microgel shrinkage above

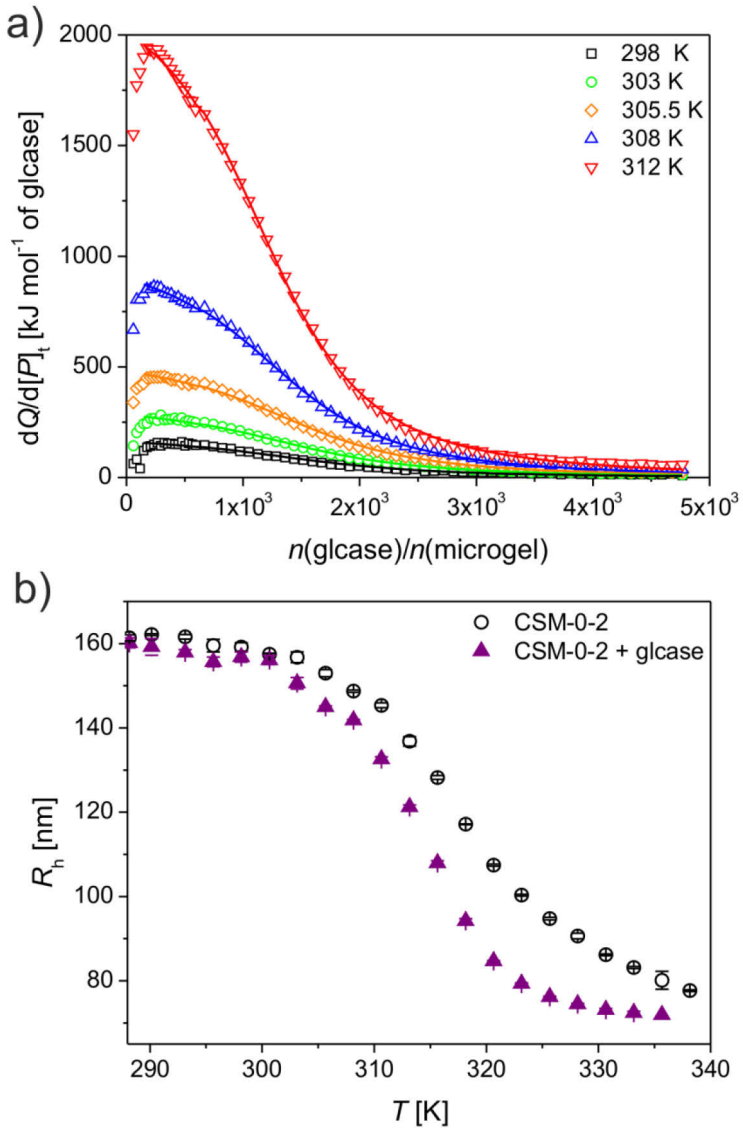

Figure 4.16: a) Integrated heats for each injection as function of the molar ratio between *β*-D-glucosidase and CSM-0-2 in 10 mM MOPS buffer *pH* 7.2 at different temperatures. The solid lines are the fits according to the SSIS model using equations (3.27) and (3.28). b) Hydrodynamic radius R_h of bare CSM-0-2 and of CSM-0-2 particles in presence of *β*-D-glucosidase with a molar ratio *n*(glcase)/*n*(CSM-0-2) of ~3 500 in 10 mM MOPS buffer *pH* 7.2 as a function of temperature.

the VPTT: [116] The contacts between a hydrophobic component, *e.g.*, the isopropyl group in case of pNiPAm, and water result in a decrease of entropy since water molecules near the hydrophobic interface are restricted in their orientations. The ordering of vicinal water is explained by noting that water cannot form strong hydrogen bonds with non-polar molecules. [81,277] To maintain energetically favourable hydrogen bonding, ordered water cages are formed. By implication, the transfer of the water-solvated hydrophobic component to the lyophilic phase leads to a large gain of entropy due to the release of structured water molecules. For the same reason, deswelling of the microgel network is entropy driven since structured water is released from the hydrophobic isopropyl groups. In analogy, the hydrophobic interactions between *β*-D-glucosidase and CSM-0-2 cause desolvation of the protein surface as well as a release of water molecules from the gel. This effect

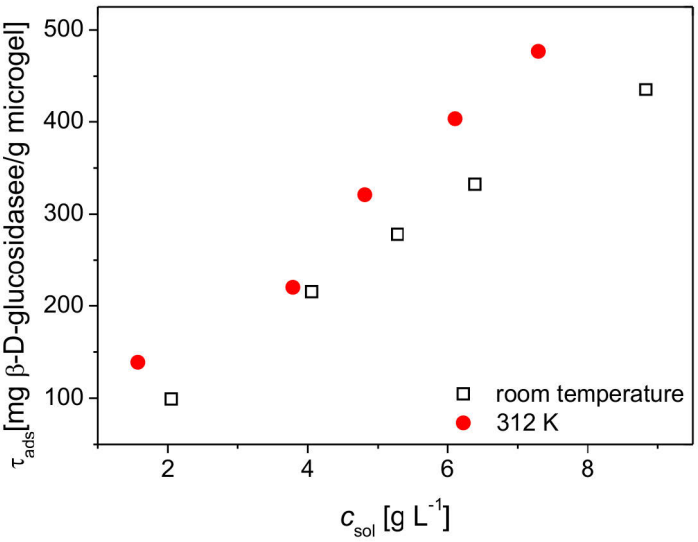

Figure 4.17: Adsorption isotherm of *β*-D-glucosidase obtained from the UF experiment. The adsorbed amount of *β*-D-glucosidase per gram CSM-0 particles (τ_{ads}) is plotted versus the specific concentration of free enzyme c_{sol} in solution.

becomes stronger with increasing temperature where the contacts between water molecules and the pNiPAm network become increasingly unfavourable, resulting in higher contact angles of the microgel above the VPTT. [278]

Additionally, binding of the negatively charged enzyme to the slightly negative charged microgel CSM-0-2 induces a shrinking of the network and a pronounced shift of the VPTT to lower temperatures as shown in Figure 4.16 b. This demonstrates that the structural properties of the microgel are changed by the adsorbing enzymes which modify the balance between the individual contributions to the osmotic pressure of the microgel (see section 3.1.2). This deswelling process cannot be explained in terms of electrostatics since *β*-D-glucosidase has a net negative charge in bulk solution. Noteworthy, the electrostatic potential of CSM-0-2 is probably too low to induce charge reversal of the enzyme and, therefore, *β*-D-glucosidase and CSM-0-2 are equally charged. Thus, both the entropic signature of the adsorption process as well as the protein induced microgel shrinkage indicate that hydrophobic interactions and the release of structured water molecules are the main driving forces for protein binding onto CSM-0-2, especially at higher temperatures. The formation of hydrogen bonds within the backbone of pNiPAm was identified to be important for binding of *β*-D-glucosidase on CSM-0 as well as for the catalytic activity of the enzyme in the adsorbed state. Therefore, hydrogen bond formation certainly contributes to protein binding on CSM-0-2 as well.

The analysis further shows that the loading capacity, *i.e.*, the maximum number of bound proteins N_b, is essentially unchanged by the volume phase transition and is even slightly decreased. This is also observed in the UF experiments at two different temperatures. Figure 4.17 shows the amount of bound protein per gram microgel τ_{ads} as function of the protein concentration in solution c_{sol} in 10 mM MOPS buffer *pH* 7.2 at room temperature and at 312 K. The amount of bound *β*-D-glucosidase after ultrafiltration is essentially unchanged when raising the temperature from room temperature to 312 K. However, if one takes the actual shell volume ($V_{CSM\text{-}0\text{-}2(T)}$-$V_{PS}$) available for the large *β*-D-glucosidase into account, it is apparent that *β*-D-glucosidase binds with higher concentrations, *i.e.*, $N_b/(V_{CSM\text{-}0\text{-}2(T)}\text{-}V_{PS})$, to the microgel above the VPTT. Consequently, *β*-D-glucosidase adsorbs with

higher affinity and higher concentration to the microgel network in the more hydrophobic state. The decreasing microgel volume with increasing temperature prevents the increase of N_b above the VPTT of the CSM-0-2 particles.

4.3.2 Thermodynamic Analysis of Adsorption of Lysozyme by ITC

Lysozyme was selected as another protein to investigate the interactions with the double-shell microgel as a function of temperature. For this protein, the raw ITC data was acquired at temperatures varying from 288 to 308 K. The ITC analysis at higher temperatures is not recommended in this case as binding of the oppositely charged protein diminishes the electrostatic stabilisation of CSM-0-2 leading to coagulation at temperatures around 313 K. Figure 4.18 (top) shows the raw ITC data obtained for the titration of lysozyme into a dispersion of CSM-0-2 in 10 mM MOPS *pH* 7.2 at 305.5 K. Moreover, the binding curves obtained from integration of the raw ITC data at all temperatures investigated are assembled in Figure 4.18 (bottom). Therein, the SSIS model was sufficient to achieve a good fit for the heat evolved in the interaction between lysozyme and the CSM-0-2 particles. The thermodynamic parameters obtained from this analysis are listed in Table 4.4.

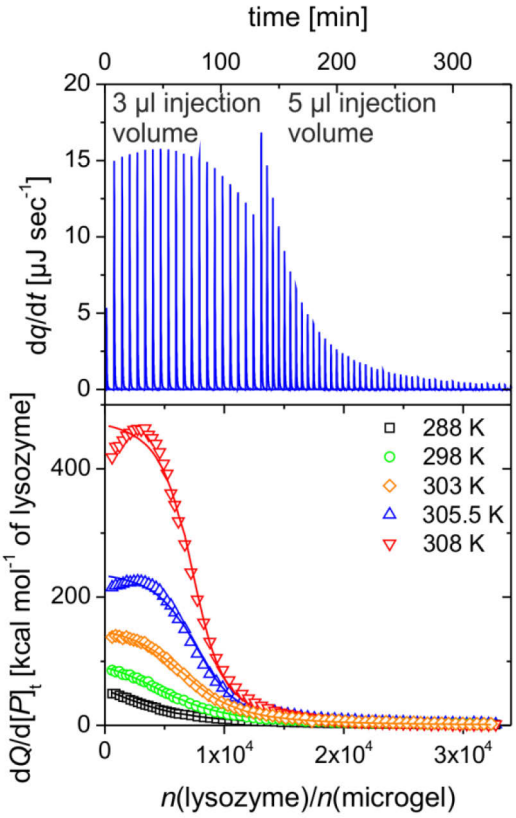

Figure 4.18: Top: Raw ITC data for lysozyme adsorption onto CSM-0-2 particles in 10 mM MOPS buffer *pH* 7.2 at 305.5 K. Bottom: Integrated heats of each injection (open symbols) obtained from the raw ITC data which have been acquired at different temperatures. The solid lines represent the fits according to the SSIS model using equations (3.27) and (3.28).

Table 4.4: Thermodynamic parameters for the adsorption of lysozyme onto CSM-0-2 particles in 10 mM MOPS buffer *pH* 7.2 at varying temperatures.

T [K]	ΔH_{ITC} [kJ mol^{-1}]	K_b [M^{-1}]	ΔG_b [kJ mol^{-1}]	N_b	$\tau_{ads,M}$ [mg protein/g microgel]
288	97 ± 5	(6.95 ± 0.21) x10^4	-26.7 ± 0.1	3 850 ± 85	105 ± 2
298	113 ± 2	(1.29 ± 0.05) x10^5	-29.2 ± 0.1	6 010 ± 64	166 ± 2
303	161 ± 2	(2.55 ± 0.10) x10^5	-31.4 ± 0.1	7 250 ± 49	199 ± 1
305.5	244 ± 3	(5.22 ± 0.38) x10^5	-33.4 ± 0.2	7 850 ± 67	215 ± 2
308	483 ± 5	(8.43 ± 0.71) x10^5	-34.9 ± 0.2	7 430 ± 61	203 ± 2

The ITC data and the fitting results demonstrate that mixing of lysozyme with CSM-0-2 is endothermic and, thus, driven by entropy. Increasing the temperature from 288 to 308 K results in a tremendous increase of ΔH_{ITC} as observed for the temperature-dependent titration experiments of *β*-D-glucosidase. This is indicative for a general binding mechanism onto CSM-0-2 particles for which hydrophobic interactions are identified as the main driving force.

It has to be emphasised that temperature-induced unfolding of the protein may generally occur in the ITC cell and adsorption of denatured proteins may result in a different caloric effect. Temperature-induced unfolding, however, is precluded in this case since ITC analysis of *β*-D-glucosidase and lysozyme on higher charged microgels (CSM-10) in the same temperature range (see section 4.4 and 4.6) record much smaller caloric effects for the whole temperature range investigated. Moreover, unfolding of the proteins induced by the contact to the hydrophobic gel network at higher temperatures is also unlikely as the high catalytic activity measured for *β*-D-glucosidase bound to the thermo-sensitive microgel CSM-0 above the VPTT (section 4.2) demonstrates the integrity of the protein. The binding constant for the lysozyme adsorption strongly depends on temperature and is increased by a factor of 12 when increasing the temperature from 288 to 305 K (Figure 4.19 a). This indicates that the adsorption of lysozyme is more temperature-sensitive than the adsorption of *β*-D-glucosidase. The higher sensitivity of the binding affinity towards the microgel size compared to the binding of *β*-D-glucosidase is probably caused by the presence of attractive electrostatic interactions between lysozyme and the CSM-0-2 particles. Thus, the temperature-induced shrinkage of CSM-0-2 increases the electrostatic potential of the latter and amplifies the electrostatic interactions between lysozyme and CSM-0-2 resulting in higher binding affinities at higher temperatures.

The strong temperature-dependence of K_b gives rise to distinct adsorption isotherms at varying temperatures. The ITC data presented here can be converted into an adsorption isotherm, *i.e.*, the fraction of occupied binding sites as function of the concentration of free lysozyme in solution c_{sol}, by using equation (3.24) and the fitting parameters K_b and N_b. Figure 4.19 b shows the adsorption isotherms $\Theta(c_{sol})$ obtained for the different temperatures. This plot demonstrates that at 308 K the microgel is saturated with lysozyme already at $c_{sol} \approx 0.1$ g L^{-1}. Reducing the temperature to 288 K while holding c_{lys} constant, decreases $\Theta(c_{lys})$ to ≈ 0.2. Thus, binding of lysozyme to CSM-0-2 at high temperatures and subsequent cooling of the microgel dispersion leads to temperature-induced release of the bound proteins. This effect is amplified by the temperature-dependent binding capacity of CSM-0-2 with having higher values close to the VPTT compared to the one at 288 K (*cf.* Table 4.4).

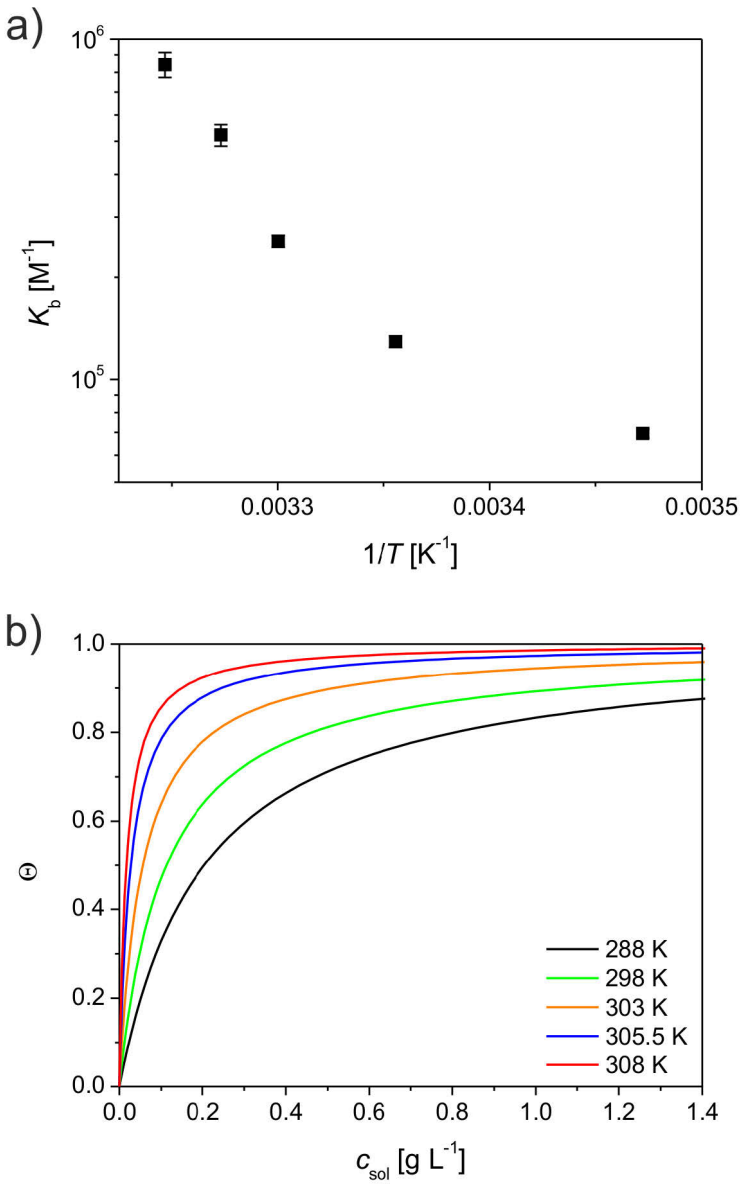

Figure 4.19: a) Binding constant K_b of binding of lysozyme onto CSM-0-2 determined from ITC analysis as a function of the reciprocal temperature T^{-1}. b) Comparison of the adsorption isotherms of lysozyme obtained for different temperatures and, thus, different swelling degrees of CSM-0-2. The isotherms were calculated from the fitted ITC data using equation (3.24).

4.3.3 Conclusion

Binding of lysozyme and *β*-D-glucosidase is endothermic and driven by entropy for the whole temperature range investigated. Additionally, the microgel deswells and the VPTT is shifted to lower temperatures when the binding sites of CSM-0-2 are occupied by *β*-D-glucosidase. This and the entropic signature of adsorption substantiate the general opinion of the hydrophobic effect as the main driving force. Moreover, the affinities to the gel non-linearly increase from 288 to 312 K which further stresses the importance of hydrophobic interactions in the binding mechanism. In case of lysozyme, the strong temperature-dependence of K_b and N gives rise to switchable adsorption and release which could be exploited for chromatographic purification of this protein. In contrast to this, the binding

strength of β-D-glucosidase is much less affected by temperature and the binding capacity is essentially temperature independent making the purification process less efficient. It has to be emphasised, that β-D-glucosidase generally binds with higher binding affinities to the gel than lysozyme. This phenomenon may be ascribed to the larger protein surface of β-D-glucosidase and, thus, to the larger number of hydrophobic contact points with the microgel network. From the relative binding affinities and the adsorption isotherms of both proteins it is concluded that the separation of β-D-glucosidase from a protein mixture containing lysozyme and β-D-glucosidase is more efficient in the swollen state of the microgel, *i.e.*, below the VPTT. This result implies that despite the stronger hydrophobic interaction with the gel matrix above the VPTT, the resolution in bioseparations is not better above the VPTT in general. Consequently, the ideal conditions for separation of proteins using pNiPAm based systems may vary and have to be identified for each protein assay before purification.

4.4 Charged Microgels as Protein Carriers

In this section, the impact of electrostatic interactions on the process of protein adsorption is studied in detail. The negatively charged microgel CSM-10 is used to investigate the adsorption of proteins as a function of temperature and ionic strength. Figure 4.20 displays the particles in schematic fashion. Lysozyme was selected as protein since it is a robust and well-studied cationic enzyme which can be used as a model protein. Thus protein binding on an oppositely charged carrier system was investigated. In many cases hydrophobic attraction, [10,85,114,279] which typically carries an entropic signature (see section 4.3) is assumed to be one of the main driving forces for protein adsorption. However, protein adsorption onto negatively charged microgels shows that the ionic strength and the *pH* value determine the amount of bound protein. [74,215] The present carrier system allows one to discern between these two forces in a systematic fashion by analysing the thermodynamics of protein adsorption at different ionic strengths. [280]

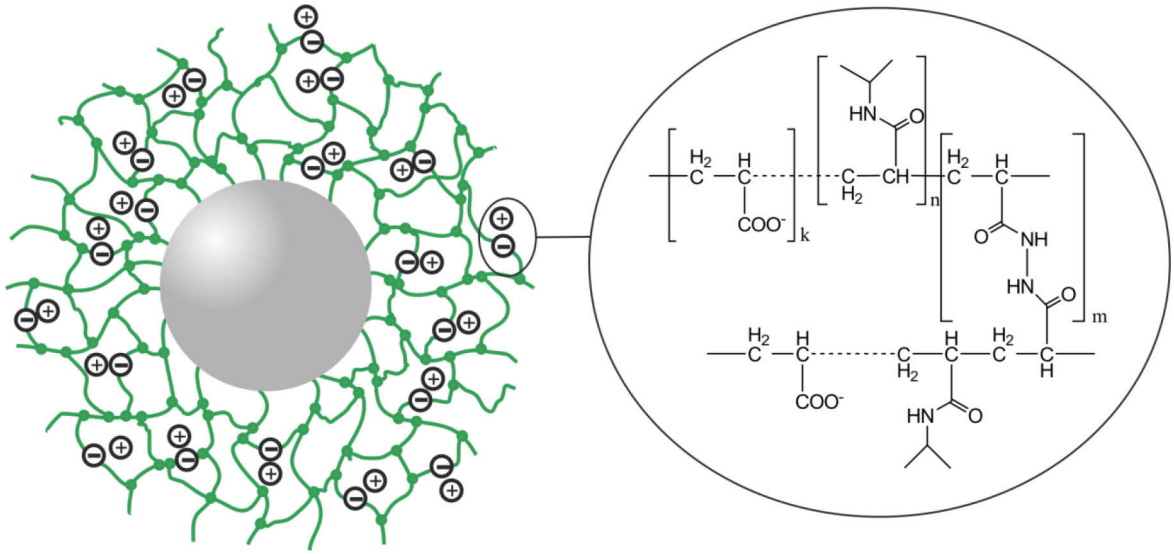

Figure 4.20: Schematic representation of the negatively charged microgel particles CSM-10 which carry a given amount of AAc (left) and the chemical structure of the charged shell of CSM-10 (right).

This section is organised as follows: The first part is dedicated to temperature and salt-dependent ITC experiments. By this means, the driving forces of the protein adsorption on oppositely charged microgels were clarified. In the second part any structural changes of the adsorbed lysozyme, *e.g.*, changes of the secondary structure and of the ionisation state of lysozyme, were analysed. In addition, a complete kinetic analysis of the lysozyme activity in terms of the Michaelis-Menten kinetics was performed. The latter gives information on the function of adsorbed lysozyme when surrounded by the charged network.

4.4.1 Thermodynamic Analysis of Protein Adsorption by ITC

In this section, the results of the thermodynamic analysis of protein binding onto CSM-10 are presented. All adsorption experiments were performed in 10 mM MOPS buffer *pH* 7.2 with varying concentrations of NaCl. At this *pH* value, the pK_a value of the carboxyl groups inside the microgel shell is 6.3 and the degree of dissociation of the charged functional groups is around 0.85 as determined from potentiometric titration experiments (see section 4.1.2). Thus, the microgel is in its highly charged and swollen state. Moreover, the temperature-dependent swelling curve of the CSM-10 particles (Figure 4.4) shows that the charged microgel is not thermo-sensitive below 330 K when dispersed in 7 mM ionic strength MOPS buffer *pH* 7.2 due to the high ionic pressure P_{ion}. Also increasing the ionic strength from 7 to 32 mM does not reduce P_{ion} sufficiently large to recover the thermo-sensitivity of the core-shell microgel at physiological temperatures. However, the swelling capability of CSM-10 at *pH* 7.2 is very sensitive towards the salt concentration of the solution. Any change of the ionic strength will modify the Donnan equilibrium inside the microgel resulting in swelling or deswelling of the gel network.

In general, there are two variables which are decisive for the adsorption of proteins to charged polymeric layers: i) the salt concentration of the solution which influences the electrostatic interaction between the enzyme and the network; and ii) the temperature, which is decisive for the hydrophilicity of the network and, thus, will determine the strength of hydrophobic attraction. In the following the adsorption at low ionic strength but different temperatures is considered at first to assess the influence of electrostatic forces.

4.4.1.1 Temperature-dependence

At first, binding of lysozyme to the CSM-10 particles was studied at 298 K. Figure 4.21 shows the ITC signal when the lysozyme solution was titrated into the microgel dispersion at 298 K. Analogously to the adsorption studies between lysozyme and the CSM-0-2 particles, the heat of dilution of lysozyme needed to be subtracted for data evaluation while the heat of dilution of CSM-10 during lysozyme titration is negligible and was not considered for further analysis. From the raw ITC data the sigmoid binding curve was calculated by integrating the heats of each injection over time and by adjusting for the concentration of injected lysozyme. It is clear from the isotherm that positively charged lysozyme strongly interacts with the negatively charged microgel at low ionic strength (Figure 4.21), as expected.

The SSIS model is suitable to achieve an excellent fit of the calorimetric data. Moreover, the validity of the Langmuir model to quantify the adsorption of proteins onto microgels is fully proven by the

analysis of the conformation (see section 4.4.2), the activity of bound lysozyme (see section 4.4.4), and of the reversibility of binding (see section 4.5). The data thus derived have good precision and provide a good basis for in-depth discussion of the thermodynamic parameters, *i.e.*, the binding constant K_b, the maximum number of bound proteins N_b (*i.e.*, N) and the enthalpy change ΔH_{ITC} of the overall process, deriving from this analysis. As it is obvious from Figure 4.21, the heat signal emerging from mixing of lysozyme with CSM-10 at 298 K and low salt concentration is positive. This means that the addition of lysozyme to the microgel dispersion is endothermic, *i.e.*, $\Delta H_{ITC} > 0$. The thermodynamic parameters for lysozyme adsorption onto CSM-10 at 298 K are listed in Table 4.5. The parameters calculated at all temperatures investigated are gathered in Table 7.3 of the supplement.

In the next step, the temperature-dependence of K_b and ΔH_{ITC} was analysed in 7 mM ionic strength MOPS buffer. Therefore, the ITC experiment was repeated for 288, 293 and 303 K to determine the thermodynamic parameters at these temperatures but otherwise identical conditions. In this temperature range, the size of CSM-10 is constant and the microgel offers the same volume of interaction to the protein. This results in a number of bound proteins N_b which is independent of the temperature of the solution (*cf.* Table 7.3). Figure 4.22 shows the temperature-dependent analysis done at low ionic strength. The marked dependence of the ITC-curves on temperature is directly discernible

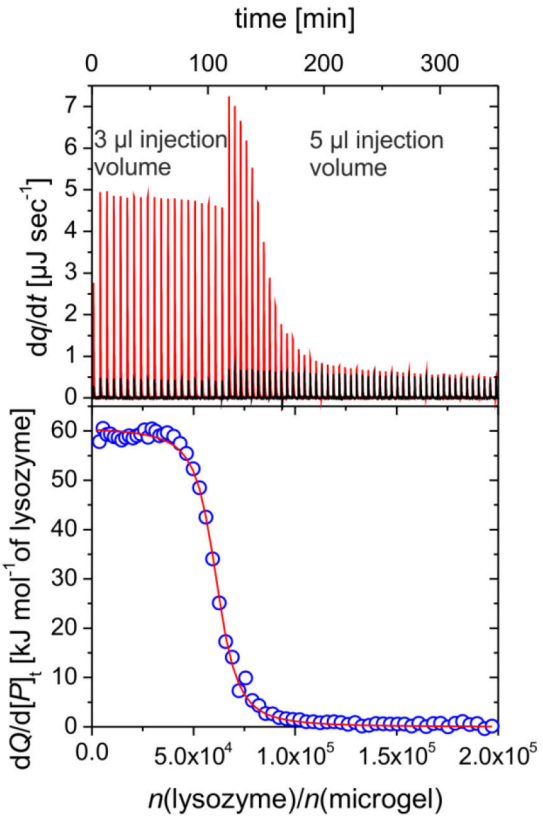

Figure 4.21: ITC data of lysozyme adsorption onto CSM-10 particles at 298 K in 10 mM MOPS buffer *pH* 7.2 (7 mM ionic strength). The upper panel shows the raw ITC data with the black spikes as the heat of dilution of lysozyme. The red spikes are the change of heat corresponding to each injection of lysozyme into the microgel dispersion. The lower panel shows the integrated heats of each injection (circles) after subtraction of the dilution signal from the overall signal. The solid line represents the fit according to the SSIS model using equations (3.27) and (3.28).

from Figure 4.22 a. Moreover, the resulting van't Hoff plot of the binding constant is found to be linear within the margin of error (Figure 4.22 b). Hence, possible contributions from the respective heat capacity to the adsorption process are neglected. Thus, the enthalpy of binding ΔH_b can be calculated by use of equation (3.31). ΔS_b can be obtained either from the intercept of the van´t Hoff analysis or from the temperature-dependence of the free energy ΔG_b according to equation (3.32).
The resulting enthalpy ΔH_b and entropy ΔS_b are assigned to the process of adsorption of lysozyme to the chains of the gel. The reason for this is that these quantities are directly correlated to the calorimetric binding constant K_b. At these experimental conditions the adsorption process of lysozyme is endothermic and accompanied by an increase of entropy, *i.e.*, ΔH_b = (22 ± 3) kJ mol^{-1} and ΔS_b = (0.194 ± 0.009) kJ mol^{-1} K^{-1}. However, ITC measures a heat signal ΔH_{ITC} which is significantly larger than the van´t Hoff enthalpy ΔH_b. Moreover, the temperature-dependence of K_b is much less pronounced as it would be expected from the measured enthalpy ΔH_{ITC}. Here, another example of a discrepancy between van´t Hoff (ΔH_{vH}) and calorimetric (ΔH_{ITC}) values is presented. However, unlike

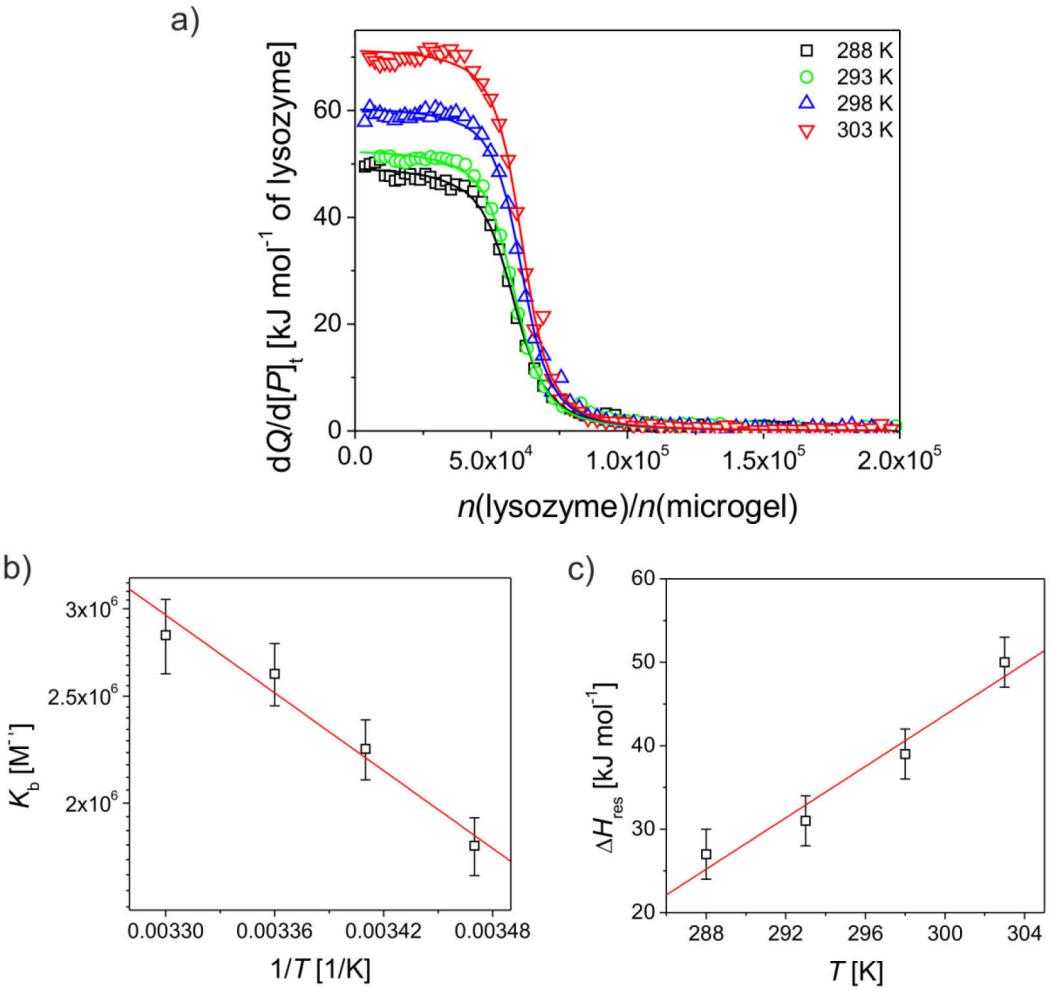

Figure 4.22: a) Integrated heats as function of the molar ratio between lysozyme and the microgel CSM-10 in 10 mM MOPS buffer *pH* 7.2 (7 mM ionic strength) at different temperatures. The solid lines are the fits according to the SSIS model using equations (3.27) and (3.28). b) Van´t Hoff analysis of lysozyme adsorption onto the microgel particles in 10 mM MOPS buffer *pH* 7.2. c) Plot of the residual enthalpy ΔH_{res} measured by ITC as function of temperature. The solid line represents the linear fit of the experimental data points.

many of the discrepancies discussed in the past [251], the large difference observed is not easily reconciled by considering, *e.g.*, experimental errors and ΔC_p.

A recent investigation of the thermodynamics of adsorption of RNase A on positively charged SPBs done by Becker *et al.* [250] stresses this point: ITC performed at different temperatures showed that the binding constant for this reaction is temperature-invariant. Thus, the ΔH_b derived from the van´t Hoff analysis was negligible. In contrast, ITC experiments with this system measured a positive caloric heat. In this special case the entire ΔH_{ITC} was sourced from processes other than protein binding and, thus, was treated as 'marker enthalpy'.

The commonly observed difference between ΔH_{vH} and ΔH_{ITC} can be understood as follows: ITC measures the overall caloric heat which is generated or taken up when, *e.g.*, nanoparticles are mixed with proteins. Thus, the molar heat of processes independent from the adsorption equilibrium, *e.g.*, the mixing of the protein with the polymer or salt and protein mediated microgel deswelling, adds to ΔH_{ITC} but not to ΔH_{vH}. From this it is clear that ΔH_{ITC} is not directly related to the adsorption

Table 4.5: Thermodynamic parameters for the adsorption of lysozyme onto negatively charged CSM-10 particles in different buffer solutions solution *pH* 7.2 at 298 K.

Ionic strength /buffer	$\mathbf{N_b}$	$\mathbf{\Delta G_b}$[a] **[kJ mol^{-1}]**	$\mathbf{\Delta H_b}$ **[kJ mol^{-1}]**	$\mathbf{\Delta S_b}$ **[kJ mol^{-1} K^{-1}]**	$\mathbf{\Delta H_{res}}$ **[kJ mol^{-1}]**	$\mathbf{\Delta C_p}$ **[kJ mol^{-1} K^{-1}]**
7mM/MOPS	60 100 ±190	-36.6 ±0.2	22 ±3	0.194 ±0.009	39 ±3	1.54 ±0.22
17mM/MOPS	52 800 ±260	-33.1 ±0.1	38 ±2	0.234 ±0.008	28 ±2	1.03 ±0.16
32mM/MOPS	37 600 ±360	-30.1 ±0.1	36 ±5	0.220 ±0.025	48 ±5	n.d.
7mM/PIPES	61 400 ±450	-35.0 ±0.3	25 ±3	0.201 ±0.010	31 ±3	0.98 ±0.14

[a] ΔG_b was calculated via $\Delta G_b = -RT\ln K_b$

equilibrium, *i.e.*, to K_b, but contains additional contributions. Thus, the binding parameters ΔH_b and ΔS_b must be calculated via the van´t Hoff analysis (equation (3.31)) of the temperature-dependence of K_b. Consequently, the measured heat ΔH_{ITC} can be divided into ΔH_b which is directly related to the binding process, *i.e.*, to the interaction of the protein with the chains of the microgel, and a residual term ΔH_{res}:

$$\Delta H_{ITC} = \Delta H_b + \Delta H_{res} \tag{4.2}$$

The ITC data of the lysozyme adsorption at different temperatures (Figure 4.22 a) demonstrate that ΔH_{res} has a positive overall heat capacity $\Delta C_{p,res}$. The latter is calculated to a value of $\Delta C_{p,res}$ = (1.54 ± 0.22) kJ mol^{-1} from the linear plot of ΔH_{res} (Figure 4.22 c) via

$$\Delta H_{res} = \Delta C_{p,res}(T_2 - T_1) \tag{4.3}$$

where T_1 and T_2 are two different absolute temperatures.

Table 4.5 summarises all thermodynamic data regarding the analysis as a function of time. Before the potential contributions to ΔH_{res} and its temperature-dependence are discussed, the salt-dependence of

K_b for binding of lysozyme was investigated first in order to clarify the driving forces for protein binding onto CSM-10 particles.

4.4.1.2 Salt-dependence – Driving Forces of Protein Adsorption

In order to analyse the salt-dependence of the thermodynamic parameters K_b, ΔH_b and ΔS_b of lysozyme adsorption ITC experiments at increasing NaCl concentrations were performed (Figure 4.23 a). The values obtained at 298 K are listed in Table 4.5 for comparison. The whole data set is gathered in Table 7.3 of the supplement. If one considers only electrostatic interactions the binding affinity for protein adsorption on oppositely charged microgels is correlated to the electrostatic potential difference $\Delta\phi$ between the bulk solution and inside the gel region. In a solution of monovalent salt, this difference can be qualitatively expressed by the Donnan potential which is given by equation (3.5) as function of the salt concentration and the charge density of the gel.

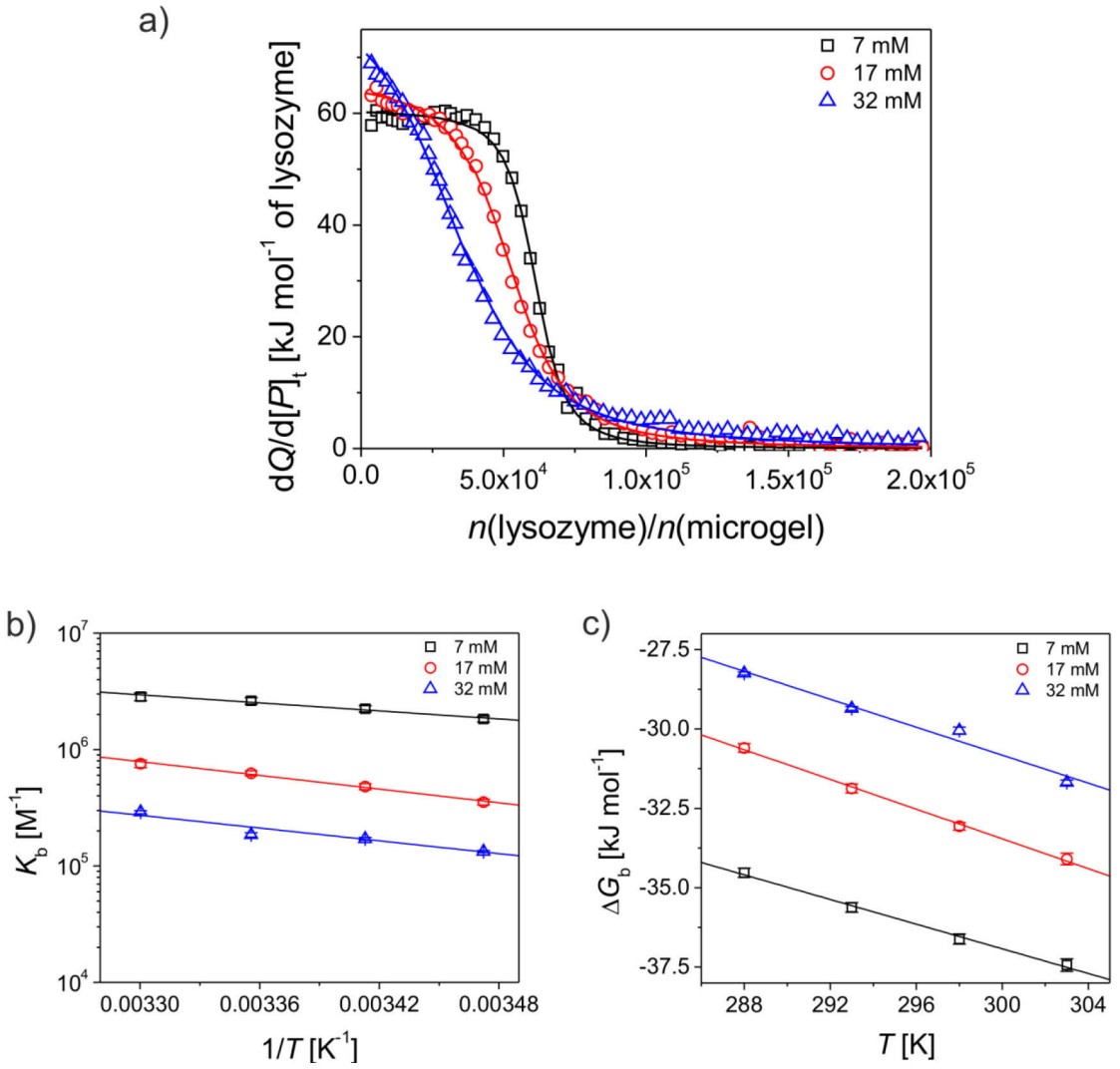

Figure 4.23: a) Integrated heats as function of the molar ratio between lysozyme and the microgel CSM-10 in 10 mM MOPS buffer *pH* 7.2 at 298 K at different ionic strengths. The solid lines are the fits according to the SSIS model. b) Van´t Hoff analysis of lysozyme adsorption on the microgel particles in 10 mM MOPS buffer *pH* 7.2 at different ionic strengths. c) Temperature-dependence of ΔG_b at different ionic strength. The solid lines are the linear fits of the data.

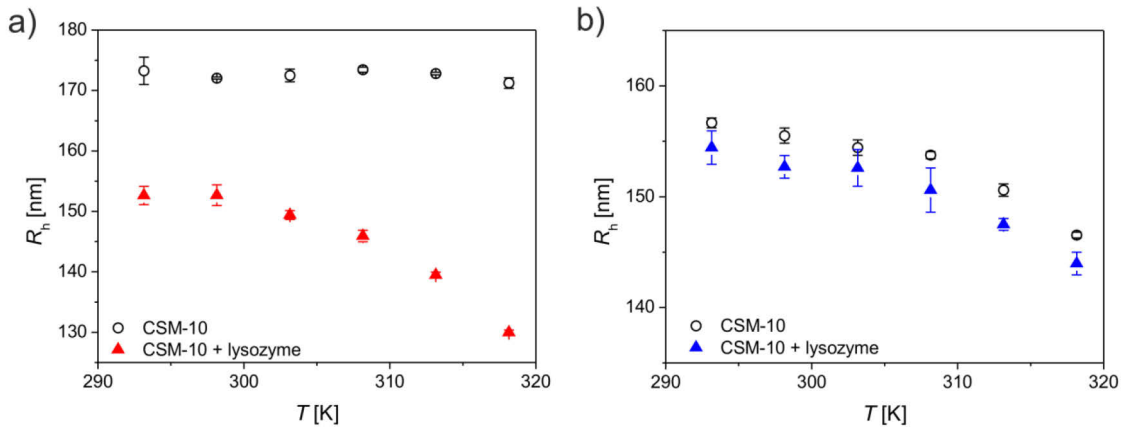

Figure 4.24: a) Temperature-dependence of R_h of CSM-10 particles in absence of lysozyme and of microgel particles with adsorbed lysozyme at a molar ratio n(lysozyme)/n(CSM-10) of ~55 000 in 7 mM ionic strength MOPS buffer *pH* 7.2 b) Temperature-dependence of R_h of CSM-10 particles in absence of lysozyme and of microgel particles with adsorbed lysozyme at a molar ratio of ~40 000 in 32 mM ionic strength MOPS buffer *pH* 7.2.

Regarding equation (3.5) a protein of positive net charge z_p will experience an electrostatic attraction $\sim z_p e \Delta\phi$, which is of the order of several $k_B T$ for the salt concentrations used. Importantly, it is apparent from equation (3.5) that the electrostatic part of the adsorption affinity will be reduced by addition of salt and that this contribution is only of entropic nature. Indeed increasing the ionic strength causes a sharp decrease of K_b by a factor of 14 when the lowest and highest salt concentration are compared in the ITC experiments (*cf.* Table 4.5). This equates to a loss of $\sim 3 k_B T$ and clearly demonstrates that attractive electrostatic interactions are important at low salt concentrations. Moreover, these observations are in agreement with previous results which concluded that the affinity to bind oppositely charged macromolecules strongly decreases with the addition of salt. [99,281]

Additionally, the thermodynamic data listed in Table 4.5 show that the adsorption of lysozyme on negatively charged microgels is endothermic, $\Delta H_b > 0$, at all salt concentrations, and is strongly driven by entropy, as predicted by equation (3.5). However, the salt-dependent change of ΔG_b and ΔS_b implies that non-electrostatic interactions play an important role for lysozyme adsorption on the CSM-10 particles as well: ΔS_b, determined from the intercept of the van´t Hoff plot (equation (3.31), Figure 4.23 b), as well as from the slopes of the plots of ΔG_b versus T (equation (3.32), Figure 4.23 c), increases by ~15 % when the ionic strength is increased (*cf.* Table 4.5). Moreover, only about 40 % of bound protein is released when the ionic strength is increased from 7 to 32 mM at 298K. Both the increase of ΔS_b and the still high amount of bound protein at 32 mM ionic strength strongly suggest that hydrophobic forces must be considered as well. As widely accepted, the conventional signature of hydrophobic association in the temperature range investigated is indeed strongly entropic in nature. [230]

It is further noted that the adsorption of lysozyme to the microgel network of CSM-10 induces a deswelling of the microgel shell at low ionic strength of about 35 % in volume (Figure 4.24 a), while at higher salt concentrations this effect is strongly reduced (Figure 4.24 b). In particular, CSM-10 particles suspended in a protein solution of a molar ratio n(lysozyme)/n(CSM-10) of ~55 000 deswell upon temperature increase from $R_h \approx 153$ nm at 293 K to $R_h \approx 130$ nm at 318 K (Figure 4.24 a). Thus,

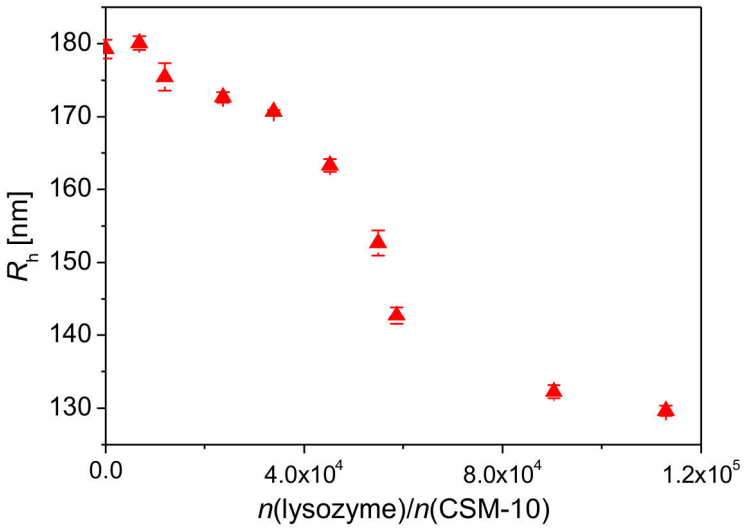

Figure 4.25: Dependence of the hydrodynamic radius R_h of CSM-10 particles in lysozyme solutions of varying molar ratios *n*(lysozyme)/*n*(CSM-10) at 298 K in 10 mM MOPS buffer *pH* 7.2.

binding of oppositely charged proteins reduces the VPTT of the microgel, resulting in a pronounced thermo-sensitivity of the gel network at physiological temperatures. This is strong evidence for the modification of the swelling pressure by the adsorbing proteins thereby reducing the ionic pressure P_{ion}, *i.e.*, the distribution of mobile ions between the microgel phase and the bulk solution. In analogy to the dependence of the microgel size on the concentration of monovalent salt, the radius of CSM-10 becomes a function of protein concentration. In Figure 4.25 an independent measurement of the microgel radius versus the molar ratio *n*(lysozyme)/*n*(CSM-10) is shown. This analysis was performed in 10 mM MOPS buffer at low salt concentration (7 mM ionic strength) where the charges are not screened by salt. The microgel size decreases monotonically with increasing protein concentration until the adsorption process is completed. At the highest molar ratio of ~$1.1x10^5$, the microgel radius is determined to R_h(ratio = $1.1x10^5$) ≈ 130.0 nm. Thus, it is smaller than the radius of the neutral reference gel R_r ≈ 138.5 nm. This implies that not only electrostatic interactions between the microgel and lysozyme are present but also specific binding effects, such as hydrophobic bonding, which lead to further network tightening. Thus, the protein-induced contraction of the microgel network may be due to charge screening when the charged protein adsorbs as well as due to tightening of the partially hydrophobic gel network.

From these experiments it can be concluded that a complex interplay between electrostatic and hydrophobic interactions drive the protein adsorption. These interactions, however, also dominate the swelling behaviour of the microgel network and binding of proteins will modify the absolute size and stiffness of the particle with possible implications for further protein adsorption. Thus, it is most likely, that the binding affinity of lysozyme is a function of the protein concentration, too, and the thermodynamic binding parameters calculated from the simple ITC analysis reflect an averaged description of the protein adsorption to the charged microgel.

However, the simple SSIS model is sufficient to describe the temperature- and salt-dependent ITC data and to identify the main driving forces of protein adsorption as well as to improve the mechanistic

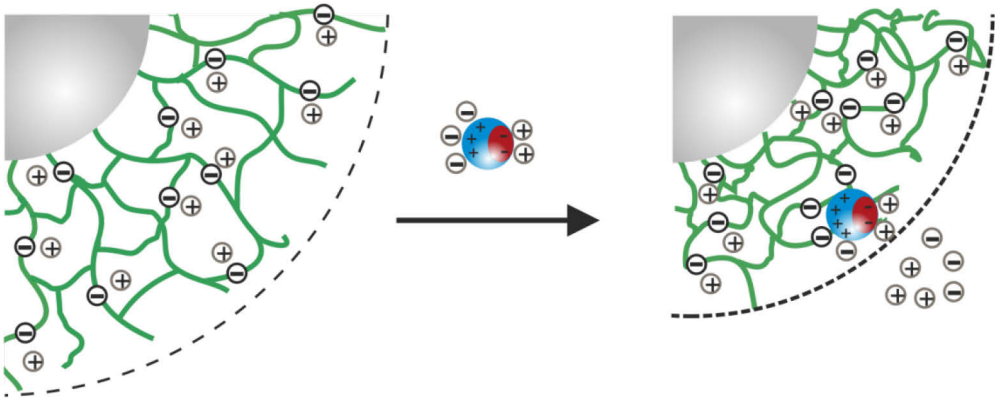

Figure 4.26: Interaction between a positively charged protein carrying charged patches and a negatively charged microgel. The dashed line illustrates the dimensions of the gel network. The protein is protonated by the electrostatic potential of the polymer network when it approaches the core-shell particle. The protein binds to the charged network due to electrostatic and hydrophobic interactions which induce deswelling of the microgel network.

understanding of the binding process. The proposed mechanism for adsorption of an overall positively charged protein on a negatively charged core-shell microgel is displayed in Figure 4.26. At low salt concentration the charge-charge interactions cause adsorption of proteins onto the microgel which has a negative electrostatic potential. However, this is not the main contributor to ΔS_b. Additionally, non-electrostatic, hydrophobic interactions are responsible for weak protein binding at higher ionic strength where electrostatic forces are screened. Both mechanisms lead to a deswelling of the gel. After having discussed the driving forces for lysozyme adsorption on charged microgels, the possible origins of the residual heat ΔH_{res} was investigated in the next step. The previous analysis assumed that this contribution to the overall measured heat is not linked to the binding equilibrium but must originate from an independent process. Two processes may be consulted to explain this independent enthalpic effect: i) a change of secondary structure, and ii) a protonation step of the enzyme upon uptake into the gel layer. In the following, both processes were discussed based on experimental observations.

4.4.2 Secondary Structure Analysis by FT-IR Spectroscopy

The secondary structure of the free and adsorbed lysozyme was investigated by using FT-IR spectroscopy in transmission mode. For this purpose, lysozyme was adsorbed onto the microgel particles at room temperature and excess amount of protein was removed by using UF against fresh buffer. The amount of bound lysozyme was calculated to 660 mg lysozyme per gram microgel according to the remarks given in section 4.2.1 and 6.5.1. This corresponds to a fraction of occupied binding sites of $\Theta \approx 0.9$. This means, that the carrier particles are nearly saturated by lysozyme. Since desorption from the microgel carrier was found to be retarded (see section 4.5), this experimental procedure ensures that all proteins in the volume are bound to the microgel. Thus, the IR signal after correction for the absorption of the microgel is solely caused by the adsorbed proteins and is not a superposition of the spectra of free and bound proteins. With this, the FT-IR intensities can be used to determine the structure of lysozyme when surrounded by the network.

The FT-IR data of the loaded microgel and the spectrum of the unloaded microgel after normalisation to the same microgel concentration of 1 wt-% are shown in Figure 4.27 a. The enhanced signals in the amide I and II region after binding of lysozyme is unambiguously ascribed to the adsorbed proteins. Figure 4.27 b shows the spectrum of free lysozyme and the spectrum of adsorbed lysozyme after subtraction of the bare microgel spectrum and normalisation to the same enzyme concentration. The information of the secondary structure was obtained by analysing the FT-IR data using a PLS algorithm (see section 3.2.2). [79,177]

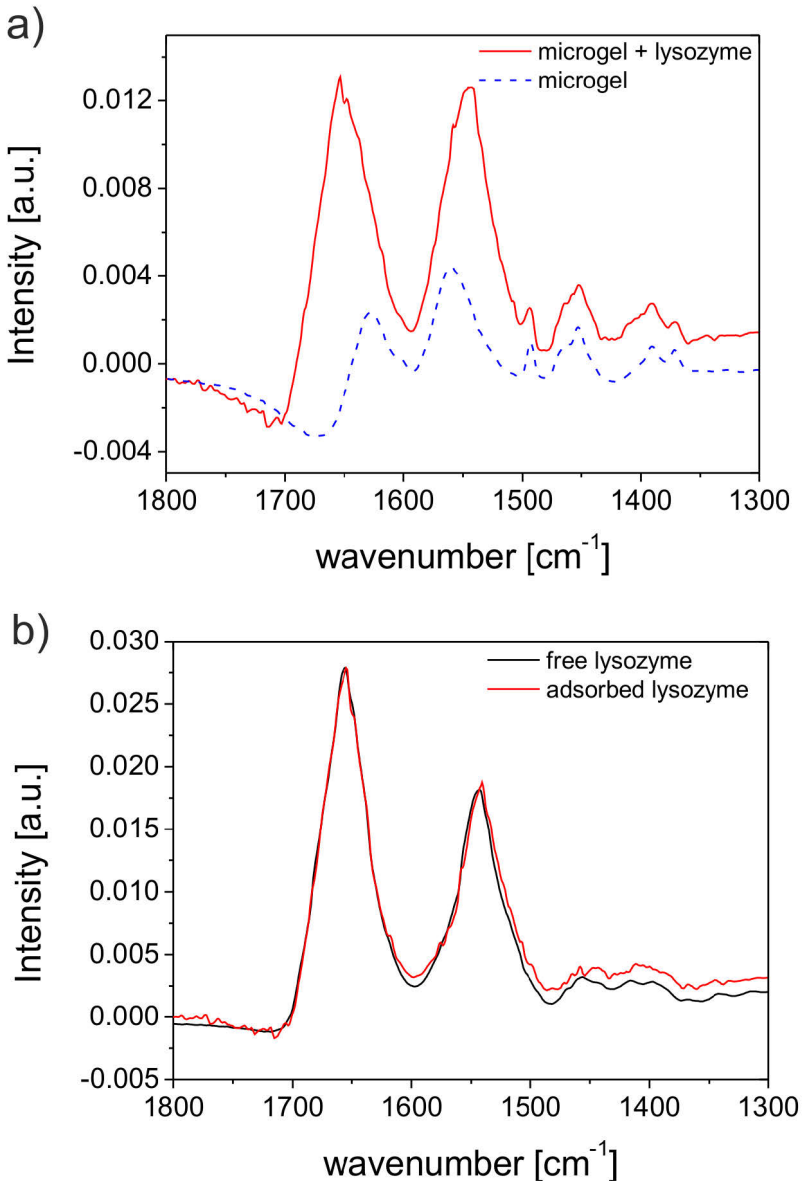

Figure 4.27: a) FT-IR spectra of the charged CSM-10 microgel before and after adsorption of lysozyme in 10 mM MOPS buffer *pH* 7.2 (7 mM ionic strength) at 298 K. The spectra were normalised to a microgel concentration of 1 wt-%. CSM-10 particles with immobilised lysozyme carry 660 mg protein per gram microgel. b) FT-IR spectra of free and adsorbed lysozyme in 10 mM MOPS *pH* 7.2 (7 mM ionic strength) at 298 K. The spectrum of adsorbed lysozyme was obtained after subtraction of the bare CSM-10 spectrum from the spectrum of loaded microgel particles. The loading of the microgel particles is 660 mg protein per gram microgel. The protein FT-IR spectra are normalised to the same enzyme concentration.

The α-helix and β-sheet content of the free lysozyme was determined to (34 ± 4) % and (4 ± 3) %, respectively, which is consistent with previous values published. [177] Adsorbed lysozyme consists of (30 ± 4) % α-helix and (2 ± 3) % β-sheet and, therefore, has the same secondary structure as the free lysozyme within the margin of error of the analysis. Concerning these experiments significant unfolding or denaturation of lysozyme was not induced by adsorption to CSM-10. Hence, the origin of the residual enthalpy ΔH_{res} cannot be found in a loss of the secondary structure of the protein. Moreover, any contribution of conformational changes to ΔS_b and ΔH_b can also be ruled out.

4.4.3 Protonation Effects during Protein Adsorption

Protonation or deprotonation of proteins which diffuse into the negatively charged network of the CSM-10 particles is another process which may account for the residual heat measured by ITC. Charge regulation of proteins is a phenomenon commonly observed in many studies and is theoretically described (compare section 3.3.1). [220,222,282] The microgel exhibits a high negative electrostatic potential $\Delta\phi$ (see equation (3.5)) which may change the local *pH* value as well as may modify the pK_a values of the polar amino acid side chains of the protein in proximity of the network (see section 3.3.1). Thus, protonation of the protein upon adsorption is likely. ITC provides a powerful method to evaluate changes of the ionisation state of proteins and other compounds in general. To determine the number of exchanged protons N_{H+}, ITC titrations in different buffers with distinct ionisation enthalpies ΔH_i^b were performed. This is because the uptake or release of protons by the protein surface induces changes of the ionisation state of the buffering compound and adds to ΔH_{ITC} measured by ITC. Baker and Murphy developed an experimental protocol that allows dissecting the protonation contributions from the overall energetics: [283]

$$\Delta H_{ITC} = \Delta H_0 + N_{H^+}\Delta H_i^b \tag{4.4}$$

where ΔH_i^b is the ionisation enthalpy of the buffer and ΔH_o is the enthalpy which would be measured in a buffer with ΔH_i^b equal to zero. [283] The value of N_{H+} is positive when protons are taken up during the ITC titration while it is negative if protons are released from the protein/microgel system. This method is widely used to investigate ionisation effects in biological processes, including protein-protein association [284] and enzyme-ligand interactions [285]. Moreover, it has been shown to play a role in protein fibrillation of glucagon and also lysozyme. [286]

For this analysis experiments on the adsorption of lysozyme were performed in MOPS buffer and 1,4-piperazinediethanesulfonic acid (PIPES) buffer with the same *pH* and ionic strength, but different ΔH_i^b, that is, MOPS: ΔH_i^{MOPS}(298K) = 21.1 kJ mol^{-1}; and PIPES: ΔH_i^{PIPES} (298K) = 11.2 kJ mol^{-1}. [287]

Figure 4.28 displays the ITC data acquired in 5 mM PIPES buffer at 298 K. The concentration of the PIPES buffer needed to be divided by 2 compared to the concentration of MOPS buffer in order to achieve an ionic strength which is identical in both buffer systems. Comparison of the integrated heats obtained in MOPS (Figure 4.21) and PIPES (Figure 4.28) buffer shows that the shape of the binding curve in both buffer systems is similar, but the ΔH_{ITC} in MOPS buffer is considerably higher than the ΔH_{ITC} in PIPES buffer. Thus, protons are taken up by lysozyme during the course of the adsorption process.

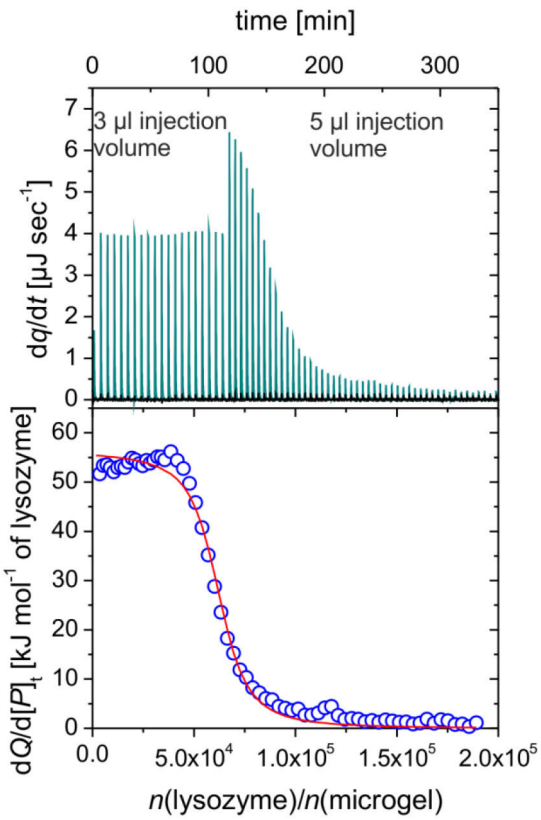

Figure 4.28 ITC data of lysozyme adsorption onto CSM-10 particles at 298 K in 5 mM PIPES buffer solution *pH* 7.2 (7 mM ionic strength). The upper panel shows the raw ITC data with the black spikes as the heat of dilution of lysozyme. The blue spikes are the change of heat corresponding to each injection of lysozyme into the microgel dispersion. The lower panel shows the integrated heats of each injection (circles) after subtraction of the dilution signal from the overall signal. The solid line represents the fit according to the SSIS model using equations (3.27) and (3.28).

In the next step, it needs to be clarified if the protonation process contributes to the enthalpy of binding ΔH_b or to the additional enthalpy ΔH_{res}. Therefore the thermodynamics of protein binding in PIPES buffer was analysed as a function of time by performing the ITC titrations at varying temperatures between 288 and 303 K (Figure 4.29 a). The ITC data were then compared to the temperature-dependent data received from the MOPS buffer system (Figure 4.23 a). The van´t Hoff analysis of the temperature-dependence of K_b measured in PIPES buffer is shown in Figure 4.29 b and is compared to the analysis of K_b measured in MOPS buffer. The thermodynamic parameters determined for the lysozyme adsorption in PIPES buffer at 298 K are listed in Table 4.5. The complete data set including the parameters at all temperatures is gathered in Table 7.4 of the supplement. According to this analysis, ΔH_b and ΔS_b in PIPES buffer equal the values obtained from the van´t Hoff plot in MOPS buffer within the margin of error. However, the adsorption of lysozyme to the microgel was found to be more endothermic in the MOPS buffer solution and gives rise to a larger ΔH_{res} when compared to the ITC experiment in PIPES buffer (Figure 4.29 c). The number of exchanged protons N_{H+} can be calculated by considering the additional enthalpies measured in MOPS and PIPES buffer, ΔH_{res}^{MOPS} and ΔH_{res}^{PIPES}, respectively:

$$N_{H^+} = \frac{\Delta H_{res}^{MOPS} - \Delta H_{res}^{PIPES}}{\Delta H_i^{MOPS} - \Delta H_i^{PIPES}} \tag{4.5}$$

N_{H+} is determined to 0.8 ± 0.4 at 298 K. From this it is suggested that lysozyme takes up ~1 proton when it enters the charged gel network. Thus, lysozyme molecules in proximity of the microgel CSM-10 adopt a more protonated state than in the surrounding solution. Moreover, the heat capacity $\Delta C_{p,res}$ obtained in PIPES buffer is smaller than the one in MOPS buffer. This directly follows from the temperature-dependence of ΔH_{res} in both MOPS and PIPES buffer (Figure 4.29 c). The difference in $\Delta C_{p,res}$ leads to a temperature-dependent protonation of lysozyme where N_{H+} is increased with

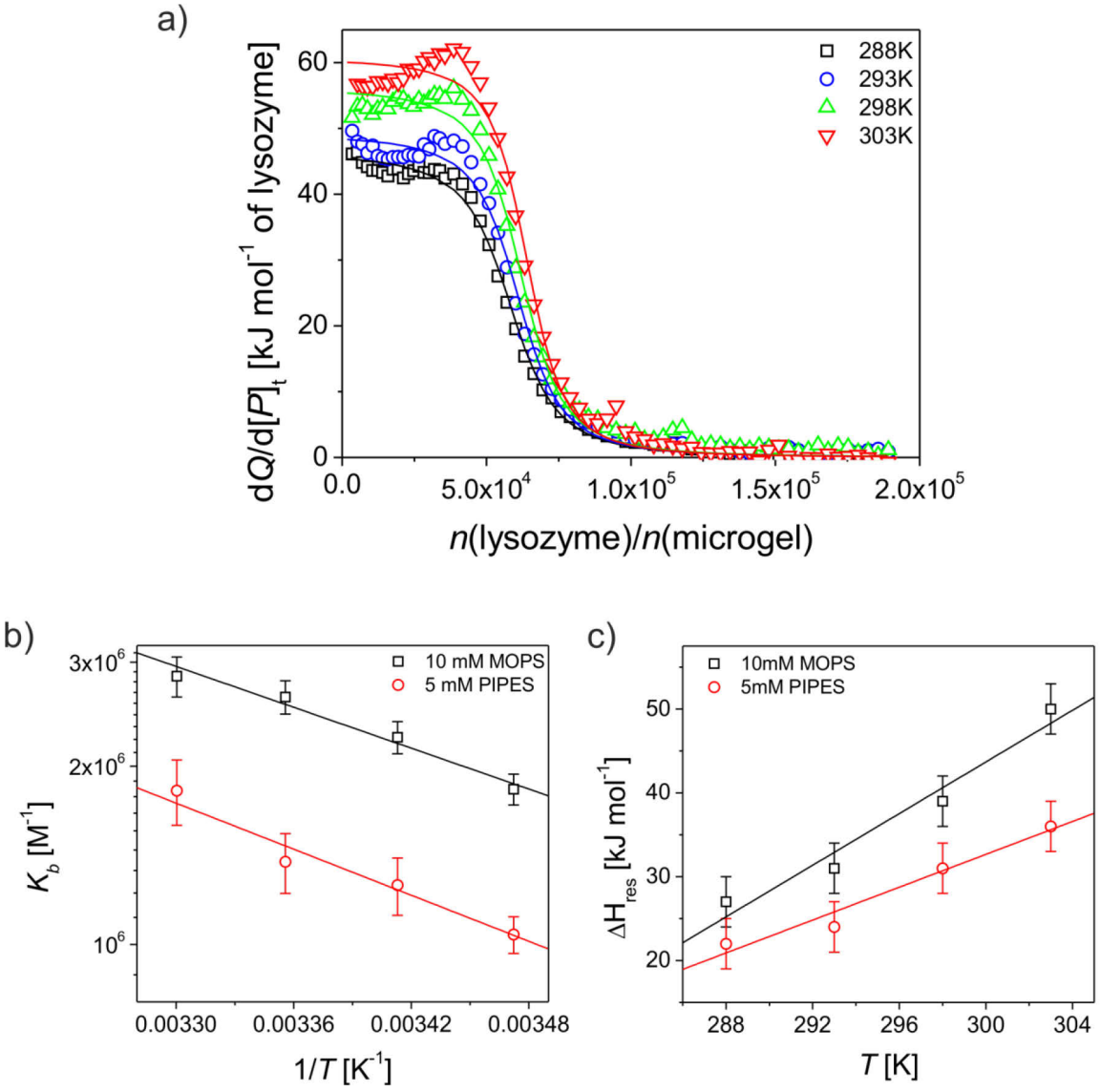

Figure 4.29: Integrated heats as function of the molar ratio between lysozyme and the microgel in 5 mM PIPES buffer *pH* 7.2 (7 mM ionic strength) at different temperatures. The solid lines are the fits according to the SSIS model using the equations (3.27) and (3.28). b) Van´t Hoff analysis of lysozyme adsorption onto the microgel particles in 10 mM MOPS and 5 mM PIPES buffer *pH* 7.2. c) Plot of the residual enthalpy ΔH_{res} measured by ITC as function of temperature in 10 mM MOPS and 5 mM PIPES buffer *pH* 7.2. The solid lines represent linear fits of the experimental data points.

increasing temperature (*cf.* Table 4.6).

It has to be emphasised that the ionisation of lysozyme is in accordance with the retained secondary structure of adsorbed lysozyme. Previous studies on the conformation of lysozyme observed that the secondary structure of lysozyme is not changed when the *pH* value is lowered from *pH* = 7 to *pH* = 5, *i.e.*, when lysozyme is protonated. [178] Thus, the FT-IR spectroscopy of lysozyme at neutral and acidic *pH* values will lead to identical spectral signals. Indeed, the analysis shows that the FT-IR spectrum of lysozyme in the bound state equals the one of the free protein. In conclusion, this analysis demonstrates that lysozyme is protonated when it enters the charged gel network, but protonation of lysozyme does not induce changes of the secondary structure. Moreover, it is not linked to the binding mechanism (that is, it is not a prerequisite for binding) and, hence, does not contribute to the thermodynamics of lysozyme adsorption, *i.e.*, ΔH_b and ΔS_b.

Table 4.6: Number of exchanged protons N_{H+} between the buffering compound and lysozyme at different temperatures at low ionic strength (7 mM).

T [K]	N_{H+}
288	0.6 ±0.4
293	0.7 ±0.4
298	0.8 ±0.4
303	1.4 ±0.4

4.4.4 Enzymatic Activity: Effect of Protonation

The thermodynamic analysis of lysozyme adsorption to the CSM-10 particles demonstrates that the negative electrostatic potential of the particles mediates the uptake of protons by the proteins. The change of the lysozyme net charge can directly be proven by the investigation of the catalytic activity due to the pronounced sensitivity of enzymes towards the *pH* value of the surrounding solution. The hydrolysing activity of lysozyme from *chicken egg white* is highest around *pH* ≈ 5 and the activity drops if the experimental conditions deviate from the *pH* optimum. [207] Thus, the protonation state of lysozyme is decisive for its catalytic activity and the observed uptake of protons by lysozyme should effect its performance. To compare the catalytic activity of lysozyme in the adsorbed and free state the water soluble substrate 4-methylumbelliferyl-*β*-D-N, N',N''-triacetylchitotrioside ((GlcNAc)$_3$-MeU)

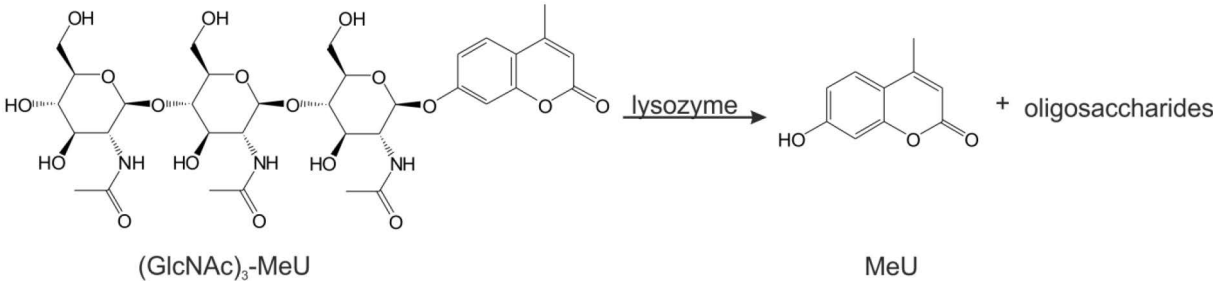

Figure 4.30: Schematic representation of the hydrolysis of (GlcNAc)$_3$-MeU into the fluorescent product MeU and oligosaccharides catalysed by lysozyme.

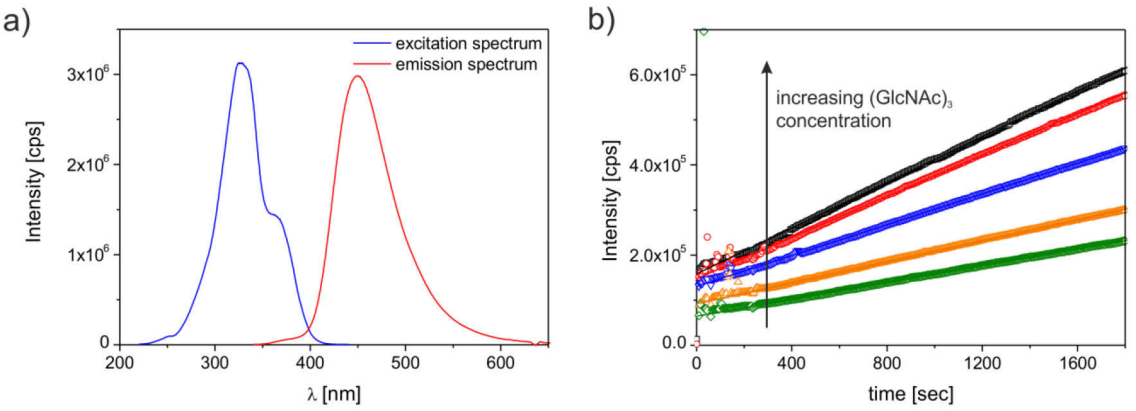

Figure 4.31: a) Extinction and emission spectra of MeU ($1.24x10^{-6}$ M) in 10 mM MOPS *pH* 7.2 at 293 K. The excitation wavelength λ_{ex} was set to 360 nm. b) Fluorescence intensity as function of time for the conversion of $(GlcNAc)_3$-MeU with concentrations ranging from $1.6x10^{-5}$ to $1.3x10^{-4}$ M at 315 K in 10 mM MOPS *pH* 7.2. The wavelength of extinction λ_{ex} and emission λ_{em} was set to 360 nm and 450 nm, respectively. The reaction was catalysed by 0.05 g L^{-1} of free lysozyme.

was used as model substrate. [207] In a solution of $(GlcNAc)_3$-MeU, lysozyme catalyses the cleavage of the (1→4)-*β*-glycosidic linkage in $(GlcNAc)_3$-MeU releasing the fluorescent compound 4-methylumbelliferone (MeU) as shown in Figure 4.30.

The substrate itself shows no fluorescence but the product MeU is fluorescent in neutral and alkaline conditions and exhibits a fluorescence emission peak at $\lambda_{em,max}$ = 450 nm when excited at λ_{ex} = 360 nm (Figure 4.31 a). [207,288] Thus, υ can be determined by monitoring the time-dependent emission fluorescence intensity, *i.e.*, the time-dependent increase of the concentration of MeU, when $(GlcNAc)_3$-MeU is hydrolysed. The time-dependent conversion of $(GlcNAc)_3$-MeU catalysed by free lysozyme is shown in Figure 4.31 b.

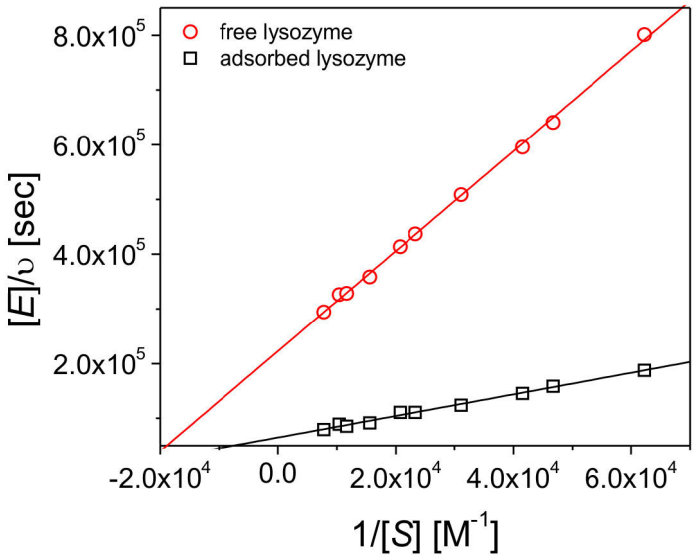

Figure 4.32: Lineweaver-Burk plot for the hydrolysis of $(GlcNAc)_3$-MeU catalysed by free and adsorbed lysozyme in 10 mM MOPS buffer *pH* 7.2 (7 mM ionic strength) at 315 K. The kinetic experiments with adsorbed lysozyme were done using a CSM-10 dispersion containing 675 mg of enzyme per gram microgel. The solid lines are linear fits to the experimental data points.

Activity tests with adsorbed lysozyme were done after ultrafiltration of the sample to remove any excess protein in solution. The CSM-10 particles contained 675 mg lysozyme per gram microgel after thorough purification. The activity measurements were performed in 10 mM MOPS buffer *pH* 7.2 at 315 K, that is, above the *pH* optimum of lysozyme. The initial rate v of the hydrolysis of $(GlcNAc)_3$-MeU was measured at concentrations of the substrate ranging from $1.6x10^{-5}$ to $1.3x10^{-4}$ M and was evaluated in terms of Michaelis-Menten kinetics (equation (3.13)). Figure 4.32 shows the Lineweaver-Burk plots for the catalytic reaction in presence of free and adsorbed lysozyme, respectively, and after normalisation to the same lysozyme concentration. A central result of this study is the pronounced increase of the hydrolytic activity of lysozyme when it is adsorbed onto the microgel. The turnover number k_{cat} of free and immobilised lysozyme was determined to $4.4x10^{-6}$ sec^{-1} and $1.5x10^{-5}$ sec^{-1}, respectively. This means that binding to the microgel particles increases the activity of lysozyme by a factor of ~3.5. In particular, the activity of lysozyme in the adsorbed and protonated state equates the k_{cat} at its *pH* optimum.[207] This analysis implies that adsorbed lysozyme adopts the protonation state which is found at the *pH* optimum. Indeed, this is also supported by the number of exchanged protons N_{H+} determined from the thermodynamic study by ITC.

4.4.5 Conclusion

In this section the adsorption of lysozyme on negatively charged core-shell microgels (CSM-10) was investigated by ITC. From these experiments it is clear that the adsorption is caused by several driving forces. The ITC analysis at varying salt concentrations shows that hydrophobic interactions contribute to protein binding to the microgels in addition to electrostatic forces which are important at low ionic strength. Following from the ITC studies in different buffer systems, a change of the ionisation state of the enzyme is induced by the negative electrostatic potential of the CSM-10 particles. These experiments indicated that lysozyme is protonated and that the protonation process is not linked to the binding equilibrium, as the enthalpy of protonation adds to the residual enthalpy ΔH_{res} measured by ITC but not to ΔH_b. Catalytic activity tests of free and adsorbed lysozyme further supported these findings: As shown in the kinetic experiments, the activity in the bound state is enhanced and corresponds to the activity of lysozyme in the protonated state at its *pH* optimum. Thus, lysozyme can act as local *pH* meter which recognises the different conditions inside the charged gel and adjusts its performance to the new environment. This study demonstrated that charged core-shell microgels serve as superior protein carriers with high loading capacity and the ability to improve the enzyme activity.

4.5 Kinetics and Reversibility of Protein Adsorption on Microgels

The investigations done so far show that large amounts of protein bind to the microgel particles and bound proteins fully retain their native conformation and catalytic activity. The full retention of the tertiary structure of bound proteins points to reversibility of the adsorption process but is no evidence that the equilibrium is indeed established. To prove the reversibility of the adsorption process the exchange of bound proteins by proteins free in solution has to be studied without perturbing the existing equilibrium. Thus, an experimental procedure must be chosen which allows studying adsorption and desorption in presence of excess proteins.

For this purpose, fluorescence spectroscopy has been selected to analyse the adsorption of proteins by the charged microgel CSM-10, as schematically depicted in Figure 4.33. This technique is widely employed in biomacromolecule binding studies. For example, the binding of labelled proteins to metal nanoparticles was followed by fluorescence spectroscopy as a function of time and the kinetics was quantified by using an appropriate kinetic model. [69] Moreover, Bunz *et al.* used the fluorescence quenching capabilities of gold nanoparticles to study the exchange of green fluorescent protein (GFP) by human serum proteins. [289] The strategy chosen in this thesis is also based on fluorescence quenching induced upon protein binding. However, unlike the fluorescence quenching experiments performed in the past [7,69], quenching of fluorescent proteins upon adsorption to the negatively charged CSM-10 particle is induced by the local *pH* gradient which is established between the charged shell network and the bulk solution (see section 4.4). The more acidic environment of the microgel network leads to changes of the protonation state of amphiphilic molecules, such as *pH*-sensitive fluorescent tags. Thus, the time-dependent binding of proteins labelled by such a *pH*-sensitive fluorophore is detected by the change of the fluorescence intensity. By this means, exchange experiments between labelled and unlabelled proteins give information about the reversibility of the

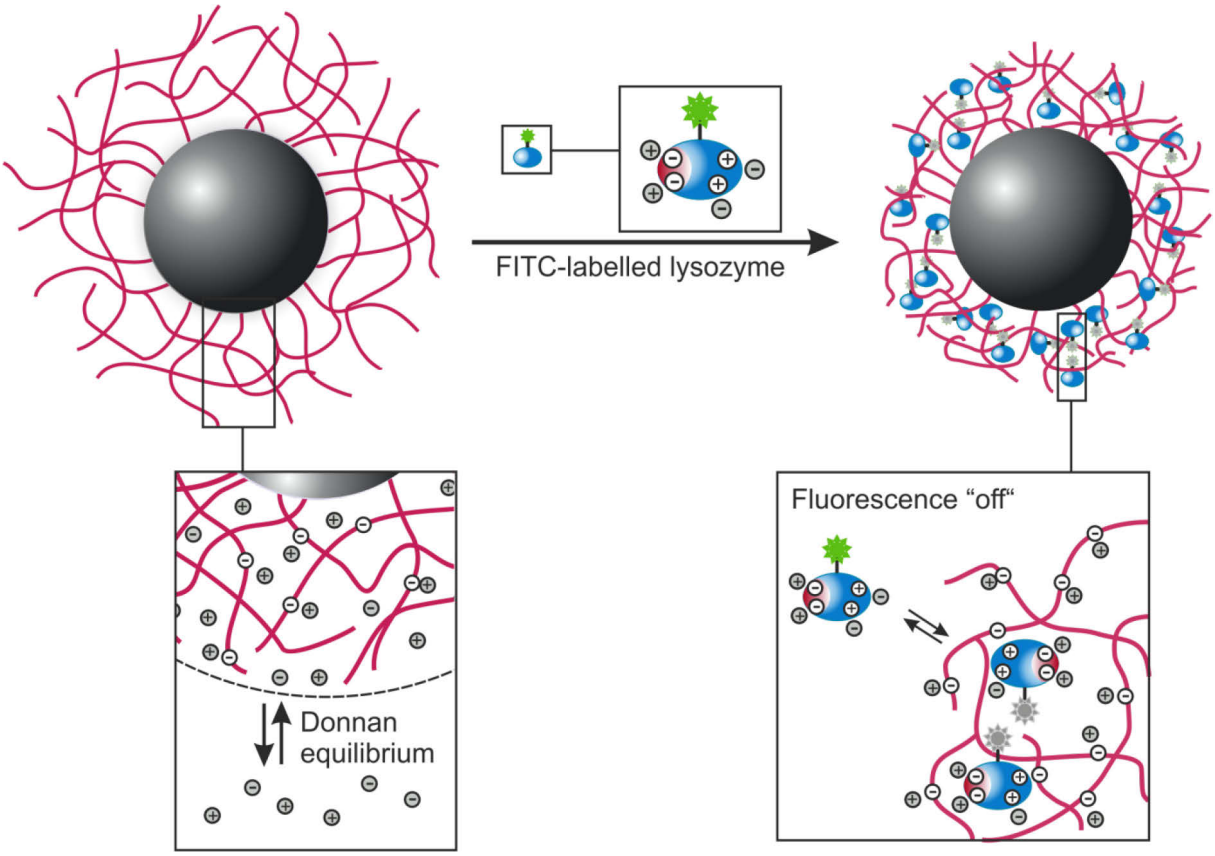

Figure 4.33: Interaction between fluorescein isothiocyanate (FITC) labelled lysozyme (lysozyme^{FITC}) and the negatively charged CSM-10 microgel (top). The concentration of the ions inside the network is determined by the ion concentration of the outer solution through the Donnan-equilibrium (bottom, left). The dashed line represents the dimension of the microgel particle. The lowered *pH* value within the network and mutual quenching of the fluorophores leads to a decrease of the fluorescence intensity upon adsorption of lysozyme^{FITC} to the microgel network (bottom right). The decrease of the intensity can be analysed as a function of time. These data are used for the quantitative analysis of the kinetics of the protein uptake.

adsorption process. The latter may be further confirmed by the triggered release of proteins caused by changes of the environmental conditions. In case of charged microgels salt might be the external trigger since electrostatic interactions between the protein and the particle are an important contributor to the binding strength of proteins. Moreover, the uptake of the labelled protein by CSM-10 can be monitored from the decrease of fluorescence intensity as a function of time. The data thus received can be used to quantify the kinetics of protein adsorption including the binding rate constants and the equilibration time of the given protein/particle system.

4.5.1 Fluorescence Spectroscopy Analysis of Protein Adsorption

The ITC analysis of lysozyme adsorption onto CSM-10 particles has revealed strong adsorption of lysozyme to the charged core-shell microgels with binding affinities in the range of 10^6 M^{-1}(compare section 4.4). Thus lysozyme is selected as model protein to study the reversibility and kinetic mechanism of the adsorption. To follow the uptake and exchange of lysozyme into the microgel network in 10 mM MOPS buffer solution of low salt concentration at *pH* 7.2, lysozyme was fluorescently tagged by fluorescein isothiocyanate (FITC). Generally, fluorescein and other xanthene dyes are characterised by their high extinction coefficient and high fluorescence quantum yield. [290] The main advantage of using fluorescein as fluorescent tag is its well-known *pH* sensitivity. [290-292] Due to its functional hydroxyl and carboxyl groups, fluorescein exists in several ionic forms which differ in their emission spectra. [293] Therefore, fluorescein emission displays a complex

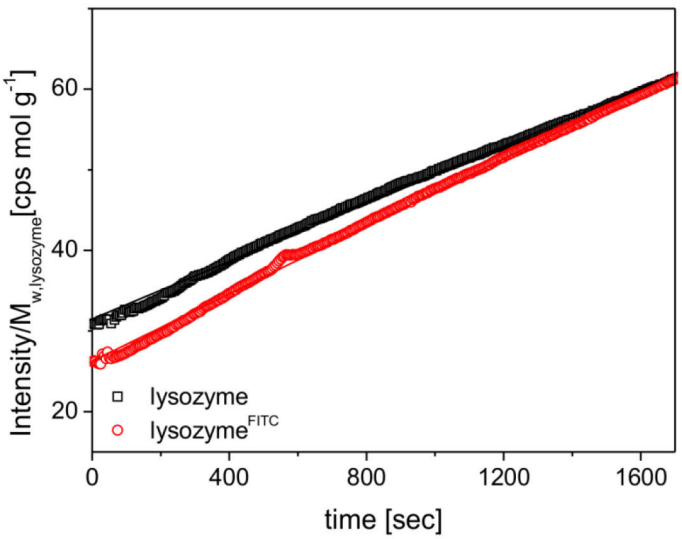

Figure 4.34: Comparison of the catalytic activity of lysozyme^{FITC} and unlabelled lysozyme. The hydrolysis of 1.3x10^{-4} M $(GlcNAc)_3$-MeU at 315 K in 10 mM MOPS buffer *pH* 7.2 was followed by the detection of the fluorescence intensity with time. The extinction wavelength λ_{ex} was set to 360 nm and the emission wavelength λ_{em} was set to 450 nm. The reaction was catalysed by 0.053 g L^{-1} native lysozyme and 0.089 g L^{-1} lysozyme^{FITC}. From the slopes of the linear change of the fluorescence intensity with time the enzymatic activity was calculated. The activity of labelled and unlabelled lysozyme was determined to 0.011 d*I* $dsec^{-1}$ mol^{-1} and 0.015 d*I* $dsec^{-1}$ mol^{-1}, respectively.

pH-dependence reflecting the equilibrium between the various ionic states of which only the monoanion and dianion forms are fluorescent. Consequently, fluorescein shows high fluorescence at neutral and alkaline conditions whereas the fluorescence intensity drops in more acidic solutions. In particular, negligible fluorescence intensity is expected below a *pH* value of 5. [290]

The strong *pH*-dependence of the fluorescence intensity of fluorescein tags is widely exploited to quantify the *pH* value of intracellular compartments. [294-296] In analogy, fluorescein will sense deviations of the proton concentration inside the charged shell network of the CSM-10 particles from the bulk *pH* value. The ITC analysis as well as the catalytic activity tests predicted a pronounced decrease of the local *pH* around the charged chains of the polymer network. The transfer of fluorescein from the bulk solution to the microgel phase will shift the ionisation equilibrium of the fluorophore to the more protonated states. Thus, the fluorescence of fluorescein-labelled proteins will be drastically decreased or even be stopped as soon as the protein enters the surface layer of the particles. Additionally, increasing the concentration of fluorescein leads to self-quenching due to the significant overlap of their absorption and emission spectra. This causes resonance energy transfer (homo RET) between fluorescein moieties and the formation of non-fluorescent dimers at higher concentration. [290,297-298] The Förster distance for homo RET between fluorescein moieties was determined to 42-56 Å which is comparable to the size of proteins. [297,299] The combination of these effects, protonation and crowding of fluorescein as consequence of protein adsorption, will lead to a marked decrease of the fluorescence intensity. Thus, by using FITC-labelled lysozyme (lysozyme^{FITC}) it is possible to detect the transfer of the protein between the bulk solution and the microgel network as a function of time. In analogy, the release of lysozyme^{FITC} can be analysed by the increase of the fluorescence intensity with time.

In general, labelling of proteins by fluorescent tags may cause changes of the protein conformation up to the denaturation in the worst case. However, for the protein binding studies the retention of the native conformation of labelled proteins is crucial. To avoid large modifications of the tertiary structure of the protein the labelling ratio of lysozyme was minimised to one fluorescein label per protein molecule. The catalytic activity test of lysozyme before and after labelling showed that lysozyme^{FITC} retains more than 70 % of its initial activity (Figure 4.34). On the basis of this result it is reasonable to assert that labelled lysozyme has similar properties to native lysozyme regarding its structure and interaction with the surrounding solution. Consequently, lysozyme is robust enough to stay in its native conformation after treatment with FITC and the fluorescein tagged protein can be used to analyse the uptake by charged microgel particles from its unperturbed conformation.

First experiments regarding this analysis are shown in Figure 4.35. There, the normalised excitation and emission spectra of the uncoupled dye FITC (Figure 4.35 a) are compared to those of lysozyme^{FITC} (Figure 4.35 b) before and after addition of the microgel dispersion. Obviously, the spectral properties of the uncoupled fluorophore are not compromised by the microgel dispersion as any significant changes of the excitation and emission fluorescence spectra are discernible. This demonstrates that excitation and emission of light by the fluorophore is not perturbed by the presence of the CSM-10 particles, at least at the low concentrations used. Moreover, the small dye shows no affinity to be accumulated into the microgel network indicating the lack of attractive interactions between FITC and the charged gel network. In contrast, injecting the same amount of microgel into a solution of lysozyme^{FITC} of comparable fluorophore concentration decreases the fluorescence intensity by more

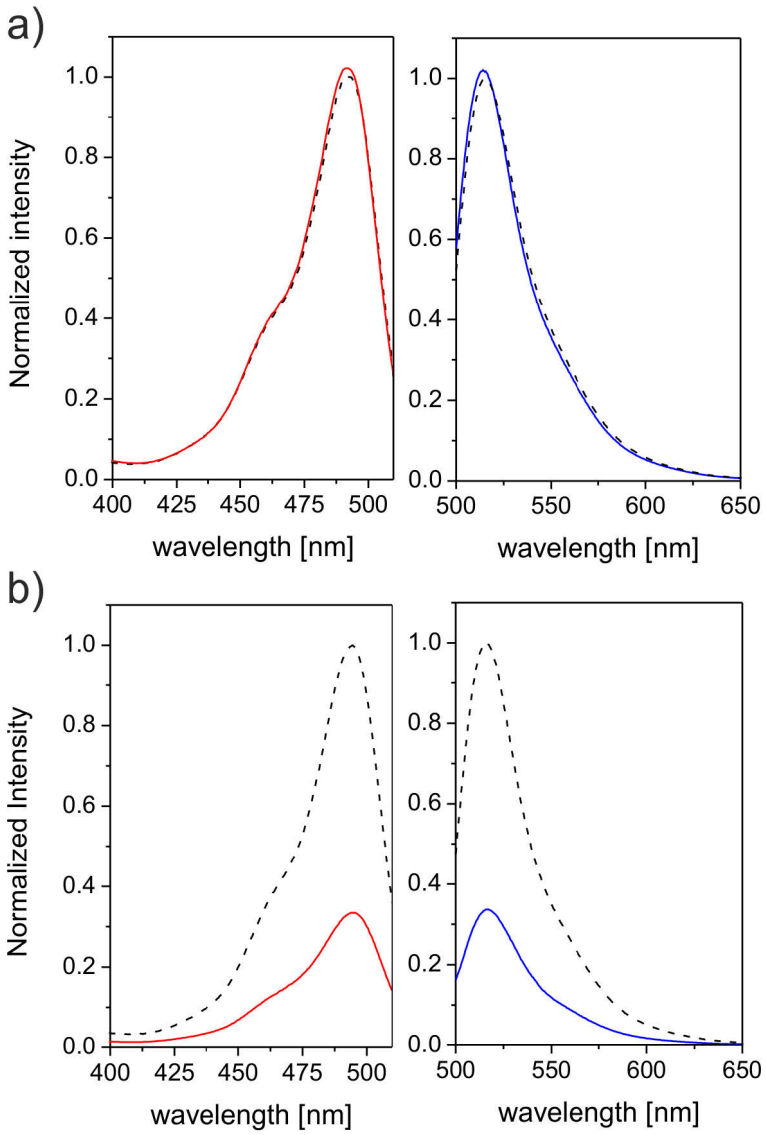

Figure 4.35: a) Normalised excitation (left) and emission spectra (right) of 1.21 µM FITC (dashed lines) and of 1.21 µM FITC in presence of 0.029 g L^{-1} CSM-10 particles (solid lines) in 10 mM MOPS buffer *pH* 7.2 at 293 K. The fluorescence intensities were normalised to the maximum excitation and emission intensity of FITC in absence of the microgel. b) Normalised excitation (left) and emission spectra (right) of 1.64 µM lysozyme^{FITC} (dashed lines) and of lysozyme^{FITC} in presence of 0.029 g L^{-1} CSM-10 particles (solid lines) in 10 mM MOPS buffer *pH* 7.2 at 293 K. The fluorescence intensities were normalised to the maximum excitation and emission intensity of lysozyme^{FITC} in absence of the microgel.

than 60%. Thus, the decrease of the fluorescence is unambiguously ascribed to the uptake of lysozyme^{FITC} by CSM-10 particles. Using this strategy, it is possible to obtain information about the reversibility of protein adsorption as well as about the kinetic mechanism of the adsorption process. Consequently, the adsorption process onto the charged microgel particles was followed by the decrease of the fluorescence intensity at 518 nm with time after microgel injection until a constant value was reached. In Figure 4.36 a the time-dependence of the fluorescence emission intensity of lysozyme^{FITC} is shown for different protein concentrations and constant microgel concentration, *i.e.*, for varying molar ratios between lysozyme and microgel. The fluorescence intensity at 518 nm was

measured as a function of time after addition of the microgel particles to the solution of the fluorescent protein. The intensity of fluorescence is strongly decreased, as expected, indicating the uptake of the protein by the particles. From the constant fluorescence intensity at the end of the experiment, the concentration of protein left free in solution was calculated. The amount of bound protein per gram microgel, τ_{ads}, was then easily extracted from the difference of the total concentration of lysozyme^{FITC} in the volume and free protein for each protein concentration. These values are plotted together with the isotherm which has been obtained from the ITC analysis in 10 mM MOPS *pH* 7.2 at 293 K (Figure 4.36 b). The latter was calculated from the ITC data according to the following procedure.

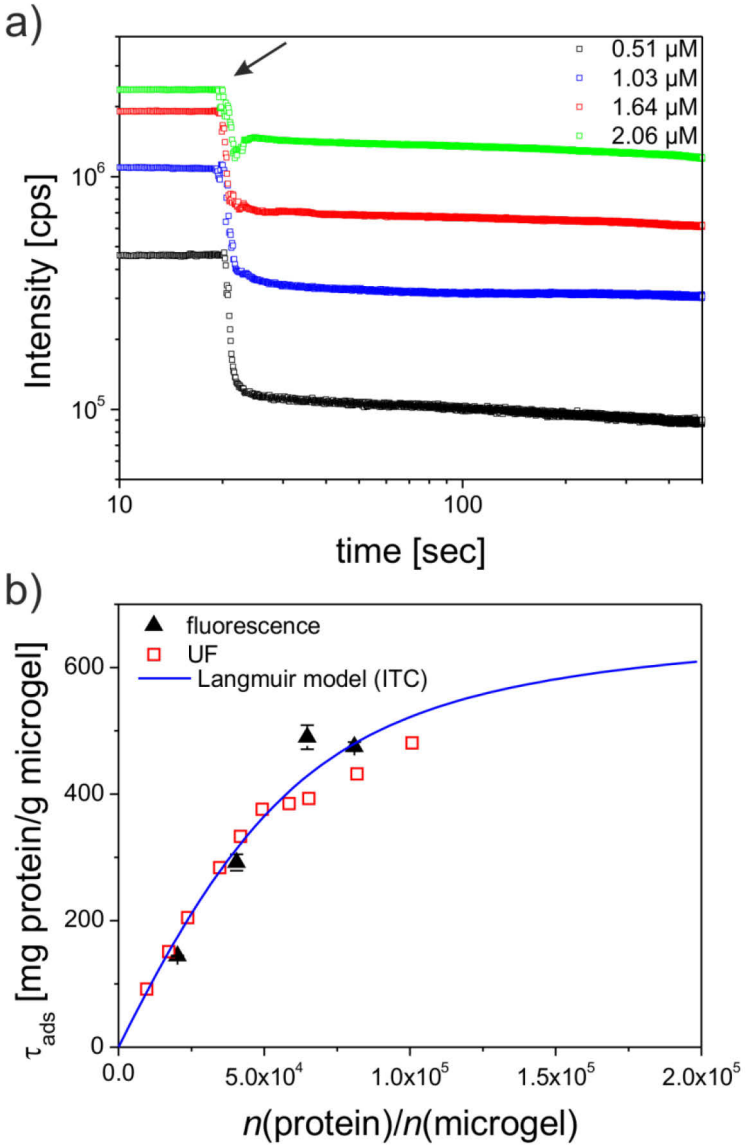

Figure 4.36: a) Fluorescence emission intensity of lysozyme^{FITC} (0.51 – 2.06 µM) as a function of time in 10 mM MOPS buffer *pH* 7.2 at 293 K. The marked decrease of the fluorescence signal is caused by the addition of 0.029 g L^{-1} CSM-10 particles to the protein solution. The arrow marks the moment of microgel injection. b) Amount of adsorbed protein per gram microgel τ_{ads} as a function of the molar ratio obtained from ITC (Langmuir-isotherm; solid line), UF, and fluorescence spectroscopy analysis. All data points were normalised to the protein and microgel concentration used in the fluorescence spectroscopy experiment. The adsorption was performed in 10 mM MOPS buffer *pH* 7.2 at 293 K for the ITC and fluorescence experiment, and at room temperature for the UF method.

The binding constant K_b determined from the ITC fitting procedure is correlated to the fraction of occupied binding sites, Θ, through the Langmuir isotherm which is given by equation (3.16). Substitution of equation (3.16) into the expression for [*P*] (equation (3.23)) gives a cubic equation which can be solved for the concentration of unbound lysozyme [*P*] for each injection:

$$[P] = \left(K_b[P]_t - NK_b[M]_t - 1 + \sqrt{(1 + NK_b[M]_t - K_b[P]_t)^2 + 4K_b[P]_t}\right)(2K_b)^{-1} \qquad (4.6)$$

From this and from the total protein concentration $[P]_t$, the fraction of bound lysozyme can be determined. Thus, the amount of adsorbed protein per gram microgel τ_{ads} for each injection can be calculated using

$$\tau_{ads} = \frac{([P]_t - [P]) \cdot 1000 \cdot M_{w,protein}}{[M]_t \cdot M_{w,microgel}} \qquad (4.7)$$

where $M_{w,protein}$ and $M_{w,microgel}$ is the molecular weight of lysozyme and the microgel, respectively. By this means, τ_{ads} can be calculated for each protein concentration in the volume $[P]_t$ by combining equations (4.6) and (4.7) which finally give the adsorption isotherm for lysozyme binding.

UF experiments were performed as third technique to quantify the adsorption of lysozyme: In this experiment non-bound and desorbing proteins are removed by filtering through a membrane while fresh protein-free buffer solution is added over several hours. The amount of adsorbed lysozyme $\tau_{ads,UF}$ is then determined from the difference between the total amount of protein used and the concentration of the depleted protein found in the filtrate. It has to be noted that the protein concentrations employed in the UF experiment was increased by a factor of ~300 compared to the concentrations needed in the fluorescence experiment. However, equation (3.24) shows that Θ is dependent on the molar ratio $[P]_t/[M]_t$ as well as on the absolute microgel concentration $[M]_t$ used. For a direct comparison between different methods, the binding isotherms therefore have to be normalised to the same protein and microgel concentrations.

The values of $\tau_{ads,UF}$ determined from UF experiments (open squares in Figure 4.36 b) virtually coincide with the values found by fluorescence spectroscopy and the Langmuir isotherm derived from ITC (solid line in Figure 4.36 b). This indicates that the fluorescence of adsorbed proteins is practically totally suppressed, also for low molar ratios. Evidently, the fluorescence of lysozyme^{FITC} is switched off even for smaller packing densities. This observation strongly points to a shift of the *pH* value as the main cause of the reduction of the fluorescence intensity because it is operative already at low packing densities. Moreover, the concentration of protein increases significantly during the course of the adsorption process: The final internal protein concentration is ~8 mM (115 g L^{-1}), which is a 4900-fold increase in the concentration of lysozyme relative to the 1.64 µM lysozyme solution used for the fluorescence measurements. The high local protein and fluorescein concentration in the shell exceeds the fluorophore concentration threshold of 1 mM at which self-quenching of the fluorescein fluorescence becomes significant. [297] Consequently, the fluorescence intensity monitored after addition of the CSM-10 particles (Figure 4.36 a) is caused by the fluorescence of labelled lysozyme which remains in solution whereas the remaining fluorescence of lysozyme^{FITC} within the microgel network is negligible.

It has to be noted that the time required performing an ITC measurement or an UF experiment is ~8 h and ~2 d, respectively, while in the fluorescence spectroscopy experiments the adsorption process is

analysed within the first 30 min. Moreover, the protein solution is injected stepwise to the microgel dispersion into the ITC cell while the final protein concentration is added all at once in case of the UF and the fluorescence spectroscopy experiments. Nevertheless, the amounts of bound protein resulting from these different techniques coincide within the margin of error. This implies that the adsorption mechanism is not changed with time. Thus, transitions of the bound protein with increasing residence time on the polymeric chains of the microgel, which may affect the total amount of bound protein [300], do not occur for a period of at least 2 d.

4.5.2 Kinetics of Protein Adsorption

Figure 4.36 a has shown that the kinetics of protein adsorption can be analysed by the decrease of the emission intensity. Before the exchange experiments between labelled and unlabelled lysozyme are discussed the kinetics of protein binding is analysed in detail: The time-dependent fluorescence data for the adsorption of lysozyme^{FITC} onto the microgel in low salt concentration first exhibits a sharp decrease of the intensity within the first seconds after microgel injection (fast regime). Then a second step follows which is much slower (slow regime) and takes several hundred seconds. Clearly the fast regime of protein binding will be related to the diffusion of the protein towards the network and its uptake by the shell. This process will be modelled in the following.

Figure 4.36 b shows that the Langmuir isotherm provides a good description (compare equation (3.16)). Because of that the kinetics of protein adsorption will be modelled in terms of the kinetic Langmuir model. [262] This model is described in section 3.3.4 and is based on the equilibrium between the adsorption of proteins on N equal adsorption sites and the desorption of proteins from these sites:

$$\frac{\mathrm{d}\Theta}{\mathrm{d}t} = k_{\mathrm{on}} \frac{[B][P]}{N[M]_{\mathrm{t}}} - k_{\mathrm{off}} \frac{[PB]}{N[M]_{\mathrm{t}}} \tag{4.8}$$

where k_{on} and k_{off} is the adsorption and desorption rate, respectively, $[M]_t$ is the total microgel concentration, and $[P]_t$ is the total protein concentration in solution. The analytical solution for $\Theta(t)$ was derived by Azizian [262] and can be found in section 3.3.4 (equation (3.38)).

Equation (4.8) can be further simplified by using the relationship $K_b = k_{on}/k_{off}$ and by substituting the parameter k_{off} for k_{on}/K_b. The value of K_b is determined from the ITC analysis of lysozyme binding, and the only unknown in equation (4.8) is the rate constant of the adsorption k_{on}. For diffusion controlled binding reactions the diffusion flux of protein molecules to the adsorption sites becomes the rate-determining step.

As visualised in Figure 4.37 a, the motion of the proteins to the adsorption sites need to be split up into 2 contributions which are quantified by the rate constants k_D and k_i: First, the protein diffuses from the bulk solution to the microgel surface which is characterised by the rate constant k_D. The latter can be described by the rate constant of diffusion-limited association reactions between small and large molecules with perfectly absorbing boundary conditions (Smoluchowski rate): [81]

$$k_{\mathrm{D}} = 4\pi D_0 R \tag{4.9}$$

where D_0 is the diffusion coefficient of the small molecule (protein) in solution and R is the radius of the large particle (microgel). Thus, k_D follows from the diffusion coefficient of lysozyme D_0 (about 10^{-10} m^2 s^{-1}) and from the hydrodynamic radius of the microgel R_h which is used for R.

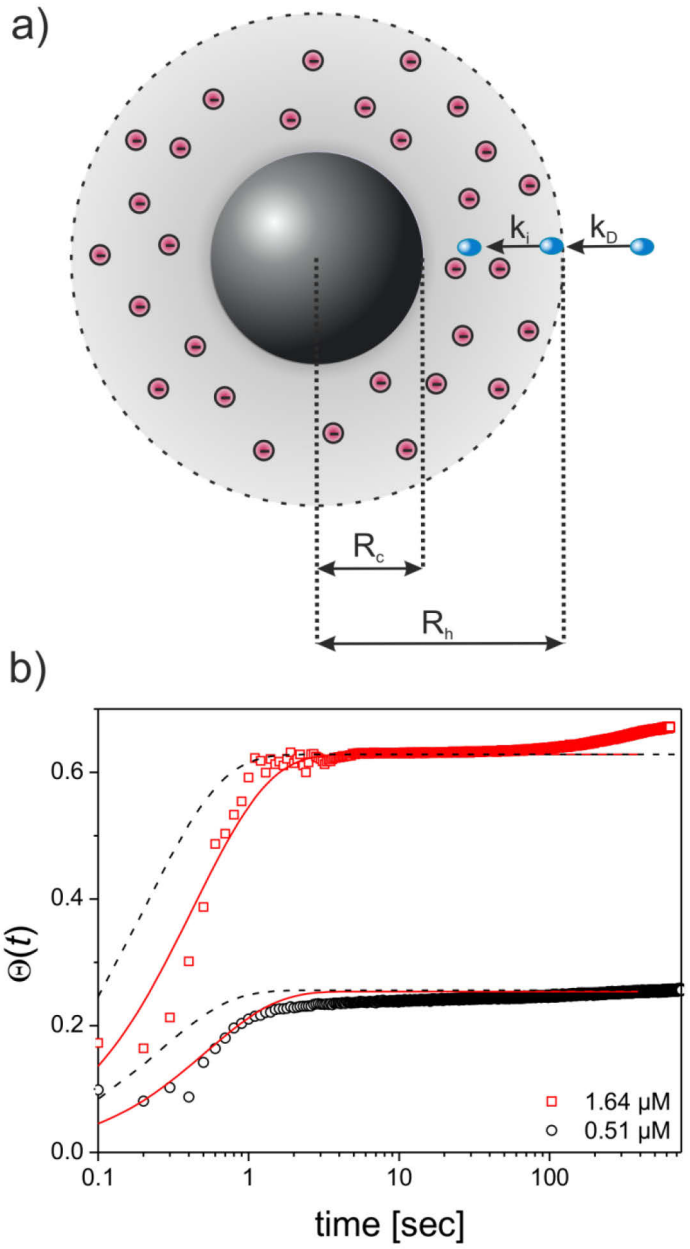

Figure 4.37: Kinetics of protein adsorption as measured by fluorescence spectroscopy. a) Schematic representation of protein adsorption towards a negatively charged microgel network with a core of radius R_c and an overall hydrodynamic radius R_h (counterions not shown). Protein diffusion on the surface of the microgel is described by the rate constant k_D while the motion of the protein along the polymer chains of the gel network is determined by the rate constant k_i. b) Fraction of occupied binding sites Θ of the charged microgel CSM-10 as a function of time after addition of 0.029 g L^{-1} CSM-10 particles into a solution of lysozyme^{FITC} of two different concentrations. The moment of microgel injection was set to t = 0. The experiments were performed in 10 mM MOPS buffer *pH* 7.2 at 293 K. The solid lines represent the fit according to equation (3.38). The dashed lines represent the theoretical curve predicted by equation (3.38) with k_{on} set to k_D/N, *i.e.*, $k_i = \infty$ in equation (4.10).

It should be noted that binding of lysozyme to the carrier particle from a solution of c(lysozyme^{FITC}) = 1.64 µM induces a shrinking of the microgel from R_h = 181 nm to R_h = 156 nm with time. This corresponds to a reduction of about 37 % in the shell volume. This change, however, has only a small impact on the total value of k_D Thus, it is sufficient to use the mean value of k_D for further analysis. The latter was calculated from the mean value of the hydrodynamic radius $< R_h >$ of the microgel which follows from from the R_h of the unloaded microgel and of the microgel in equilibrium with a given concentration of lysozyme^{FITC} (*cf.* Table 4.7).

The second contribution to k_{on} considers the uptake of the proteins into the charged microgel network and the diffusion of the protein within the microgel network towards its adsorption site. This term will be described by the rate of internal diffusion k_i. Consequently, k_{on} is expressed by k_D and k_i, with k_i being the sole unknown parameter of equation (4.10):

$$k_{on}{}^{-1} = \left(\frac{k_D}{N}\right)^{-1} + \left(\frac{k_i}{N}\right)^{-1} \tag{4.10}$$

The uptake of labelled lysozyme at concentrations of 0.51 and 1.64 µM from Figure 4.36 a is converted into $\Theta(t)$ and is plotted in Figure 4.37 b versus time. The analytical expression of $\Theta(t)$ (see equation (3.38)) was used to fit the experimental data points (solid lines in Figure 4.37 b). The rate constant k_i can be calculated from the fitted values of k_{on} using equation (4.10). The results of this analysis are listed in Table 4.7. For comparison, the theoretical prediction for the limiting case with $k_i = \infty$ is shown in Figure 4.37 b (dashed lines), too. This plot corresponds to the time evolution of the fraction of occupied binding sites which is expected if the kinetics of this process is solely determined by the diffusion of proteins from solution to the microgel particle. Obviously, the adsorption process is found to be slower than predicted by this theoretical approach. Thus, the time-dependent motion of proteins inside the microgel towards the binding sites must be taken into account.

Table 4.7: Kinetic parameters of the adsorption of lysozyme^{FITC} onto CSM-10 particles in 10 mM MOPS buffer *pH* 7.2 at 293 K.

c(lysozyme^{FITC}) [M]	$<R_h>$ [nm][a]	k_D [M^{-1} sec^{-1}]	k_{on} [M^{-1} sec^{-1}]	k_i [M^{-1} sec^{-1}]
0.51	177.5	1.34×10^{11}	$1.0 \times 10^{6} \pm 8.6 \times 10^{2}$	$1.10 \times 10^{11} \pm 9.6 \times 10^{7}$
1.64	168.0	1.27×10^{11}	$9.74 \times 10^{5} \pm 3.2 \times 10^{4}$	$1.04 \times 10^{11} \pm 3.5 \times 10^{9}$

[a] $<R_h>$ corresponds to the mean value of the hydrodynamic radius of CSM-10 in presence of lysozyme^{FITC} with c(lysozyme^{FITC}).

Evidently, this model is able to distinguish between the two essential kinetic steps of the fast adsorption regime. Moreover, the analysis shows that the two time constants k_D and k_i are of comparable order. This implies that the motion of lysozyme^{FITC} inside the microgel network towards the binding sites is as fast as the diffusion of lysozyme^{FITC} in solution towards the outer boundary of the microgel. Indeed, if $k_i = \infty$ (dashed lines in Figure 4.37 b), the theory predicts an adsorption reaction too fast by a factor of 2.

However, k_i is generally expected to be much smaller than the rate constant of diffusion in solution k_D inasmuch as it reflects the slow diffusion of the protein through a network towards a small nanometre-sized target. However, a direct comparison of the free diffusion and the diffusion in a network is not

possible. Most probably the protein motion within the gel network is reduced from three dimensions to one dimension and may be envisioned as a one-dimensional "sliding" of the proteins along the polymer chains towards the binding sites. [82] It is indeed well-established that the diffusional search in reduced dimensionality is much more efficient for proteins that bind to DNA. [301-302]

K_b obtained from ITC analysis and k_{on} determined from the fit of equation (3.38) lead to the desorption rate constant k_{off} which is ~0.5 sec^{-1}. Consequently, the mean residence time of lysozyme^{FITC} on the microgel network k_{off}^{-1} is around 2 sec. However, Figure 4.37 b indicates that only 90 % of the protein is taken up in the fast adsorption regime whereas the remaining protein fraction is adsorbed much more slowly in a following step. This slow adsorption regime has a time constant of a few hundred seconds. The second binding mode may arise from cooperative phenomena caused by the rearrangement of adsorbed proteins within the microgel. As mentioned above, binding of oppositely charged proteins causes shrinking of the microgel network (see section 4.4.1.2) Thus, it is likely that the time-dependent increase of the network-density during the binding process induces reorientation of the protein molecules towards the charged polymer chains of the network. Further studies with, *e.g.*, time-resolved small-angle scattering experiments [82] would be necessary to elucidate the possible migration of the proteins within the network.

4.5.3 Reversibility of Protein Adsorption

The discrimination between lysozyme^{FITC} and unlabelled lysozyme can be exploited to investigate the reversibility of protein adsorption into the charged CSM-10 particles. In case of reversible association, addition of unlabelled lysozyme to a solution of particles loaded with lysozyme^{FITC} should decrease the concentration of adsorbed lysozyme^{FITC} according to the molar ratio between lysozyme^{FITC} and untagged protein in the total volume, and vice versa. Figure 4.38 displays these exchange experiments. First, the microgel was loaded with lysozyme^{FITC} to a saturation of ~60 % and the adsorption was followed with time in analogy to Figure 4.36 (data not shown). Then an equimolar amount of unlabelled lysozyme was injected into this solution and the fluorescence intensity was monitored at 518 nm over 2 000 sec. Thus, the ratio between labelled and unlabelled protein was set to 1:1. As obvious from Figure 4.38 (blue data points), the fluorescence emission intensity is enhanced upon addition of unlabelled lysozyme, again in a process consisting of a fast and slow binding regime. Consequently, lysozyme^{FITC} is desorbed from the microgel particles and replaced by an equivalent amount of unlabelled lysozyme. The amount of exchanged lysozyme^{FITC} is ~46 %, that is, approximately half of the tagged lysozyme molecules have been released from the microgel. Hence, the tagged and the untagged molecules equilibrate on the network according to their molar ratios in the total volume.

Changing the order of adding labelled and unlabelled lysozyme has no influence on the final composition of the protein-enriched network: To prove this, a solution of unlabelled lysozyme was first mixed with a given quantity of CSM-10 particles and equilibrated for 30 min at room temperature. Then the solution was injected into a solution containing an equimolar amount of lysozyme^{FITC} and the fluorescence emission intensity was followed at 518 nm over 2 000 sec. Figure 4.38 (black data points) shows that the fluorescence signal is decreased and reaches the same plateau at the end of the experiment as for the reversed case. Thus, lysozyme^{FITC} binds to the microgel particles which are pre-loaded with unlabelled proteins. From the final fluorescence intensity it can be

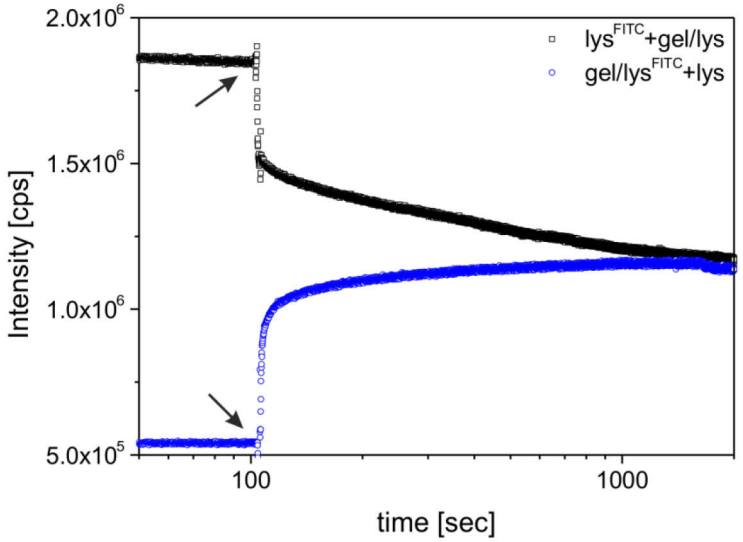

Figure 4.38: Time-dependent fluorescence intensity of 1.64 µM lysozyme^{FITC} before and after addition of 0.029 g L^{-1} CSM-10 particles loaded with an equimolar amount of unlabelled lysozyme (black data points). The blue data points display the reverse experiment: Here the fluorescence intensity of 0.029 g L^{-1} microgel particles loaded with lysozyme^{FITC} (1.64 µM bulk concentration) is measured after addition of an equimolar amount of unlabelled lysozyme. The arrows mark the moment of injection of the microgel/lysozyme suspension (black data points) and of the lysozyme solution (blue data points), respectively. All experiments were performed in 10 mM MOPS buffer *pH* 7.2 at 293 K.

calculated that about half of the binding sites which are occupied at these conditions are filled with tagged lysozyme^{FITC} at the end of the measurement. These experiments give clear evidence that adsorbed proteins are dynamically exchanged by proteins in solution. Moreover, the order of binding of tagged and untagged lysozyme to the microgel particles was found to be irrelevant for the equilibration of the system.

The exchange experiment was repeated for different ratios n(lysozyme)/n(lysozyme^{FITC}) (Figure 4.39). The microgel was first loaded with lysozyme^{FITC} and then different lysozyme concentrations (0.4-36.1 µM) were added to the dispersion (Figure 4.39 a). The initial fraction of binding sites occupied by lysozyme^{FITC} was $\Theta = 0.6$. The addition of unlabelled lysozyme increases the total protein concentration and shifts Θ(protein) and τ_{ads}(protein) to higher values. This was taken into account in the present analysis. The fraction of adsorbed lysozyme^{FITC} relative to the total amount of adsorbed protein after injection of untagged lysozyme is shown in Figure 4.39 b as a function of the total fraction of lysozyme^{FITC} in the volume. Good agreement between the measured and expected amounts of adsorbed proteins is found. Thus, the adsorption of lysozyme is reversible and the application of equilibrium binding models, such as the Langmuir isotherm is justified.

This result demonstrates the reversibility of protein adsorption. Moreover, it is shown that the equilibrium between adsorbed protein and proteins free in solution is settled within seconds. This is in concordance with the short residence time of lysozyme on the microgel chains of ~2 sec. Thus, protein bound to one “binding site” within the gel particle is readily exchanged by proteins in solution or by bound proteins in close proximity. Despite this short residence time of proteins on the microgel particles and the short equilibration time, complete desorption from the gel by removal of unbound

proteins will need much more time. Desorption of proteins with high binding affinities is strongly retarded due to the high rebinding probability and the small equilibrium concentration of free protein in solution [303], especially at higher $[M]_t$. This is observed in the UF experiment (Figure 4.36 b). Even prolonged flushing of the particles with buffer solution for ~10 h does not remove the protein, but the concentration found in the UF experiment coincides with the ones found by ITC and fluorescence spectroscopy.

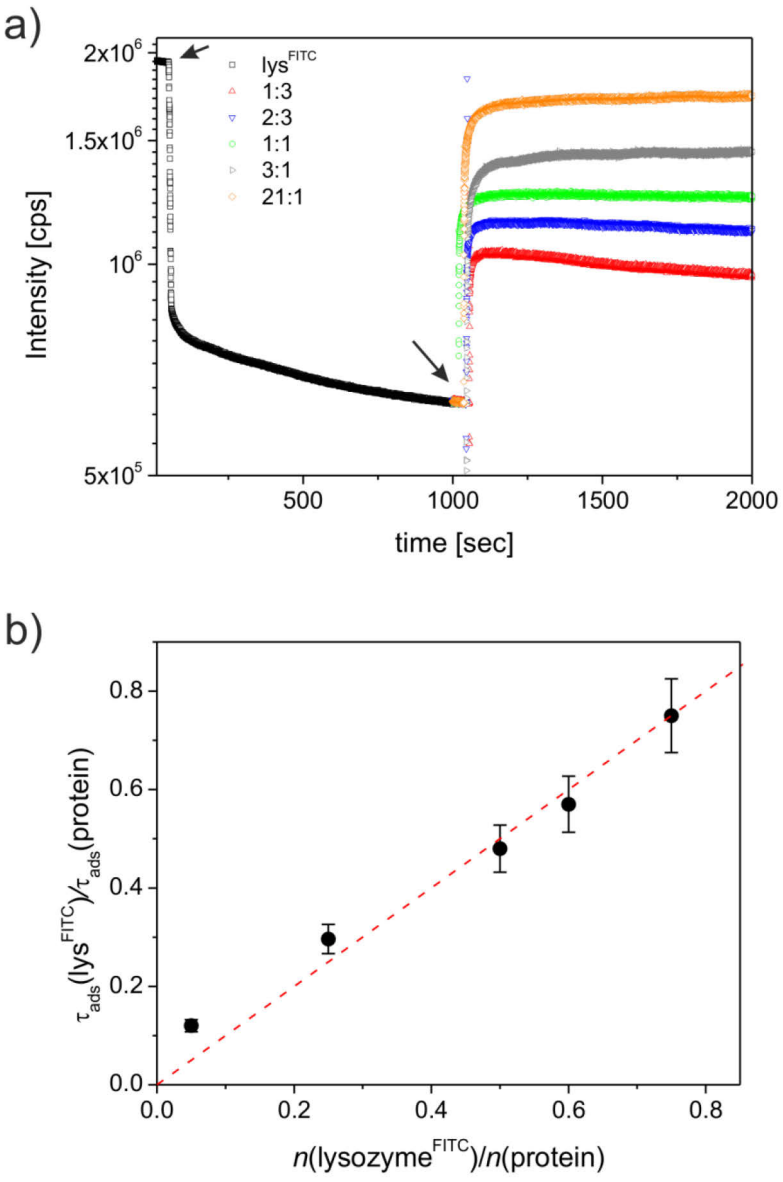

Figure 4.39: a) Time-dependence of the fluorescence intensity of lysozyme^{FITC} (1.64 µM bulk concentration) during adsorption onto the CSM-10 particles in absence of unlabelled lysozyme (black data points) in 10 mM MOPS buffer, *pH* 7.2 at 293K. The first arrow marks the moment at which 0.029 g L^{-1} microgel dispersion was injected into the protein solution. After 1 000 sec a solution of unlabelled lysozyme of different concentrations (0.4-36.1 µM) was added into the solution (second arrow) and the fluorescence intensity of lysozyme^{FITC} was recorded for another 1 000 sec (coloured data points). The legend assigns each data set to its ratio n(lysozyme)/n(lysozyme^{FITC}). b) Fraction of bound lysozyme^{FITC} as a function of the fraction of lysozyme^{FITC} in the volume. The values were calculated from the fluorescence intensity shown in a) at equilibrium of the exchange experiment.

4.5.4 Salt-triggered Release of Bound Lysozyme^{FITC}

In the previous section it was demonstrated that lysozyme strongly adsorbs to the microgel and that the binding process is reversible. Due to the slow desorption kinetics, protein depletion of the surrounding solution does not induce protein release for several hours. However, triggered release of the protein would be beneficial for many applications.

In section 4.4.1.2 it is shown by ITC that the amount and strength of protein binding can be adjusted by altering the salt concentration of the buffer solution. Thus, salt seems to be an appropriate trigger to detach proteins from the charged microgel. Therefore, lysozyme^{FITC} was adsorbed onto the microgel in a solution of low ionic strength (7 mM) by addition of 0.029 g L^{-1} CSM-10 to a solution of 1.64 µM

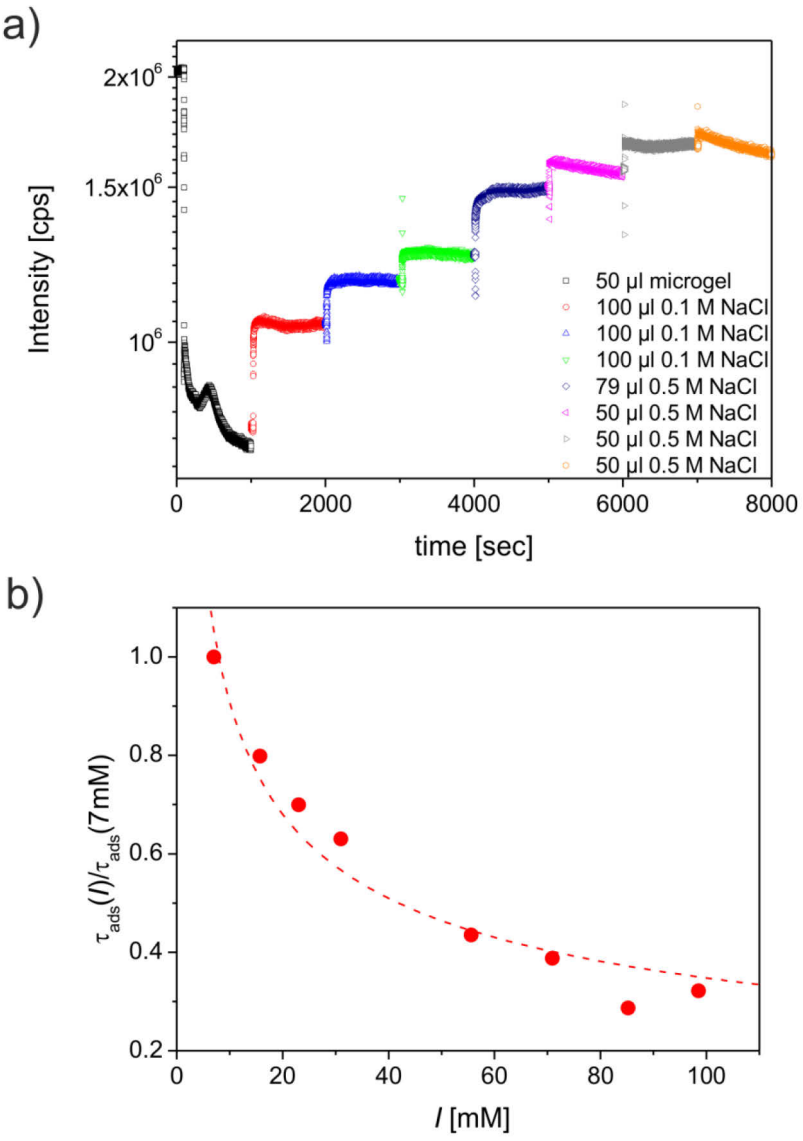

Figure 4.40: a) Time-dependent fluorescence intensity of lysozyme^{FITC} after addition of 0.029 g L^{-1} CSM-10 particles (black data points) and after consecutive addition of different amounts of NaCl solution (0.1-0.5 M). The legend assigns each data set to the volume and concentration of injected NaCl solution. The measurements were performed in 10 mM MOPS buffer *pH* 7.2 at 293 K. b) Normalised amount of bound lysozyme^{FITC} as a function of ionic strength (red data points). The dashed line serves as guide for the eye.

lysozyme^{FITC}. Protein desorption induced by consecutive addition of salt was then followed as a function of time (Figure 4.40 a). These measurements show that salt triggered release of the proteins is very fast and the equilibrium is reached within a few seconds. Figure 4.40 b displays the normalised amount of lysozyme^{FITC} which remains bound as a function of the ionic strength in 10 mM MOPS buffer *pH* 7.2 at 293 K. Binding of lysozyme^{FITC} is strongly reduced by addition of small amounts of monovalent salt due to the screening of the electrostatic interactions. The fraction of bound lysozyme^{FITC} levels off at higher ionic strength which demonstrates that also non-electrostatic interactions are involved in protein adsorption on charged CSM-10 particles. These results give further evidence of the reversibility of protein binding regardless of the ionic strength of the system used.

4.5.5 Conclusion

In this section the binding of lysozyme onto the three-dimensional charged network of the CSM-10 microgel has been characterised regarding its reversibility and kinetic mechanism. The *pH* value and the salt concentration within the network of these core-shell microgels are fully determined by the salt concentration outside the network and a full kinetic and thermodynamic analysis of protein adsorption could be performed. For this purpose lysozyme was labelled with the *pH*-sensitive fluorophore fluorescein to study the time evolution of protein uptake by the microgel as well as the exchange of proteins within the network. Thus, adsorption and release of lysozyme^{FITC} is followed by a change of the fluorescence intensity, respectively, which is mainly induced by the lowered local *pH* value inside the microgel. The experiments demonstrated that i) the adsorption is a true equilibrium process and its description in terms of a Langmuir isotherm is fully justified; ii) the binding strength is determined by the salt concentration and fast protein release is triggered by increasing the concentration of monovalent salt, and iii) the kinetics of protein adsorption is described as a two-step process in which the fast step is limited by diffusion towards the adsorption sites (time constant: ~0.6 sec). The second step is much slower (several hundred seconds) and is most probably related to a collective rearrangement of the proteins within the network.

4.6 Competitive Protein Adsorption

The experimental setup chosen for the investigation of the adsorption kinetics and the reversibility of binding can be further employed in competitive protein adsorption experiments. Because the binding affinities of the individual proteins will be one of the determining factors of the equilibrium composition of the protein corona, the analysis of the competitive adsorption process has to start from the thermodynamic investigation of single proteins. Then, the adsorption of proteins from mixtures can be analysed in the second step. In particular, the investigation of competitive binding from binary mixtures represents the simplest case of competitive protein adsorption. To study this process, lysozyme was tagged by FITC to distinguish lysozyme from the second protein used in the experiments. The time-dependent exchange of the fluorescence-labelled protein bound to the microgel network by the addition of the second protein was then followed by monitoring the fluorescence intensity as a function of time. It has to be emphasised that this process is different from the Vroman effect inasmuch the latter describes the competitive adsorption of proteins from the same solution.

Here the change of the amount of pre-adsorbed protein was analysed by the addition of a second protein in a subsequent step. At equilibrium, however, the composition of bound proteins should be the same regardless whether the proteins were adsorbed from the same solution or the proteins were added stepwise to the microgel particles. This is especially true for reversible protein adsorption where bound proteins are dynamically exchanged by proteins free in solution.

Cytochrome c and *β*-D-glucosidase, respectively, were chosen as the second protein which competes together with lysozyme for the binding sites of CSM-10. This is schematically shown in Figure 4.41. Cytochrome c and *β*-D-glucosidase strongly differ in their molecular weight and surface charge and, thus, are expected to compete with lysozyme for the binding sites of the microgel in very different ways. Cytochrome c has a similar molecular weight and isoelectric point compared to lysozyme. Moreover, both cytochrome c and lysozyme carry a net charge of about +7 near neutral solution. [187] Thus, it is expected that the microgel network offers cytochrome c and lysozyme the same number of binding sites where the binding affinities to these sites depend on the specific hydrophobic and electrostatic interactions of the protein surface. Moreover, adsorption of cytochrome c and lysozyme have the same influence on the electrostatic potential of the particle and, thus, on the shell volume of the microgel. Therefore the mixture of lysozyme and cytochrome c represents an ideal system to study the influence of the binding affinities of the individual proteins on the composition of the protein corona. In contrast, *β*-D-glucosidase has a molecular weight of 135 000 g mol^{-1} as homodimer and an isoelectric point of 4.4. Hence, *β*-D-glucosidase serves as an example for a much larger protein than lysozyme which binds to larger adsorption sites. Moreover, it is negatively charged at the adsorption conditions and the adsorption on the equally charged microgels takes place on the "wrong side" of the isoelectric point. [304]

In the first part of this section, the thermodynamics adsorption of cytochrome c and *β* -D-glucosidase onto CSM-10 is analysed in a solution of low salt concentration. Secondly, the competitive binding experiments were performed in a solution of low ionic strength and at one temperature. The equilibrium composition determined at the end of the experiment was then theoretically described by an appropriate competitive binding model.

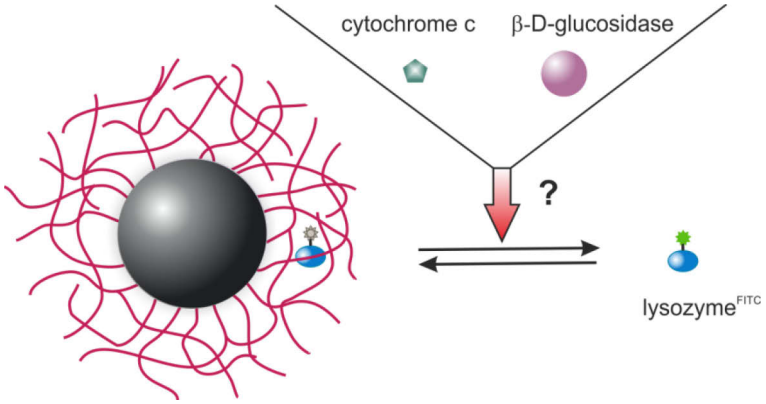

Figure 4.41: Schematic representation of the competitive adsorption between lysozyme^{FITC} and cytochrome c and *β*-D-glucosidase, respectively, onto the charged shell network of CSM-10. Cytochrome c has a molecular weight of ~12 300 g mol^{-1} and is positively charged at *pH* 7.2 while *β*–D-glucosidase has a molecular weight of ~135 000 g mol^{-1} as homo-dimer and is overall negatively charged at *pH* 7.2. Due to the distinct properties of both proteins they are expected to compete with lysozyme^{FITC} for the binding sites of CSM-10 very differently.

4.6.1 ITC Analysis of Protein Adsorption of Individual Proteins

In the first step, the binding affinity of cytochrome c and *β*-D-glucosidase were analysed separately. The thermodynamic binding parameters were obtained by ITC in 10 mM MOPS buffer *pH* 7.2 at 7 mM ionic strength. The ITC data for the cytochrome c adsorption are depicted in Figure 4.42 a (top). Analogously to the lysozyme adsorption data, the SSIS model was sufficient to achieve a good fit of the data (Figure 4.42 a, bottom). The thermodynamic parameters received for adsorption at 298 K are given in Table 4.8. The values of the parameters for cytochrome c binding for all temperatures investigated are listed in Table 7.6 of the supplement.

The adsorption of cytochrome c onto the charged microgel particles is found to be about 10-fold weaker than the adsorption of lysozyme, resulting in a binding constant of cytochrome c which is smaller than the K_b of lysozyme by a factor of ~10. The binding of cytochrome was further examined using the van´t Hoff analysis to calculate the binding enthalpy ΔH_b and entropy ΔS_b.

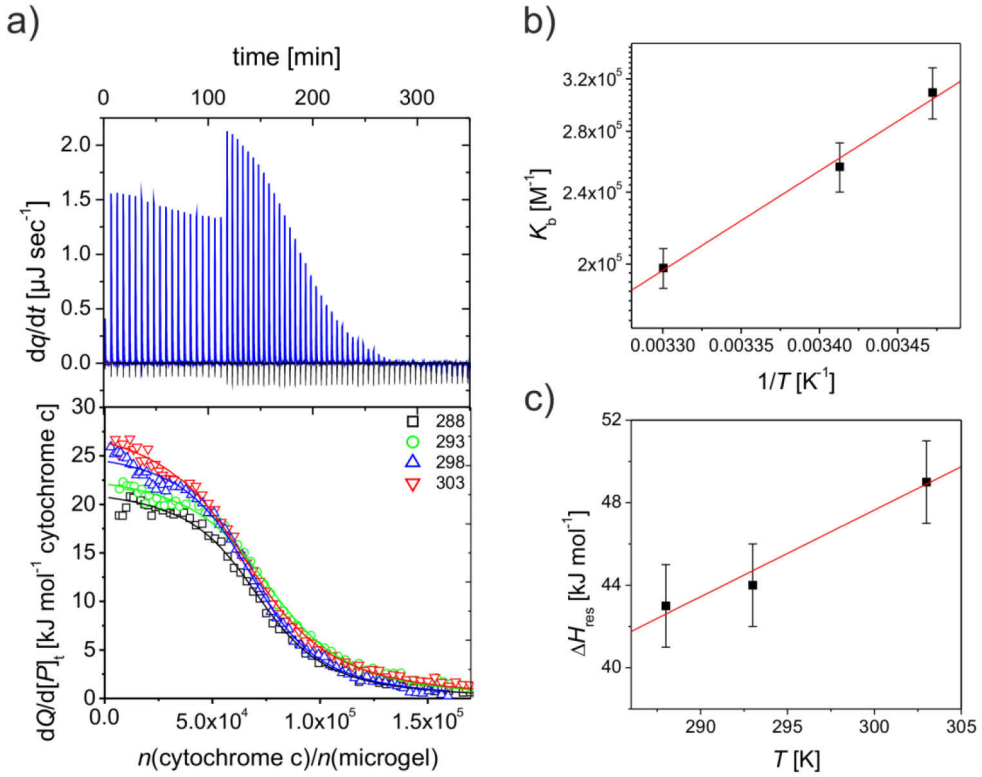

Figure 4.42: ITC data of the cytochrome c adsorption onto CSM-10 particles in 10 mM MOPS buffer *pH* 7.2 (7 mM ionic strength). The upper panel shows the raw ITC data obtained at 298 K with the black spikes as the heat of dilution of cytochrome c. The green spikes are the change of heat corresponding to each injection of cytochrome c into the microgel dispersion. The lower panel shows the integrated heats of each injection (open symbols) after subtraction of the dilution signal from the overall signal for different temperatures. The solid lines represent the fits to the data according to the SSIS model using equations (3.27) and (3.28). b) Van´t Hoff analysis of cytochrome c binding onto the microgel particles in 10 mM MOPS buffer *pH* 7.2. c) Plot of the residual enthalpy ΔH_{res} measured by ITC as a function of temperature. The solid line represents the linear fit to the experimental data points.

As shown in Figure 4.42 b, K_b depends on temperature, resulting in an exothermic ΔH_b and a positive change of the entropy ΔS_b, *i.e.*, $\Delta H_b < 0$ and $\Delta S_b > 0$ (Table 4.8). Thus, binding of cytochrome c to the CSM-10 particles is both driven by entropy and enthalpy. In contrast, the total heat ΔH_{ITC} measured by ITC for mixing of the protein with the microgel suspension is positive for the whole temperature range investigated. The discrepancy between ΔH_{ITC} and ΔH_b regarding the sign as well as the total value demonstrates that additional endothermic processes contribute to ΔH_{ITC} also in case of cytochrome c. In case of mixing of this protein with a suspension of CSM-10, these additional contributions dominate which leads to an overall endothermic heat signal ΔH_{ITC}.

Despite the similarity of lysozyme and cytochrome c regarding their molecular weight and net charge, the ITC analysis reveals large differences in the binding affinities as well as in ΔH_b and ΔS_b. For comparison, the thermodynamic parameters of the lysozyme adsorption are gathered in Table 4.8, too. Thus, in addition to the size and net charge, the charge distribution on the protein surface as well as specific interactions, such as hydrophobic binding, are decisive for the thermodynamics of adsorption. Cytochrome c is known to have an anisotropic charge distribution with a positively charged front face and a negatively charged back face while the charges of lysozyme are more homogeneously distributed on the protein surface (see section 3.2.1). This difference in the charge distribution may explain the distinct binding affinities of cytochrome c and lysozyme towards CSM-10 to some extent. Although large disparities were observed for K_b, ΔH_b and ΔS_b, the number of binding sites N calculated from the adsorption data of cytochrome c and lysozyme are found to be of comparable value. This result identifies the protein size as determinant factor for the value of N.

Table 4.8: Thermodynamic data of protein adsorption onto negatively charged microgel particles in 10 mM MOPS buffer *pH* 7.2 at 298 K determined by ITC.

protein	N_b	$N_b x M_w^{2/3}$ [g mol^{-1}]	K_b [M^{-1}]	ΔH_b [kJ mol^{-1}]	ΔS_b [kJ mol^{-1} K^{-1}]	ΔH_{ITC} [kJ mol^{-1}]	ΔC_p [kJ mol^{-1} K^{-1}]
lysozyme	60 100 ±190	3.5x10^7	(2.62 ±0.17)x10^6	22 ±3	0.194 ±0.009	60.7 ±0.3	1.54 ±0.22
cytochrome c	71 200 ±470	3.3x10^7	(3.06 ±0.18)x10^5	-22 ±2	0.032 ±0.006	25.7 ±0.2	0.42 ±0.05
β-D-glucosidase	12 500 ±120	3.8x10^7	(5.45 ±0.61)x10^6	13 ±9	0.170 ±0.030	103.7 ±1.3	-0.47±0.53

In contrast to lysozyme, *β*-D-glucosidase is negatively charged at the solution conditions chosen for the adsorption experiment. From the ITC analysis in 7 mM ionic strength MOPS buffer solution *pH* 7.2 it is clear that the enzyme binds to the equally charged microgel particles. Thus, *β*-D-glucosidase adsorbs to the microgel also on the "wrong side" of its isoelectric point. Figure 4.43 a depicts the raw ITC data acquired at 298 K as well as the integrated heats after correction for the dilution of the protein at temperatures ranging from 298 to 312 K. High protein uptakes on the wrong side of the isoelectric point were also observed for other systems including polyelectrolyte brushes [77,84], multi-layered films assembled by the layer-by-layer technique [305], and for the assembly of charged macromolecules in general [306]. This phenomenon was related to different mechanisms, such as counterion release [84] and charge regulation [222]. As shown from the ITC analysis of lysozyme adsorption (section 4.4), charge regulation occurs in CSM-10 as well and, thus, is

considered to reduce the electrostatic repulsion of equally charged proteins. In analogy to lysozyme binding, the interaction of *β*-D-glucosidase and the resulting binding curve is well described by the SSIS model. The thermodynamic parameters obtained from the fitting of the ITC data at 298 K are listed in Table 4.8 and for all temperatures in Table 7.5 of the supplement. Moreover, the van´t Hoff analysis of the temperature-dependence of K_b leads to a positive binding enthalpy with $\Delta H_b = (13 \pm 9)$ kJ mol^{-1} (Figure 4.43 b). The adsorption of *β*-D-glucosidase therefore is slightly endothermic and is determined to be entropy driven. As consequence of the small positive ΔH_b, the considerably high caloric heat ΔH_{ITC} is mainly ascribed to processes other than protein binding, resulting in a residual enthalpy of $\Delta H_{res} \approx 90$ kJ mol^{-1} for the temperature range investigated (Figure 4.43 c). Concluding this, the additional endothermic heat measured by ITC is a general phenomenon for mixing of proteins with charged microgels and seems to scale with the size of the protein interacting with the gel network.

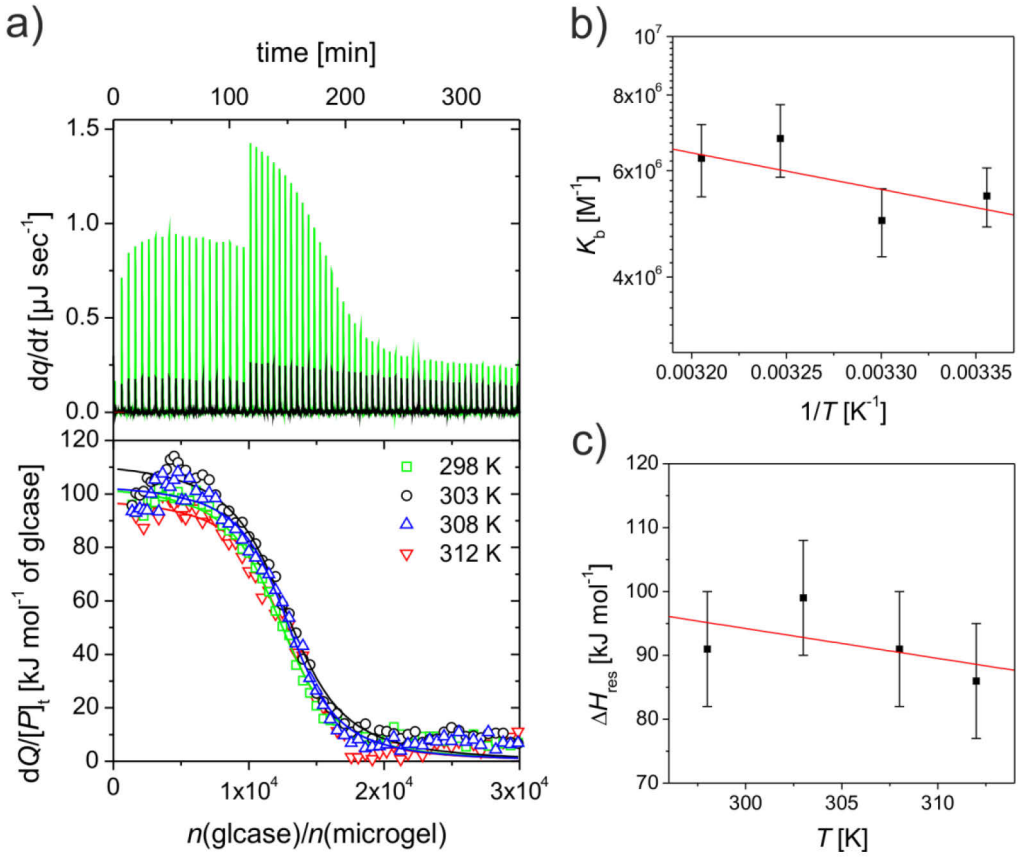

Figure 4.43: a) ITC data of *β*-D-glucosidase adsorption onto CSM-10 particles in 10 mM MOPS buffer *pH* 7.2 (7 mM ionic strength). The upper panel shows the raw ITC data obtained at 298 K with the black spikes as the heat of dilution of *β*-D-glucosidase. The green spikes are the change of heat corresponding to each injection of *β*-D-glucosidase into the microgel dispersion. The lower panel shows the integrated heats of each injection (open symbols) after subtraction of the dilution signal of the protein from the overall signal for different temperatures. The solid lines represent the fits according to the SSIS model using equations (3.27) and (3.28).b) Van´t Hoff analysis of lysozyme adsorption to the microgel particles in 10 mM MOPS buffer *pH* 7.2. c) Plot of the residual enthalpy ΔH_{res} measured by ITC as a function of temperature. The solid line represents the linear fit to the experimental data points.

The comparison of the adsorption of lysozyme and β-D-glucosidase indicates that larger proteins (*i.e.*, β-D-glucosidase) exhibit higher binding affinities than smaller proteins (*i.e.*, lysozyme) even though the larger ones have the same overall charge at bulk conditions. Additionally, the number of adsorption sites is much smaller in the case of the larger protein β-D-glucosidase. Thus, N seems to scale with $M_w^{2/3}$ in case of cytochrome c, lysozyme and β-D-glucosidase (*cf.* Table 4.8) which suggests that the number of sites is proportional to the total surface area of the protein.

4.6.2 Competitive Adsorption from Binary Protein Solutions

For the competitive adsorption experiments monitored by fluorescence spectroscopy, the microgel particles were first loaded with 1.64 µM lysozyme^{FITC} where the fraction of binding sites occupied by lysozyme^{FITC} Θ_X is calculated to be ~60 %. Then an equimolar amount of cytochrome c or β-D-glucosidase, respectively, was added to the mixture and the fluorescence intensity was monitored for 1 000 sec. From the change of the emission intensity, the remaining Θ_X and the amount of freed lysozyme^{FITC} can be calculated.

Figure 4.44 shows that the amount of desorbed lysozyme^{FITC} depends on the second protein which was injected into the solution. Thus, ~70 % and ~10 % of initially bound lysozyme^{FITC} was replaced by β-D-glucosidase and cytochrome c, respectively. The preferential binding of larger proteins is in good agreement with earlier observations related to competitive protein adsorption. [86,114,233] In contrast, the much higher binding affinity of lysozyme compared to cytochrome c explains that only a small fraction is exchanged by the latter protein. In the following, this system is treated quantitatively and compared to a simple theoretical model.

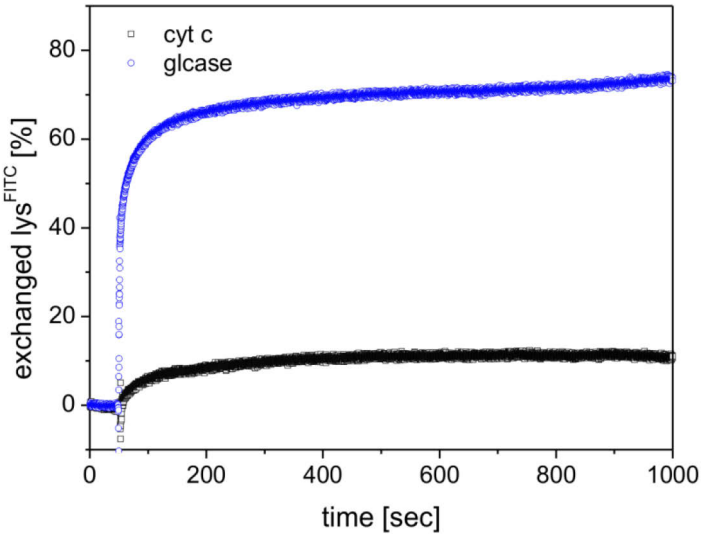

Figure 4.44: Competitive adsorption of lysozyme and cytochrome c and β-D-glucosidase onto the microgel CSM-10, respectively. The microgel particles were first injected into a solution of 1.64 µM lysozyme^{FITC} and equilibrated with the labelled protein. The amount of lysozyme^{FITC} desorbed from the microgel particles upon addition of an equimolar amount of cytochrome c and β-D-glucosidase, respectively, was measured as a function of time.

Exchange experiments were done for different molar ratios between cytochrome c and lysozyme^{FITC}. The microgel dispersion was injected into a solution of 1.64 µM lysozyme^{FITC} and the fluorescence intensity was monitored until equilibrium was reached. Then different concentrations of cytochrome c were added to this solution and the change of the fluorescence intensity was followed for 1 000 sec (Figure 4.45 a). The time-dependent fluorescence data show that the exchange of both proteins is very fast and that the equilibrium is settled after a few minutes. This is in concordance to the kinetic analysis of lysozyme adsorption on bare CSM-10 particles (compare section 4.5.2) where the final adsorption equilibrium is reached within several hundred seconds as well.

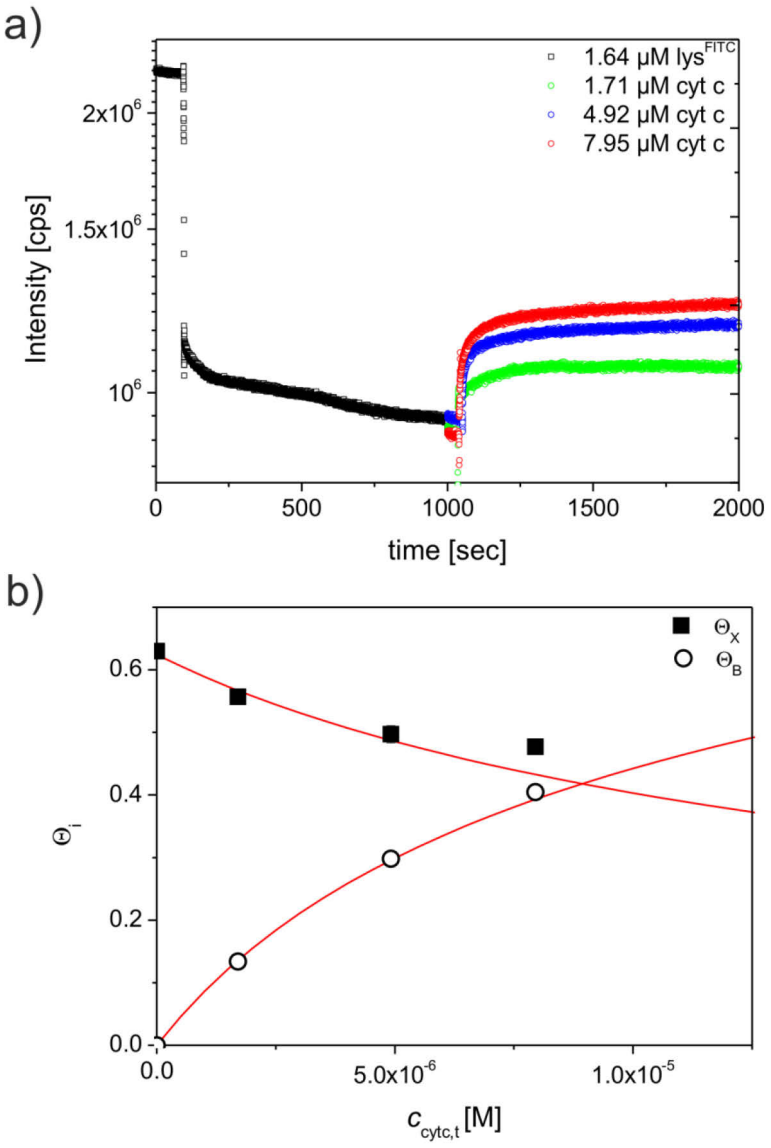

Figure 4.45: a) Time-dependent fluorescence intensity of 1.64 µM lysozyme^{FITC} after addition of 0.029 g L^{-1} CSM-10 particles (black data points) and after consecutive addition of different amounts of cytochrome c (coloured data points). The legend assigns each data set to the final concentration of cytochrome c in the total volume. The measurements were performed in 10 mM MOPS buffer *pH* 7.2 at 293 K. b) Fraction of binding sites occupied by lysozyme^{FITC} Θ_X and cytochrome c Θ_Y as a function of the total concentration of cytochrome c $c_{cytc,t}$. The values for Θ_Y were calculated using the experimental values of Θ_X and equation (3.22). The solid lines are the theoretical curves of Θ_X and Θ_Y which were predicted by equations (3.21) and (3.22).

In Figure 4.45 b the resulting values of Θ_X at equilibrium are plotted as a function of the total concentration of cytochrome c $c_{cytc,t}$. The foregoing analysis of single protein adsorption demonstrated that protein adsorption onto CSM-10 is reversible and that the protein conformation and function is not compromised by the adsorption to the polymer chains. Additionally, protein binding is well-described by the Langmuir isotherm. On the basis of these results it is consistent to use the competitive Langmuir isotherm (equation (3.21)) for the modelling of the competitive adsorption of lysozyme (*X*) and cytochrome c (*Y*) at equilibrium, *i.e.*, $\Theta_X(t = \infty)$ and $\Theta_Y(t = \infty)$. The competitive Langmuir isotherm gives the fraction of occupied binding sites of *X* and *Y* in a mixture of both proteins as a function of the adsorption constants $K_{b,X}$ and $K_{b,Y}$ which correspond to the ones in the single protein solutions. Thus, $K_{b,X}$ and $K_{b,Y}$ are the respective binding constants obtained from ITC experiments for the adsorption of the single protein. Moreover, equation (3.21) presumes that the number of binding sites *N* applies to both enzymes. In case of cytochrome c, N_Y = 71 200 which is comparable to N_X = 60 100 obtained for lysozyme (see Table 4.8). Thus, it is reasonable to assume that cytochrome c may replace one lysozyme molecule and a mean value for the number of adsorption sites of $N = N_X = N_Y$ = 65 600 is assumed.

Equation (3.21) can be rearranged to give a quadratic equation for $\Theta_X([P_X], [P_Y])$. The solution of this expression, given in equation (3.22), can be used to calculate the theoretical values for Θ_X and Θ_Y. For this calculation only the values of $K_{b,X}$, $K_{b,Y}$, and *N* have to be known. The theoretical predictions for Θ_X (lysozyme) and Θ_Y (cytochrome) are compared to the experiments in Figure 4.45 b. Obviously, the competitive Langmuir isotherm describes the experimental data points very well. Thus, there seems to be little mutual interaction of the two proteins (lysozyme and cytochrome c) in the network despite the dense packing within the gel. In essence, these experiments show that proteins with similar molecular weights adsorb to the same number of binding sites *N* even if the thermodynamic parameters K_b, ΔH_b, and ΔS_b exhibit large differences. If these proteins also carry the same net charge, the electrostatic potential of the charged microgel is modified by both proteins to the same extent and cooperative phenomena are less probable also at high packing densities.

The same set of experiments has been done for *β*-D-glucosidase. First lysozyme^{FITC} was equilibrated with the microgel particles. Then different total concentrations of *β*-D-glucosidase ($c_{glcase,t}$) were added and the fluorescence was monitored as a function of time as shown in Figure 4.46 a. Figure 4.46 b displays the resulting values of Θ_X as a function of $c_{glcase,t}$. The replacement of lysozyme by *β*-D-glucosidase is much more pronounced than in case of cytochrome c as expected for a larger protein. On the other hand, the value of N_Y for *β*-D-glucosidase is of the order of 12 000 and, hence, much smaller than the number of binding sites for lysozyme N_X. Hence, the competitive adsorption with lysozyme cannot be treated quantitatively in terms of the competitive Langmuir isotherm expressed in equation (3.21).

However, the present results can be understood qualitatively on the basis of the thermodynamic parameters gathered in Table 4.8: According to the adsorption experiments of single proteins, the binding affinity of *β*-D-glucosidase is larger than the one of lysozyme by a factor of 2. Moreover, by comparing the number of binding sites available for *β*-D-glucosidase and lysozyme it can be further concluded that *β*-D-glucosidase may replace approximately 5 molecules of lysozyme. This leads to a significant increase of entropy and is one reason for the preferential adsorption of larger proteins. Moreover, cooperative phenomena also need to be taken into consideration in case of the competing adsorption of lysozyme and *β*-D-glucosidase. Both proteins have different net charges which modulate

the electrostatic potential of the microgel network: β-D-glucosidase carries a net negative charge while lysozyme and cytochrome c have an overall positive charge. Hence, the latter proteins are attracted to the negatively charged microgels. β-D-glucosidase, on the other hand, has an electrostatic penalty when bound to the network, unless the electrostatic potential of CSM-10 causes charge reversal of the enzyme. In case of competitive adsorption, the electrostatic repulsion of β-D-glucosidase is reduced by the presence of lysozyme since lysozyme decreases the negative potential of the microgel. This leads to a stronger adsorption of β-D-glucosidase. Thus, the exchange of lysozyme by β-D-glucosidase is

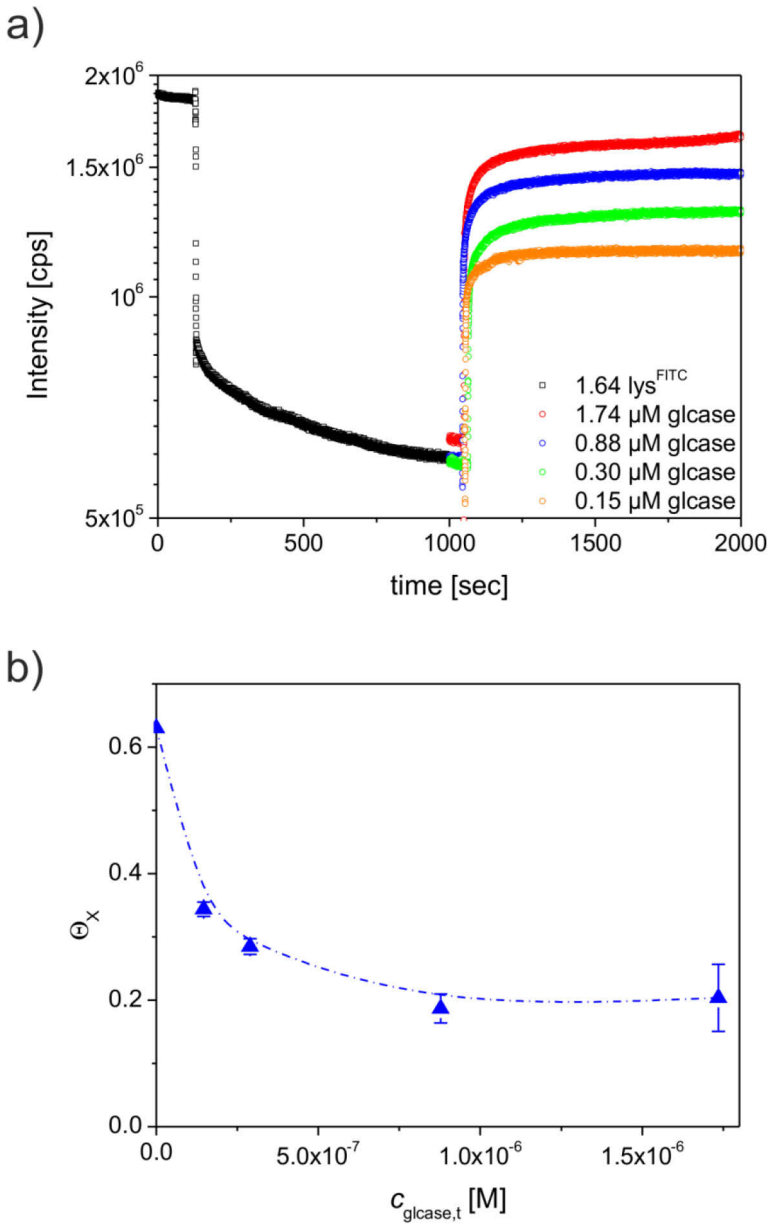

Figure 4.46: a) Time-dependent fluorescence intensity of lysozyme^{FITC} after addition of 0.029 g L^{-1} CSM-10 particles (black data points) and after consecutive addition of different amounts of β-D-glucosidase (coloured data points). The legend assigns each data set to the final concentration of β-D-glucosidase in the total volume. The measurements were performed in 10 mM MOPS buffer *pH* 7.2 at 293 K. b) Competitive adsorption of lysozyme^{FITC} and β-D-glucosidase. Dependence of the fraction of binding sites occupied by lysozyme^{FITC} Θ_X on the concentration of β-D-glucosidase $c_{glcase,t}$. The dashed lines serve as a guide for the eye.

even more pronounced than expected from the binding constants, determined from single protein solutions and the entropic gain caused by the release of lysozyme.

4.6.3 Conclusion

The competitive adsorption of lysozyme with β-D-glucosidase and cytochrome c, respectively, on the charged CSM-10 particles was analysed using fluorescence spectroscopy. In case of using cytochrome c as competing protein, the resulting equilibrium state was successfully modelled in terms of a competitive Langmuir isotherm using the adsorption constants of the single proteins determined from ITC. Competitive binding of β-D-glucosidase represents a more complicated process due to the larger dimensions and the opposite charge compared to lysozyme. However, the binding affinity of β-D-glucosidase obtained from the single protein analysis nevertheless leads to a qualitatively correct prediction of the preferential adsorption of this protein. Hence, it was demonstrated that the thermodynamic factors leading to competitive protein adsorption can be quantitatively modelled for a well-controlled polymeric surface.

5 Summary and Outlook

The focus of this thesis was aimed at the investigation of protein adsorption on well-defined core-shell microgels which respond differently towards changes of the temperature, *pH* and salt concentration of the solution. The microgel particles employed in this work have dimensions ranging between 100 and 200 nm and offer high surface areas for the interaction with proteins. The adsorption studies were systematically performed using three different proteins, that is, *β*-D-glucosidase from *almonds*, lysozyme from *chicken egg white* and cytochrome c from *bovine heart*:

- First, the adsorption of proteins to uncharged microgels has been analysed in detail. These particles are responsive with respect to temperature and undergo a volume phase transition at ~32 °C from a swollen and hydrophilic state to a shrunken and more hydrophobic state. Binding experiments with *β*-D-glucosidase revealed high loading capacities of the uncharged microgel shell even for large proteins. The Langmuir isotherm was well-suited to describe the adsorption to thermo-sensitive microgels. A systematic study of the thermodynamics of binding by isothermal titration calorimetry at varying temperatures demonstrated a strong influence of the microgel volume on the thermodynamic parameters and indicated that hydrophobic interactions are the main driving forces of this process. Investigations of the secondary structure by FT-IR spectroscopy as well as of the catalytic activity showed that the native protein structure was largely retained after immobilisation to the particle. Moreover, an enhanced activity of bound *β*-D-glucosidase was recorded where the activity of the immobilised enzyme exceeded the one of the free enzyme by a factor of ~3. This finding could be ascribed to the formation of hydrogen bonds to the microgel network as detected by FT-IR spectroscopy. In addition, temperature-dependent measurements pointed to the modification of the catalytic activity of immobilised *β*-D-glucosidase by the volume phase transition of the gel network. These results show that soft polymeric layers attached to particles are well-suited to bind proteins and enzymes with retention of the native structure and even enhanced catalytic activity. This is particularly important for the use of colloidal systems in biomedical as well as in catalytic applications.
- The second part of this thesis was devoted to protein adsorption onto negatively-charged microgels which primarily respond to changes of the ionic strength and the *pH* value of the system. The Langmuir isotherm was again suitable to describe the protein adsorption data indicating that proteins bind to one kind of binding sites without mutual interactions of the bound proteins. The studies with lysozyme demonstrated that these particles interact with the proteins via electrostatic forces in addition to hydrophobic interactions as determined by the ITC analysis at varying ionic strengths. Moreover, the dynamic light scattering data of the microgels in presence of lysozyme indicated network tightening due to the hydrophobic interactions between the proteins and the gel network. A systematic investigation of the thermodynamics gave clear evidence for protonation of the bound lysozyme. The latter was induced by the lowered *pH* value within the microgel particles. To supplement this analysis the kinetic constants of bound enzymes were determined in terms of Michaelis-Menten kinetics. Here a ~3.5 times higher activity of the enzyme in the adsorbed state has been noted compared to the one of the free enzyme. This result

conforms to the microgel-induced change of the protonation state. From the secondary structure analysis it could be concluded that the protein conformation was not perturbed. These results prove that the microenvironment of a colloidal particle may be drastically altered from the bulk solution. Changes of the local microenvironment, *e.g.*, a lowered local *pH* value, have enormous importance for many applications of colloidal particles, such as for the design of drug delivery systems with triggered release of the drug, and need to be considered for future applications.

- In a next step lysozyme has been tagged with a *pH* sensitive fluorophore to analyse the kinetic uptake of proteins on negatively charged microgels. Upon binding to the network, the fluorescence of the labelled proteins is switched off, mainly due to a lowered *pH* value within the microgel. Using this strategy it was possible to detect the binding of lysozyme as a function of time. The kinetic mechanism of protein adsorption could be proposed by combining the experimental data with the kinetic Langmuir model: Adsorption onto microgels is divided into two steps, a fast binding regime and a subsequent second slow binding regime. The first step is determined by the diffusion of proteins onto the outer boundary of the particle followed by the internal motion of proteins to the distinct binding sites within the network. The slow regime is affiliated by the rearrangement of the proteins within the network as consequence of the decrease of the microgel volume which is induced by the adsorbing proteins. The first binding regime has a characteristic time constant of ~0.6 sec, while the second binding step lasts over a few hundred seconds. Remarkably, already about 90 % of the proteins bind to the gel network within the fast binding regime. This demonstrates that soft polymeric layers exposed to biological media are immediately covered by proteins.
- The same analytical method was suitable to figure out whether proteins are reversibly or irreversibly bound to the microgel network. The dynamics of protein binding to the microgel was investigated using fluorescence spectroscopy and a combination of fluorescence-labelled and untreated lysozyme. The analysis of the fluorescence intensity as a function of time gave clear evidence for a fast settling equilibrium between bound proteins and those free in solution, justifying the application of equilibrium binding models, *e.g.*, the Langmuir model, to the binding experiments. Moreover, the reversible protein binding onto these microgels demonstrates that this class of systems is generally suitable for protein purification and other biotechnological fields.
- Finally, the investigation of protein adsorption was extended to binary protein mixtures of lysozyme. Time-resolved fluorescence spectroscopy was applied to follow the displacement of bound lysozyme by the addition of cytochrome c or β-D-glucosidase as competing protein. The combination of experimental findings and theoretical considerations allows in-depth investigation of the competitive adsorption process. Within the work of this thesis a simple theoretical model - based on the competitive Langmuir isotherm and on the thermodynamic parameters of single protein adsorption - could be developed which predicts the composition of the protein corona on the microgel particles at equilibrium.

In conclusion, this thesis provides a deeper insight into the adsorption mechanism of proteins on colloidal microgel particles. In particular, several analytical methods have been established to identify the thermodynamic driving forces and to elucidate the kinetics of protein binding. Moreover, an important contribution to a more complete understanding of protein adsorption from protein mixtures is made which is essential for many applications, *e.g.*, nanomedicine, affinity chromatography, and other biotechnological fields.

6 Materials and Experimental Procedures

6.1 Materials

6.1.1 Chemicals

The monomers acrylic acid (AAc), N-isopropylacrylamide (NiPAm) and styrene, the cross-linker N,N-methylenebisacryalamide (BIS) and the initiator potassium peroxodisulfate (KPS) were purchased from Sigma-Aldrich (Schnelldorf, Germany). Styrene was destabilised for polymerisation by flushing over a column filled with inhibitor remover (replacement packing, for removing tert-butyl catechol, Sigma Aldrich). AAc was distilled under reduced pressure (1 mbar, 40-45 °C) prior to use to remove the stabiliser hydroquinone monomethylether. NiPAm, BIS, and KPS were used as received. The buffer components 3-(N-morpholino)propane sulfonic acid (MOPS) and sodium azide (NaN_3) were received from Sigma-Aldrich, while 1,4-piperazinediethanesulfonic acid disodium salt (PIPES) was provided by AppliChem (Darmstadt, Germany). For the enzymatic activity tests, the fluorescent compound 4-methylumbelliferone (MeU), the model substrate 4-methylumbelliferyl-β-D-N,N´,N´´-triacetylchitotrioside ($(GlcNAc)_3$-MeU), the yellow compound ortho-nitrophenol and the model substrate ortho-nitrophenyl-β-D-glucopyranoside (*o*-NPG) were purchased from Sigma-Aldrich. For the protein labelling experiments fluorescein isothiocyanate (FITC) isomer 1 was obtained from Serva (Heidelberg, Germany). All other chemicals were purchased from Sigma-Aldrich, Merck (Darmstadt, Germany), VWR (Darmstadt, Germany) or Roth (Karlsruhe, Germany) and were used without further purification. Water for all purposes was purified using reverse osmosis (Millipore Milli-Q) and was deionised preliminarily (Millipore Milli-Q).

6.1.2 Proteins and Buffer Systems

In this work, three different proteins, namely β-D-glucosidase, lysozyme and cytochrome c, were used to study the interactions with the core-shell microgels. Details regarding, *e.g.*, the supplier and origin of the proteins are listed in Table 6.1.

Table 6.1: Overview of the proteins used for the binding studies.

Protein	Origin	Supplier	Cat.-No.	LOT.-No.	Purity[a]
β-D-glucosidase	almonds	Sigma-Aldrich	G0395	058K4066 108K4118	5.20 units/mg solid 2.52 units/mg solid
lysozyme	chicken egg white	Calbiochem (Merck)	4403	D00077070	>23 500/mg solid
cytochrome c	bovine heart	Fluka (Sigma-Aldrich)	30398	STBB0476	100 %

[a] regarding contamination by other proteins.

All proteins were received as lyophilised powders with low content of additional salt or other impurities. These proteins were used in the adsorption studies without further purification.
All studies regarding the characterisation of the microgel particles as well as the interactions between the core-shell microgels and the proteins were performed in buffered solutions. Two buffer systems were used with this regard: 10 mM MOPS buffer *pH* 7.2 and 5 mM PIPES buffer *pH 7.2*. The buffer solutions were prepared by dissolving 50 mmol MOPS and 25 mmol PIPES, respectively, in a 5 L volumetric flask. The *pH* value of the solution was adjusted by addition of 1 M NaOH to *pH* = 7.2. Additionally, 2 mM of NaN_3 were added to the buffer solutions to avoid microbial growth. The thus prepared buffers are characterised by an ionic strength of 7 mM. For the experiments which require higher salt concentrations the ionic strength of the solutions was increased by adding an appropriate amount of NaCl.

6.2 Synthesis and Purification of the Core-Shell Microgels

6.2.1 Synthesis of the Polystyrene (PS) Core

The synthesis of the PS core via emulsion polymerisation was carried out using a 2 L three-necked flask equipped with a stirrer, reflux condenser, and thermometer. The emulsifier SDS (1.83 g) and the comonomer NiPAm (10.87 g) were dissolved in 700 g of water while stirring at 300 rpm and the solution was degassed by repeated evacuation and flushing with nitrogen. After addition of freshly destabilised styrene (200.07 g) the solution was heated to 80 °C under a nitrogen atmosphere. The reaction was started by addition of the initiator KPS (0.392 g dissolved in 16 mL of water). After 8 h of stirring at 80 °C the latex was allowed to cool to room temperature and filtered through glass wool afterwards to remove traces of coagulum. The core particles were purified by serum replacement (ultrafiltration, see section 6.2.3) against water for approximately two weeks.

6.2.2 Synthesis of the Microgel Shell

The shell of the microgel CSM-0 and CSM-10, respectively, was polymerised onto the PS core latex according to the following procedure:
The seeded emulsion polymerisation of the core-shell microgel was done in a 2 L three-necked flask equipped with a stirrer, reflux condenser and thermometer. Given amounts of the PS core latex (*cf.* Table 6.2) were diluted with water to a concentration of ~2.7 wt-%. After addition of the main monomer NiPAm and the cross-linker BIS the mixture was degassed by repeated evacuation and flushing with nitrogen. The amounts of the educts used for the synthesis of these particles are gathered in Table 6.2. The mixture was heated to 80 °C under nitrogen atmosphere while stirring at 200 rpm. In case of the synthesis of CSM-10, AAc was added at this point. Then the reaction was initiated by addition of an aqueous solution of KPS and the reaction was allowed to stir for another 5 h at the given temperature. After this time the dispersion was allowed to cool to room temperature and filtered through glass wool afterwards.
In case of the double-shell microgel CSM-0-2 the synthesis of the two shells was carried out in a batch reaction. The first shell was prepared along the lines given for the synthesis of CSM-0 and CSM-10.

However, the reaction time was reduced from 5 to 4 h. After this time, the monomers for the synthesis of the second shell as well as a second portion of KPS were added and the reaction was allowed to proceed at 80 °C under nitrogen atmosphere for another 6 h. After this time, the latex was allowed to cool to room temperature and filtered through glass wool afterwards. The core-shell microgel particles thus prepared were purified by exhaustive ultrafiltration (see section 6.2.3) against water for approximately four weeks.

Table 6.2: Weighed portions of the educts used for the synthesis of the core-shell microgels used in this study.

	CSM-0	**CSM-0-2**	**CSM-10**
m(PS core) [g]	131.2 of 14.73 wt-%	137.6 of 10.03 wt-%	76.2 of 13.11 wt-%
m(H_2O) [g]	592.1	423.5	281.3
m(KPS) [g]	0.504 (in 20.3 g H_2O)	1. shell: 0.121 (in 15.0 g H_2O) 2. shell: 0.422 (in 10.0 g H_2O)	0.226 (in 20.1 g H_2O)
m(NiPAm) [g]	23.8	1. shell: 5.70 2. shell: 20.00	10.0
m(BIS) [g]	1.62	1. shell: 0.12 2. shell: 0.41	0.68
m(AAc) [g]	0	1. shell: 0 2. shell: 0.32	0.64

6.2.3 Purification of the Particles

The ultrafiltration of the PS core as well as of the core-shell microgels was carried out in 0.75 L serum replacement cells as schematically shown in Figure 6.1. The cells contain membranes based on cellulose nitrate (Schleicher & Schuell and Millipore) with pore sizes of 50 or 100 nm. Using this technique, dissolved polymers, unreacted monomers, as well as surfactant molecules can be removed from the polymer dispersion. For the purification of the PS core membranes having pores of 50 nm were chosen while the core-shell microgels were purified using membranes of 100 nm pore size.
The cells were filled with about 500 mL of the polymer dispersion with concentrations ranging from 2.0 to 5.0 wt-%. Serum replacement against Milli-Q water was carried out at an overpressure of nitrogen of 1.2 bar. The progress of the purification process was monitored by measuring the conductivity of the replaced serum at different times and the ultrafiltration was stopped as soon as the conductivity of the serum had approached the conductivity of pure water ($\kappa < 0.5$ µS cm^{-1}). Generally, for this purification process about 15 to 36 L of water was consumed.
Using the ultrafiltration technique for purification of the core-shell microgels allows one to estimate the molecular weight of the gel particles $M_{w,microgel}$. Therefore, the mass of NiPAm, BIS, and AAc which was not polymerised into the microgel shell is determined from the mass balance of the microgel dispersion before and after purification. From this, the mass fraction of the core w_{core}

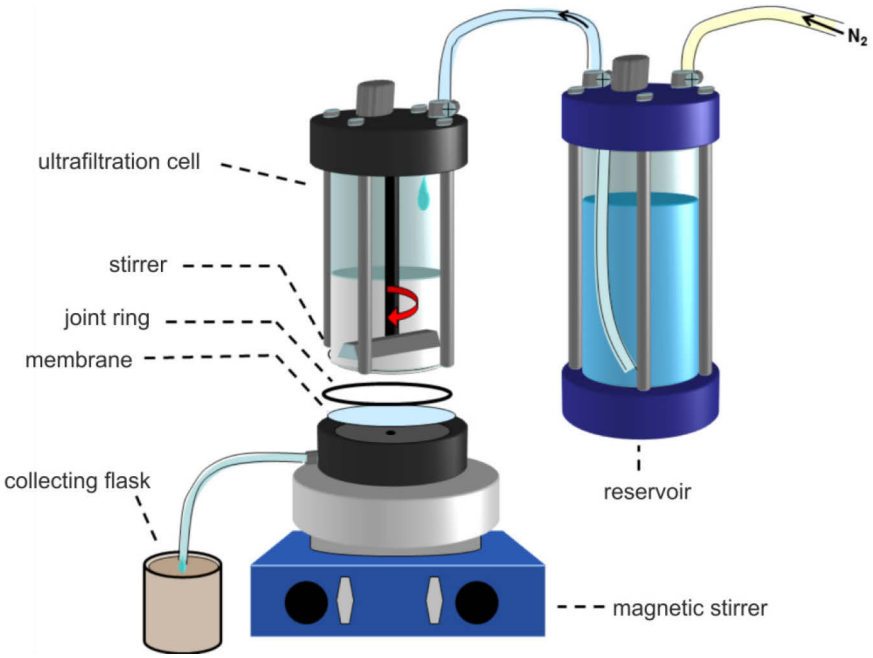

Figure 6.1: Sketch of an ultrafiltration cell used for the purification of the microgel dispersions and for the protein adsorption experiments.

can be calculated via $w_{core} = m_{core}/(m_{shell} + m_{core})$, where m_{shell} is the mass of the microgel shell per particle and m_{core} is the mass of the PS core. The latter is defined by $m_{core} = 4/3\pi\rho_{core}R_{h,core}^3$ with ρ_{core} as the density of PS (ρ_{core} = 1.055x10^{-21} g nm^{-3}) and $R_{h,core}$ as the hydrodynamic radius of the PS core determined by DLS. The molar mass $M_{w,microgel}$ is then given by

$$M_{w,microgel} = (m_{core} + m_{shell})N_A = \frac{\rho_{core}\frac{4}{3}\pi R_{h,core}^3}{w_{core}}N_A \quad (6.1)$$

The respective values of the core-shell microgels are gathered in Table 6.3.

The UF method was also used to adjust the concentration of the polymer dispersions. Moreover, it was applied for the solvent exchange of the core-shell microgels from water to buffer solution of given ionic strength. The replacement of the serum by eight times the volume of the sample volume was generally sufficient to adjust the buffer concentration. After this, the microgel particles were subjected to the protein binding studies.

Table 6.3: Calculated mass fractions of the PS core w_{core} and molecular weights $M_{w,microgel}$ of the core-shell microgels CSM-0, CSM-0-2, and CSM-10.

Microgel	w_{core}	$M_{w,microgel}$ [g mol^{-1}]
CSM-0	0.45	1.42x10^9
CSM-0-2	0.39	5.22x10^8
CSM-10	0.54	1.18x10^9

6.3 Characterisation of the Core-Shell Microgels

6.3.1 Dynamic Light Scattering (DLS)

The hydrodynamic radius of the microgel particles was determined using dynamic light scattering. DLS measures fluctuations of the scattering intensity of highly diluted samples. The intensity fluctuations are related to the Brownian motion of the particles since the interference of the scattered light waves depends on the positions of the particles relative to each other. In thermal equilibrium, smaller particles show higher rate constants of diffusion then larger ones. By analysing the field autocorrelation function and the relaxation rate, respectively, the diffusion coefficient of the particles is obtained. [307] For analysing the time-dependent intensity fluctuations, high sensitive detection systems, such as photomultipliers, are required to resolve the incoming intensity at short times.
The DLS measurements were performed using either a Peters-ALV goniometer setup or a Zetasizer Nano ZS instrument (ZEN 3500, Malvern Instruments, Herrenberg, Germany). Measurements performed with both instruments show that these instruments are equally good to analyse the size of spherical microgel particles of narrow size distribution. The Peters-ALV instrument is equipped with a 50 mV He-Ne laser (λ = 632.8 nm), focusing lenses, a measuring cell, and an ALV-500 correlator and is suitable for measuring samples having sizes in the range between 1 nm and 1 µm. The temperature of the samples was adjusted using a tempered bath containing toluene as index matching substance. All experiments with this apparatus were done at a scattering angle of 90°. The Zetasizer Nano ZS instrument consists of a 532 nm laser and can be used for the analysis of particle sizes ranging from 0.6 nm and 6 µm. In this case the scattering experiments were performed at a scattering angle of 173°.
For the analysis of the microgels dispersed in protein free buffer solution, the microgels were diluted to a concentration of $5\text{x}10^{-2}$ g L^{-1} using the respective buffer solution. Perturbation of the measurement by the presence of dust particles was avoided by filtering the buffer solution through a syringe filter (0.2 µm pore width, polyethersulfone, VWR). To study the influence of protein adsorption on the microgel size, a microgel dispersion of 0.1 wt-% was mixed with the respective protein solution to a given molar ratio *n*(protein)/*n*(microgel) and incubated for 30 min. Afterwards the microgel/protein mixture was diluted to the concentration of $5\text{x}10^{-2}$ g L^{-1} required for the DLS analysis. The DLS experiments were executed at temperatures between 283 and 333 K. Before running the experiment, the microgel dispersion was incubated at the desired temperature for 20 min to attain thermal equilibration. For each sample and temperature, a set of 3 measurements was performed each consisting of 10 single runs. The measured intensity correlation functions were analysed using the methods of cumulants which provides the *z*-averaged translational diffusion coefficient <*D*>. [308] The hydrodynamic radius is obtained from the diffusion coefficient using the Stokes-Einstein equation which reads: [81]

$$\langle D \rangle = \frac{k_\mathrm{B} T}{6\pi\eta R_\mathrm{h}} \tag{6.2}$$

where k_B is the Boltzmann constant, T is the absolute temperature, and η is the viscosity of the solution.

6.3.2 ζ-Potential Measurements

The electrophoretic mobility μ_E of the microgels was determined using a Zetasizer Nano ZS instrument (ZEN 3500, Malvern Instruments, Herrenberg, Germany). The measurements were performed under a scattering angle of 17° at 298 K with folded capillary cells (Malvern Instruments). Before using the cells for the experiment, the inner part of the cells was carefully rinsed with ethanol, water, and subsequently with the buffer solution, which was used to dilute the microgel particles, several times. For the sample preparation, the concentration of the microgel particles was adjusted to a concentration of 0.001 wt-% by immersing the microgel into the respective buffer solution. The microgel dispersion and the cells were allowed to equilibrate to the required temperature for 10 minutes. For each sample a series of 5 measurements was performed each consisting of 20-25 single runs. Therein, the determination of the electrophoretic mobility by this apparatus is based on the combination of the laser doppler velocimetry method and phase analysis light scattering.
The ζ-potential of spherical particles is directly correlated to μ_E via the Henry equation which reads:

$$\mu_E = \frac{v}{E} = \frac{2\varepsilon_r \varepsilon_0 \zeta}{3\eta} f_1(\kappa a) \tag{6.3}$$

where v is the particle velocity in presence of the electric field E, ε_r and ε_0 is the dielectric constant of the solvent and vacuum, respectively, η is the viscosity of the solution, and $f_1(\kappa a)$ is the Henry formula with κ as reciprocal Debye screening length, and a as particle radius. The Henry formula depends on the ionic strength of the solution as well as on the particle radius and is expressed by the following equation:

$$f_1(\kappa a) = 1 + \left\{2 + \left[1 + 2.5\left(\left(1 + 2\exp(-\kappa a)\right)\kappa a\right)^{-1}\right]^3\right\}^{-1} \tag{6.4}$$

For systems which are described by κa >>1 the Smoluchowski approximation can be used which sets the Henry formula to 1.5. Although this approximation is valid for the microgel systems, the ζ-potential of the microgels studied was calculated using the exact definition given by equation (6.4) with a set to R_h.

6.3.3 Conductometric and Potentiometric Titration

Simultaneous conductometric and potentiometric measurements were performed using the 809 Titrando system (Metrohm Ion analysis, Herisau, Switzerland) equipped with an external dosing device (807 Dosing Unit, Metrohm Ion analysis), a stirrer (801 Stirrer, Metrohm Ion analysis), *pH* electrode (*pH* 0-14, Metrohm Ion analysis), and a conductivity module (856 Conductivity Module, Metrohm Ion analysis). The Titrando system was controlled by the tiamo 2.0 software (Metrohm Ion analysis). For the titration experiment, the microgel dispersion was diluted with water to a total concentration of 0.5 wt-%. in case of CSM-10 and of 1 wt-% in case of CSM-0-2. Then, 20 mL of the microgel suspension were titrated with 0.01 M NaOH. The titrations were run in a thoroughly cleaned 50 mL beaker fitted with the *pH* and the conductivity electrode. The NaOH solution was slowly added to the microgel dispersion (0.1 mL min^{-1} for the titration of CSM-10 and 0.05 mL min^{-1} for the titration

of CSM-0-2), because the relaxation time required for attaining equilibrium between the aqueous and gel phase is considerably longer than for the corresponding low molecular weight acid. [309-310]
The potentiometric and conductometric titration curve of CSM-10 are shown in Figure 4.3 a. From the equivalent point of both titration curves the amount of acrylic acid polymerised into the microgel particles is determined. Additionally, the dissociation degree α_{diss} of the carboxylic acid functional groups can be calculated as a function of the amount of added NaOH and, thus, as a function of the *pH* according to [309]

$$\alpha_{\mathrm{diss}} = \frac{[V]_{\mathrm{pH}}}{[V]_{\mathrm{eq}}} \tag{6.5}$$

where $[V]_{\mathrm{pH}}$ and $[V]_{\mathrm{eq}}$ is the volume of added NaOH at a given *pH* value and at the equivalent point, respectively. To calculate the apparent pK_{a} value of the carboxylic acid functional groups as a function of the dissociation degree, the following equation is used: [310]

$$pK_{\mathrm{a}} = pH - \log\left(\frac{\alpha_{\mathrm{diss}}}{1-\alpha_{\mathrm{diss}}}\right) \tag{6.6}$$

6.3.4 Electron Microscopy

6.3.4.1 Field Emission Scanning Electron Microscopy (FE-SEM)

The FE-SEM micrographs were acquired using a LEO gemini microscope (LEO 1530, Zeiss, Germany) equipped with a field emission cathode. The electron high tension was set to 3 keV. The PS core latex was diluted to a concentration of 0.01 wt-% and put on a cleaned silica wafer. After drying at room temperature the silica wafer was fixed by using an aluminium foil. In order to provide for electric conductivity a platinum layer of 0.9 nm thickness was sputtered onto the samples before the measurement using the Cressington Sputter Coater208HR.

6.3.4.2 Cryogenic Transmission Electron Microscopy (Cryo-TEM)

Samples for Cryo-TEM were prepared by placing a small drop of the microgel dispersion with a concentration of 0.2-wt-% onto a TEM copper grid (Agar, G 600HH, Polysciences, Eppelheim, Germany). Excess of the microgel solution was removed by blotting with filter paper. The samples were kept at room temperature and rapidly vitrified in liquid ethane at its freezing point in a cryo-box. The samples were inserted into a cryo-transfer holder (CT3500, Gatan, Munich, Germany) and transferred to a Zeiss EM922EFTEM (Zeiss NTS GmbH, Oberkochen, Germany). Examination was carried out at temperatures around 90 K. The Cryo-TEM was operated at an acceleration voltage of 200 kV. The images were recorded digitally by a bottom-mounted CCD camera system (Ultra Scan 1000, Gatan, Munich, Germany) and processed with a digital imaging processing system (Digital Micrograph 3.9 for GMS 1.4, Gatan, Munich, Germany).

6.4 Characterisation of the Proteins

6.4.1 SDS Polyacrylamide Gel Electrophoresis (SDS- PAGE)

The molecular weight of β-D-glucosidase was determined by performing a SDS-PAGE in a vertical setup supplied from Biorad (Mini Protean 3 Cell) and Serva (Blue Vertical 101). Power supply was ensured using a device supplied by Consort (Microcomputer Electrophoresis Power Supply E 143).
To enhance the sharpness of the bands within the gel, a discontinuous buffer system, that is, the Laemmli system, was used. [311] The latter consists of a stacking gel with larger pores and a *pH* value of 6.8 and a resolving gel with having smaller pores and a *pH* value of 8.8. The lower *pH* value of the stacking gel forms an ion gradient of the small components in the buffer which concentrates the SDS-coated proteins in a thin zone. At this stage all proteins migrate with the same velocity. Separation of the proteins by size is achieved as the proteins access the resolving gel. Due to the higher *pH* value of the resolving gel the dissociation degree and, thus, the electrophoretic mobility of the buffer components is enhanced while the proteins have now the smallest mobility. The smaller pores in the resolving gel then lead to the sieving effect of the proteins and to a separation of the proteins in bands according to their relative molecular weights.
For the electrophoresis the following chemicals were required:

- Sample buffer (reducing):
  3.21 g tris(hydroxymethyl)aminomethane (Tris), 2.0 g SDS, 0.8 g 1.4 dithiothreitol, a small portion of bromphenol blue, and 10 mL of glycerine were dissolved in water to a total volume of 100 mL.
- Lower Tris buffer (buffer A, *pH* 8.8):
  18.3 g of Tris was dissolved in 40 mL water. The solution was adjusted to a *pH* value of 8.8 using HCl and diluted to a total volume of 50 mL.
- Upper Tris buffer (buffer B, *pH* 6.8):
  9.6 mL of 1 M Tris solution was diluted by adding 40 mL of water. The solution was adjusted to a *pH* value of 6.8 using HCl and diluted to a total volume of 50 mL.
- Acrylamide/BIS Solution (solution C, Roth Rotiphorese Gel 30):
  a solution of 100 mL contains 29.2 g acrylamide and 0.8 g BIS
- 20 wt-% aqueous SDS solution
- 20 wt-% ammonium persulfate solution (APS)
- Tris glycine reservoir buffer (electrode buffer, *pH* 8.8)
  12.0 g Tris, 57.6 g glycine, and 4.0 g SDS were dissolved in water to a total volume of 1 L. The buffer solution was diluted by 1:4 before usage.
- Fixing solution:
  100 mL of glacial acetic acid and 450 mL of ethanol were added to 450 mL of water.
- Staining solution:
  0.1 g of Coomassie R 250 was dissolved in a solution of 450 mL of ethanol and 50 mL of glacial acetic acid. The solution was diluted with water to a total volume of 1 L.
- Destaining solution:
  300 mL of ethanol and 50 mL of glacial acetic acid were added to 650 mL of water.

For the sample preparation, β-D-glucosidase was dissolved in a solution of 20 wt-% glycerine to a concentration of 3 g L^{-1}. Afterwards the protein solution was diluted by 1:2 using the reducing sample buffer. For complete binding of the SDS molecules around the protein and for complete denaturation of the protein the samples were heated to 95 °C for at least 3 min.

Then, the 0.75 mm thick slab gels were prepared in two steps using APS as initiator and N,N,N′,N′-tetramethylethylenediamine (TEMED) as catalyst. The acrylamide concentration of the stacking and resolving gel was set to 5 % and 12 %, respectively. The amounts of the educts and buffer solutions used for the synthesis of the stacking and the resolving gel are listed Table 6.4. In the first step, the resolving gel was polymerised. After initiation of the polymerisation the forming gel was covered by water to avoid the formation of air bubbles. The reaction was finished to completion after 15 min and the stacking gel was polymerised on top of the resolving gel. The pockets within the stacking gel were formed by placing a small comb into the polymerisation mixture at the beginning of the reaction. The slab gel prepared this way is suitable to separate proteins within a range of 10 to 100 kDa. For the SDS-PAGE, 7 µL of β-D-glucosidase and 10 µL of the protein standard (Roti®-Mark Standard) were filled into the pockets of the slab gel. The electrophoresis was carried out at a constant current of 25 mA.

After running the electrophoresis the gel was incubated for 30 min in a bath containing the fixing solution. The latter removes the SDS molecules from the proteins and fixates the proteins to the gel. Afterwards the gel was rinsed with water and shaken in a bath containing the staining solution for about 2 h. Then the gel was transferred to a bath with destaining solution. The gel was kept in this solution as long as the background of the slab became essentially colourless. Finally the gel was transferred to a solution of pure water for several hours. The gel was shrink-wrapped in water and photographed to precisely analyse the bands on the gel.

Table 6.4: Amounts used for the synthesis of the resolving and the stacking gel applied in the SDS-PAGE. Abbreviations: % T: total concentration of acrylamide, % C: concentration of BIS.

Gel	% T	% C	H_2O [mL]	buffer A [mL]	buffer B [mL]	solution C [mL]	SDS sol. [mL]	TEMED [µL]	APS sol. [µL]
stacking gel	4.8	0.4	1.2	-	0.5	0.33	-	4	14
resolving gel	1.2	0.3	2.3	0.65	-	2.0	25	10	25

6.4.2 Isoelectric Focusing (IEF)

The isoelectric point of β-D-glucosidase was determined by performing IEF in a flatbed system for horizontal electrophoresis with a cooling plate to provide for homogeneous tempering (BlueHorizon Flatbed System, Serva Electrophoresis Heidelberg, Germany). Power supply was ensured using a device supplied by Serva (BluePower 3000, Serva Electrophoresis). The gels used were received as prefabricated ampholyte/polyacrylamide gels from Serva (Servalyt® Precotes® Wide Range) with dimensions of 12.5 cm x 12.5 cm which are suitable for a *pH* range from 3 to 10.

The gels were focused at 10 mA to form a *pH* gradient. Therefore, the electrode wicks were soaked with anode (Serva Anode Fluid 3, *pH* = 3.05) and cathode fluid (Serva Cathode Fluid 10, *pH* = 12.26),

respectively, and placed onto the ends of the gel. During this run, the voltage was increased in 6 steps starting from 150 to 2125 V. Afterwards, 8 µl of protein standard (Serva Liquid Mix, IEF Markers 3-10) and 8 µl of a solution containing 20 wt-% glycerine and 3 g L^{-1} β-D-glucosidase were placed onto the centre of the gel by using an applicator strip. The electrophoresis was carried out at a constant current of 3.0 mA, while the voltage was increased in seven steps from 150 to 2500 V.
After completion of the IEF, the gel was placed into a fixing solution containing 10 wt-% trichloroacetic acid and 5 wt-% sulfosalicylic acid. The subsequent treatment of the IEF gel is identical to the one of the SDS-PAGE gels.

6.5 Protein Adsorption

6.5.1 The Ultrafiltration (UF) Technique

To obtain the adsorption isotherms by UF, small ultrafiltration cells were used with a maximum filling capacity of 150 mL. For this purpose 5 to 10 samples of varying protein concentrations were prepared in parallel. First, given amounts of protein were dissolved each in 10 mM MOPS buffer solution *pH* 7.2 to which the buffer-matched microgel dispersion was added in a second step. The final microgel concentration in the mixtures was 1 wt-%. The amounts of protein and microgel used for the UF experiments as well as the temperatures chosen for the binding experiments are gathered in Table 6.5. Depending on the temperature of the adsorption experiment, the adsorption reaction was allowed to proceed for 4 to 24 h under stirring. After this equilibration time the samples were transferred to the UF cells equipped with membranes having a pore size of 100 nm. In this way, unbound and desorbing proteins were removed from the microgel dispersion. During the experiment the ultrafiltration cells were kept either at room temperature or at 312 K using the Variomag™ Telesystem 6.2 (Thermo Scientific, VWR) equipped with a stirring unit and a thermostat as temperature control unit. Generally, replacement of the dispersion medium by 15 to 20 times against fresh buffer solution was sufficient to separate the protein loaded microgels from excess protein. This corresponds to a total volume of

Table 6.5: Experimental conditions and amounts of protein and microgel used for the UF experiments.

System	m(protein) [mg]	Total volume [mL]	m(microgel)[a] [mg]	Adsorption time [h]	*T*(adsorption) [K]	*T*(UF) [K]
β-D-glucosidase /CSM-0	10 to 160	10	100	24	277	room temperature
β-D-glucosidase /CSM-0-2	15 to 65	5	50	10	room temperature	room temperature
β-D-glucosidase /CSM-0-2	15 to 65	5	50	3.5	312	312
lysozyme/CSM-10	4 to 50	4	40	14.5	room temperature	room temperature

[a] The amount of microgel corresponds to the particle dry weight.

exchanged serum of 150 to 200 mL. Further serum replacement did not lead to additional protein desorption, at least for the amounts of buffer used. The amount of protein in the collecting serum was determined by ultraviolet-visible (UV-vis) spectroscopy at 278 nm using a photodiode array (PDA) spectrophotometer (Agilent 8453, Agilent Technologies, Böblingen, Germany) equipped with tempered 8-position cell holder. The spectrophotometer is operated by the Agilent ChemStation software for UV-vis spectroscopy. Its radiation source is a combination of a deuterium-discharge lamp for the UV wavelength range and a tungsten lamp for the visible and short-wave near infrared (SW-NIR) wavelength range. In contrast to traditional scanning instruments, PDA spectrophotometers allow simultaneous access to all wavelength information. Therein, the sample is irradiated by the incoming beam containing the whole spectral range. After passing through the sample, the light is dispersed onto the diode array by holographic grating to obtain the absorption spectrum. Irradiation induced reactions of the sample are avoided due to the mounted shutter which closes between measurements and, thus, limits the exposure of the sample to light. The simultaneous recording of the whole spectra by using such a PDA spectrophotometer results in a fundamental reduction of measurement time.

All measurements were performed in quartz sample cells with an optical path length of 1 cm. Background correction was done by measuring a blank, that is, the quartz cell filled with buffer solution. Since the PDA spectrophotometer is a single beam instrument the blank measurements have to be performed before the samples are measured. The protein spectra were recorded between 200 and 800 nm at a temperature of 293 K. Therefore, the cuvettes were filled with sample solution and equilibrated at 293 K for 5 min. After thermal equilibration was attained the measurements were performed and repeated at least three times. From the averaged absorption intensities the protein concentration of the sample solution was calculated using the Lambert-Beer law which is given by [290]

$$E(\lambda) = -\lg\left(\frac{I}{I_0}\right) = \varepsilon_\lambda^{\mathrm{T}} c d \tag{6.7}$$

where $E(\lambda)$ is the extinction at wavelength λ, I_0 and I is the intensity of the incoming and transmitted light, respectively, $\varepsilon_\lambda^{\mathrm{T}}$ is the decadal molar extinction coefficient of the protein at λ, and temperature T, c is the protein concentration, and d is the optical path length, that is, the thickness of the quartz sample cell. The protein concentration was determined from the intensities at 278 nm since the protein spectra exhibit a pronounced absorption peak at this wavelength. This is caused by the presence of the aromatic residues of the proteins, such as tryptophan. The molar extinction coefficient of proteins in this wavelength range is related to the number of aromatic residues of the protein and is determined by recording the extinction at 278 nm of protein solutions of known concentration. The slope of this plot then gives $\varepsilon_\lambda^{\mathrm{T}}$. The standard curves of β-D-glucosidase and lysozyme dissolved in 10 mM MOPS buffer *pH* 7.2 at 293 K are shown in Figure 6.2. The extinction coefficients of β-D-glucosidase and lysozyme were determined to (51 263 ± 1 865) and (35 093 ± 870) L mol^{-1} cm^{-1}, respectively. Using these extinction coefficients and equation (6.7), the protein concentration in the collecting sera of the ultrafiltration experiment was calculated. Then, the amount of protein adsorbed onto the microgel particles were determined by subtracting the amount of protein in the serum from the total mass of protein used. Relating of the amount of adsorbed protein to the mass of the microgel particles in solution then gives the loading of the microgel particles τ_{ads} in [mg protein per gram microgel].

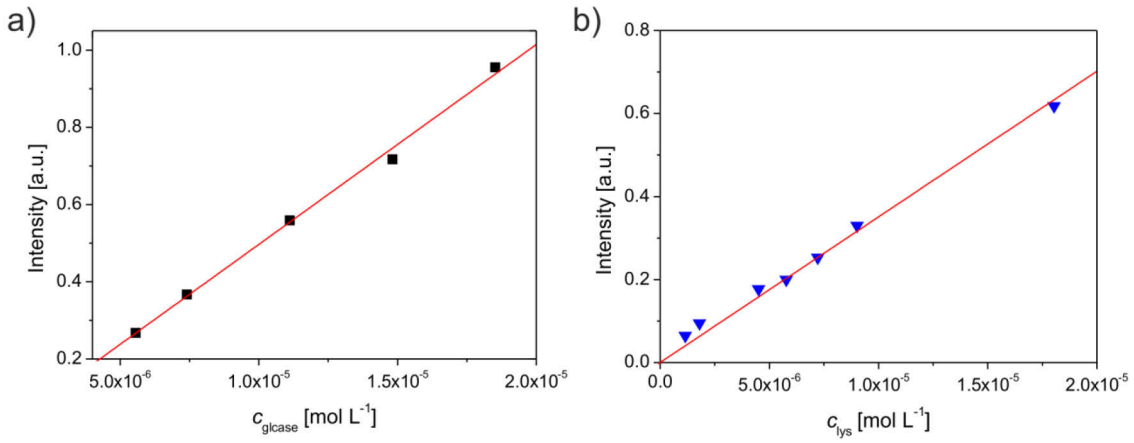

Figure 6.2: a) Absorption intensities of *β*-D-glucosidase at 278 nm dissolved in 10 mM MOPS buffer *pH* 7.2 at 293 K. b) Absorption intensities of lysozyme at 278 nm dissolved in 10 mM MOPS buffer *pH* 7.2 at 293 K.

6.5.2 Isothermal Titration Calorimetry (ITC)

The ITC experiments were performed using a VP-ITC instrument (MicroCal, GE Healthcare, Freiburg, Germany) which is controlled by the VPViewer software (MicroCal). The typical setup of an ITC instrument is schematically shown in Figure 6.3. The isothermal titration calorimeter consists of two identical cells which are composed of a highly efficient thermal conducting material and are enclosed by an adiabatic jacket. [312] The ITC unit directly measures the heat evolved or taken up in liquid samples as a result of mixing precise amounts of reactants. For injecting the reactant and subsequent mixing of the solution the instrument is equipped with a high-precision spinning syringe. Sensitive thermocouple circuits are used to detect temperature differences between the reference cell, which is filled with water, and the sample cell. The latter is calibrated to power units and the direct observable signal is the time-dependent input of power in µcal sec^{-1} which is needed to maintain temperature equilibrium. Therefore, a small constant amount of power is continuously applied to the offset heater of the reference cell throughout the ITC experiment. This causes the differential power (DP) feedback system to become positive to supply compensating power to the sample cell that will equilibrate the temperatures. During an exothermic reaction the temperature is increased in the sample cell. This causes a negative change from the DP feedback since less power is required to maintain equal temperatures between the cells. The opposite is true for endothermic reactions. The time integral of the peaks caused by injecting reactants into the sample cell then gives the thermal energy of the reaction.

The reference and sample cell of the VP-ITC instrument are composed of Hastelloy® Alloy C-276 which is a highly efficient thermal conductive material and is inert to many different solvents. The working volume of the sample cell is 1.4 mL and a total of 300 µl of reactant can be injected using the supplied spinning syringe. According to the manufacturer, the detection limit of the instrument is about 0.1 µcal. Thus, reliable measurements are performed when the recorded power is 0.1 µcal sec^{-1} or higher.

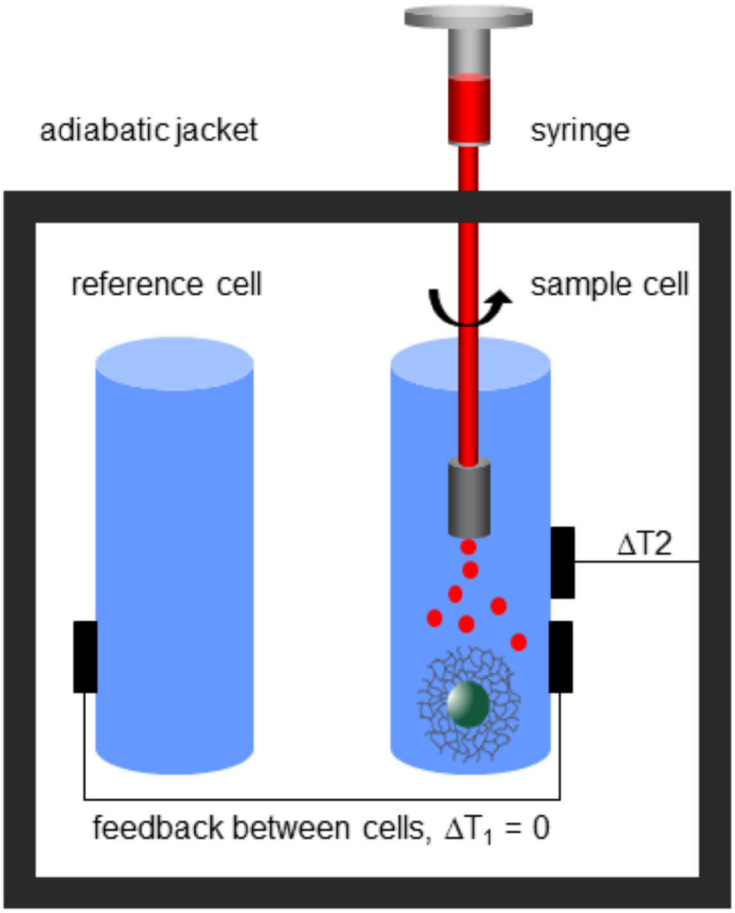

Figure 6.3: Schematic diagram of an isothermal titration calorimeter. The instrument consists of a reference and a sample cell which are surrounded by an adiabatic outer shield (jacket). A high-precision spinning syringe titrates the ligand (*e.g.*, the protein solution) into the sample cell filled with the macromolecule (*e.g.*, the microgel dispersion). Temperature differences between the reference and sample cell caused by the injection of the ligand are sensed by thermocouples. Depending on the nature of the reaction (*i.e.*, exothermic or endothermic) the feedback circuit will either increase or decrease the power applied to the sample cell in order to maintain the cells at an identical temperature. The heat flow per unit of time ($\mathrm{d}q/\mathrm{d}t$) is the observable signal in an ITC experiment.

To successfully set up an ITC experiment the concentration of the ligand and macromolecule have to be properly chosen. The optimal values for both concentrations, however, depend on the mechanism of binding as well as on the binding constant K_b. For a ligand which binds to a single set of independent binding sites the shape of the binding isotherm is strongly dependent on K_b. In particular, The shape of the binding isotherm changes according to the product c given by equation (6.8): [239,249]

$$c = NK_\mathrm{b}[M]_\mathrm{t} \tag{6.8}$$

Figure 6.4 shows a set of simulated ITC titration curves for reactions of 1:1 stoichiometry and with different binding constants, *i.e.*, varying values of c. [249] Accurate values for ΔH_ITC are determined from the early points of the titration curves with $c > 50$ because the reaction is near completion and ΔH_ITC is nearly independent of K_b. On the other hand, accurate fitting of the binding constant K_b

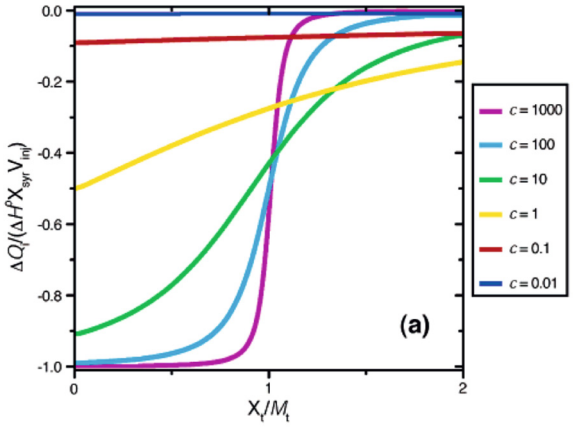

Figure 6.4: Simulated ITC titration curve for varying values of c and with *N* set to 1. Reprinted with permission from Turnbull, W. B.; Daranas, A. H. *J. Am. Chem. Soc.* **2003**, *125*, 14859-14866. Copyright © 2003, American Chemical Society.

requires $c < 500$. Under these conditions enough data points are measured to describe the curvature in the titration curve around the equivalence point. For values of c less than approximately 50, K_b and ΔH_{ITC} become interdependent and the fitting results are accompanied by large errors. Thus, only in the range between 50 and 500 the ITC isotherms can be deconvoluted to obtain accurate thermodynamic values. Consequently, the concentration of the carrier particle $[M]_t$ should be chosen properly in order to fulfil this requirement. By this means, K_b, N and ΔH_{ITC} can be determined with high precision from this fitting procedure.

Having optimised the concentrations of protein and microgel for the ITC analysis, the ITC experiments were conducted as follows:

Prior to the ITC experiment the protein and microgel solutions were stirred and degassed for 5 min at 1 K below the experimental temperature using the ThermoVac degassing and thermostatting station. Degassing of the samples ensures bubble free loading of each and avoids the formation of bubbles during the ITC experiment. A total of 300 µl of the protein solution of given concentration was titrated into the sample cell filled with 1.4 mL of buffer-matched microgel dispersion using a stirring speed of 290 rpm. The reference power was set to 10 µcal sec^{-1} for all experiments performed. The concentrations of protein and microgel used for the ITC experiments are listed in Table 6.6. During the course of the experiments the injection volume as well as the time interval between the injections was changed to allow for optimal data acquisition. During the first 20 injections the volume of the injected protein was set to 3 µL with an interval of 350 sec between each injection. For the subsequent 48 injections an injection volume of 5 µL and a spacing of 300 sec were chosen. The smaller injection volumes in the first part of the measurements lead to a high density of data points near the equivalence point where the slope and curvature of the binding isotherm is drastically altered. Control experiments were conducted by titrating the appropriate buffer solution into the microgel dispersion and by injecting the protein solution into the buffer, respectively.

After each experiment the sample cell and the syringe were cleaned using the ThermoVac apparatus. The sample cell and auto-pipette are connected to the ThermoVac via plastic tubings and the cell cleaning apparatus. After removal of the sample solution from the sample cell, about 200 mL of detergent solution was passed through the syringe and sample cell and collected by the vacuum flask which was interposed between the sample cell and the ThermoVac system. Then the sample cell and the syringe was incubated with 15 vol-% hydrogen peroxide solution for 10 min. Afterwards the

hydrogen peroxide solution was removed and the compartments were rinsed with another 100 mL of detergent solution and with about 800 mL of water. Finally, the cell and syringe were dried by using a small amount of acetone and by subsequent flushing with air.
Briefly, the acquired ITC data were analysed as follows: First, the baseline of the raw ITC data was set manually. Then the data points were integrated with respect to time and divided by the moles of injected protein. The integrated heats of the adsorption experiment were corrected for the integrated heat of dilution of the protein. Afterwards the ITC data were fitted using the supplied ITC module for ORIGIN 7.0 (MicroCal). The SSIS model was used to fit the adsorption data. A detailed description of the fitting procedure including the underlying equations is found in section 3.3.3.1.

Table 6.6: Experimental parameters of the thermodynamic analysis of protein adsorption performed by ITC.

System	Buffer/ionic strength	*T*[K]	c(protein) [mM]	c(microgel) [mM]
lysozyme/ CSM-10	MOPS/7mM	288; 293; 298; 303	0.695	8.42×10^{-7}
	MOPS/17 mM	288; 293; 298; 303	0.702	8.11×10^{-7}
	MOPS/32 mM	288; 293; 298; 303	0.698	8.10×10^{-7}
	PIPES/7 mM	288; 293; 298; 303	0.708	8.42×10^{-7}
lysozyme/ CSM-0-2	MOPS/7mM	288; 298; 303; 305.5; 308;	0.691	4.81×10^{-6}
β-D-glucosidase/ CSM-10	MOPS/7mM	298; 303; 308; 312	0.073	8.33×10^{-7}
β-D-glucosidase/ CSM-0-2	MOPS/7mM	298; 303: 305.5; 308; 312	0.071	3.36×10^{-6}
cytochrome c/ CSM-10	MOPS/7mM	288; 293; 298; 303	0.598	8.55×10^{-7}

6.5.3 Fluorescence Spectroscopy

6.5.3.1 Fluorescein Isothiocyanate (FITC)-Labelling of Lysozyme

Lysozyme was dissolved in 50 mM bicarbonate buffer *pH* 8.75 to a concentration of 10.02 g L^{-1}. Previous to the reaction, a fresh solution of 5 g L^{-1} FITC in anhydrous dimethyl sulfoxide was prepared. An equimolar amount of FITC solution was added to the lysozyme solution and the mixture was allowed to stir for 1 h at room temperature. After this period of time the labelled lysozyme solution was adjusted to $pH \approx 2.0$ using a 20 vol-% HCl solution and dialysed against 10 mM MOPS buffer solution *pH* 7.2 (Spectra Pore CE membrane, MWCO 1000) to remove excess FITC and to adjust the *pH* value and the ionic strength to the conditions used in the adsorption experiments. The degree of labelling and the concentration of lysozyme were determined by UV-vis spectroscopy (Agilent 8453, Agilent Technologies, Böblingen, Germany) at 293 K. Therefore the diluted solutions of FITC-labelled lysozyme (lysozyme^{FITC}) were subjected to UV-vis spectroscopy and the extinction

was measured at 278 and 495 nm (*i.e.*, the extinction maximum of FITC). The concentration of the protein [*P*] was calculated according to

$$[P] = \frac{E_{278} - E_{495}CF}{\varepsilon_{278,protein}} \tag{6.9}$$

where E_{278} and E_{495} are the values of extinction at 278 nm and 495 nm, respectively, and $\varepsilon_{278,protein}$ is the decadal molar extinction coefficient of lysozyme in 10 mM MOPS buffer *pH* 7.2 at 278 nm and at 293 K ((35 093 ± 870) L mol^{-1} cm^{-1}, see section 6.5.1). *CF* is the correction factor which is given by $CF = E_{278,\text{free FITC}}/E_{495,\text{free FITC}}$. It considers the extinction of FITC at 278 nm and it was determined to 0.41 by measuring the extinction of free FITC at 278 and 495 nm. The degree of labelling was calculated using

$$\frac{n(FITC)}{n(protein)} = \frac{E_{495}}{\varepsilon_{495,FITC}[P]} \tag{6.10}$$

where $\varepsilon_{495,\text{FITC}}$ is the decadal molar extinction coefficient of FITC in 10 mM MOPS buffer *pH* 7.2 at 495 nm and 293 K. The latter was determined from the slope of the standard curve of intensity versus the FITC concentration to $\varepsilon_{495,\text{FITC}}$ = (51 191 ± 180) L mol^{-1} cm^{-1} (Figure 6.5). In this way, the degree of labelling was calculated to ~1.06. Thus, each protein molecule carries one fluorescent tag in average.

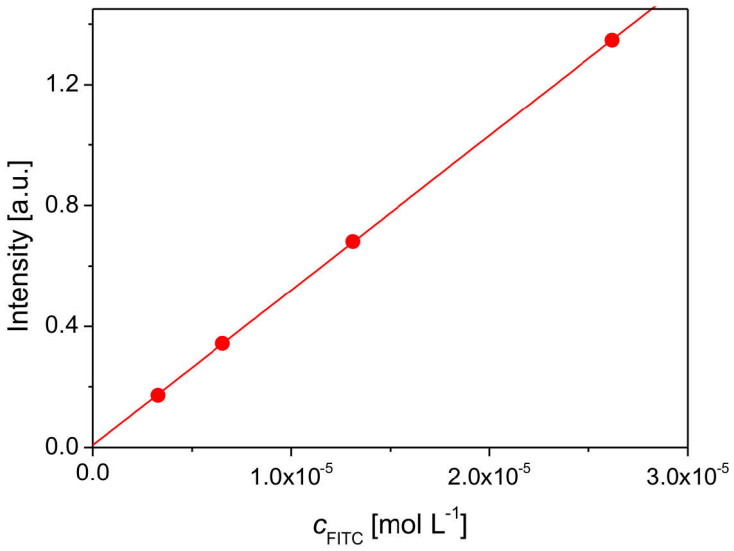

Figure 6.5: Absorption intensities of FITC at 495 nm dissolved in 10 mM MOPS buffer *pH* 7.2 at 293 K.

6.5.3.2 Fluorescence Quenching Experiments

Adsorption of lysozyme$^{\text{FITC}}$ onto the microgel network of CSM-10 in 10 mM MOPS buffer *pH* 7.2 at 293 K and its release/exchange was monitored using fluorescence spectroscopy. The time-dependent fluorescence was recorded using a FluoroMax-3 spectrometer, (JY-Horiba, Unterhaching, Germany) with the bandpass set to 1.5 nm and with an optical path length of 1 cm. The spectrometer was operated using the DataMax spectrometer software (Version 2.20, JY-Horiba, Unterhaching,

Germany). The excitation wavelength was set to 495 nm and the emission at 518 nm was monitored as a function of time (fluorescein shows a fluorescence peak at $\lambda_{em,max}$ = 518 nm and at $pH \approx 7$). To study the adsorption of lysozyme ^{FITC} onto CSM-10, given amounts of the microgel dispersion were added into the quartz sample cell filled with a solution of fluorescent-labelled protein. Thereby, the fluorescence measurement was started previous to the microgel injection in order to obtain the whole time-dependent adsorption data. The fluorescence data were acquired over a time frame of 1 000 sec. The concentrations of lysozyme^{FITC} and microgel used are mentioned in section 4.5.1.

The reversibility tests of the protein adsorption described in section 4.5.3 were performed as follows: First, the microgel particle is loaded with lysozyme^{FITC} analogously to the binding experiments described in section 4.5.1. Having attained binding equilibrium, varying amounts of unlabelled lysozyme were added to the quartz sample cell and the change of the fluorescence intensity was monitored for another 1 000 sec. In another experiment the chronological order of binding lysozyme^{FITC} and of untagged lysozyme was reversed at otherwise identical experimental conditions. For the salt-triggered release experiments of lysozyme^{FITC} as well as for the competitive protein binding experiments the CSM-10 particles were added to a solution of lysozyme^{FITC}. The fluorescence intensity was followed with time until equilibrium was reached. Then different amounts of salt and given amounts of the competing protein, respectively, were added to the quartz cell and the release of labelled lysozyme was investigated as a function of time.

For all measurements performed, the amount of lysozyme^{FITC} bound to CSM-10 was determined from the total lysozyme^{FITC} concentration in the volume and the concentration of non-adsorbed protein. The latter is identical to the amount of lysozyme which is still fluorescing. Thus, the concentration of non-adsorbed protein was calculated from the remaining fluorescence intensity and the linear calibration line of lysozyme^{FITC} (intensity versus protein concentration). The standard curve is shown in Figure 6.6. In the next step, the quantity of adsorbed (*i.e.*, non-fluorescent) protein was determined by subtraction of the amount of fluorescing protein from the total amount of lysozyme^{FITC} in the volume.

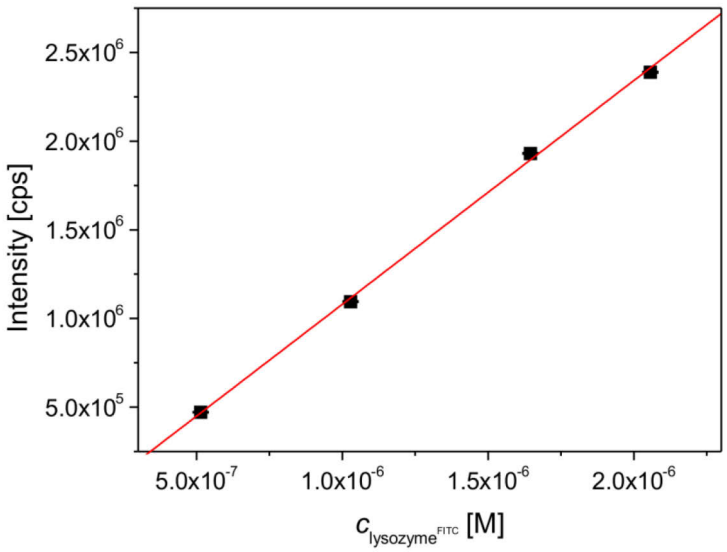

Figure 6.6: Fluorescence emission intensity of lysozyme^{FITC} of varying concentration in 10 mM MOPS buffer solution *pH* 7.2 at 293 K. The excitation wavelength λ_{ex} was set to λ_{ex} = 495 nm and the intensity of emission was recorded at λ_{em} = 518 nm.

6.6 Enzyme Activity Tests

The substrates used to study the catalytic activity of the enzymes in the free and adsorbed state contain a dye or fluorescent group, which, cleaved from the substrate by the enzymatic reaction, shows high absorption of visible light and strong fluorescence, respectively. In the first stage of the enzyme catalysed reaction the concentration of the products increases linear with time. Thus, monitoring the intensity of absorption or fluorescence as a function of time gives a straight line for the initial phase of the reaction and the initial rate υ is determined from the slope m of the spectral data:

$$\upsilon = \frac{\mathrm{d}[P]}{\mathrm{d}t} = \frac{m}{\varepsilon_\lambda^{\mathrm{T}}} \tag{6.11}$$

where $[P]$ is the concentration of the product, $\varepsilon_\lambda^{\mathrm{T}}$ is the molar extinction coefficient of the dye or the slope of the linear calibration line of the fluorophore in solution (*i.e.*, fluorescence emission intensity versus fluorophore concentration) at the specific wavelength λ and temperature T, respectively.
The photometrically measured values of υ are plotted as a function of the substrate concentration $[S]$ according to the Michaelis-Menten equation (3.13). Non-linear curve fitting of these data points leads to the Michaelis constant K_m and the maximum rate υ_{max}. The turnover number k_{cat} is calculated from υ_{max}, by dividing υ_{max} by the enzyme concentration $[E]$ of the enzyme assay. Therefore, the mass concentration of immobilised enzyme must be calculated by the following equation:

$$[E] = \frac{sc}{100}\frac{\tau_{\mathrm{ads}}}{(1000+\tau_{\mathrm{ads}})}\frac{1000}{x} \tag{6.12}$$

where sc is the percentage solid content of the stock solution, τ_{ads} the loading of the microgel particles with enzyme [mg protein/g microgel], and x as the dilution factor. In the following the respective enzyme assays for the analysis of the activity of β-D-glucosidase and lysozyme are briefly described.

6.6.1 β-D-Glucosidase

The activities of free and bound β-D-glucosidase were determined using *o*-NPG as substrate. The course of the hydrolysis of *o*-NPG was followed by measuring the absorption intensity at 405 nm as a function of time using a PDA spectrophotometer (Agilent 8453, Agilent Technologies, Böblingen, Germany) which was operated by the Agilent ChemStation software for UV-vis spectroscopy. All kinetic studies were performed in 10 mM MOPS buffer *pH* 7.2 and with an optical path length of 1 cm. To study the enzyme activity in terms of the Michaelis-Menten kinetics the concentration *o*-NPG was varied between 1.0 and 20.0 mM. Therein, the kinetic parameters for β-D-glucosidase were determined at distinct temperatures between 285 and 333 K. The final concentration of free enzyme in the enzyme assay was adjusted to 0.01 g L^{-1} for experiments conducted at temperatures between 285 and 303 K and to 0.005 g L^{-1} for those performed at temperatures ranging from 308 to 333 K. Activity tests with β-D-glucosidase bound to the CSM-0 microgel particles were done with ultrafiltrated samples. The loading of the microgel was determined to 620 mg enzyme per gram CSM-0. In case of immobilised β-D-glucosidase, the enzyme concentration in the enzyme assay was

set to 0.01 g L^{-1} for the reactions executed at temperatures ranging from 287 to 293 K. For reactions carried out at temperatures between 298 and 304 K and temperatures ranging from 309 to 328 K, the concentration of β-D-glucosidase was adjusted to 0.005 and 0.0035 g L^{-1}, respectively. To attain thermal equilibrium, the substrate solutions were incubated for 15 min at the respective temperatures prior to the UV-vis measurement. Then the reaction was initiated by addition of 50 µL of the ice-cooled enzyme solution. The absorption was measured at 405 nm for 12 min with an interval of 10 sec between each data point. The slope of the linear increase of the extinction with time and the decadal molar extinction coefficient of *o*-NPG at 405 nm ε_{405} directly lead to the initial rate of the enzymatic cleavage v (see equation (6.11)). Due to the temperature-dependence of the extinction coefficient, ε_{405} had to be determined for each temperature used (Figure 6.7 a). As obvious from Figure 6.7 b the extinction coefficient of *o*-NPG decreases in a polynomial fashion when the temperature is raised from 289 to 329 K.

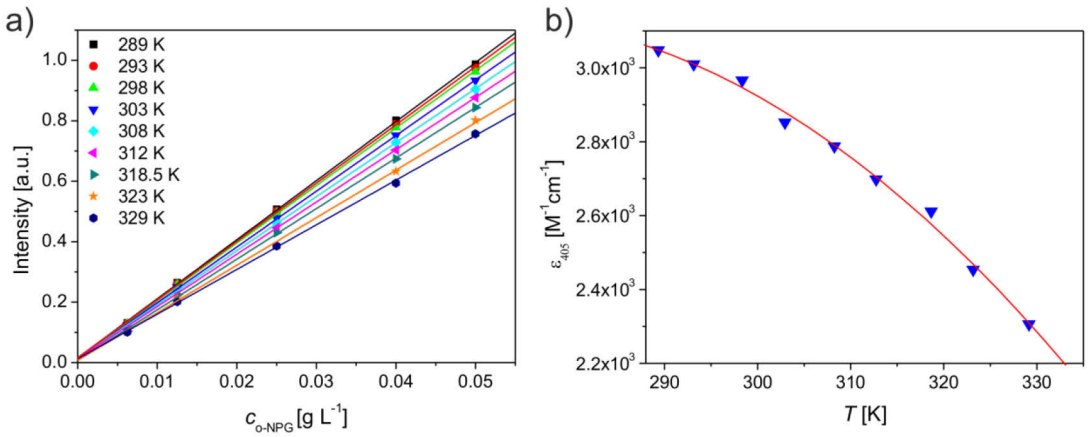

Figure 6.7: a) Absorption intensities of *o*-NPG of varying concentrations in 10 mM MOPS buffer *pH* 7.2 for temperatures ranging from 289 to 329 K. b) Decadal molar extinction coefficient ε_{405} of *o*-NPG at 405 nm as a function of temperature (filled symbols). The solid line is the polynomial fit of the experimental data points.

6.6.2 Lysozyme

The activities of free and adsorbed lysozyme were analysed by using $(GlcNAc)_3$-MeU as fluorescent substrate. Lysozyme cleaves the glycosidic bond between GlcNAc and the fluorescent aglycon MeU. MeU cleaved from the oligosaccharide shows a fluorescent peak at $\lambda_{em,max}$ = 450 nm when excited at λ_{ex} = 360 nm (see section 4.4.4). To study the catalytic activity of lysozyme adsorbed to the CSM-10 particles, protein-loaded particles were subjected to ultrafiltration. In this way, excess protein is removed from the solution. Therefore, 43 mg of lysozyme was added to 5 mL of 1 wt-% CSM-10 dispersed in 10 mM MOPS buffer *pH* 7.2. After incubation at room temperature for 15 h the protein-loaded CSM-10 particles were separated from unbound protein via ultrafiltration. Using this procedure, the loading of the particles τ_{ads} was determined to 675 mg lysozyme per gram of CSM-10. The final concentration of free and adsorbed lysozyme in the enzyme assay was adjusted to 0.05 g L^{-1} and 0.02 g L^{-1}, respectively. For the kinetic analysis according to the Michaelis-Menten kinetics the concentration of $(GlcNAc)_3$-MeU was varied between 1.6×10^{-5} and 1.3×10^{-4} M. All the kinetic studies were performed in 10 mM MOPS buffer *pH* 7.2 at 315 K. Prior to the fluorescence measurements the

$(GlcNAc)_3$-MeU solutions were incubated at 315 K for 15 min for thermal equilibration. The time-dependent fluorescence emission intensity at 450 nm was recorded for 1800 sec with a time increment and integration time of 5 sec each using a FluoroMax-3 spectrometer (JY-Horiba, Unterhaching, Germany). Therein, the spectrometer was controlled by the DataMax spectrometer software (Version 2.20, JY-Horiba, Unterhaching, Germany). The bandpass was set to 5 nm by the slits and the optical path length was 1 cm. Moreover, the substrate solution of the appropriate concentration was used as reference spectrum. The initial rate v of the conversion of $(GlcNAc)_3$-MeU was calculated from the initial slopes m of the time-dependent emission and from the linear calibration line of MeU (see equation (6.11)). The calibration line of MeU is shown in Figure 6.8.

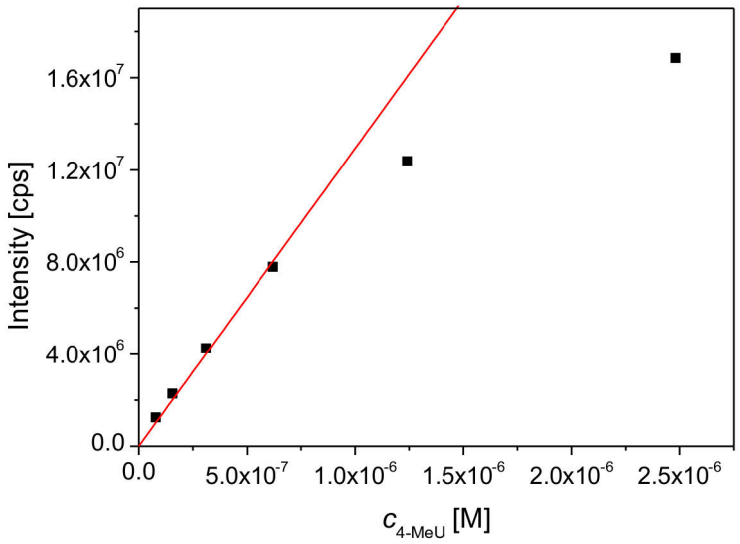

Figure 6.8: Fluorescence emission intensity of MeU of varying concentration in 10 mM MOPS buffer *pH* 7.2 at 315 K. The excitation wavelength λ_{ex} was set to 360 nm and the intensity of emission was recorded at λ_{em} = 450 nm.

6.7 Fourier Transform Infrared (FT-IR) Spectroscopy

The analysis of the secondary structure of free and immobilised proteins as well as the dehydration studies of the microgel CSM-0 were performed using a FT-IR spectroscopy setup developed for protein analytics (Bruker Optik Confocheck, Ettlingen, Germany) including a FT-IR spectrometer (Tensor 27, Bruker Optik, Ettlingen, Germany), a calcium fluoride flow-through cell of 6.5 µm path length (Aqua Spec™ AS 1100), and a highly sensitive photovoltaic $Hg_{1-x}Cd_xTe$ (MCT) detector. The latter is cooled by liquid nitrogen during operation. The flow-through cell is directly fixed to a tempering plate to adjust the temperature of the cell with high precision. In Figure 6.9 the cell compartments are schematically displayed. The sample cell is surrounded by a teflon jacket which serves for thermal insulation. Moreover, the sample solutions are injected into the sample cell through a filter frit of 2 µm pore size to avoid blocking as well as damage of the thin flow through cell. The FT-IR spectrometer was operated by the OPUS spectrometer software (OPUS Version 4.2, Bruker Optik, Ettlingen, Germany).

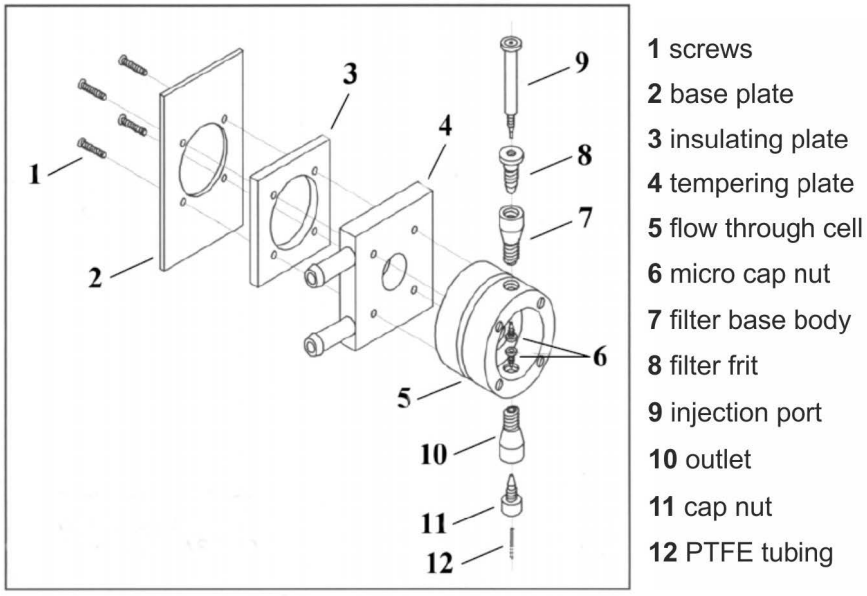

Figure 6.9: Schematic representation of the 6.5 µm thick flow-through cell (Aqua Spec^{TM} AS 1100) of the FT-IR spectrophotometer. The cell is equipped with a tempering plate for precise thermostatting and with a filter frit connected to the injection port to prevent blocking of the thin cell by dust particles and polymer agglomerates.

The measurements of the secondary structure of lysozyme and *β*-D-glucosidase were conducted in 10 mM MOPS buffer *pH* 7.2 at 298 K. To study the structure of the free proteins, lysozyme and *β*-D-glucosidase, respectively, were dissolved in 10 mM MOPS buffer *pH* 7.2 to a concentration of 15 g L^{-1}. The effect of immobilisation on the secondary structure was analysed using ultrafiltrated samples. Protein binding of the microgels and ultrafiltration of the protein-loaded microgel suspension were done along the lines given in section 6.5.1. Details regarding the kind of microgel and protein used as well as the protein loading of investigated samples are described in Table 6.7. Prior to the FT-IR experiments the enzyme-loaded microgels were adjusted with 10 mM MOPS buffer to a concentration of 0.75 to 2 wt-%. Measurements of the pure microgel particles were accomplished at concentrations between 2 and 3 wt-% of the respective microgel suspension. All samples were filtrated through a membrane syringe filter (0.8 µm pore width, PALL, Acrodisc) to remove dust particles and polymer agglomerates which could block the integrated filter frit and the cell. Then the sample solution was injected into the flow through cell using a 50 µl HPLC syringe and the solution was incubated in the cell for 5 min to attain thermal equilibration. The spectra were recorded in transmission mode of the spectrometer between 400 and 4 000 cm^{-1} and with a spectral resolution of 4 cm^{-1}. To minimise the absorption of the IR radiation by water vapour and carbon dioxide the interior of the spectrometer was flushed with dried nitrogen. Additionally, the spectrometer is equipped with two desiccant cartridges to minimise the water vapour inside the spectrometer compartments. Moreover, the recorded spectra were automatically corrected for the water vapour absorption bands. For each sample two spectra were recorded at 20 kHz each consisting of 128 scans and averaged. The buffer solution was measured subsequently after recording of the sample spectrum and was used as reference spectrum. For the dehydration study of the temperature-sensitive microgel CSM-0, FT-IR spectra at different temperatures had to be acquired. For this purpose, a temperature ramp was chosen

at which the temperature was raised from 293 to 313 K in steps of 5 K. At each temperature the cell and the sample solution was equilibrated for 5 min.

The secondary structure, *i.e.*, the α-helix and β-sheet content, was evaluated by using the Quant 2 analysis in the spectrometer software which is predicated on a protein database (Bruker Protein Library, Bruker Optik, Ettlingen, Germany). This databank comprises IR spectra of 30 reference proteins with elucidated X-ray structure (source: the PDB [168]). The α-helix and β-sheet content of lysozyme and β-D-glucosidase in the free and adsorbed state were calculated from the experimental FT-IR spectra by comparison with the whole set of reference spectra using a PLS algorithm. [201] The absolute experimental error of the cross correlation of the reference data in the spectrophotometer is 4 % for α-helix and 3 % for β-sheet.

Table 6.7: Description of the samples used in the FT-IR experiments. All microgel dispersions were dispersed in 10 mM MOPS buffer *pH* 7.2.

System	**τ_{ads} [mg protein/g microgel]**	**c(microgel)[a] [wt-%]**	**c(protein)[a] [g L^{-1}]**
β-D-glucosidase/ CSM-0	620	1.1	7
CSM-0	-	3	-
lysozyme/ CSM-10	660	0.75	5
CSM-10	-	2	-

[a] Microgel and protein concentration in the flow through cell of the FT-IR spectrometer, respectively.

7 Supplement

7.1 Overview of the Kinetic Constants of β-D-Glucosidase

Table 7.1: Michaelis constant K_m and turnover number k_{cat} of free β-D-glucosidase for varying temperatures. The parameters are related to the hydrolysis of *o*-NPG in 10 mM MOPS buffer *pH* 7.2.

T [K]	k_{cat} [sec^{-1}]	K_m [mM]
285.8	6.7	3.0
287.3	8.3	3.8
290.5	12.4	5.4
293.0	20.4	6.7
297.7	25.2	7.3
303.4	36.7	6.4
307.7	44.5	7.1
312.8	57.8	6.8
317.8	85.3	7.4
322.7	96.2	7.9
328.7	94.3	7.9
335.7	60.1	3.1

Table 7.2: Michaelis constant K_m and turnover number k_{cat} of β-D-glucosidase bound to CSM-0 microgel particles (τ_{ads} = 620 mg protein per gram microgel) for varying temperatures. The parameters are related to the hydrolysis of *o*-NPG in 10 mM MOPS buffer *pH* 7.2.

T [K]	k_{cat} [sec^{-1}]	K_m [mM]
287.2	22.2	5.4
290.5	44.0	8.0
293.0	65.5	9.4
298.0	72.8	8.8
301.1	91.1	10.2
303.2	101.5	9.0
305.0	144.9	13.5
307.5	164.4	12.4
310.0	169.0	11.1
313.0	204.2	11.3
318.0	247.8	11.5
322.7	262.6	10.1
329.2	231.5	7.4

7.2 Overview of the Thermodynamic Parameters of Protein Adsorption by ITC

Table 7.3: Thermodynamic and binding parameters for lysozyme adsorption on CSM-10 microgel particles in 10 mM MOPS buffer *pH* 7.2 at different temperatures and salt concentrations.

T [K]	Buffer[a]	N_b	K_b [M^{-1}]	ΔG_b [kJ mol^{-1}]	ΔH_{ITC} [kJ mol^{-1}]
288	10 mM MOPS	57 300 ±210	$1.83x10^6$ $\pm1.1x10^5$	-34.5 ±0.1	49.4 ±0.2
293	10 mM MOPS	57 400 ±190	$2.24x10^6$ $1.4x10^5$	-35.6 ±0.2	53.4 ±0.3
298	10 mM MOPS	60 100 ±190	$2.62x10^6$ $\pm1.7x10^5$	-36.6 ±0.2	60.7 ±0.3
303	10 mM MOPS	60 100 ±220	$2.84x10^6$ $\pm2.2x10^5$	-37.4 ±0.2	71.6 ±0.4
288	10 mM MOPS 10 mM NaCl	50 200 ±390	$3.54x10^5$ $\pm2.0x10^4$	-30.6 ±0.1	58.4 ±0.6
293	10 mM MOPS 10 mM NaCl	50 900 ±340	$4.81x10^5$ $\pm2.8x10^4$	-31.2 ±0.1	61.2 ±0.5
298	10 mM MOPS 10 mM NaCl	52 800 ±260	$6.25x10^5$ $\pm3.0x10^4$	-33.1 ±0.1	66.1 ±0.4
303	10 mM MOPS 10 mM NaCl	54 700 ±370	$7.55x10^5$ $\pm5.5x10^4$	-34.1 ±0.2	74.0 ±0.6
288	10 mM MOPS 25 mM NaCl	34 300 ±200	$1.33x10^5$ $\pm2.7x10^3$	-28.3 ±0.1	69.7 ±0.6
293	10 mM MOPS 25 mM NaCl	39 500 ±220	$1.71x10^5$ $\pm4.3x10^3$	-29.4 ±0.1	65.7 ±0.5
298	10 mM MOPS 25mM NaCl	37 600 ±360	$1.85x10^5$ $\pm8.1x10^3$	-30.1 ±0.1	83.8 ±1.0
303	10 mM MOPS 25 mM NaCl	45 900 ±220	$2.90x10^5$ $\pm8.8x10^3$	-31.7 ±0.1	73.3 ±0.5

[a] all buffers contain 2 mM NaN_3.

Table 7.4: Thermodynamic and binding parameters for lysozyme adsorption on CSM-10 microgel particles in 5 mM PIPES buffer *pH* 7.2 at different temperatures.

T [K]	N_b	K_b [M^{-1}]	ΔG_b [kJ mol^{-1}]	ΔH_{ITC} [kJ mol^{-1}]
288	58 100 ±310	$1.04x10^6$ $\pm7.4x10^4$	-33.2 ±0.2	46.3 ±0.3
293	60 500 ±440	$1.26x10^6$ $1.4x10^5$	-34.2 ±0.3	49.1 ±0.4
298	61 400 ±450	$1.38x10^6$ $\pm1.6x10^5$	-35.0 ±0.3	56.2 ±0.5
303	63 100 ±450	$1.82x10^6$ $\pm2.3x10^5$	-36.3 ±0.3	60.7 ±0.6

Table 7.5: Thermodynamic and binding parameters for *β*-D-glucosidase adsorption on CSM-10 microgel particles in 10 mM MOPS buffer *pH* 7.2 at different temperatures.

T [K]	N_b	K_b [M^{-1}]	ΔG_b [kJ mol^{-1}]	ΔH_{ITC} [kJ mol^{-1}]
298	12 500 ±120	$5.45x10^6$ $\pm6.1x10^5$	-38.4 ±0.3	103.7 ±1.3
303	13 000 ±150	$4.96x10^6$ $6.5x10^5$	-38.8 ±0.3	112.4 ±1.6
308	13 000 ±140	$6.78x10^6$ $\pm9.3x10^5$	-40.3 ±0.4	104.0 ±1.4
312	12 700 ±140	$6.29x10^6$ $\pm8.6x10^5$	-40.6 ±0.4	98.6 ±1.4

Table 7.6: Thermodynamic and binding parameters for cytochrome c adsorption on CSM-10 microgel particles in 10 mM MOPS buffer *pH* 7.2 at different temperatures.

T [K]	N_b	K_b [M^{-1}]	ΔG_b [kJ mol^{-1}]	ΔH_{ITC} [kJ mol^{-1}]
288	73 400 ±540	$3.09x10^5$ $\pm2.0x10^4$	-23.7 ±0.2	21.8 ±0.2
293	80 100 ±590	$2.56x10^5$ $1.6x10^4$	-23.6 ±0.2	23.3 ±0.2
298[a]	71 200 ±470	$3.06x10^5$ $\pm1.8x10^4$	-24.3 ±0.1	25.7 ±0.2
303	71 300 ±510	$1.98x10^5$ $\pm1.0x10^4$	-23.2 ±0.1	28.5 ±0.3

[a] The protein solution and microgel dispersion used for the ITC experiment at 298 K differ from the solutions used at the other temperatures.

Bibliography

[1]. Caruso, F., Nanoengineering of particle surfaces. *Adv. Mater.* **2001,** *13*, 11-22.

[2]. Ballauff, M.; Lu, Y., "Smart" nanoparticles: Preparation, characterization and applications. *Polymer* **2007,** *48*, 1815-1823.

[3]. Mizrahi, B.; Irusta, S.; McKenna, M.; Stefanescu, C.; Yedidsion, L.; Myint, M.; Langer, R.; Kohane, D. S., Microgels for efficient protein purification. *Adv. Mater.* **2011,** *23*, H258-262.

[4]. Nagase, K.; Kobayashi, J.; Kikuchi, A.; Akiyama, Y.; Kanazawa, H.; Okano, T., Thermoresponsive Polymer Brush on Monolithic-Silica-Rod for the High-Speed Separation of Bioactive Compounds. *Langmuir* **2011,** *27*, 10830-10839.

[5]. You, C.-C.; Agasti, S. S.; De, M.; Knapp, M. J.; Rotello, V. M., Modulation of the Catalytic Behavior of α-Chymotrypsin at Monolayer-Protected Nanoparticle Surfaces. *J. Am. Chem. Soc.* **2006,** *128*, 14612-14618.

[6]. Rana, S.; Yeh, Y. C.; Rotello, V. M., Engineering the nanoparticle-protein interface: applications and possibilities. *Curr. Opin. Chem. Biol.* **2010,** *14*, 828-834.

[7]. De, M.; Rana, S.; Akpinar, H.; Miranda, O. R.; Arvizo, R. R.; Bunz, U. H. F.; Rotello, V. M., Sensing of proteins in human serum using conjugates of nanoparticles and green fluorescent protein. *Nat. Chem.* **2009,** *1*, 461-465.

[8]. Banerjee, I.; Pangule, R. C.; Kane, R. S., Antifouling coatings: recent developments in the design of surfaces that prevent fouling by proteins, bacteria, and marine organisms. *Adv. Mater.* **2011,** *23*, 690-718.

[9]. Mahmoudi, M.; Lynch, I.; Ejtehadi, M. R.; Monopoli, M. P.; Bombelli, F. B.; Laurent, S., Protein-nanoparticle interactions: opportunities and challenges. *Chem. Rev.* **2011,** *111*, 5610-5637.

[10]. Nel, A. E.; Madler, L.; Velegol, D.; Xia, T.; Hoek, E. M. V.; Somasundaran, P.; Klaessig, F.; Castranova, V.; Thompson, M., Understanding biophysicochemical interactions at the nano-bio interface. *Nat. Mater.* **2009,** *8*, 543-557.

[11]. Calderon, M.; Quadir, M. A.; Sharma, S. K.; Haag, R., Dendritic Polyglycerols for Biomedical Applications. *Adv. Mater.* **2010,** *22*, 190-218.

[12]. Caruso, F.; Becker, A. L.; Johnston, A. P. R., Layer-By-Layer-Assembled Capsules and Films for Therapeutic Delivery. *Small* **2010,** *6*, 1836-1852.

[13]. Hong, R.; Han, G.; Fernandez, J. M.; Kim, B. J.; Forbes, N. S.; Rotello, V. M., Glutathione-mediated delivery and release using monolayer protected nanoparticle carriers. *J. Am. Chem. Soc.* **2006,** *128*, 1078-1079.

[14]. Ghosh, P.; Yang, X.; Arvizo, R.; Zhu, Z. J.; Agasti, S. S.; Mo, Z.; Rotello, V. M., Intracellular delivery of a membrane-impermeable enzyme in active form using functionalized gold nanoparticles. *J. Am. Chem. Soc.* **2010,** *132*, 2642-2645.

[15]. Raemdonck, K.; Demeester, J.; De Smedt, S., Advanced nanogel engineering for drug delivery. *Soft Matter* **2009,** *5*, 707-715.

[16]. Bysell, H.; Månsson, R.; Hansson, P.; Malmsten, M., Microgels and microcapsules in peptide and protein drug delivery. *Adv. Drug Deliver. Rev.* **2011,** *63*, 1172-1185.

[17]. Murthy, N.; Xu, M.; Schuck, S.; Kunisawa, J.; Shastri, N.; Frechet, J. M., A macromolecular delivery vehicle for protein-based vaccines: acid-degradable protein-loaded microgels. *Proc. Natl. Acad. Sci. U.S.A.* **2003,** *100*, 4995-5000.

[18]. Caruso, F.; Trau, D.; Möhwald, H.; Renneberg, R., Enzyme Encapsulation in Layer-by-Layer Engineered Polymer Multilayer Capsules. *Langmuir* **2000,** *16*, 1485-1488.

[19]. Zelikin, A. N.; Becker, A. L.; Johnston, A. P. R.; Wark, K. L.; Turatti, F.; Caruso, F., A General Approach for DNA Encapsulation in Degradable Polymer Microcapsules. *ACS Nano* **2007,** *1*, 63-69.

[20]. Sukhorukov, G. B.; Volodkin, D. V.; Gunther, A. M.; Petrov, A. I.; Shenoy, D. B.; Mohwald, H., Porous calcium carbonate microparticles as templates for encapsulation of bioactive compounds. *J. Mater. Chem.* **2004,** *14*, 2073-2081.

[21]. Ranquin, A.; Versées, W.; Meier, W.; Steyaert, J.; Van Gelder, P., Therapeutic Nanoreactors: Combining Chemistry and Biology in a Novel Triblock Copolymer Drug Delivery System. *Nano Lett.* **2005,** *5*, 2220-2224.

[22]. De Temmerman, M. L.; Demeester, J.; De Vos, F.; De Smedt, S. C., Encapsulation Performance of Layer-by-Layer Microcapsules for Proteins. *Biomacromolecules* **2011,** *12*, 1283-1289.

[23]. Shu, S. J.; Sun, C. Y.; Zhang, X. G.; Wu, Z. M.; Wang, Z.; Li, C. X., Hollow and degradable polyelectrolyte nanocapsules for protein drug delivery. *Acta Biomater.* **2010,** *6*, 210-217.

[24]. Basset, C.; Harder, C.; Vidaud, C.; Dejugnat, C., Design of double stimuli-responsive polyelectrolyte microcontainers for protein soft encapsulation. *Biomacromolecules* **2010,** *11*, 806-814.

[25]. Tanaka, M.; Sackmann, E., Polymer-supported membranes as models of the cell surface. *Nature* **2005,** *437*, 656-663.

[26]. Caruso, F.; Schuler, C., Enzyme multilayers on colloid particles: Assembly, stability, and enzymatic activity. *Langmuir* **2000,** *16*, 9595-9603.

[27]. Caruso, F.; Möhwald, H., Protein Multilayer Formation on Colloids through a Stepwise Self-Assembly Technique. *J. Am. Chem. Soc.* **1999,** *121*, 6039-6046.

[28]. Mertz, D.; Vogt, C.; Hemmerle, J.; Mutterer, J.; Ball, V.; Voegel, J.-C.; Schaaf, P.; Lavalle, P., Mechanotransductive surfaces for reversible biocatalysis activation. *Nat. Mater.* **2009,** *8*, 731-735.

[29]. Abdelrahman, A. I.; Thickett, S. C.; Liang, Y.; Ornatsky, O.; Baranov, V.; Winnik, M. A., Surface Functionalization Methods to Enhance Bioconjugation in Metal-Labeled Polystyrene Particles. *Macromolecules* **2011,** *44*, 4801-4813.

[30]. Musyanovych, A.; Adler, H.-J. P., Grafting of Amino Functional Monomer onto Initiator-Modified Polystyrene Particles. *Langmuir* **2005,** *21*, 2209-2217.

[31]. Tahir, M. N.; Natalio, F.; Berger, R.; Barz, M.; Theato, P.; Schroder, H.-C.; Muller, W. E. G.; Tremel, W., Growth of fibrous aggregates of silica nanoparticles: Fibre growth by mimicking the biogenic silica patterning processes. *Soft Matter* **2009,** *5*, 3657-3662.

[32]. Heredia, K. L.; Bontempo, D.; Ly, T.; Byers, J. T.; Halstenberg, S.; Maynard, H. D., In situ preparation of protein-"smart" polymer conjugates with retention of bioactivity. *J. Am. Chem. Soc.* **2005,** *127*, 16955-16960.

[33]. Adamczyk, Z.; Bratek-Skicki, A.; Dąbrowska, P.; Nattich-Rak, M., Mechanisms of Fibrinogen Adsorption on Latex Particles Determined by Zeta Potential and AFM Measurements. *Langmuir* **2012,** *28*, 474-485.

[34]. Palocci, C.; Chronopoulou, L.; Venditti, I.; Cernia, E.; Diociaiuti, M.; Fratoddi, I.; Russo, M. V., Lipolytic enzymes with improved activity and selectivity upon adsorption on polymeric nanoparticles. *Biomacromolecules* **2007,** *8*, 3047-3053.

[35]. Saraiva, A. M.; Cardoso, I.; Saraiva, M. J.; Tauer, K.; Pereira, M. C.; Coelho, M. A. N.; Möhwald, H.; Brezesinski, G., Randomization of Amyloid-β-Peptide(1-42) Conformation by Sulfonated and Sulfated Nanoparticles Reduces Aggregation and Cytotoxicity. *Macromol. Biosci.* **2010,** *10*, 1152-1163.

[36]. Bharti, B.; Meissner, J.; Findenegg, G. H., Aggregation of silica nanoparticles directed by adsorption of lysozyme. *Langmuir* **2011,** *27*, 9823-9833.

[37]. Shang, W.; Nuffer, J. H.; Muñiz-Papandrea, V. A.; Colón, W.; Siegel, R. W.; Dordick, J. S., Cytochrome c on Silica Nanoparticles: Influence of Nanoparticle Size on Protein Structure, Stability, and Activity. *Small* **2009,** *5*, 470-476.

[38]. Casals, E.; Pfaller, T.; Duschl, A.; Oostingh, G. J.; Puntes, V., Time Evolution of the Nanoparticle Protein Corona. *ACS Nano* **2010,** *4*, 3623-3632.

[39]. Monopoli, M. P.; Walczyk, D.; Campbell, A.; Elia, G.; Lynch, I.; Bombelli, F. B.; Dawson, K. A., Physical-Chemical Aspects of Protein Corona: Relevance to in Vitro and in Vivo Biological Impacts of Nanoparticles. *J. Am. Chem. Soc.* **2011,** *133*, 2525-2534.

[40]. Walczyk, D.; Bombelli, F. B.; Monopoli, M. P.; Lynch, I.; Dawson, K. A., What the Cell "Sees" in Bionanoscience. *J. Am. Chem. Soc.* **2010,** *132*, 5761-5768.

[41]. Cedervall, T.; Lynch, I.; Foy, M.; Berggard, T.; Donnelly, S. C.; Cagney, G.; Linse, S.; Dawson, K. A., Detailed identification of plasma proteins adsorbed on copolymer nanoparticles. *Angew. Chem. Int. Ed.* **2007,** *46*, 5754-5756.

[42]. Tenzer, S.; Docter, D.; Rosfa, S.; Wlodarski, A.; Kuharev, J.; Rekik, A.; Knauer, S. K.; Bantz, C.; Nawroth, T.; Bier, C.; Sirirattanapan, J.; Mann, W.; Treuel, L.; Zellner, R.; Maskos, M.; Schild, H.; Stauber, R. H., Nanoparticle Size Is a Critical Physicochemical Determinant of the Human Blood Plasma Corona: A Comprehensive Quantitative Proteomic Analysis. *ACS Nano* **2011,** *5*, 7155-7167.

[43]. Lacerda, S. H. D. P.; Park, J. J.; Meuse, C.; Pristinski, D.; Becker, M. L.; Karim, A.; Douglas, J. F., Interaction of Gold Nanoparticles with Common Human Blood Proteins. *ACS Nano* **2009,** *4*, 365-379.

[44]. Maiorano, G.; Sabella, S.; Sorce, B.; Brunetti, V.; Malvindi, M. A.; Cingolani, R.; Pompa, P. P., Effects of Cell Culture Media on the Dynamic Formation of Protein-Nanoparticle Complexes and Influence on the Cellular Response. *ACS Nano* **2010,** *4*, 7481-7491.

[45]. Aggarwal, P.; Hall, J. B.; McLeland, C. B.; Dobrovolskaia, M. A.; McNeil, S. E., Nanoparticle interaction with plasma proteins as it relates to particle biodistribution, biocompatibility and therapeutic efficacy. *Adv. Drug Deliver. Rev.* **2009,** *61*, 428-437.

[46]. Ehrenberg, M. S.; Friedman, A. E.; Finkelstein, J. N.; Oberdörster, G.; McGrath, J. L., The influence of protein adsorption on nanoparticle association with cultured endothelial cells. *Biomaterials* **2009,** *30*, 603-610.

[47]. Dobrovolskaia, M. A.; Germolec, D. R.; Weaver, J. L., Evaluation of nanoparticle immunotoxicity. *Nat. Nanotechnol.* **2009,** *4*, 411-414.

[48]. Radomski, A.; Jurasz, P.; Alonso-Escolano, D.; Drews, M.; Morandi, M.; Malinski, T.; Radomski, M. W., Nanoparticle-induced platelet aggregation and vascular thrombosis. *Brit. J. Pharmacol.* **2005,** *146*, 882-893.

[49]. Deng, Z. J.; Liang, M. T.; Monteiro, M.; Toth, I.; Minchin, R. F., Nanoparticle-induced unfolding of fibrinogen promotes Mac-1 receptor activation and inflammation. *Nat. Nanotechnol.* **2011,** *6*, 39-44.

[50]. Colvin, V. L.; Kulinowski, K. M., Nanoparticles as catalysts for protein fibrillation. *Proc. Natl. Acad. Sci. U.S.A.* **2007,** *104*, 8679-8680.

[51]. Linse, S.; Cabaleiro-Lago, C.; Xue, W. F.; Lynch, I.; Lindman, S.; Thulin, E.; Radford, S. E.; Dawson, K. A., Nucleation of protein fibrillation by nanoparticles. *Proc. Natl. Acad. Sci. U.S.A.* **2007,** *104*, 8691-8696.

[52]. Cabaleiro-Lago, C.; Quinlan-Pluck, F.; Lynch, I.; Lindman, S.; Minogue, A. M.; Thulin, E.; Walsh, D. M.; Dawson, K. A.; Linse, S., Inhibition of amyloid beta protein fibrillation by polymeric nanoparticles. *J. Am. Chem. Soc.* **2008,** *130*, 15437-15443.

[53]. Goppert, T. M.; Muller, R. H., Adsorption kinetics of plasma proteins on solid lipid nanoparticles for drug targeting. *Int. J. Pharm.* **2005,** *302*, 172-186.

[54]. Hasadsri, L.; Kreuter, J.; Hattori, H.; Iwasaki, T.; George, J. M., Functional protein delivery into neurons using polymeric nanoparticles. *J. Biol. Chem.* **2009,** *284*, 6972-6981.

[55]. Rivera Gil, P.; Oberdorster, G.; Elder, A.; Puntes, V.; Parak, W. J., Correlating Physico-Chemical with Toxicological Properties of Nanoparticles: The Present and the Future. *ACS Nano* **2010,** *4*, 5527-5531.

[56]. Dawson, K. A.; Salvati, A.; Lynch, I., Nanotoxicology: nanoparticles reconstruct lipids. *Nat. Nanotechnol.* **2009,** *4*, 84-85.

[57]. Bhabra, G.; Sood, A.; Fisher, B.; Cartwright, L.; Saunders, M.; Evans, W. H.; Surprenant, A.; Lopez-Castejon, G.; Mann, S.; Davis, S. A.; Hails, L. A.; Ingham, E.; Verkade, P.; Lane, J.; Heesom, K.; Newson, R.; Case, C. P., Nanoparticles can cause DNA damage across a cellular barrier. *Nat. Nanotechnol.* **2009,** *4*, 876-883.

[58]. Xia, X. R.; Monteiro-Riviere, N. A.; Riviere, J. E., An index for characterization of nanomaterials in biological systems. *Nat. Nanotechnol.* **2010,** *5*, 671-675.

[59]. Fang, F.; Szleifer, I., Kinetics and thermodynamics of protein adsorption: a generalized molecular theoretical approach. *Biophys. J.* **2001,** *80*, 2568-2589.

[60]. Baier, G.; Costa, C.; Zeller, A.; Baumann, D.; Sayer, C.; Araujo, P. H. H.; Mailander, V.; Musyanovych, A.; Landfester, K., BSA Adsorption on Differently Charged Polystyrene Nanoparticles using Isothermal Titration Calorimetry and the Influence on Cellular Uptake. *Macromol. Biosci.* **2011,** *11*, 628-638.

[61]. Lundqvist, M.; Stigler, J.; Cedervall, T.; Berggård, T.; Flanagan, M. B.; Lynch, I.; Elia, G.; Dawson, K., The Evolution of the Protein Corona around Nanoparticles: A Test Study. *ACS Nano* **2011,** *5*, 7503-7509.

[62]. Lundqvist, M.; Stigler, J.; Elia, G.; Lynch, I.; Cedervall, T.; Dawson, K. A., Nanoparticle size and surface properties determine the protein corona with possible implications for biological impacts. *Proc. Natl. Acad. Sci. U.S.A.* **2008,** *105*, 14265-14270.

[63]. Gessner, A.; Lieske, A.; Paulke, B. R.; Müller, R. H., Influence of surface charge density on protein adsorption on polymeric nanoparticles: analysis by two-dimensional electrophoresis. *Eur. J. Pharm. Biopharm.* **2002,** *54*, 165-170.

[64]. Koutsopoulos, S.; Patzsch, K.; Bosker, W. T. E.; Norde, W., Adsorption of trypsin on hydrophilic and hydrophobic surfaces. *Langmuir* **2007,** *23*, 2000-2006.

[65]. Kumar, S.; Aswal, V. K.; Kohlbrecher, J., SANS and UV-vis spectroscopy studies of resultant structure from lysozyme adsorption on silica nanoparticles. *Langmuir* **2011,** *27*, 10167-10173.

[66]. De, M.; You, C. C.; Srivastava, S.; Rotello, V. M., Biomimetic interactions of proteins with functionalized nanoparticies: A thermodynamic study. *J. Am. Chem. Soc.* **2007,** *129*, 10747-10753.

[67]. Dobrovolskaia, M. A.; Patri, A. K.; Zheng, J.; Clogston, J. D.; Ayub, N.; Aggarwal, P.; Neun, B. W.; Hall, J. B.; McNeil, S. E., Interaction of colloidal gold nanoparticles with human blood:

effects on particle size and analysis of plasma protein binding profiles. *Nanomed.-Nanotechnol.* **2009,** *5*, 106-117.

[68]. Treuel, L.; Malissek, M.; Gebauer, J. S.; Zellner, R., The influence of surface composition of nanoparticles on their interactions with serum albumin. *Chem. Phys. Chem.* **2010,** *11*, 3093-3099.

[69]. Rocker, C.; Potzl, M.; Zhang, F.; Parak, W. J.; Nienhaus, G. U., A quantitative fluorescence study of protein monolayer formation on colloidal nanoparticles. *Nat. Nanotechnol.* **2009,** *4*, 577-580.

[70]. Caracciolo, G.; Pozzi, D.; Capriotti, A. L.; Cavaliere, C.; Foglia, P.; Amenitsch, H.; Lagana, A., Evolution of the protein corona of lipid gene vectors as a function of plasma concentration. *Langmuir* **2011,** *27*, 15048-15053.

[71]. Herrwerth, S.; Eck, W.; Reinhardt, S.; Grunze, M., Factors that Determine the Protein Resistance of Oligoether Self-Assembled Monolayers − Internal Hydrophilicity, Terminal Hydrophilicity, and Lateral Packing Density. *J. Am. Chem. Soc.* **2003,** *125*, 9359-9366.

[72]. Louguet, S.; Kumar, A. C.; Guidolin, N.; Sigaud, G.; Duguet, E.; Lecommandoux, S.; Schatz, C., Control of the PEO Chain Conformation on Nanoparticles by Adsorption of PEO-block-Poly(l-lysine) Copolymers and Its Significance on Colloidal Stability and Protein Repellency. *Langmuir* **2011,** *27*, 12891-12901.

[73]. Wittemann, A.; Haupt, B.; Ballauff, M., Adsorption of proteins on spherical polyelectrolyte brushes in aqueous solution. *Phys. Chem. Chem. Phys.* **2003,** *5*, 1671-1677.

[74]. Li, Y.; de Vries, R.; Kleijn, M.; Slaghek, T.; Timmermans, J.; Stuart, M. C.; Norde, W., Lysozyme Uptake by Oxidized Starch Polymer Microgels. *Biomacromolecules* **2010,** *11*, 1754-1762.

[75]. Malmsten, M.; Bysell, H.; Hansson, P., Biomacromolecules in microgels - Opportunities and challenges for drug delivery. *Curr. Opin. Colloid Interface Sci.* **2010,** *15*, 435-444.

[76]. Czeslik, C.; Jackler, G.; Hazlett, T.; Gratton, E.; Steitz, R.; Wittemann, A.; Ballauff, M., Salt-induced protein resistance of polyelectrolyte brushes studied using fluorescence correlation spectroscopy and neutron reflectometry. *Phys. Chem. Chem. Phys.* **2004,** *6*, 5557-5563.

[77]. Wittemann, A.; Ballauff, M., Interaction of proteins with linear polyelectrolytes and spherical polyelectrolyte brushes in aqueous solution. *Phys. Chem. Chem. Phys.* **2006,** *8*, 5269-5275.

[78]. Rosenfeldt, S.; Wittemann, A.; Ballauff, M.; Breininger, E.; Bolze, J.; Dingenouts, N., Interaction of proteins with spherical polyelectrolyte brushes in solution as studied by small-angle x-ray scattering. *Phys. Rev. E* **2004,** *70*, 061403.

[79]. Wittemann, A.; Ballauff, M., Secondary structure analysis of proteins embedded in spherical polyelectrolyte brushes by FT-IR spectroscopy. *Anal. Chem.* **2004,** *76*, 2813-2819.

[80]. Jackler, G.; Wittemann, A.; Ballauff, M.; Czeslik, C., Spherical polyelectrolyte brushes as carrier particles for proteins: An investigation of the structure of adsorbed and desorbed bovine serum albumin. *Spectroscopy* **2004,** *18*, 289-299.

[81]. Jackson, M. B., *Molecular and Cellular Biophysics*. Cambridge University Press: New York, 2006.

[82]. Henzler, K.; Rosenfeldt, S.; Wittemann, A.; Harnau, L.; Finet, S.; Narayanan, T.; Ballauff, M., Directed motion of proteins along tethered polyelectrolytes. *Phys. Rev. Lett.* **2008,** *100*, 158301.

[83]. Bittrich, E.; Rodenhausen, K. B.; Eichhorn, K. J.; Hofmann, T.; Schubert, M.; Stamm, M.; Uhlmann, P., Protein adsorption on and swelling of polyelectrolyte brushes: A simultaneous ellipsometry-quartz crystal microbalance study. *Biointerphases* **2010,** *5*, 159-167.

[84]. Henzler, K.; Haupt, B.; Lauterbach, K.; Wittemann, A.; Borisov, O.; Ballauff, M., Adsorption of beta-Lactoglobulin on Spherical Polyelectrolyte Brushes: Direct Proof of Counterion Release by Isothermal Titration Calorimetry. *J. Am. Chem. Soc.* **2010,** *132*, 3159-3163.

[85]. Lindman, S.; Lynch, I.; Thulin, E.; Nilsson, H.; Dawson, K. A.; Linse, S., Systematic investigation of the thermodynamics of HSA adsorption to N-iso-propylacrylamide/N-tert-butylacrylamide copolymer nanoparticles. Effects of particle size and hydrophobicity. *Nano Lett.* **2007,** *7*, 914-920.

[86]. Noh, H.; Vogler, E. A., Volumetric interpretation of protein adsorption: Competition from mixtures and the Vroman effect. *Biomaterials* **2007,** *28*, 405-422.

[87]. Slack, S. M.; Horbett, T. A., Changes in the strength of fibrinogen attachment to solid surfaces: An explanation of the influence of surface chemistry on the Vroman effect. *J. Colloid Interface Sci.* **1989,** *133*, 148-165.

[88]. Slack, S. M.; Horbett, T. A., Changes in fibrinogen adsorbed to segmented polyurethanes and hydroxyethylmethacrylate-ethylmethacrylate copolymers. *J. Biomed. Mater. Res.* **1992,** *26*, 1633-1649.

[89]. Brash, J. L.; Ten Hove, P., Protein adsorption studies on 'standard' polymeric materials. *J. Biomater. Sci., Polym. Ed.* **1993,** *4*, 591-599.

[90]. LeDuc, C. A.; Vroman, L.; Leonard, E. F., A Mathematical Model for the Vroman Effect. *Ind. Eng. Chem. Res.* **1995,** *34*, 3488-3495.

[91]. Jung, S. Y.; Lim, S. M.; Albertorio, F.; Kim, G.; Gurau, M. C.; Yang, R. D.; Holden, M. A.; Cremer, P. S., The Vroman effect: A Molecular Level Description of Fibrinogen Displacement. *J. Am. Chem. Soc.* **2003,** *125*, 12782-12786.

[92]. Vroman, L.; Adams, A. L., Identification of rapid changes at plasma-solid interfaces. *J. Biomed. Mater. Res.* **1969,** *3*, 43-67.

[93]. Vroman, L.; Adams, A. L., Findings with the recording ellipsometer suggesting rapid exchange of specific plasma proteins at liquid/solid interfaces. *Surf. Sci.* **1969,** *16*, 438-446.

[94]. Nayak, S.; Lyon, L. A., Soft nanotechnology with soft nanoparticles. *Angew. Chem. Int. Ed.* **2005,** *44*, 7686-7708.

[95]. Heyes, D. M.; Branka, A. C., Interactions between microgel particles. *Soft Matter* **2009,** *5*, 2681-2685.

[96]. Peppas, N. A.; Hilt, J. Z.; Khademhosseini, A.; Langer, R., Hydrogels in Biology and Medicine: From Molecular Principles to Bionanotechnology. *Adv. Mater.* **2006,** *18*, 1345-1360.

[97]. Butun, V.; Atay, A.; Tuncer, C.; Bas, Y., Novel Multiresponsive Microgels: Synthesis and Characterization Studies. *Langmuir* **2011,** *27*, 12657-12665.

[98]. Kabanov, A. V.; Vinogradov, S. V., Nanogels as Pharmaceutical Carriers: Finite Networks of Infinite Capabilities. *Angew. Chem. Int. Ed.* **2009,** *48*, 5418-5429.

[99]. Li, Y. A.; Kleijn, J. M.; Stuart, M. A. C.; Slaghek, T.; Timmermans, J.; Norde, W., Mobility of lysozyme inside oxidized starch polymer microgels. *Soft Matter* **2011,** *7*, 1926-1935.

[100]. Pelton, R., Temperature-sensitive aqueous microgels. *Adv. Colloid Interface Sci.* **2000,** *85*, 1-33.

[101]. Tanaka, T.; Fillmore, D. J., Kinetics of Swelling of Gels. *J. Chem. Phys.* **1979,** *70*, 1214-1218.

[102]. Hertle, Y.; Zeiser, M.; Hasenöhrl, C.; Busch, P.; Hellweg, T., Responsive P(NIPAM-co-NtBAM) microgels: Flory–Rehner description of the swelling behaviour. *Colloid Polym. Sci.* **2010,** *288*, 1047-1059.

[103]. Trongsatitkul, T.; Budhlall, B. M., Multicore-Shell PNIPAm-co-PEGMa Microcapsules for Cell Encapsulation. *Langmuir* **2011,** *27*, 13468-13480.

[104]. Thorne, J.; Vine, G.; Snowden, M., Microgel applications and commercial considerations. *Colloid Polym. Sci.* **2011,** *289*, 625-646.

[105]. Alarcon, C. D. H.; Pennadam, S.; Alexander, C., Stimuli responsive polymers for biomedical applications. *Chem. Soc. Rev.* **2005,** *34*, 276-285.

[106]. Ionov, L.; Houbenov, N.; Sidorenko, A.; Stamm, M.; Minko, S., Stimuli-responsive command polymer surface for generation of protein gradients. *Biointerphases* **2009,** *4*, Fa45-Fa49.

[107]. Stuart, M. A. C.; Huck, W. T. S.; Genzer, J.; Muller, M.; Ober, C.; Stamm, M.; Sukhorukov, G. B.; Szleifer, I.; Tsukruk, V. V.; Urban, M.; Winnik, F.; Zauscher, S.; Luzinov, I.; Minko, S., Emerging applications of stimuli-responsive polymer materials. *Nat. Mater.* **2010,** *9*, 101-113.

[108]. Berndt, I.; Pedersen, J. S.; Richtering, W., Structure of multiresponsive "intelligent" core-shell microgels. *J. Am. Chem. Soc.* **2005,** *127*, 9372-9373.

[109]. Karg, M.; Wellert, S.; Pastoriza-Santos, I.; Lapp, A.; Liz-Marzan, L. M.; Hellweg, T., Thermoresponsive core-shell microgels with silica nanoparticle cores: size, structure, and volume phase transition of the polymer shell. *Phys. Chem. Chem. Phys.* **2008,** *10*, 6708-6716.

[110]. Hendrickson, G. R.; Lyon, L. A., Bioresponsive hydrogels for sensing applications. *Soft Matter* **2009,** *5*, 29-35.

[111]. Blackburn, W. H.; Dickerson, E. B.; Smith, M. H.; McDonald, J. F.; Lyon, L. A., Peptide-functionalized nanogels for targeted siRNA delivery. *Bioconjugate Chem.* **2009,** *20*, 960-968.

[112]. Sorrell, C. D.; Lyon, L. A., Bimodal swelling responses in microgel thin films. *J. Phys. Chem. B* **2007,** *111*, 4060-4066.

[113]. Deen, G. R.; Alsted, T.; Richtering, W.; Pedersen, J. S., Synthesis and characterization of nanogels of poly(N-isopropylacrylamide) by a combination of light and small-angle X-ray scattering. *Phys. Chem. Chem. Phys.* **2011,** *13*, 3108-3114.

[114]. Huber, D. L.; Manginell, R. P.; Samara, M. A.; Kim, B. I.; Bunker, B. C., Programmed adsorption and release of proteins in a microfluidic device. *Science* **2003,** *301*, 352-354.

[115]. Shamim, N.; Liang, H.; Hidajat, K.; Uddin, M. S., Adsorption, desorption, and conformational changes of lysozyme from thermosensitive nanomagnetic particles. *J. Colloid Interface Sci.* **2008,** *320*, 15-21.

[116]. Lopez-Leon, T.; Fernandez-Nieves, A., Macroscopically probing the entropic influence of ions: Deswelling neutral microgels with salt. *Phys. Rev. E* **2007,** *75*, 011801.

[117]. Mano, J. F., Stimuli-responsive polymeric systems for biomedical applications. *Adv. Eng. Mater.* **2008,** *10*, 515-527.

[118]. Hendrickson, G. R.; Smith, M. H.; South, A. B.; Lyon, L. A., Design of Multiresponsive Hydrogel Particles and Assemblies. *Adv. Funct. Mater.* **2010,** *20*, 1697-1712.

[119]. Kleinen, J.; Klee, A.; Richtering, W., Influence of Architecture on the Interaction of Negatively Charged Multisensitive Poly(N-isopropylacrylamide)-co-Methacrylic Acid Microgels with Oppositely Charged Polyelectrolyte: Absorption vs Adsorption. *Langmuir* **2010,** *26*, 11258-11265.

[120]. Nayak, S.; Gan, D.; Serpe, M. J.; Lyon, L. A., Hollow thermoresponsive microgels. *Small* **2005,** *1*, 416-421.

[121]. Hu, X. B.; Tong, Z.; Lyon, L. A., Multicompartment Core/Shell Microgels. *J. Am. Chem. Soc.* **2010,** *132*, 11470-11472.

[122]. Nayak, S.; Lee, H.; Chmielewski, J.; Lyon, L. A., Folate-mediated cell targeting and cytotoxicity using thermoresponsive microgels. *J. Am. Chem. Soc.* **2004,** *126*, 10258-10259.

[123]. Naha, P. C.; Casey, A.; Tenuta, T.; Lynch, I.; Dawson, K. A.; Byrne, H. J.; Davoren, M., Preparation, characterization of NIPAM and NIPAM/BAM copolymer nanoparticles and their acute toxicity testing using an aquatic test battery. *Aquat. Toxicol.* **2009,** *92*, 146-154.

[124]. Hoare, T.; Pelton, R., Impact of microgel morphology on functionalized microgel-drug interactions. *Langmuir* **2008,** *24*, 1005-1012.

[125]. Johansson, C.; Hansson, P.; Malmsten, M., Interaction between lysozyme and poly(acrylic acid) microgels. *J. Colloid Interface Sci.* **2007,** *316*, 350-359.

[126]. Kabanov, V. A.; Skobeleva, V. B.; Rogacheva, V. B.; Zezin, A. B., Sorption of proteins by slightly cross-linked polyelectrolyte hydrogels: Kinetics and mechanism. *J. Phys. Chem. B* **2004,** *108*, 1485-1490.

[127]. Dingenouts, N.; Norhausen, C.; Ballauff, M., Observation of the volume transition in thermosensitive core-shell latex particles by small-angle X-ray scattering. *Macromolecules* **1998,** *31*, 8912-8917.

[128]. Seelenmeyer, S.; Deike, I.; Dingenouts, N.; Rosenfeldt, S.; Norhausen, C.; Ballauff, M.; Narayanan, T., Analysis of the volume transition in thermosensitive core-shell particles by synchrotron small-angle X-ray scattering. *J. Appl. Crystallogr.* **2000,** *33*, 574-576.

[129]. Dingenouts, N.; Seelenmeyer, S.; Deike, I.; Rosenfeldt, S.; Ballauff, M.; Lindner, P.; Narayanan, T., Analysis of thermosensitive core-shell colloids by small-angle neutron scattering including contrast variation. *Phys. Chem. Chem. Phys.* **2001,** *3*, 1169-1174.

[130]. Crassous, J. J.; Wittemann, A.; Siebenburger, M.; Schrinner, M.; Drechsler, M.; Ballauff, M., Direct imaging of temperature-sensitive core-shell latexes by cryogenic transmission electron microscopy. *Colloid Polym. Sci.* **2008,** *286*, 805-812.

[131]. Crassous, J. J.; Rochette, C. N.; Wittemann, A.; Schrinner, M.; Ballauff, M.; Drechsler, M., Quantitative Analysis of Polymer Colloids by Cryo-Transmission Electron Microscopy. *Langmuir* **2009,** *25*, 7862-7871.

[132]. Crassous, J. J.; Siebenburger, M.; Ballauff, M.; Drechsler, M.; Henrich, O.; Fuchs, M., Thermosensitive core-shell particles as model systems for studying the flow behavior of concentrated colloidal dispersions. *J. Chem. Phys.* **2006,** *125*, 204906.

[133]. Senff, H.; Richtering, W.; Norhausen, C.; Weiss, A.; Ballauff, M., Rheology of a temperature sensitive core-shell latex. *Langmuir* **1999,** *15*, 102-106.

[134]. Siebenburger, M.; Fuchs, M.; Winter, H.; Ballauff, M., Viscoelasticity and shear flow of concentrated, noncrystallizing colloidal suspensions: Comparison with mode-coupling theory. *J. Rheol.* **2009,** *53*, 707-726.

[135]. Flory, P. J.; Rehner, J. J., Statistical Mechanics of Cross-Linked Polymer Networks I. Rubberlike Elasticity. *J. Chem. Phys.* **1943,** *11*, 512-520.

[136]. Flory, P. J.; Rehner, J. J., Statistical Mechanics of Cross-Linked Polymer Networks II. Swelling. *J. Chem. Phys.* **1943,** *11*, 521-526.

[137]. Kratz, K.; Hellweg, T.; Eimer, W., Influence of charge density on the swelling of colloidal poly(N-isopropylacrylamide-co-acrylic acid) microgels. *Colloids Surf., A* **2000,** *170*, 137-149.

[138]. Capriles-Gonzalez, D.; Sierra-Martin, B.; Fernandez-Nieves, A.; Fernandez-Barbero, A., Coupled deswelling of multiresponse microgels. *J. Phys. Chem. B* **2008,** *112*, 12195-12200.

[139]. Horkay, F.; Tasaki, I.; Basser, P. J., Osmotic swelling of polyacrylate hydrogels in physiological salt solutions. *Biomacromolecules* **2000,** *1*, 84-90.

[140]. Dubrovskii, S. A.; Rakova, G. V.; Lagutina, M. A.; Kazanskii, K. S., Osmotic properties of poly(ethylene oxide) gels with localized charged units. *Polymer* **2001,** *42*, 8075-8083.

[141]. Fernandes, P. A. L.; Schmidt, S.; Zeiser, M.; Fery, A.; Hellweg, T., Swelling and mechanical properties of polymer gels with cross-linking gradient. *Soft Matter* **2010,** *6*, 3455-3458.

[142]. Geissler, E.; Horkay, F.; Hecht, A.-M., Structure and thermodynamics of flexible polymer gels. *J. Chem. Phys.* **1994,** *100*, 8418-8424.

[143]. Obukhov, S. P.; Rubinstein, M.; Colby, R. H., Network Modulus and Superelasticity. *Macromolecules* **1994,** *27*, 3191-3198.

[144]. Horkay, F.; Zrinyi, M., Studies on the mechanical and swelling behavior of polymer networks based on the scaling concept. 4. Extension of the scaling approach to gels swollen to equilibrium in a diluent of arbitrary activity. *Macromolecules* **1982,** *15*, 1306-1310.

[145]. Hu, Z.; Li, C.; Li, Y., The scaling exponents of polyacrylamide and acrylamide-sodium acrylate copolymer gels. *J. Chem. Phys.* **1993,** *99*, 7108-7114.

[146]. Fernandez-Barbero, A.; Suarez, I. J.; Sierra-Martin, B.; Fernandez-Nieves, A.; de las Nieves, F. J.; Marquez, M.; Rubio-Retama, J.; Lopez-Cabarcos, E., Gels and microgels for nanotechnological applications. *Adv. Colloid Interface Sci.* **2009,** *147-48*, 88-108.

[147]. Hirotsu, S., Softening of bulk modulus and negative Poisson's ratio near the volume phase transition of polymer gels. *J. Chem. Phys.* **1991,** *94*, 3949-3957.

[148]. Puhse, M.; Keerl, M.; Scherzinger, C.; Richtering, W.; Winter, R., Influence of pressure on the state of poly(N-isopropylacrylamide) and poly(N,N-diethylacrylamide) derived polymers in aqueous solution as probed by FTIR-spectroscopy. *Polymer* **2010,** *51*, 3653-3659.

[149]. Cheng, H.; Shen, L.; Wu, C., LLS and FTIR studies on the hysteresis in association and dissociation of poly(N-isopropylacrylamide) chains in water. *Macromolecules* **2006,** *39*, 2325-2329.

[150]. Lin, S. Y.; Chen, K. S.; Liang, R. C., Thermal micro ATR/FT-IR spectroscopic system for quantitative study of the molecular structure of poly(N-isopropylacrylamide) in water. *Polymer* **1999,** *40*, 2619-2624.

[151]. Maeda, Y.; Yamabe, M., A unique phase behavior of random copolymer of N-isopropylacrylamide and N,N-diethylacrylamide in water. *Polymer* **2009,** *50*, 519-523.

[152]. Maeda, Y.; Yamamoto, H.; Ikeda, I., Effects of ionization on the phase behavior of poly(N-isopropylacrylamide-co-acrylic acid) and poly(N,N-diethylacrylamide-co-acrylic acid) in water. *Colloid Polym. Sci.* **2004,** *282*, 1268-1273.

[153]. Maeda, Y.; Nakamura, T.; Ikeda, I., Change in solvation of poly(N,N-diethylacrylamide) during phase transition in aqueous solutions as observed by IR spectroscopy. *Macromolecules* **2002,** *35*, 10172-10177.

[154]. Maeda, Y.; Higuchi, T.; Ikeda, I., Change in hydration state during the coil-globule transition of aqueous solutions of poly(N-isopropylacrylamide) as evidenced by FTIR spectroscopy. *Langmuir* **2000,** *16*, 7503-7509.

[155]. Sun, B. J.; Lin, Y. N.; Wu, P. Y.; Siesler, H. W., A FTIR and 2D-IR spectroscopic study on the microdynamics phase separation mechanism of the poly(N-isopropylacrylamide) aqueous solution. *Macromolecules* **2008,** *41*, 1512-1520.

[156]. Keerl, M.; Smirnovas, V.; Winter, R.; Richtering, W., Interplay between hydrogen bonding and macromolecular architecture leading to unusual phase behavioir in thermosensitive micirogels. *Angew. Chem. Int. Ed.* **2008,** *47*, 338-341.

[157]. Sun, S.; Hu, J.; Tang, H.; Wu, P., Spectral interpretation of thermally irreversible recovery of poly(N-isopropylacrylamide-co-acrylic acid) hydrogel. *Phys. Chem. Chem. Phys.* **2011,** *13*, 5061-5067.

[158]. Sun, S.; Hu, J.; Tang, H.; Wu, P., Chain Collapse and Revival Thermodynamics of Poly(N-isopropylacrylamide) Hydrogel. *J. Phys. Chem. B* **2010,** *114*, 9761-9770.

[159]. Jackson, M.; Mantsch, H. H., The use and misuse of FTIR spectroscopy in the determination of protein structure. *Crit. Rev. Biochem. Mol. Biol.* **1995,** *30*, 95-120.

[160]. Tribolo, S.; Berrin, J.-G.; Kroon, P. A.; Czjzek, M.; Juge, N., The Crystal Structure of Human Cytosolic β-Glucosidase Unravels the Substrate Aglycone Specificity of a Family 1 Glycoside Hydrolase. *J. Mol. Biol.* **2007,** *370*, 964-975.

[161]. Henrissat, B.; Davies, G., Structural and sequence-based classification of glycoside hydrolases. *Curr. Opin. Struct. Biol.* **1997,** *7*, 637-644.

[162]. Zechel, D. L.; Withers, S. G., Glycosidase Mechanisms: Anatomy of a Finely Tuned Catalyst. *Acc. Chem. Res.* **2000,** *33*, 11-18.

[163]. Sengupta, S.; Ghosh, A. K.; Sengupta, S., Purification and characterisation of a β-glucosidase (cellobiase) from a mushroom Termitomyces clypeatus. *Biochim. Biophys. Acta, Protein Struct. Mol. Enzymol.* **1991,** *1076*, 215-220.

[164]. Bhat, M. K.; Bhat, S., Cellulose degrading enzymes and their potential industrial applications. *Biotechnol. Adv.* **1997,** *15*, 583-620.

[165]. Grover, A. K.; David MacMurchie, D.; Cushley, R. J., Studies on almond emulsin βd-glucosidase I. Isolation and characterization of a bifunctional isozyme. *Biochim. Biophys. Acta, Enzymol.* **1977,** *482*, 98-108.

[166]. He, S.; Withers, S. G., Assignment of Sweet Almond β-Glucosidase as a Family 1 Glycosidase and Identification of Its Active Site Nucleophile. *J. Biol. Chem.* **1997,** *272*, 24864-24867.

[167]. Czjzek, M.; Cicek, M.; Zamboni, V.; Burmeister, W. P.; Bevan, D. R.; Henrissat, B.; Esen, A., Crystal structure of a monocotyledon (maize ZMGlu1) beta-glucosidase and a model of its complex with p-nitrophenyl beta-D-thioglucoside. *Biochem. J.* **2001,** *354*, 37-46.

[168]. Protein Data Bank PDB. http://www.rcsb.org/pdb/.

[169]. Newman, J.; Cacatian, A.; Josephson, A.; Tsang, A., Spinal-Fluid Lysozyme in the Diagnosis of Central-Nervous-System Tumors. *Lancet* **1974,** *304*, 756-757.

[170]. Arnheim, N.; Wilson, A. C., Quantitative Immunological Comparison of Bird Lysozymes. *J. Biol. Chem.* **1967,** *242*, 3951-3956.

[171]. Callewaert, L.; Walmagh, M.; Michiels, C. W.; Lavigne, R., Food applications of bacterial cell wall hydrolases. *Curr. Opin. Biotechnol.* **2011,** *22*, 164-171.

[172]. Sava, G., Pharmacological aspects and therapeutic applications of lysozymes. *EXS* **1996,** *75*, 433-449.

[173]. Blake, C. C. F.; Koenig, D. F.; Mair, G. A.; North, A. C. T.; Phillips, D. C.; Sarma, V. R., Structure of Hen Egg-White Lysozyme: A Three-dimensional Fourier Synthesis at 2 Angstrom Resolution. *Nature* **1965,** *206*, 757-761.

[174]. Kubiak-Ossowska, K.; Mulheran, P. A., Mechanism of Hen Egg White Lysozyme Adsorption on a Charged Solid Surface. *Langmuir* **2010,** *26*, 15954-15965.

[175]. Canfield, R. E., The Amino Acid Sequence of Egg White Lysozyme. *J. Biol. Chem.* **1963,** *238*, 2698-2707.

[176]. Yano, Y. F.; Uruga, T.; Tanida, H.; Toyokawa, H.; Terada, Y.; Takagaki, M.; Yamada, H., Driving Force Behind Adsorption-Induced Protein Unfolding: A Time-Resolved X-ray Reflectivity Study on Lysozyme Adsorbed at an Air/Water Interface. *Langmuir* **2009,** *25*, 32-35.

[177]. Dousseau, F.; Pezolet, M., Determination of the Secondary Structure-Content of Proteins in Aqueous-Solutions from Their Amide-I and Amide-Ii Infrared Bands - Comparison between Classical and Partial Least-Squares Methods. *Biochemistry* **1990,** *29*, 8771-8779.

[178]. Vertegel, A. A.; Siegel, R. W.; Dordick, J. S., Silica nanoparticle size influences the structure and enzymatic activity of adsorbed lysozyme. *Langmuir* **2004,** *20*, 6800-6807.

[179]. Izutsu, K.-i.; Fujimaki, Y.; Kuwabara, A.; Hiyama, Y.; Yomota, C.; Aoyagi, N., Near-infrared analysis of protein secondary structure in aqueous solutions and freeze-dried solids. *J. Pharm. Sci.* **2006,** *95*, 781-789.

[180]. Kuehner, D. E.; Engmann, J.; Fergg, F.; Wernick, M.; Blanch, H. W.; Prausnitz, J. M., Lysozyme Net Charge and Ion Binding in Concentrated Aqueous Electrolyte Solutions. *J. Phys. Chem. B* **1999,** *103*, 1368-1374.

[181]. Jensen, H.; Hartvig, R. A.; van de Weert, M.; Ostergaard, J.; Jorgensen, L., Protein Adsorption at Charged Surfaces: The Role of Electrostatic Interactions and Interfacial Charge Regulation. *Langmuir* **2011,** *27*, 2634-2643.

[182]. Phillips, D. C., THE Hen Egg-White Lysozyme Molecule. *Proc. Natl. Acad. Sci. U.S.A.* **1967,** *57*, 483-495.

[183]. Salemme, F. R., Structure and Function of Cytochromes C. *Annu. Rev. Biochem.* **1977,** *46*, 299-330.

[184]. Mirkin, N.; Jaconcic, J.; Stojanoff, V.; Moreno, A., High resolution X-ray crystallographic structure of bovine heart cytochrome c and its application to the design of an electron transfer biosensor. *Proteins: Struct., Funct., Bioinf.* **2008,** *70*, 83-92.

[185]. Smith, M. H.; Lyon, L. A., Tunable Encapsulation of Proteins within Charged Microgels. *Macromolecules* **2011,** *44*, 8154-8160.

[186]. Nakashima, T.; Higa, H.; Matsubara, H.; Benson, A. M.; Yasunobu, K. T., The Amino Acid Sequence of Bovine Heart Cytochrome c. *J. Biol. Chem.* **1966,** *241*, 1166-1177.

[187]. Carbeck, J. D.; Colton, I. J.; Anderson, J. R.; Deutch, J. M.; Whitesides, G. M., Correlations Between the Charge of Proteins and the Number of Ionizable Groups They Incorporate: Studies Using Protein Charge Ladders, Capillary Electrophoresis, and Debye−Hückel Theory. *J. Am. Chem. Soc.* **1999,** *121*, 10671-10679.

[188]. Pelton, J. T.; McLean, L. R., Spectroscopic Methods for Analysis of Protein Secondary Structure. *Anal. Biochem.* **2000,** *277*, 167-176.

[189]. Barrera, F. N.; Garzón, M. T.; Gómez, J.; Neira, J. L., Equilibrium Unfolding of the C-Terminal SAM Domain of p73†. *Biochemistry* **2002,** *41*, 5743-5753.

[190]. Butler, B. C.; Hanchett, R. H.; Rafailov, H.; MacDonald, G., Investigating Structural Changes Induced By Nucleotide Binding to RecA Using Difference FTIR. *Biophys. J.* **2002,** *82*, 2198-2210.

[191]. Castellanos, I. J.; Cruz, G.; Crespo, R.; Griebenow, K., Encapsulation-induced aggregation and loss in activity of γ-chymotrypsin and their prevention. *J. Controlled Release* **2002,** *81*, 307-319.

[192]. Vanstokkum, I. H. M.; Linsdell, H.; Hadden, J. M.; Haris, P. I.; Chapman, D.; Bloemendal, M., Temperature-Induced Changes in Protein Structures Studied by Fourier-Transform Infrared-Spectroscopy and Global Analysis. *Biochemistry* **1995,** *34*, 10508-10518.

[193]. Nölting, B., *Methods in Modern Biophysics*. Springer: Berlin, 2003.

[194]. Winter, R.; Noll, F.; Czeslik, C., *Methoden der Biophysikalischen Chemie*. 2nd ed.; Vieweg und Teubner: Wiesbaden, 2011.

[195]. Protein Infrared Database. http://www.unco.edu/nhs/faculty/dong/irdata/htm.

[196]. Fabian, H.; Schultz, C. P., Fourier Transform Infrared Spectroscopy in Peptide and Protein Analysis. In *Encyclopedia of Analytical Chemistry*, John Wiley & Sons, Ltd: 2006.

[197]. Kalnin, N. N.; Baikalov, I. A.; Venyaminov, S., Quantitative IR spectrophotometry of peptide compounds in water (H2O) solutions. III. Estimation of the protein secondary structure. *Biopolymers* **1990,** *30*, 1273-1280.

[198]. Rahmelow, K.; Hübner, W., Secondary Structure Determination of Proteins in Aqueous Solution by Infrared Spectroscopy: A Comparison of Multivariate Data Analysis Methods. *Anal. Biochem.* **1996,** *241*, 5-13.

[199]. Surewicz, W. K.; Mantsch, H. H.; Chapman, D., Determination of protein secondary structure by Fourier transform infrared spectroscopy: A critical assessment. *Biochemistry* **1993,** *32*, 389-394.

[200]. Kauppinen, J. K.; Moffatt, D. J.; Cameron, D. G.; Mantsch, H. H., Noise in Fourier self-deconvolution. *Appl. Opt.* **1981,** *20*, 1866-1879.

[201]. Haaland, D. M.; Thomas, E. V., Partial least-squares methods for spectral analyses. 1. Relation to other quantitative calibration methods and the extraction of qualitative information. *Anal. Chem.* **1988,** *60*, 1193-1202.

[202]. Henzler, K.; Wittemann, A.; Breininger, E.; Ballauff, M.; Rosenfeldt, S., Adsorption of bovine hemoglobin onto spherical polyelectrolyte brushes monitored by small-angle x-ray scattering and Fourier transform infrared Spectroscopy. *Biomacromolecules* **2007,** *8*, 3674-3681.

[203]. Copeland, R. A., *Enzymes*. 2nd ed.; Wiley-VCH: New York, 2000.

[204]. Bisswanger, H., *Enzyme Kinetics*. Wiley-VCH: Weinheim, 2002.

[205]. Peterson, M. E.; Daniel, R. M.; Danson, M. J.; Eisenthal, R., The dependence of enzyme activity on temperature: determination and validation of parameters. *Biochem. J.* **2007,** *402*, 331-337.

[206]. Guohua, C.; Hoffman, A. S., Synthesis of carboxylated poly(NIPAAm) oligomers and their application to form thermo-reversible polymer-enzyme conjugates. *J. Biomater. Sci., Polym. Ed.* **1994,** *5*, 371-382.

[207]. Yang, Y.; Hamaguchi, K., Hydrolysis of 4-Methylumbelliferyl N-Acetyl-Chitrotrioside Catalyzed by Hen and Turkey Lysozymes - pH-Dependence of the Kinetic Constants. *J. Biochem.* **1980,** *87*, 1003-1014.

[208]. Kawaguchi, H.; Fujimoto, K.; Mizuhara, Y., Hydrogel microspheres III. Temperature-dependent adsorption of proteins on poly-N-isopropylacrylamide hydrogel microspheres. *Colloid Polym. Sci.* **1992,** *270*, 53-57.

[209]. Grabstain, V.; Bianco-Peled, H., Mechanisms Controlling the Temperature-Dependent Binding of Proteins to Poly(N-isopropylacrylamide) Microgels. *Biotechnol. Prog.* **2003,** *19*, 1728-1733.

[210]. Halperin, A.; Kroger, M., Collapse of Thermoresponsive Brushes and the Tuning of Protein Adsorption. *Macromolecules* **2011,** *44*, 6986-7005.

[211]. Cole, M. A.; Voelcker, N. H.; Thissen, H.; Horn, R. G.; Griesser, H. J., Colloid probe AFM study of thermal collapse and protein interactions of poly(N-isopropylacrylamide) coatings. *Soft Matter* **2010,** *6*, 2657-2667.

[212]. Cole, M. A.; Jasieniak, M.; Thissen, H.; Voelcker, N. H.; Griesser, H. J., Time-of-Flight-Secondary Ion Mass Spectrometry Study of the Temperature Dependence of Protein Adsorption onto Poly(N-isopropylacrylamide) Graft Coatings. *Anal. Chem.* **2009,** *81*, 6905-6912.

[213]. Cheng, X. H.; Canavan, H. E.; Graham, D. J.; Castner, D. G.; Ratner, B. D., Temperature dependent activity and structure of adsorbed proteins on plasma polymerized N-isopropyl acrylamide. *Biointerphases* **2006,** *1*, 61-72.

[214]. Hoshino, Y.; Koide, H.; Furuya, K.; Haberaecker, W. W.; Lee, S. H.; Kodama, T.; Kanazawa, H.; Oku, N.; Shea, K. J., The rational design of a synthetic polymer nanoparticle that neutralizes a toxic peptide in vivo. *Proc. Natl. Acad. Sci. U.S.A.* **2012,** *109*, 33-38.

[215]. Johansson, C.; Gernandt, J.; Bradley, M.; Vincent, B.; Hansson, P., Interaction between lysozyme and colloidal poly(NIPAM-co-acrylic acid) microgels. *J. Colloid Interface Sci.* **2010,** *347*, 241-251.

[216]. Huo, D.; Li, Y.; Qian, Q.; Kobayashi, T., Temperature-pH sensitivity of bovine serum albumin protein-microgels based on cross-linked poly(N-isopropylacrylamide-co-acrylic acid). *Colloids Surf., B* **2006,** *50*, 36-42.

[217]. Yan, C.; Elaissari, A.; Pichot, C., Loading and Release Studies of Proteins Using Poly(N-isopropylacrylamide) Based Nanogels. *J. Biomed. Nanotechnol.* **2006,** *2*, 208-216.

[218]. Lund, M.; Jonsson, B., On the charge regulation of proteins. *Biochemistry* **2005,** *44*, 5722-5727.

[219]. Lund, M., Electrostatic Chameleons in Biological Systems. *J. Am. Chem. Soc.* **2010,** *132*, 17337-17339.

[220]. da Silva, F. L. B.; Jonsson, B., Polyelectrolyte-protein complexation driven by charge regulation. *Soft Matter* **2009,** *5*, 2862-2868.

[221]. Kirkwood, J. G.; Shumaker, J. B., Forces between Protein Molecules in Solution Arising from Fluctuations in Proton Charge and Configuration. *Proc. Natl. Acad. Sci. U.S.A.* **1952,** *38*, 863-871.

[222]. de Vos, W. M.; Leermakers, F. A. M.; de Keizer, A.; Stuart, M. A. C.; Kleijn, J. M., Field Theoretical Analysis of Driving Forces for the Uptake of Proteins by Like-Charged Polyelectrolyte Brushes: Effects of Charge Regulation and Patchiness. *Langmuir* **2010,** *26*, 249-259.

[223]. Biesheuvel, P. M.; Wittemann, A., A modified box model including charge regulation for protein adsorption in a spherical polyelectrolyte brush. *J. Phys. Chem. B* **2005,** *109*, 4209-4214.

[224]. Zydney, A. L.; Pujar, N. S., Protein transport through porous membranes: effects of colloidal interactions. *Colloids Surf., A* **1998,** *138*, 133-143.

[225]. Longo, G. S.; Olvera de la Cruz, M.; Szleifer, I., Molecular Theory of Weak Polyelectrolyte Gels: The Role of pH and Salt Concentration. *Macromolecules* **2011,** *44*, 147-158.

[226]. Biesheuvel, P. M.; van der Veen, M.; Norde, W., A modified Poisson-Boltzmann model including charge regulation for the adsorption of ionizable polyelectrolytes to charged interfaces, applied to lysozyme adsorption on silica. *J. Phys. Chem. B* **2005,** *109*, 4172-4180.

[227]. Bysell, H.; Hansson, P.; Malmsten, M., Effect of Charge Density on the Interaction between Cationic Peptides and Oppositely Charged Microgels. *J. Phys. Chem. B* **2010,** *114*, 7207-7215.

[228]. Bysell, H.; Ransson, P.; Schmidtchen, A.; Malmsten, M., Effect of Hydrophobicity on the Interaction between Antimicrobial Peptides and Poly(acrylic acid) Microgels. *J. Phys. Chem. B* **2010,** *114*, 1307-1313.

[229]. Langmuir, I., The Adsorption of Gases on Plane Surfaces of Glass, Mica and Platinum. *J. Am. Chem. Soc.* **1918,** *40*, 1361-1403.

[230]. Dill, K. A.; Bromberg, S., *Molecular Driving Forces*. Garland Science Taylor & Francis Group: New York, 2003.

[231]. Felsovalyi, F.; Mangiagalli, P.; Bureau, C.; Kumar, S. K.; Banta, S., Reversibility of the Adsorption of Lysozyme on Silica. *Langmuir* **2011,** *27*, 11873-11882.

[232]. Lassen, B.; Malmsten, M., Competitive Protein Adsorption at Plasma Polymer Surfaces. *J. Colloid Interface Sci.* **1997,** *186*, 9-16.

[233]. Green, R. J.; Davies, M. C.; Roberts, C. J.; Tendler, S. J., Competitive protein adsorption as observed by surface plasmon resonance. *Biomaterials* **1999,** *20*, 385-391.

[234]. Wojciechowski, P.; Ten Hove, P.; Brash, J. L., Phenomenology and mechanism of the transient adsorption of fibrinogen from plasma (Vroman effect). *J. Colloid Interface Sci.* **1986,** *111*, 455-465.

[235]. Gun'ko, V. M.; Mikhalovska, L. I.; Tomlins, P. E.; Mikhalovsky, S. V., Competitive adsorption of macromolecules and real-time dynamics of Vroman-like effects. *Phys. Chem. Chem. Phys.* **2011,** *13*, 4476-4485.

[236]. Gong, P.; Szleifer, I., Competitive adsorption of model charged proteins: the effect of total charge and charge distribution. *J. Colloid Interface Sci.* **2004,** *278*, 81-90.

[237]. Černík, M.; Borkovec, M.; Westall, J. C., Affinity Distribution Description of Competitive Ion Binding to Heterogeneous Materials. *Langmuir* **1996,** *12*, 6127-6137.

[238]. Ladbury, J. E.; Chowdhry, B. Z., *Biocalorimtery*. JohnWiley&Sons: Chichester, 1998.

[239]. Ladbury, J. E.; Doyle, M. L., *Biolaclorimetry 2*. JohnWiley&Sons: Chichester, 2004.

[240]. Demers, J. P.; Mittermaier, A., Binding Mechanism of an SH3 Domain Studied by NMR and ITC. *J. Am. Chem. Soc.* **2009,** *131*, 4355-4367.

[241]. Bergqvist, S.; O'Brien, R.; Ladbury, J. E., Site-specific cation binding mediates TATA binding protein-DNA interaction from a hyperthermophilic archaeon. *Biochemistry* **2001,** *40*, 2419-2425.

[242]. Duff, M. R.; Kumar, C. V., Protein-Solid Interactions: Important Role of Solvent, Ions, Temperature, and Buffer in Protein Binding to alpha-Zr(IV) Phosphate. *Langmuir* **2009,** *25*, 12635-12643.

[243]. Rieger, J.; Freichels, H.; Imberty, A.; Putaux, J. L.; Delair, T.; Jerome, C.; Auzely-Velty, R., Polyester Nanoparticles Presenting Mannose Residues: Toward the Development of New Vaccine Delivery Systems Combining Biodegradability and Targeting Properties. *Biomacromolecules* **2009,** *10*, 651-657.

[244]. Dubin, P. L.; Xu, Y. S.; Mazzawi, M.; Chen, K. M.; Sun, L. H., Protein Purification by Polyelectrolyte Coacervation: Influence of Protein Charge Anisotropy on Selectivity. *Biomacromolecules* **2011,** *12*, 1512-1522.

[245]. Chen, K. M.; Xu, Y. S.; Rana, S.; Miranda, O. R.; Dubin, P. L.; Rotello, V. M.; Sun, L. H.; Guo, X. H., Electrostatic Selectivity in Protein-Nanoparticle Interactions. *Biomacromolecules* **2011,** *12*, 2552-2561.

[246]. Brown, A., Analysis of cooperativity by isothermal titration calorimetry. *Int. J. Mol. Sci.* **2009,** *10*, 3457-3477.

[247]. Wiseman, T.; Williston, S.; Brandts, J. F.; Lin, L. N., Rapid Measurement of Binding Constants and Heats of Binding Using a New Titration Calorimeter. *Anal. Biochem.* **1989,** *179*, 131-137.

[248]. Indyk, L.; Fisher, H. F., Theoretical aspects of isothermal titration calorimetry. *Methods Enzymol.* **1998,** *295*, 350-364.

[249]. Turnbull, W. B.; Daranas, A. H., On the value of c: Can low affinity systems be studied by isothermal titration calorimetry? *J. Am. Chem. Soc.* **2003,** *125*, 14859-14866.

[250]. Becker, A. L.; Welsch, N.; Schneider, C.; Ballauff, M., Adsorption of RNase A on Cationic Polyelectrolyte Brushes: A Study by Isothermal Titration Calorimetry. *Biomacromolecules* **2011,** *12*, 3936-3944.

[251]. Chaires, J. B., Possible origin of differences between van't Hoff and calorimetric enthalpy estimates. *Biophys. Chem.* **1997,** *64*, 15-23.

[252]. Nielsen, P. K.; Bonsager, B. C.; Berland, C. R.; Sigurskjold, B. W.; Svensson, B., Kinetics and energetics of the binding between barley alpha-amylase/subtilisin inhibitor and barley alpha-amylase 2 analyzed by surface plasmon resonance and isothermal titration calorimetry. *Biochemistry* **2003,** *42*, 1478-1487.

[253]. Winzor, D. J.; Jackson, C. M., Interpretation of the temperature dependence of equilibrium and rate constants. *J. Mol. Recognit.* **2006,** *19*, 389-407.

[254]. Kaya, H.; Chan, H. S., Polymer principles of protein calorimetric two-state cooperativity. *Proteins: Struct., Funct., Genet.* **2000,** *40*, 637-661.

[255]. Naghibi, H.; Tamura, A.; Sturtevant, J. M., Significant Discrepancies between van´t Hoff and Calorimetric Enthalpies. *Proc. Natl. Acad. Sci. U.S.A.* **1995,** *92*, 5597-5599.

[256]. Zhou, Y.; Hall, C. K.; Karplus, M., The calorimetric criterion for a two-state process revisited. *Protein Sci.* **1999,** *8*, 1064-1074.

[257]. Niedzwiecka, A.; Stepinski, J.; Darzynkiewicz, E.; Sonenberg, N.; Stolarski, R., Positive heat capacity change upon specific binding of translation initiation factor eIF4E to mRNA 5 ' cap. *Biochemistry* **2002,** *41*, 12140-12148.

[258]. Horn, J. R.; Russell, D.; Lewis, E. A.; Murphy, K. P., van't Hoff and calorimetric enthalpies from isothermal titration calorimetry: Are there significant discrepancies? *Biochemistry* **2001,** *40*, 1774-1778.

[259]. Horn, J. R.; Brandts, J. F.; Murphy, K. P., van't Hoff and calorimetric enthalpies II: Effects of linked equilibria. *Biochemistry* **2002,** *41*, 7501-7507.

[260]. Nilsson, A.; Wernet, P.; Nordlund, D.; Bergmann, U.; Cavalleri, M.; Odelius, M.; Ogasawara, H.; Näslund, L.-Å.; Hirsch, T. K.; Ojamäe, L.; Glatzel, P.; Pettersson, L. G. M., Comment on "Energetics of Hydrogen Bond Network Rearrangements in Liquid Water". *Science* **2005,** *308*, 793.

[261]. Smith, J. D.; Cappa, C. D.; Wilson, K. R.; Cohen, R. C.; Geissler, P. L.; Saykally, R. J., Unified description of temperature-dependent hydrogen-bond rearrangements in liquid water. *Proc. Natl. Acad. Sci. U.S.A.* **2005,** *102*, 14171-14174.

[262]. Azizian, S., Kinetic models of sorption: a theoretical analysis. *J. Colloid Interface Sci.* **2004,** *276*, 47-52.

[263]. Kim, J.; Deike, I.; Dingenouts, N.; Norhausen, C.; Ballauff, M., The volume transition in thermosensitive core-shell latex particles investigated by small-angle X-ray scattering and dynamic light scattering. *Macromol. Symp.* **1999,** *142*, 217-225.

[264]. Crassous, J. J.; Ballauff, M.; Drechsler, M.; Schmidt, J.; Talmon, Y., Imaging the volume transition in thermosensitive core-shell particles by cryo-transmission electron microscopy. *Langmuir* **2006,** *22*, 2403-2406.

[265]. Lide, D. R., *CRC Handbook of Chemistry and Physics*. 88th ed.; CRC Press Taylor & Francis Group: Boca Raton, 2008.

[266]. Morawetz, H., *High Polymers/Macromolecules in solution*. 2nd ed.; John Wiley & Sons: New York, 1975; Vol. 21.

[267]. Hoare, T.; Pelton, R., Titrametric characterization of pH-induced phase transitions in functionalized microgels. *Langmuir* **2006,** *22*, 7342-7350.

[268]. Taha, M.; Gupta, B. S.; Khoiroh, I.; Lee, M.-J., Interactions of Biological Buffers with Macromolecules: The Ubiquitous “Smart” Polymer PNIPAM and the Biological Buffers MES, MOPS, and MOPSO. *Macromolecules* **2011,** *44*, 8575-8589.

[269]. Burmistrova, A.; Richter, M.; Uzum, C.; Klitzing, R., Effect of cross-linker density of P(NIPAM-co-AAc) microgels at solid surfaces on the swelling/shrinking behaviour and the Young’s modulus. *Colloid Polym. Sci.* **2011,** *289*, 613-624.

[270]. Haupt, B.; Neumann, T.; Wittemann, A.; Ballauff, M., Activity of enzymes immobilized in colloidal spherical polyelectrolyte brushes. *Biomacromolecules* **2005,** *6*, 948-955.

[271]. Henzler, K.; Haupt, B.; Ballauff, M., Enzymatic activity of immobilized enzyme determined by isothermal titration calorimetry. *Anal. Biochem.* **2008,** *378*, 184-189.

[272]. Taniguchi, T.; Duracher, D.; Delair, T.; Elaïssari, A.; Pichot, C., Adsorption/desorption behavior and covalent grafting of an antibody onto cationic amino-functionalized poly(styrene-N-isopropylacrylamide) core-shell latex particles. *Colloids Surf., B* **2003,** *29*, 53-65.

[273]. Hansen, S. U.; Plesner, I. W.; Bols, M., Direct NMR-Spectroscopic Determination of Active-Enzyme Concentration by Titration with a Labeled Inhibitor: Determination of the kcat Value of Almond β-Glucosidase. *ChemBioChem* **2000,** *1*, 177-180.

[274]. Weber, J. P.; Fink, A. L., Temperature-dependent change in the rate-limiting step of beta-glucosidase catalysis. *J. Biol. Chem.* **1980,** *255*, 9030-9032.

[275]. Lu, Y.; Mei, Y.; Ballauff, M.; Drechsler, M., Thermosensitive core-shell particles as carrier systems for metallic nanoparticles. *J. Phys. Chem. B* **2006,** *110*, 3930-3937.

[276]. Ortega, N.; Busto, M. D.; Perez-Mateos, M., Optimisation of beta-glucosidase entrapment in alginate and polyacrylamide gels. *Bioresour. Technol.* **1998,** *64*, 105-111.

[277]. Israelachvili, J., *Intermolecular and Surface Forces*. Academic Press: London, 1995.

[278]. Zhang, J.; Pelton, R.; Deng, Y., Temperature-Dependent Contact Angles of Water on Poly(N-isopropylacrylamide) Gels. *Langmuir* **1995,** *11*, 2301-2302.

[279]. Chandler, D., Interfaces and the driving force of hydrophobic assembly. *Nature* **2005,** *437*, 640-647.

[280]. Dubin, P. L.; Chen, K. M.; Xu, Y. S.; Rana, S.; Miranda, O. R.; Rotello, V. M.; Sun, L. H.; Guo, X. H., Electrostatic Selectivity in Protein-Nanoparticle Interactions. *Biomacromolecules* **2011,** *12*, 2552-2561.

[281]. Leermakers, F. A. M.; Ballauff, M.; Borisov, O. V., On the mechanism of uptake of globular proteins by polyelectrolyte brushes: A two-gradient self-consistent field analysis. *Langmuir* **2007,** *23*, 3937-3946.

[282]. de Vos, W. M.; Biesheuvel, P. M.; de Keizer, A.; Kleijn, J. M.; Stuart, M. A. C., Adsorption of the protein bovine serum albumin in a planar poly(acrylic acid) brush layer as measured by optical reflectometry. *Langmuir* **2008,** *24*, 6575-6584.

[283]. Baker, B. M.; Murphy, K. P., Evaluation of linked protonation effects in protein binding reactions using isothermal titration calorimetry. *Biophys. J.* **1996,** *71*, 2049-2055.

[284]. Jelesarov, I.; Bosshard, H. R., Thermodynamics of Ferredoxin Binding to Ferredoxin:NADP+ Reductase and the Role of Water at the Complex Interface. *Biochemistry* **1994,** *33*, 13321-13328.

[285]. Ahl, I. M.; Jonsson, B. H.; Tibell, L. A. E., Thermodynamic Characterization of the Interaction between the C-Terminal Domain of Extracellular Superoxide Dismutase and Heparin by Isothermal Titration Calorimetry. *Biochemistry* **2009,** *48*, 9932-9940.

[286]. Jeppesen, M. D.; Westh, P.; Otzen, D. E., The role of protonation in protein fibrillation. *FEBS Lett.* **2010,** *584*, 780-784.

[287]. Goldberg, R. N.; Kishore, N.; Lennen, R. M., Thermodynamic quantities for the ionization reactions of buffers. *J. Phys. Chem. Ref. Data* **2002,** *31*, 231-370.

[288]. Gee, K. R.; Sun, W.-C.; Bhalgat, M. K.; Upson, R. H.; Klaubert, D. H.; Latham, K. A.; Haugland, R. P., Fluorogenic Substrates Based on Fluorinated Umbelliferones for Continuous Assays of Phosphatases and β-Galactosidases. *Anal. Biochem.* **1999,** *273*, 41-48.

[289]. Bunz, U. H.; Rotello, V. M., Gold nanoparticle-fluorophore complexes: sensitive and discerning "noses" for biosystems sensing. *Angew. Chem. Int. Ed.* **2010,** *49*, 3268-3279.

[290]. Lakowicz, J. R., *Principles of Fluorescence Spectroscopy*. 3rd ed.; Springer New York, 2006.

[291]. Martin, M. M.; Lindqvist, L., PH-Dependence of Fluorescein Fluorescence. *J. Lumin.* **1975,** *10*, 381-390.

[292]. Togashi, D. M.; Szczupak, B.; Ryder, A. G.; Calvet, A.; O'Loughlin, M., Investigating tryptophan quenching of fluorescein fluorescence under protolytic equilibrium. *J. Phys. Chem. A* **2009,** *113*, 2757-2767.

[293]. Margulies, D.; Melman, G.; Shanzer, A., Fluorescein as a model molecular calculator with reset capability. *Nat. Mater.* **2005,** *4*, 768-771.

[294]. Ohkuma, S.; Poole, B., Fluorescence probe measurement of the intralysosomal pH in living cells and the perturbation of pH by various agents. *Proc. Natl. Acad. Sci. U.S.A.* **1978,** *75*, 3327-3331.

[295]. Sipe, D. M.; Murphy, R. F., High-resolution kinetics of transferrin acidification in BALB/c 3T3 cells: exposure to pH 6 followed by temperature-sensitive alkalinization during recycling. *Proc. Natl. Acad. Sci. U.S.A.* **1987,** *84*, 7119-7123.

[296]. Lee, R. J.; Wang, S.; Low, P. S., Measurement of endosome pH following folate receptor-mediated endocytosis. *Biochim. Biophys. Acta, Mol. Cell Res.* **1996,** *1312*, 237-242.

[297]. Chen, R. F.; Knutson, J. R., Mechanism of fluorescence concentration quenching of carboxyfluorescein in liposomes: Energy transfer to nonfluorescent dimers. *Anal. Biochem.* **1988,** *172*, 61-77.

[298]. Lakowicz, J. R.; Malicka, J.; D'Auria, S.; Gryczynski, I., Release of the self-quenching of fluorescence near silver metallic surfaces. *Anal. Biochem.* **2003,** *320*, 13-20.

[299]. Hungerford, G.; Benesch, J.; Mano, J. F.; Reis, R. L., Effect of the labelling ratio on the photophysics of fluorescein isothiocyanate (FITC) conjugated to bovine serum albumin. *Photochem. Photbiol. Sci.* **2007,** *6*, 152-158.

[300]. Jönsson, U.; Ivarsson, B.; Lundström, I.; Berghem, L., Adsorption behavior of fibronectin on well-characterized silica surfaces. *J. Colloid Interface Sci.* **1982,** *90*, 148-163.

[301]. von Hippel, P. H.; Berg, O. G., Facilitated target location in biological systems. *J. Biol. Chem.* **1989,** *264*, 675-678.

[302]. Iwahara, J.; Clore, G. M., Detecting transient intermediates in macromolecular binding by paramagnetic NMR. *Nature* **2006,** *440*, 1227-1230.

[303]. Lazzara, T. D.; Mey, I.; Steinem, C.; Janshoff, A., Benefits and Limitations of Porous Substrates as Biosensors for Protein Adsorption. *Anal. Chem.* **2011,** *83*, 5624-5630.

[304]. Lu, Y.; Wittemann, A.; Ballauff, M., Supramolecular Structures Generated by Spherical Polyelectrolyte Brushes and their Application in Catalysis. *Macromol. Rapid Commun.* **2009,** *30*, 806-815.

[305]. Ladam, G.; Schaaf, P.; Decher, G.; Voegel, J.-C.; Cuisinier, F. J. G., Protein adsorption onto auto-assembled polyelectrolyte films. *Biomol. Eng.* **2002,** *19*, 273-280.

[306]. Laugel, N.; Betscha, C.; Winterhalter, M.; Voegel, J.-C.; Schaaf, P.; Ball, V., Relationship between the Growth Regime of Polyelectrolyte Multilayers and the Polyanion/Polycation Complexation Enthalpy. *J. Phys. Chem. B* **2006,** *110*, 19443-19449.

[307]. Hunter, R. J., *Foundations of Colloid Science*. 2nd ed.; Oxford University Press: Oxford, 2009.

[308]. Kratz, K.; Hellweg, T.; Eimer, W., Structural changes in PNIPAM microgel particles as seen by SANS, DLS, and EM techniques. *Polymer* **2001,** *42*, 6631-6639.

[309]. Kawaguchi, S.; Yekta, A.; Winnik, M. A., Surface characterization and dissociation properties of carboxylic acid core-shell latex particle by potentiometric and conductometric titration. *J. Colloid Interface Sci.* **1995,** *176*, 362-369.

[310]. Hoare, T.; Pelton, R., Highly pH and temperature responsive microgels functionalized with vinylacetic acid. *Macromolecules* **2004,** *37*, 2544-2550.

[311]. Westermeier, R., *Electrophoresis in Practice*. 3rd ed.; Wiley-VCH: Weinheim, 2001.

[312]. Pierce, M. M.; Raman, C. S.; Nall, B. T., Isothermal titration calorimetry of protein-protein interactions. *Methods* **1999,** *19*, 213-221.

List of Figures

List of Tables

List of Abbreviations

AAc	acrylic acid
APS	ammonium persulfate
BIS	N,N´-methylenebisacrylamide
BLG	beta-lactoglobulin
cyt c	cytochrome c
Cryo-TEM	cryogenic transmission electron microscopy
DSC	differential scanning calorimetry
DLS	dynamic light scattering
DNA	deoxyribonucleic acid
DP	differential power
FE-SEM	field emission scanning electron microscopy
FT-IR	Fourier transform infrared spectroscopy
FITC	fluorescein isothiocyanate
GFP	green fluorescent protein
$(GlcNAc)_3$-MeU	4-methylumbelliferyl-β-D-N, N',N"-triacetylchitotrioside
glcase	β-D-glucosidase
HSA	*human serum* albumin
IEF	isoelectric focusing
ITC	isothermal titration calorimetry
KPS	potassium peroxodisulfate
LCST	lower critical solution temperature
$lysozyme^{FITC}$	lysozyme tagged with FITC
MEMA	2-(N-morpholino)-ethyl methacrylate
MeU	4-methylumbelliferone
MOPS	3-(N-morpholino)propane sulfonic acid
MPS	mononuclear phagocyte system
NiPAm	N-isopropylacrylamide

o-NPG	ortho-nitrophenyl-β-D-glucopyranoside
PDA	photo diode array
PDB	protein data bank
pI	isoelectric point
PIPES	1,4-piperazinediethanesulfonic acid
PLS	partial least square method
pMEMA	poly(2-(N-morpholino)-ethyl methacrylate)
pNiPAm	poly(N-isopropylacrylamide)
PS	polystyrene
RET	resonance energy transfer
RNA	ribonucleic acid
SAXS	small angle x-ray scattering
SANS	small angle neutron scattering
SDS-PAGE	sodium dodecyl sulfate polyacrylamide gel electrophoresis
SPB	spherical polyelectrolyte brush
SPR	surface plasmon resonance
SSIS	single set of independent binding sites
SW-NIR	short wave near-infrared
TEMED	N,N,N´,N´-tetramethylethylenediamine
Tris	tris(hydroxymethyl)aminomethane
UF	ultrafiltration
UV-vis	ultraviolet-visible light
VPTT	volume phase transition temperature

List of Publications

- Welsch, N.; Wittemann, A.; Ballauff, M., Enhanced Activity of Enzymes Immobilized in Thermoresponsive Core-Shell Microgels. *J. Phys. Chem. B* **2009**, *113*, 16039-16045.

- Welsch, N.; Ballauff, M.; Lu, Y., Microgels as Nanoreactors: Applications in Catalysis. *Adv. Polym. Sci.* **2010**, *234*, 129-163.

- Becker, A. L.; Welsch, N.; Schneider, C.; Ballauff, M., Adsorption of RNase A on Cationic Polyelectrolyte Brushes: A Study by Isothermal Titration Calorimetry. *Biomacromolecules* **2011**, *12*, 3936-3944.

- Welsch, N.; Becker, A. L.; Dzubiella, J.; Ballauff, M., Core-Shell Microgels as "Smart" Carriers for Enzymes. *Soft Matter* **2012**, *8*, 1428-1436.

- Becker, A. L.; Henzler, K.; Welsch, N.; Ballauff, M.; Borisov, O., Proteins and Polyelectrolytes: A Charged Relationship. *Curr. Opin. Colloid Interface Sci.* **2012**, *17*, 90-96.

- Welsch, N.; Dzubiella, J.; Graebert, A.; Ballauff, M., Protein Binding to Soft Polymeric Layers: A Quantitative Study by Fluorescence Spectroscopy. *Soft Matter* **2012**, DOI: 10.1039/c2sm26798e.

- Yigit, C.; Welsch, N.; Ballauff, M.; Dzubiella, J.; Sorption of Proteins to Charged Microgels: Characterizing Binding Isotherms and Driving Forces. *Langmuir* **2012**,*28*, 14373-14385.

Presentations at Conferences and Meetings

- PNI-Meeting, Bonn, Germany, November 30 – December 1, 2009, *poster presentation*: Enhanced Activity of Enzymes Immobilized in Thermoresponsive Core-Shell Microgels.
- DPG-Frühjahrstagung, Regensburg, Germany, March 21 – 26, 2010, *poster presentation*: Enhanced Activity of Enzymes Immobilized in Thermoresponsive Core-Shell Microgels.
- 3rd International NanoBio Conference, Zurich, Switzerland, August 24 – 27, 2010, *poster presentation*: Investigating the Interactions between Proteins and Thermosensitive Microgels.
- SPP-Workshop "Hydrogels-Analysis", Aachen, Germany, October 7 – 8, 2010, *oral presentation*: Adsorption of Proteins on Thermosensitive Core-Shell Microgels.
- Frontiers in Polymer Science Conference, Lyon, France, May 29 – 31, 2011, *poster presentation*: Adsorption of Proteins on Thermosensitive Core-Shell Microgels.
- SPP-Conference Intelligente Hydrogele, Cologne, Germany, July 14 – 15, 2011, *oral presentation*: Interactions between Proteins and Charged Microgels.
- 242nd ACS National Meeting, Denver, USA, August 28 – September 1, 2011, *oral presentation*: Interactions between Proteins and Stimuli-Sensitive Core-Shell Nanoparticles Probed by Isothermal Titration Calorimetry.
- Dechema Jahrestreffen der Fachgruppe Grenzflächenbestimmte Systeme und Prozesse & Zerkleinern und Klassieren, Bad Dürkheim, Germany, March 13 – 14, 2012, *oral presentation*: Interactions between Proteins and Hydrogel Layers in Aqueous Solution.
- 243rd ACS National Meeting, San Diego, USA, March 25 – 29, 2012, *oral presentation*: Core-Shell Microgels as "Smart" Carriers for Enzymes.

Danksagung

Ich möchte mich an dieser Stelle bei all den Menschen bedanken, die mir während meines Studiums und meiner Promotion zur Seite gestanden haben.

An erster Stelle bedanke ich mich bei Prof. Dr. Matthias Ballauff für die anspruchsvolle und interessante Themenstellung, für seine Diskussionsbereitschaft und sein fortwährendes Interesse an meiner Arbeit. Des Weiteren möchte ich mich für sein Vertrauen und die Freiheit, meine Arbeit weitgehend selbst gestalten zu können, sowie die zahlreichen Möglichkeiten, an nationalen und internationalen Konferenzen teilnehmen zu können, herzlich bedanken.
Für die finanzielle Unterstützung danke ich der Deutschen Forschungsgemeinschaft (DFG) im Rahmen des Projekts „Hydrogele“ und des Sonderforschungsbereichs SFB 481 sowie dem Helmholtz-Zentrum Berlin für Materialien und Energie.
Bei Prof. Dr. Joachim Dzubiella möchte ich mich für die gute Zusammenarbeit bei der theoretischen Beschreibung der Thermodynamik und der Kinetik der Proteinadsorption bedanken. Diesbezüglich bedanke ich mich auch für die vielen, intensiven Gespräche und für die gute Zusammenarbeit bei den Veröffentlichungen.
Weiterhin möchte ich mich bei Prof. Dr. Alexander Wittemann für seine Einführung in das Thema dieser Arbeit sowie für seine Diskussionsbereitschaft und sein fortwährendes Interesse an meiner Arbeit bedanken.
Allen Mitarbeitern des Lehrstuhls für Physikalische Chemie I der Universität Bayreuth und des Instituts für Weiche Materie und Funktionale Materialien am Helmholtz-Zentrum Berlin danke ich für das gute Arbeitsklima und für die ständige Hilfs- und Diskussionsbereitschaft. Im Besonderen möchte ich mich bei Dr. Katja Henzler für die vielen wertvollen Gespräche in Zusammenhang meiner Arbeit und bei Dr. Alisa Becker für die hilfreichen Diskussionen und Anregungen im Bereich der Isothermalen Titrationskalorimetrie bedanken.
Des Weiteren danke ich all meinen Studienkollegen an der Universität Bayreuth und meinen Freunden. Besonders herzlich möchte ich mich bei meiner Familie bedanken, die mich während meines Studiums und der Promotion unterstützt und nie den Glauben an mich verloren hat.
André, ich danke dir für deinen unnachgiebigen Rückhalt in den letzten Jahren, für dein Verständnis und deine stets aufmunternden und motivierenden Worte. Du bist die Stütze und der Rückzugspunkt in meinem Leben und ich bin froh den Weg mit dir gemeinsam zu gehen.

Schlusserklärung

Hiermit erkläre ich, dass ich die vorliegende Arbeit selbstständig verfasst und keine anderen als die hier angegebenen Quellen und Hilfsmitteln benutzt habe.

Ferner erkläre ich, dass ich nicht anderweitig mit oder ohne Erfolg versucht habe, eine Dissertation einzureichen oder mich einer Doktorprüfung zu unterziehen.

Berlin, den 21.06.2012

…….

Nicole Welsch